The University of Sheffield

Department of Materials Science and Engineering

Understanding the wear and tribocorrosion processes and mechanisms of Titanium alloys in bovine serum solution

Submitted for the Degree of Doctor of Philosophy

Mozart Queiroz Neto

Supervisor: Professor W. Mark Rainforth

June 2019

Declaration

This thesis has been composed by me and has not been submitted or accepted in any previous degree application. The work has been conducted by me, except where due acknowledgement has been given.

- Presentations in conferences during this project:

1. Wear characteristics of Ti alloys for total hip replacement in simulated body fluid. 4th International Conference on BioTribology. Montreal, Canada. 2018.

2. An analysis of the body simulated deterioration of Ti alloys through tribocorrosion. NACE CORROSION 2018 Conference and Expo. Phoenix, USA. 2018.

3. Tribocorrosion properties of a titanium–based alloy in simulated biological environment. Student conference 2018, Sheffield, UK.

Acknowledgments

Abstract

With economic and health care improvements, the number of elderly people demanding failed tissue replacement growing rapidly due to aged population increases in representative countries. To date, people at the age of 65 have a life expectance of 17.9 years and implants have on average 15 years of durability. It has been given focus on the use of titanium in biomaterials owing to its properties, such as low density, high corrosion resistance and biocompatibility. The chemical stability as well as corrosion resistance and fast repassivation in a wide range of environments are due to the formation of a protective passive film. Furthermore, titanium–based alloys are free of toxic elements in their composition. Nevertheless, titanium–based alloys show poor tribological properties and the failures have been related to that characteristic. The failure rate of replacements is a consequence of the poor knowledge of the degradation mechanism. While wear and corrosion have long been identified as the problem limiting the long–term endurance of orthopaedic implants there remains a lack of understanding about the fundamental mechanisms and effects of tribocorrosion.

The aim of this work is to analyse four different titanium–based alloys Ti–13Nb–13Zr (αβ alloy), Ti–12Mo–6Zr–2Fe (Near β alloy), Ti–35Nb–13Ta–4.6Zr aged at 400ºC (β alloy) and Ti–35Nb–13Ta–4.6Zr aged at 300ºC (βω alloy) over wear tests at cathodic potential (–1 V vs OCP), open circuit potential and anodic potential (0.3 V vs OCP) at 0.5N, 1N and 2N normal load to understand the mechanisms and phenomena that occur when composition and production procedures change as a result of wear in a body simulated fluid approaching factors not well investigated in the literature.

This work is divided in two parts. The first part characterizes the tribocorrosion behaviour of those four titanium alloys at 0.5N and the second part compares these results to the effect of increasing normal load to 1N and 2N as well as the synergistic and mechanistic approach to analyse the material loss.

All alloys present a good corrosion resistance, but they become more active with rubbing contact. At 0.5N, 1N and 2N the COF does vary with electrochemical condition and material composition. All alloys show similar wear behaviour that changes only with applied potential, namely, the material loss, specific wear rate and wear rate increase with load and are lower at anodic

4

potential than at OCP or cathodic conditions. This suggests the formation of a tribofilm that acts as a lubricant reducing friction. The worn surface presented the same ploughing characteristics with no debris, reflecting abrasive wear as the main wear mechanism and a rougher surface at anodic potential. The organic layer was identified by backscattered electron images and confirmed by Raman spectroscopy in all electrochemical conditions and normal loads.

The mechanistic approach identified that mechanical wear was the dominant material removal mechanism in all of these alloys, with the electrochemical contribution irrelevant at all applied potentials. The electrochemical and mechanical contributions increased with normal load. In addition, the synergistic approach identified that wear enhanced corrosion rates and corrosion has a positive effect of reducing wear rate on these alloys and for this these alloys present an antagonistic effect. The synergistic approach confirms that mechanical wear is the predominant factor on material loss.

The reduced elastic modulus and nanohardness of the unworn and worn surfaces were measured by nanoindentation. Worn surfaces present higher values of these mechanical properties due to the formation of a nanocrystalline area at the subsurface. All alloys experienced minor α'' and ω phase induced transformation due to strain hardening, except the $\alpha\beta$ alloy.

Contents

Chapter 1 – Introduction

With economic and health care improvements, the number of elderly people demanding failed tissue replacement is growing rapidly due to aged population increases, as can be seen in Fig. 1.1 [1-3]. To date, people at the age of 65 have a life expectance of 17.9 years and implants have 15 years of durability [4-6].

Human joints suffer from degenerative problems such as osteoarthritis and osteoporosis. These degenerative problems bring degradation of the mechanical properties of the bone [1, 2]. However, 30% of all replacement surgical procedures are required by people aged below 65 years old. Not only elderly people need bone replacement, athletes and people that have suffered accident and trauma often require surgical procedure. In such cases, the prosthesis should have a longer lifetime [3, 4]. Although the failure percentage is low (10%), surgical revision procedure is difficult to perform and less likely to be successful in comparison to the initial surgical procedure, which adds to trauma and health care costs [5, 6]. Artificial biomaterials provide solutions for many of these issues. The application of biomaterials for orthopaedics include: hip, knee, shoulders, spinal fixation devices, cardiovascular stents and spinal discs [7, 8].
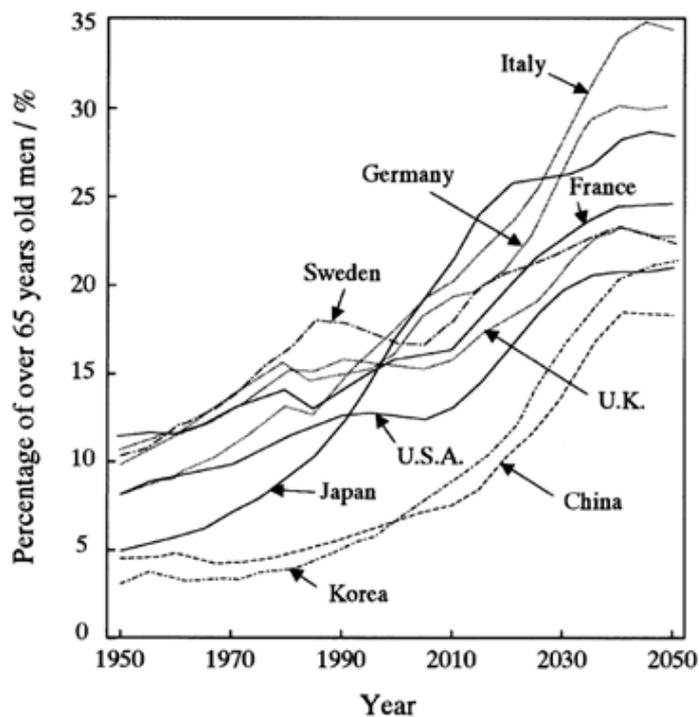
Fig. 1.1 – Growth of aged people in countries with large population [9].

The 16th National Joint Registry (NJR) Annual Report provides outcome data in relation to hip, knee, ankle, shoulder and elbow replacements in the United Kingdom. It describes activity between 1 April 2003 and 31 December 2018. There were 2,766,764 procedures entered into the NJR across all joint types, performed up to 31 December 2018. After removing procedures without linkage identifiers and those procedures where the linkage was not sufficiently clear to allow their use, there remained 2,332,798 primary cases and 66,248 linked revisions. This represents over a quarter of a million new cases being registered during the year. There were 1,091,892 primary total hip replacements, 1,193,830 knee replacements, 5,587 ankle replacements, 37,916 shoulder replacements and 3,573 elbow replacements, Fig. 1.2 [10].
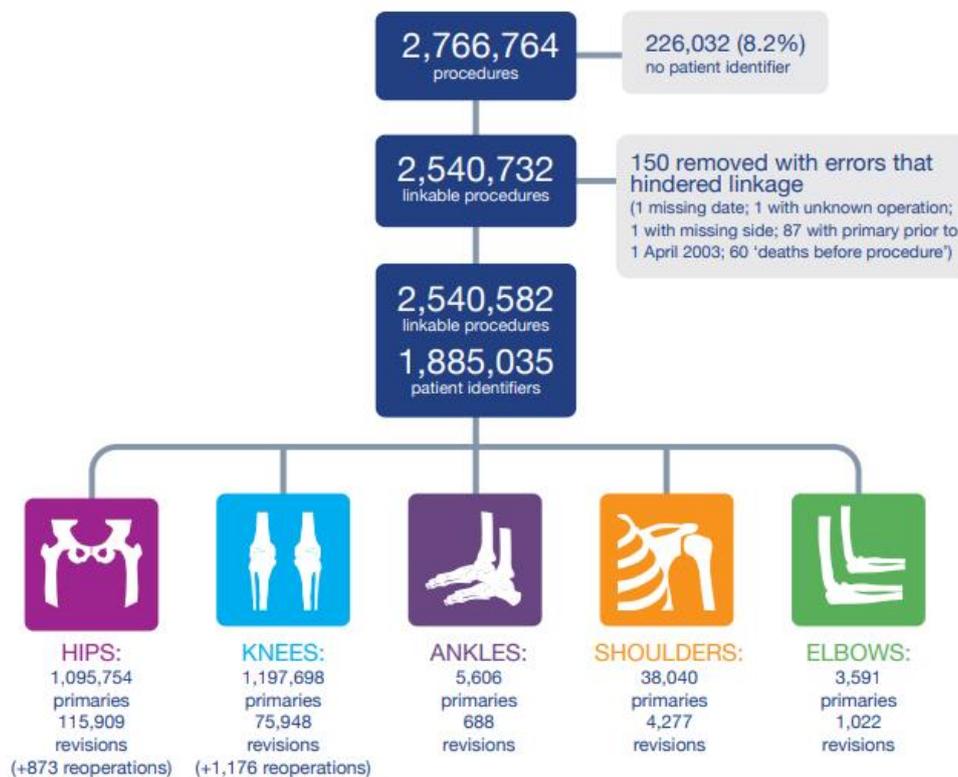
Fig. 1.2 – Joint replacements registered by NJR from 2003 to 2018 [10].

The causes for revision surgical procedure include the stress shielding effect between bone and prosthesis, which is the most common [6]; and necrosis caused by corrosion and wear debris around the prosthesis. Necrosis is often related to loaded replacements [11]. The revision operation percentage is low is comparison to the number of patients with only one primary joint operation, Table 1.1 [10].

Table 1.1 – Comparison of number of patients with only one primary joint operation and revision operation from 2003 to 2018 [10].

	Joints				
	Hips	Knees	Ankles	Shoulders	Elbows
Number of patients	927,571	963,846	5,330	35,265	3,441
Number (%) of patients with only one primary joint operation	763,074 (82.3%)	733,732 (76.1%)	5,073 (95.2%)	32,614 (92.5%)	3,309 (96.2%)
Number (%) of patients with both a left and right side primary operation but on different dates	159,561 (17.2%)	217,791 (22.6%)	249 (4.7%)	2,625 (7.4%)	129 (3.7%)
Number (%) of patients with both a left and right side operation on the same date (bilateral operations)	4,936 (0.5%)	12,323 (1.3%)	8 (0.2%)	26 (0.1%)	3 (0.1%)
Total number of primary joints	1,092,068	1,193,960	5,587	37,916	3,573
Number with at least one revision operation linked to the primary	31,410	33,292	265	1,158	123
Number with more than one revision procedure	4,739*	5,801*	29 (15)**	152 (105)**	22 (13)**

Table 1.2 shows the breakdown of cases by the method of fixation and within each fixation sub-group, by bearing surfaces. The most commonly used operation type overall cemented metal-on-polyethylene (88.0% of all cemented primaries, 28.5% of all primaries) between 2003 and 2019 in UK [10].

Table 1.2 - Number and percentage of primary hip replacements by fixation and bearing [10].

Fixation	N (%)	Bearing surface within fixation group	N (%)
All cases	1,091,892 (100)		1,091,892 (100)
All cemented	353,050 (32.3)	MoP	310,690 (28.5)
		MoM	394 (<0.1)
		CoP	41,955 (3.8)
		Others	11 (<0.1)
All uncemented	410,296 (37.6)	MoP	161,460 (14.8)
		MoM	29,066 (2.7)
		CoP	92,258 (8.4)
		CoC	125,287 (11.5)
		CoM	2,119 (0.2)
		Others	106 (<0.1)
All hybrid	227,432 (20.8)	MoP	135,831 (12.4)
		MoM	2,369 (0.2)
		CoP	63,532 (5.8)
		CoC	25,621 (2.3)
		Others	79 (<0.1)
All reverse hybrid	28,789 (2.6)	MoP	19,745 (1.8)
		CoP	8,998 (0.8)
		Others	46 (<0.1)
All resurfacing	39,246 (3.6)	MoM	39,104 (3.6)
		Others	142 (<0.1)
Unsure	33,079 (3.0)	Unsure	33,079 (3.0)

The biomaterials used for prosthesis include metals such as Cobalt Chromium alloys and Titanium alloys, polymer such as UHMWPE and ceramics such as alumina. None of them are free of concerns. Metals are linked to the toxic nature of some elements. Polymeric materials show good biocompatibility;

however, the lifetime is short and ceramics lack good mechanical proprieties [12, 13].

The most used metallic materials for joint replacement are Cobalt Chromium based alloys, stainless steel and Titanium alloys [3]. However, Titanium and its alloys are emerging as the optimum choice because of their qualities and benefits: elastic modulus lower than Cobalt Chromium alloy or stainless steel; exceptional biocompatibility and corrosion resistance. Nevertheless, these alloys were originally developed for aerospace use [14].

The focus of biomaterials development are to develop a lower elastic modulus material with more acceptable biocompatibility and better corrosion resistance than those materials found in the market such as CoCr alloys and stainless steel. β Titanium alloys already have these properties, but the poor wear resistance of these alloys is a drawback. Ti alloys are not used for tribological interface (joints) due to their inherent bad properties, they are used normally as stem. Pins, bone plates, screws, fracture plates, expandable rib cages, intramedullary rods and dental prosthetics are common applications for Ti alloys. CoCr alloys are often used in combination with Ti alloys to significantly lower micro-motions and fretting corrosion.

Then, developing new Titanium alloys with improved wear resistance could be a solution. Moreover, the tribocorrosion processes and mechanisms of titanium alloys are not fully understood. Thus, this project aims to contribute and to understand the tribocorrosion behaviour of Titanium alloys in simulated body solution, important for future alloy developments.

The ASTM F1108 alloy (Ti–6Al–4V) is the most used Titanium alloy in the biomedical field and it has been a central long-standing biomedical Titanium alloy. This alloy is an αβ type alloy and has toxic alloying elements: Vanadium (V) and Aluminium (Al). That can bring problems associated with inflammatory cell reaction and the progress of Alzheimer's disease [15, 16]. Ti–6Al–4V alloy has an elastic modulus of 110 GPa, much higher than the elastic modulus of bone, 20 GPa. Lately, alloying elements like Niobium, Tantalum, Zirconium, Tin and Molybdenum have been widely used to produce new beta Titanium alloys because of their β stabilizer features, better biocompatibility and mechanical properties, and outstanding corrosion resistance [5, 17].

CP Ti was initially used as dental and orthopaedic application and no toxicity was observed [14, 18]. However, this alloy did not have appropriated wear

resistance and high strength [19]. This is the reason for the development of new alloys for this application. The most used Titanium alloy (TI64) is composed of two toxic elements (Al and V), has high elastic modulus and poor wear resistance. The presence of Al and V also might cause neurological disorder and can delay osseointegration [19, 20]. Sahu [21] reported that corrosion rate of Ti alloys with more than one phase is higher than a single phase alloy.

There is limited work which is focused on the tribocorrosion behaviour of Ti alloys and that relates to the microstructure. However, tribocorrosion is a crucial factor oin biomedical applications such as joints and generally all types of Ti alloys are subjected to tribocorrosion when implanted [22, 23]. Also, retrieved materials studies revealed that all implants containing metals suffer degradation due to tribocorrosion effect. It causes implant loosening, fatigue failures and adverse reactions on the interfaces. The market growth rate of this area is 20% – 25% because of life span growth that will keep increasing. This can stimulate the market, but there is still a gap between the supply and demand related to undeveloped medical technology. Researchers in materials science and engineering are looking for development of β–titanium alloys for different applications with improved properties. The significance of the theme, growing research concern and enormous unexplored potential are the motivating factors for development and design of new β–titanium alloys for biomedical application [2]. The biomaterial investigation has a clear aim and likely applications. Implantation materials, comprehensive properties of low elastic modulus, high strength, outstanding wear and corrosion resistance, and enhanced biocompatibility are features that scientists have been pursuing [4, 17].

It is not clear yet what is the optimum composition and optimum microstructure for resistance to tribocorrosion. There has not been clear investigations into whether a single β phase alloy or an αβ alloy is preferable. Is a metastable β phase alloy better or worse than a fully stabilised β phase alloy. The effect of the presence of ω phase on tribocorrosion has not been considered at all. Also, corrosion and wear are not normally considered in synergy and are usually studied separately [23, 24]. Ti can be alloyed with Nb, Mo, Ta and Zr and produce β phase alloys with wide range of composition and microstructure. On the basis of these unknowns, this study aims to understand four different Titanium alloys with systematic differences in microstructure and with different

compositions to understand the effect of these key variables on the tribocorrosion behaviour.

Reproducing in–vivo conditions using in–vitro tests is not an easy task. However, it is essential to understand the material behaviour. One of the drawbacks is the use of lubricant ideal to mimic synovial fluid. In this study, new-born bovine serum was used because it gives a comparable protein response. In order to compare to other studies, it was used a concentration of 25% volume of new–born calf serum solution that gives a protein concentration of 15.5 g/L. This study focused on the reciprocating sliding wear behaviour of Titanium alloys in that solution. This project has the following main aims related to the Titanium alloys studied:

1. To understand the effects of microstructure and composition on tribology, corrosion and tribocorrosion behaviour in bovine serum and generate recommendations for the ideal microstructure and composition.
2. To understand the synergism of corrosion and wear of Titanium alloys in bovine serum when normal load and potential change.
3. To analyse the tribofilm formation and nanocrystalline formation and their relationship with tribocorrosion performance.

In the current study, reciprocating sliding wear tests of titanium alloys were carried out in the above lubricant using a ball–on–flat configuration. Loads used were 0.5N, 1N and 2N and the reciprocating frequency was 5 Hz over a stroke length of 2 mm. The worn surfaces were characterised in detail using Scanning Electron Microscopy (SEM) and Focused Ion Beam (FIB) cross–section milling. Transmission Electron Microscopy (TEM) was used to identify the modifications on subsurface. 3D microscope (ContourGT) was used to analyse the morphology of the wear track and finally Raman spectroscopy to identify the presence of the organic layer.

The thesis has been structured in the following way:

Chapter 2: gives the necessary literature to this project. It contains details about hip replacement surgery, the current status of biomaterials, biocompatibility, metallic materials used as biomaterials, the metallurgy of Titanium, tribocorrosion proprieties and biocompatibility of titanium and its alloys, limitation of titanium alloys, basics of corrosion, tribology and tribocorrosion.

Chapter 3: gives details about sample composition and sample preparation by arc melting, heat treatment and rolling and details of experimental procedures, equipment and techniques used in this project such as tribocorrosion machine and electrochemical parameters, XRD, Raman spectroscopy, 3D microscope, scanning electron microscopy, nanoindentation, focus ion beam and transmission electron microscopy for structure analysis, as well as the preparation of the electrolyte (bovine serum) used.

Chapter 4: gives the characteristics and proprieties of the materials used in this project. It details the microstructure by backscattered electrons image as well as XRD and the polarization behaviour by Tafel curves of the alloys.

Chapter 5: this chapter shows the results and discussion and it is divided in two parts. The first part studies the tribocorrosion behaviour of the titanium alloys at 0.5N using data from tribocorrosion test, 3D microscope, SEM and Raman spectroscopy. Also, it presents the mechanical proprieties (nanoindentation) and TEM images from the worn surface and subsurface respectively. The second part is focused on the effect of normal load on tribocorrosion behaviour of Titanium alloys. It is focused on a comparison of results from 1N and 2N using data from tribocorrosion test, 3D microscope, SEM and Raman spectroscopy. The synergism of wear and corrosion is also studied by mechanistic and synergistic approach. Finally, an analysis of the tribolayer formed at 2N at anodic potential is made by TEM and EDX.

Chapter 6: discusses the tribocorrosion process as well as its characterization of the studied alloys presented on chapter 5.

Chapter 7: summarises all the chapters and gives conclusions and new finding for this project.

Chapter 8: recommendations and suggestions for future work is presented.

Chapter 2 – Literature Review

2.2   Introduction

This chapter presents the literature review. First it presents the background of total hip replacement surgery, biocompatibility, corrosion and the wear resistance of metals, their use as biomaterials and in Total Hip Replacement. The background to Titanium and its alloys is then presented, including the physical metallurgy of Titanium, types of Titanium alloys, tribological properties, biocompatibility and corrosion properties and the limitations. Finally, basic theories of corrosion and its principles are presented, including corrosion of biomaterials, tribology, principles and mechanisms and current status of Titanium alloys as orthopaedic implants are reviewed.

2.3   Total hip replacement

2.3.1   Background of hip replacement surgery

Osteoarthritis is the cause health issues for around 15% of adults [25]. A medical procedure where the whole joint is replaced by a prothesis is called a total joint replacement [26, 27]. The most common procedures are Total Hip Replacement (THR) and Total Knee Replacement (TKR) with around £2 billion a year is spent globally on THR. Currently about 50,000 hip replacements are performed in the United Kingdom annually while worldwide the number is over 300,000. [28, 29]. According to the Swedish National Hip Arthroplasty Register, 91% of this cost is new surgery and 9% is revision [26].

The main group receiving prosthesis in the UK are people aged from 45 to 70 years old, in the early period of joint issues. However, the group of young people is growing due to accidental damage and health issues such as arthritis. This group need a safer prothesis that lasts longer [30-32]. It means the number of people who have hip joint issues is rising. According to the National Joint Registry UK the most common material used as femoral head replacements are metals (76%) [25]. Moreover, metallic prothesis release metallic ions to the body and it is an area of concern [33]. Also, 10% of the prothesis need a revision before

5 years for several factors [25, 32]. Wear is the main reason connected to these revisions and corrosion is another issue since it is a cause of ion release. These two factors are the focus of the research to improve wear behaviour and biocompatibility of alloys used as biomaterials [34].

THR is a well-developed and successful procedure, with the procedure and material science developed in synchrony. The first THR took place in 1891 in Berlin by Gluck that used an Ivory ball in socket [35, 36]. The following 50 years showed a slow development where several materials were tested but there were many failures. [37, 38]. Reports concluded that those materials had a poor wear behaviour. After 1950, metal on metal, metal on polymer and ceramic on ceramic prostheses were developed and lasted longer [39-41]. Polymers are still used now because they show low wear [42]. However, combination of metals and polymers are linked to loosening effect. It is now possible to find materials combination that last 15 or more years. Although these combinations suit elder people, these materials do not suit young people because this group of people will need to change the replacement at least once during life which brings pain, high costs and the chance of success is low [43].

Mechanical proprieties of the prothesis are important, such as toughness and ductility, due to constant movement and gravity [44]. The other important mechanical proprieties of prothesis will be discussed later. During walking, the relative movement of the joint prothesis causes wear [36]. The femoral head, which is in contact with the bone, needs appropriate material selection, polished surface, low friction, low wear and be compatible to reduce material degradation such as corrosion and wear [44].

Also very important is that the implant should have capacity to integrate with nearby bone. Also, the implant should not suffer micromotions because it may cause implant failure. In addition, fibrous tissue will appear on contact with bone and the implant, if it is not incorporated into the bone. Thus, biomaterials with a suitable surface are vital for the replacement to incorporate to nearby bone. Proprieties related to development of acceptable osseointegration are: surface chemistry, surface roughness and surface morphology. In addition, Titanium based alloys and ceramic materials like Alumina and Zirconia are inert materials to the body environment [45].

2.3.2 Metals used as biomaterials

Biomaterials can be defined by all materials that can replace a failed biological structure. Biomaterials can be natural or artificial [12]. Not all parts of the body can be replaced by natural biomaterials to date [14]. In addition, the characteristics of a biomaterial rely on the application [46].

The properties that materials for bio–application should have are biomechanical properties (stiffness, strength, fracture toughness, wear resistance and low friction, fatigue strength, low elastic modulus, dimensional stability and processability or workability) and biomedical properties (no toxicity, corrosion resistance and good osseointegration) [12]. In addition, the elastic modulus should be closer to bone to avoid the stress shielding effect and it should support tissue and blood growth (compatibility) [14]. Several reactions occur when materials are inserted in human body and the tolerability of these materials by our body relies on these reactions. Concerns relating to biocompatibility are thrombosis and the fibrous tissue encapsulation [46].

The issues caused by toxicity of metals is called metallosis. It is usually defined as aseptic fibrosis, local necrosis, or loosening of a device secondary to metallic corrosion and release of wear debris and only 2% to 5% of patients present metallosis. However, metallosis leads to several issues such as heart problems, depression, anxiety, visual impairment, cognitive impairment, nerve problems, thyroid problem, auditory impairment, infection and implant loosening. It is normally associated to CoCr alloys [47-52]. The mechanical properties are important factors to select the type of material for a particular use. The fatigue strength of the material is a reaction to the repetitive cyclic loads or strains. The durable success of the replacement subjected to cyclic loading relies on this property [12]. Biomechanical incompatibility is defined as a fracture due to incompatibility in the mechanical properties between bone and the replacement device. In particular the elastic modulus of the replacement and the bone should be as close as possible. If there is no stress being transferred to surrounding bone because of the higher stiffness of the implant than bone, implant loosening will occur. The effect that promotes death of bone cells is named stress shielding. Healthy bone needs to be mechanically stimulated to promote cell growth and if

this does not happen, atrophy will occur [18]. The elastic modulus of biometallic materials is about 20 times higher than of bone, see in Fig. 2.1 [53].
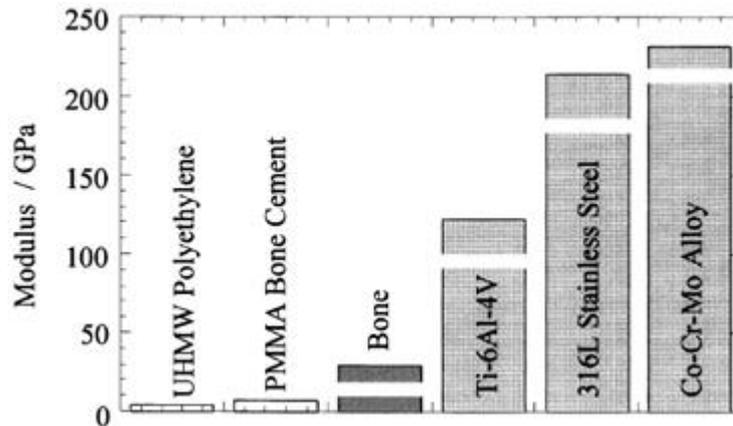

Fig. 2.1 – Comparison of elastic modulus: bone and other biomaterials [9].

In comparison to adult bones, youthful bones have higher elasticity and lower strength and hardness [12]. The bones of elderly people show lower elasticity, plasticity and strength in comparison to adults. In addition, there is no difference on mechanical properties among male and female samples [18, 53].

The tensile strength can be adjusted by the addition alloying elements or via heat treatment. It leads to solid solution strengthening or precipitation of phases. However, the elastic modulus is quite different. This propriety is not sensitive to grain size [18] and an important way to reduce the elastic modulus is introducing porosity into material. At about 30% of porosity, Titanium's elastic modulus is close to human bone, as can be seen in Fig. 2.2. However, porosity severely reduces all the mechanical properties [54].

The elastic modulus for a material that contains two phases is dependent upon the elastic modulus of the microconstituents of the alloys and it is calculated by equation 1 [18, 54].

$$E = V1 \times E1 + (1-V1) \times E2 \qquad \text{Eq. 1}$$

Where:

V1 = Volume fraction of phase 1

E1 = Elastic modulus of phase 1

E2 = Elastic modulus of phase 2
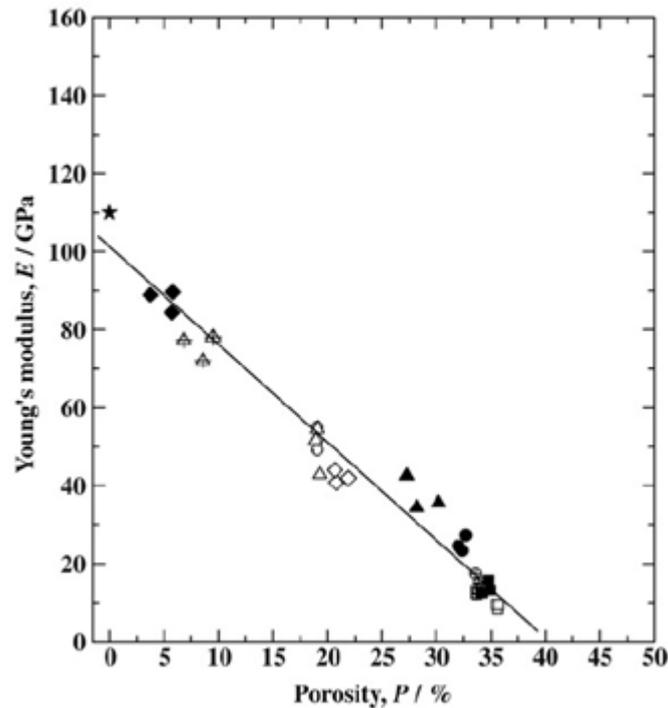
Fig. 2.2 – Relationship between elastic modulus and porosity [54].

Artificial implant materials can be made of metallic materials, ceramic materials and polymeric materials. New generation of biomaterials have been developed such as carbon–carbon and carbon polymer composites because their elastic modulus is nearer to bone. However, they are prone to degradation on the human body [14, 55].

Metallic biomaterials have the largest history among biomedical materials and approximately 80% of biomedical replacements are made of metallic materials. To date, the metallic materials used for biomedical application are 316L stainless steel, Cobalt Chromium alloys and Titanium alloys [4]. Stainless steel was the first one to be successfully used as an implant. After this, Cobalt–based alloys were introduced with the trademark Vitallium alloy. Titanium was the last metal to be used as a biomaterial and it is the most popular biometalic alloy to date [6]. These materials tend to fail after long–term implantation due to reasons already cited, such as the elastic modulus being higher than bone and problems with biocompatibility related to corrosion and wear resistance [9].

Where implants have been introduced, Nickel (Ni), Chromium (Cr) and Cobalt (Co) are usually found in the body due to ion release from stainless steel and CoCr alloys from corrosion. Co is a carcinogenic element. Moreover, both elements are found in alloys which have a higher elastic modulus than bone [9].

The elastic modulus of different alloys is shown in Fig. 2.3. CoCr alloys are an important group of alloys in the biomedical field because they have a wear resistance better than stainless steel and Titanium alloys [56]. New CoCr alloys have been developed free from Nickel. They are usually used as the head of hip prosthesis [57].
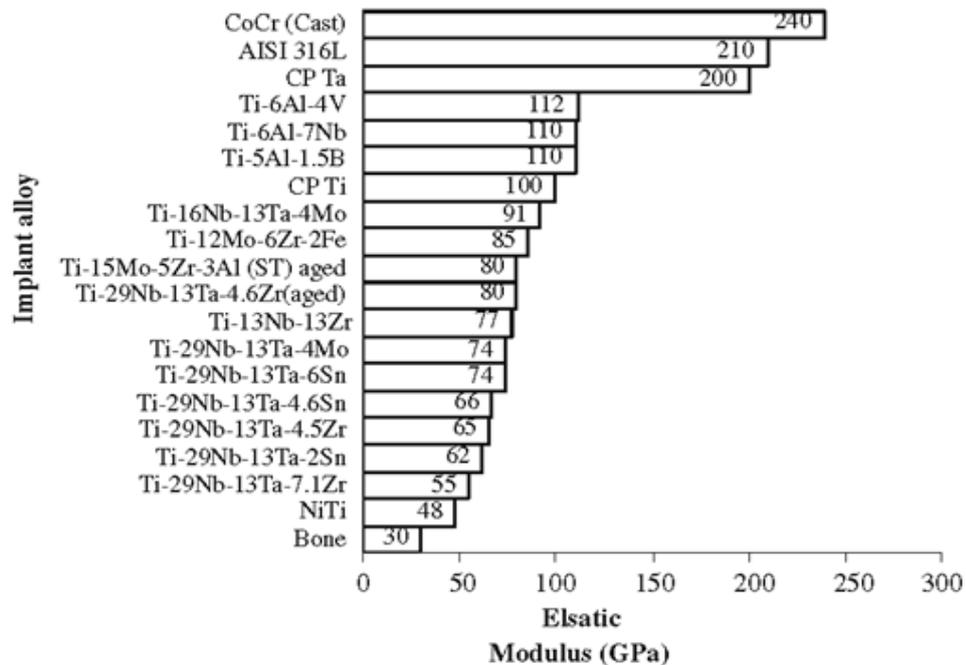

Fig. 2.3 – Comparison of elastic modulus among different alloys and bone [12].

The elastic modulus of Titanium alloys is lower than other alloys used as biomaterial like stainless steel and Cobalt chromium alloys. Likewise, the elastic modulus of β–titanium alloys is lower than α–titanium alloys and αβ –titanium alloys. However, the elastic modulus of β–titanium alloys is still higher than human bone [58]. Some publications report that the elastic deformation behaviour depends on crystal orientation. Therefore a low modulus single crystal of Titanium alloy may present an elastic modulus less than the lowest elastic modulus of β–titanium alloys and therefore this single crystal alloy may be appropriate as a biomaterial. The elastic modulus of β titanium alloys increases with precipitation of α on aging treatment, with the strength also increasing from heat treatment. In addition, elastic modulus cannot be controlled by aging treatment [18].

Cobalt based alloys for biomedical uses are in two groups: cast and wrought. Cast alloys may have a significant quantity of nickel to enhance the process of casting. Also, another group is the low nickel Cobalt–based alloys. Wrought Cobalt based biomedical alloys, the amount of Nickel is minimised due the Nickel allergy problems. The same occurs in stainless steel for biomedical

application. The quantity of carbon is also minimised due to its effect on the workability. The development of these kinds of alloys have not yet been concluded. The wear resistance is usually enhanced by the dispersed carbides and the reason is the existence of a low quantity of carbon. The wear resistance can be enhanced by deformation–induced conversion of the metastable phases of these alloys [45]. The CoCr alloys for this application are: ASMT F 75, ASTM F 799 and ASTM F 1537. The composition of these alloys are Co (bal.), Cr (19-35%), Mo (0-10%) and Ni (0-37%). They are particularly useful due to the superior wear resistance, corrosion resistance and fatigue strength [14].

Stainless steels are valuable biomaterials. The austenitic 316L stainless steel is the only stainless steel used as a biomaterial [45]. The 316L stainless steel have a large quantity of Nickel and therefore there is a risk of the Nickel sensitivity. Problems related to pitting corrosion and crevice corrosion on prosthesis made of this alloy have been reported [56]. A stainless steel containing no Nickel was created at an initial step pursuing a significant quantity of Nitrogen and Manganese [57]. Ni is used because it is the most effective austenite stabilizer. Given that the biocompatibility of Manganese is not fully known, a methodology to produce a large quantity of Nitrogen stainless steel by the pressurized electron spin resonance (ESR) technique has been established. Nevertheless, it is challenging to produce final goods of high–N stainless steel given the difficulty in mechanically working them [59]. The ASTM F 138 alloy is the only stainless steel applied as a biomaterial. Its composition is Fe (bal.), Cr (17-20%), Ni (12-14%) and Mo (2-4%). They are particularly useful due to the cost, availability and processing [14].

Tantalum and Niobium are candidates for biomaterial use because of their good electrochemical performance and biocompatibility. However, they have poor mechanical strength. Other candidates for biomedical application are amorphous alloys because their strength, corrosion resistance and low elastic modulus. Nevertheless, they contain a high quantity of toxic elements [9].

The first attempt to use Titanium as a biomaterial was in the 1930s in cat femurs. However, it was chosen for biomaterial application due to its corrosion resistance [9, 56]. The strength of Titanium alloys and 316L stainless steel are very similar, but Titanium has a density 55% lower than that stainless steel. The Titanium alloys used for biomedical application are: ASTM F 67, ASTM F 136 and ASTM F 1295. Their composition are: Ti (bal.), Al (6%), V (4%) and Nb (7%).

They are used particularly due to the acceptable biocompatibility, corrosion resistance, lower elastic modulus and fatigue strength. Table 2.1 gives a comparison of some features on metallic biomaterials [57].

Table 2.1 – Advantages, disadvantages and main characteristics of stainless steel, cobalt base alloys and titanium alloys [14].

	Stainless steels	Cobalt-base alloys	Ti & Ti-base alloys
Designation	ASTM F-138 ('316 LDVM')	ASTM F-75 ASTM F-799 ASTM F-1537 (Cast and wrought)	ASTM F-67 (ISO 5832/II) ASTM F-136 (ISO 5832/II) ASTM F-1295 (Cast and wrought)
Principal alloying elements (wt%)	Fe(bal.) Cr(17–20) Ni(12–14) Mo(2–4)	Co(bal.) Cr(19–30) Mo(0–10) Ni(0–37)	Ti(bal.) Al(6) V(4) Nb(7)
Advantages	• cost, availability • processing	• wear resistance • corrosion resistance • fatigue strength	• biocompatibility • corrosion • minimum modulus • fatigue strength
Disadvantages	• long term behavior • high modulus	• high modulus • biocompatibility	• power wear resistance • low shear strength
Primary utilisations	Temporary devices (fracture plates, screws, hip nails) Used for THRs stems in UK (high Nitrogen)	Dentistry castings Prostheses stems Load-bearing components in TJR (wrought alloys)	Used in THRs with modular (CoCrMo or ceramic) femoral heads Long-term, permanent devices (nails, pacemakers)

2.3.3 Biocompatibility, corrosion and wear resistance of metals

A material is biocompatible if no allergic and inflammatory reaction occurs between the material and the body. An ideal material should be inert to the body environment, but all metals will be toxic to the human body at certain levels, but it is not certain which level may be acceptable. Reactions and deterioration due to the material implanted are important factors for biocompatibility. The consequence of each alloying element should be understood due to its importance in wear, corrosion resistance and toxicity [60]. The elements that are related to acceptable biocompatibility are: Titanium, Boron, Magnesium, Silicon, Phosphorus, Calcium, Strontium, Zirconium, Niobium, Molybdenum, Indium, Tin, Tantalum, Platinum and Gold. However, the acceptable level of these elements in the human body is still unclear. The elements that are related to reported toxicity: Beryllium, Aluminium, Vanadium, Chromium, Manganese, Cobalt, Nickel, Copper, Zinc and Silver. Some researchers have reported that Iron is a harmful element and other has reported that it is not [61].

The human body is a complex electrochemical structure and strong corrosion environment for implants. Body liquids have aggressive substances and implants are in contact with them. Therefore, corrosion resistance is an important propriety to investigate. Poor corrosion resistance will generate the release of non–compatible ions from implants to body and it is a cause of toxic reactions [62]. The lifetime of a replacement is determined by wear resistance. In addition, the effect of a poor wear resistance is implant loosening and wear debris [63]. Natural joints have great tribological properties due to the intrinsic properties of cartilage and superior lubrication of synovial fluid [64].

Looking to solve problems related to wear debris, alumina was adopted in the biomedical field. This material presents higher wear resistance than CoCr on polymers and metal on metal. In addition, alumina has lower toxicity than CoCr alloys. In contrast, this material does not have good mechanical properties in particular toughness. To achieve better properties than alumina, zirconia was introduced and to date more 600,000 head prosthesis have been undertaken in United States and Europe. However, all these materials mentioned tend to fail early [12, 14]. Due to problem regarding to wear and ion release into the body by stainless steel and titanium alloys, CoCrMo alloys are still the first choice for this

kind of application. Ti6A14V is reported to be >15% softer than CoCrMo which have better wear resistance but its elastic modulus and presence of Cr (toxic element to human body) is a drawback [65, 66].

2.3.4 Metals used as THR.

Modern total hip replacements comprise primarily of three components: stem, head and socket. The first generations of alloys THR were not successful because the rate of revision procedures was high [67]. Stainless steels were first used in total hip replacements by Philip Wiles in 1938, and a CoCr alloy was chosen by Austin Moore in the 1950s. The issues associated with the poor corrosion, fatigue and wear resistances of stainless steels and the consequent issue of heavy metal toxicity have since barred them from applications in permanent implants, and stainless steels are rarely used in permanent implant devices anymore. Nowadays, the stem portions of most hip implants are made of Orthinox, CoCr or Ti alloys. CoCr alloys or ceramic materials (aluminium oxide or zirconium oxide) are used in making the ball portions, which are polished smooth to allow easy rotation within the acetabular socket. This can be made of metal, UHMWPE, or a combination of polyethylene backed by metal [68].

Although these three metals are not perfect implant materials, they predominate in current orthopaedics. Each alloy has advantages and disadvantages. The ideal alloy should have the modulus of bone, the strength of CoCr alloys, the corrosion resistance and biocompatibility of Ti alloys, and the fabrication cost of stainless steels [68].

The developments were only concentrated on CoCr–based alloys and these alloys are still the first choice for this kind of application because they have good wear and corrosion proprieties [14]. Titanium was introduced as counterpart with metal on polymer or metal on ceramic due to the good corrosion proprieties, but its alloys presents poor wear resistance and some have toxic elements. Ti alloys are largely involved with bone-cemented or cementless femoral head stems [69, 70].

Titanium alloys are applied as modular neck and femoral stem and the use of these alloys as acetabular cup is avoided because of their poor wear resistance. Although Ti-based alloy heads function well under clean articulating

conditions, they have fallen into disuse because of their low wear resistance to bone or cement particles. These features can lead to the formation of fragments and inflammatory reaction, Fig. 2.4. In order to improve the wear resistance of titanium alloys, surface treatments and coatings are generally undertaken such as ion implantation and plasma spray coating, nitriding, carburization and boriding [23, 71-75].

It is essential to understand how coatings perform under different tribocorrosion conditions, in order to predict the service life of the equipment and to explore ways to enhance it. Manhabosco [76] studied the tribocorrosion behaviour of DLC coated Ti-6Al-4V alloy and bare Ti-6Al-4V in a phosphate buffered solution. The DLC coated materials presented better wear resistance under dry conditions. Moreover, the coated film life is decreased by between 2 and 10 times during tribocorrosion tests. There is still scope for new approaches. Mallia [77] studied three coating compositions, Cr–13 at.% Ti, Cr–33 at.% Ti and Cr–48 at.%Ti, that were synthesised by unbalanced magnetron sputter deposition and applied to Ti-6Al-4V substrates. All the coated materials were more tribocorrosion resistant than uncoated Ti-6Al-4V.

Hill [78] studied Ti-6Al-4V with nanostructured diamond (NSD) coatings deposited with via microwave plasma-assisted CVD, with hydrogen-rich (H-NSD) and helium-rich (He-NSD) feed gas mix. Pin-on-disc wear tests of polyethylene against NSD and CoCr alloy were carried out in serum lubrication (electrolyte) at 37°C. No differences in wear coefficients were observed on polyethylene on H-NSD, He-NSD and CoCr. However, higher roughness and coefficients of friction were observed for the He-NSD and H-NSD coatings compared with CoCr. Therefore, as counter face to polyethylene, the NSD coatings produced wear coefficients comparable to CoCr. Then, NSD-coated Ti-6Al-4V is considered promising for use in total hip joint bearing applications. The tribocorrosion performance of nanostructured coatings has also been recently studied for biomedical applications. Basak [79] studied the corrosion and tribocorrosion behaviour of a thermal sprayed nanostructured FeCu/WC–Co coating in Hank's solution and compared to 304 stainless steel and nanostructured WC–Co coatings. The multiphase structure of the FeCu/WC–Co coating induced complex corrosion processes but exhibited a depassivation/repassivation behaviour comparable to that of 304 stainless steel and the nanostructured WC–Co coatings.

During wear, metallic particles are detached and these particles enhance the wear process. These particles are nanometric in the size range and normally uniform in shape. In contact with polymers, the degradation will be higher than compared to contact with metals, which is the cause of loosening [28]. High levels of metal ions and wear debris have been found in synovial fluid of patients with badly functioning joint replacements [66] and this may also be harmful for human health [80]. This can be controlled by a better understanding of the material behaviour related to wear and corrosion [34].

Nowadays hip joint prostheses are made with metals, ceramics and plastic materials. Most used are titanium alloys, stainless steel, special high-strength alloys, alumina, zirconia, zirconia toughened alumina (ZTA), and UHMWPE. Usually, stems and necks are composed of metals, whereas femoral heads can be both metal and ceramic, and the acetabulum can be made of metals, ceramics or polymers. There are several combinations that can be realized by using these materials with the aim of coupling with the fewest concerns and the highest long-term success odds [81].
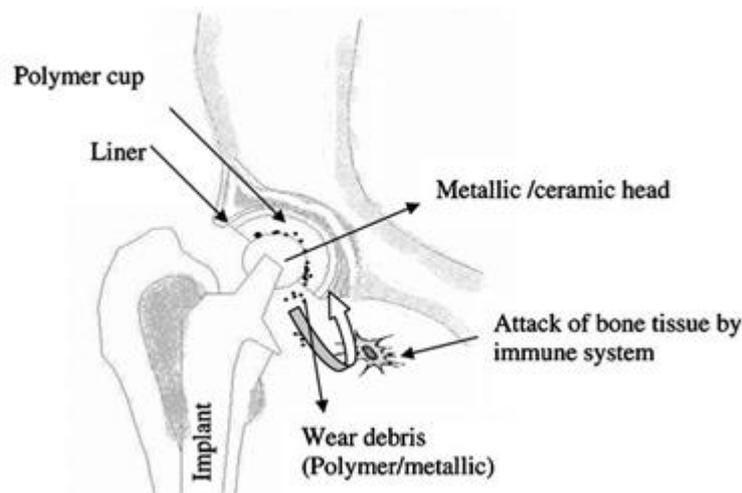
Fig. 2.4 – Wear process of hip replacement [12].

The most common used hip joint type is a femoral head articulating against an ultra-high-molecular weight polyethylene (UHMWPE) acetabular cup. From the implant retrieval studies of femoral head of CoCrMo, 316L stainless steel and Ti–6Al–4V that suffered aseptic loosening, it was noted that Ti64 femoral heads consistently had the maximum wear averaging 74.3% against high molecular weight polyethylene acetabular component. CoCr alloy was found to wear the least and wear of 316L stainless steel was in between CoCr and Ti alloy. Further,

high metal concentrations were found in tissue around Ti alloy prostheses and the debris level were low in the tissues around the CoCr and 316L that were articulating against polyethylene. In order to overcome this issue, efforts have been made to change the use of cup material from polymer to metal or ceramic. Therefore, the long-term problems associated with UHMWPE wear debris have led to explore the possibility of the use of metal on metal prostheses. Also, Ti64/UHMWPE combination is used in TJR prosthesis, the wear rate of UHMWPE for Ti64 is found to be 35% greater than for Co–Cr–Mo in hip simulator testing [12].

Titanium alloys form a passive film mainly composed of TiO_2 when in contact with oxygen and their corrosion resistance relies on its formation [13]. The passive layer formed on titanium alloys is an important factor in biocompatibility as well. Although this film is stable, the wear resistance and corrosion activated by mechanical removal on these alloys relies on mechanical and electrochemical conditions [82, 83].

Ti alloys are considered to have a poor oxidative wear resistance when submitted to tribocorrosion system. Tribology studies of Ti64 show the presence of martensite around the worn area and particle detachment is related to plastic deformation of the surface and subsurface [84] and high levels of Ti were reported in serum from some patients [85].

Studies focus on the formation of the oxide layer and the effect of heat treatment on wear properties of Ti alloys [86, 87]. Also, different Titanium alloys have been studied at different load and speed conditions and these alloys presented similar wear behaviour at different conditions [88]. It has also been reported that the main wear mechanism for Titanium alloys is abrasive wear [89-92]. However, studies of corrosion and wear of titanium alloys are still lacking in the literature [93].

2.4   Titanium and its alloys

Titanium, a metal was discovered in 1791 by a British mineralogist called William Gregor in Cornwall. Its alloys are widely used in the medical field and have been extensively used in THRs [94, 95].

Titanium alloys have a wide range of applications in engineering due to their high strength, low density in comparison to steel and excellent corrosion resistance so have been subject to much research [96-99]. Also, Titanium can resist corrosion up to 600ºC and is resistant to corrosion in seawater [100]. The most successful application for these alloys are in aerospace, automotive, petrochemical, naval and medical industries [101]. Aerospace and naval industries were the first industries to be concerned about material degradation in their facilities and developed materials resistant to corrosion [102, 103].

The most used alloy is Ti64 (Ti–6Al–4V), which is an α and β phase alloy developed by the aerospace industry [104]. However, this alloy shows problems related to cytotoxicity due to the presence of Vanadium and Aluminium which is related to Alzheimer's disease when used as biomaterial [105]. Moreover, the high elastic modulus of the αβ alloys and the problems associated with toxicity were the reason for the researcher to focus on β–titanium alloys for that application [106]. Titanium alloys have a good corrosion resistance imparted by stable oxide passive film (TiO_2) formed on the surface [107]. Also, β–titanium alloys show better corrosion resistance in comparison to αβ alloys and have a good biocompatibility [108, 109].

There is concern about the poor wear resistance demonstrated by these Titanium alloys [19, 110]. The poor wear resistance results in the release of debris into human body [100, 111]. The debris of metal and ions are spread throughout the body via body fluid, and acts as a corrosive fluid [102, 110], which results in prosthesis loosening and resultant pain in the joint. A proper joint prosthesis must also be low friction, which is a challenge for titanium alloys [112-114].

2.4.1 Physical metallurgy of Titanium

Titanium exhibits two allotropic forms: alpha (α), which has an hcp structure and beta (β) that has a bcc structure. α–titanium exists up to 883ºC and transforms to β–titanium above this 'transus β temperature'. Titanium alloys are usually classified as α, αβ or β, arising from the microstructure at room temperature [115, 116].

The transus temperature can be modified with adding alloying elements because some elements can stabilize α or β phases. These elements are called α stabilizers: Aluminium, Oxygen, Nitrogen and Carbon. β stabilizers are: Molybdenum, Vanadium, Niobium, Tantalum (Isomorphous), Iron, Tungsten, Chromium, Silicon, Nickel, Cobalt and Manganese. In addition, there are two elements neutral to Titanium allotropic transformation: Zirconium and Tin, as can be seen in Fig. 2.5 [14]. For β–titanium alloys for biomedical application, the quantity of alloying elements must be up to 20% of the weight because above this value, phase precipitation can be raised, which increases the strength and elastic modulus of β–titanium alloys [12].
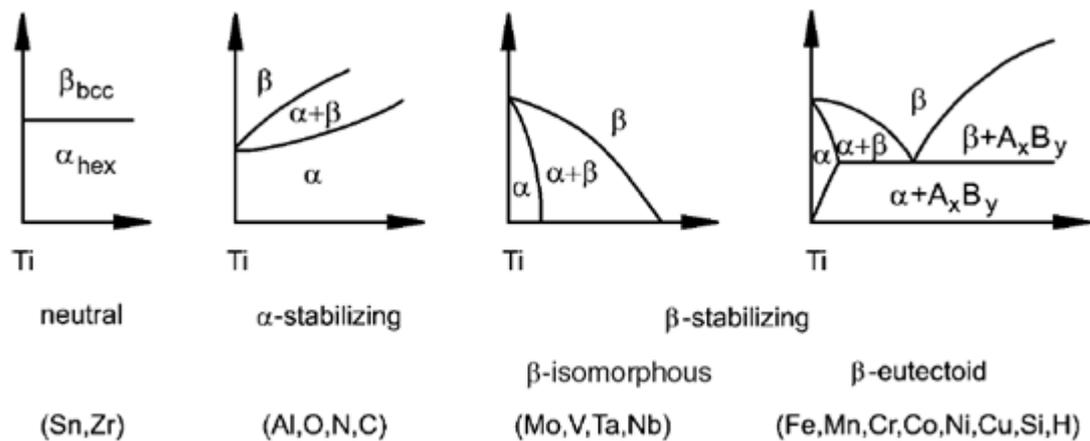
Fig. 2.5 – Influence of alloying elements on phase diagrams of Ti alloys [94].

Zirconium and Niobium have been receiving attention from researchers in biomedicine. Zirconium presents good features for biomedical application, tensile strength, good biocompatibility and corrosion resistance and osseointegration. In addition, Zirconium, like Titanium, is a transitional element and both form solid solutions. Recent research has found that Niobium, Zirconium, Molybdenum and Tantalum are the most appropriate elements to use to design new β–titanium alloys due to the reduction in the elastic modulus of this phase and they are nontoxic [117].

α–titanium alloys offer good corrosion resistance. However, while α and β phases in αβ titanium alloys improve the strength they also lower corrosion resistance due to risk of galvanic corrosion. In addition, β titanium presents good strength and formability and good hardenability. This alloy is the only one to combine lower Young's modulus and high corrosion resistance. Titanium β–alloy

has enough stabilizers to retain 100% β when quenching from over the β transus temperature, as can be seen in Fig. 2.6 [14].
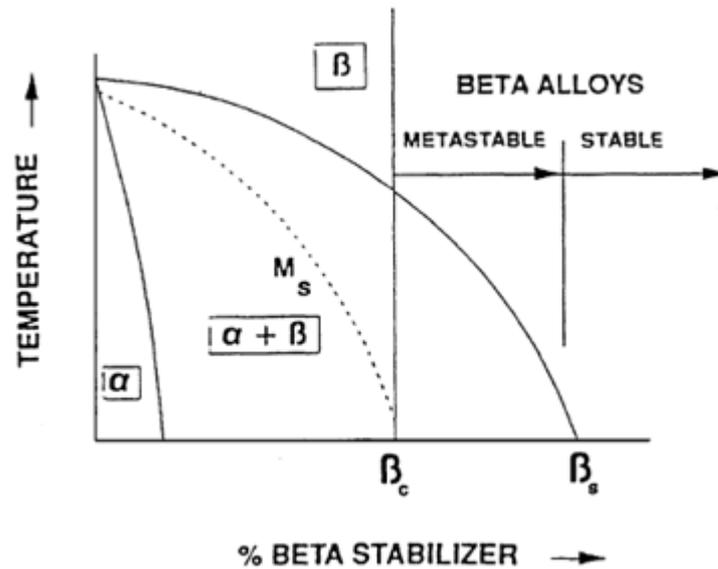
Fig. 2.6 – Effect of β stabilizers elements on formation of β phases during cooling [14].

Different processes are applied to control the microstructure and enhance properties such as ductility, strength, fatigue and toughness. Other important phases (metastable phases) can be found in Titanium alloys are α′ (hexagonal martensitic structure), α″ (orthorhombic martensitic structure) and ω (hexagonal structure) [18]. Alloys with low content of β–stabilizer elements form α′ hexagonal martensite and, while higher content allows for the formation of α″ orthorhombic martensite and this phase is required for shape memory application. They are formed either by nucleation and growth during aging or plane collapse of the bcc structure upon quenching. These phases usually appear after heat treatment, such as annealing, solution treatment, quenching or aging treatment [118].

The ω phase was discovered in 1954 and has the greatest elastic modulus among the other phases in Titanium alloys and can be formed by cold plastic deformation [18, 119]. The transformations of ω phase are: athermal or deformation process, which is formed by quenching and there is no diffusion, and isothermal which is precipitated by atomic diffusion during aging. Both processes lead to the same crystal structure of ellipsoid–like [120-122]. This phase cause ductility and embrittlement [84, 123, 124].

Two methods are used to reinforce the β phase: alloy additions and decreasing grain size. Through the Hall–Petch effect, a reduction of grain size to the nanometre scale gives a significant rise in strength [18, 125].

The activation energy for β–titanium alloys for deformation was found to be about 130–175 kJ mol^{-1}. This energy is close to the energy of activation for self–diffusion (153 kJ mol^{-1}) in β alloys. The process of recrystallization in β phase is not usually dynamic recrystallization where the nucleation and the growth of the new recrystallized grains are happening through hot working. Controlling the grain size, and homogeneity is very important to the secondary processing to enhance the final mechanical properties [126].

Working in the β phase area occasionally leads to the development of a mixed grain structure of large and small grains. The reason for this is that there is selective recrystallization in regions of high strain at grain boundaries in the β phase, whereas there is a lower driving force for recrystallization in the core grain, which is dominated by dynamic recovery. If a mixed grain structure is formed, it is difficult to eliminate by heat treatment as reheating times can change microstructure by grain growth [127].

2.4.2 The αβ–titanium alloys

Commercial purity Titanium (CP Ti) has been applied as a biomaterial on stents and spinal fixation replacements [128]. However, this material has not got sufficient mechanical strength for joint prosthesis. Thus, Ti64 was introduced and extensively used in this application [129]. In order to use a Vanadium free biomedical alloy, another αβ-titanium alloy, Ti–6Al–7Nb has been introduced, which has similar properties to Ti64. Another alloy introduced on this field was Ti–13Nb–13Zr because it has strength properties that are also similar than Ti64 [130-132].

Three microstructures can be found in Ti64, as can be seen in Fig. 2.7. These microstructures can be achieved by controlling different parameters on heat treatment and cooling rate [130, 131].
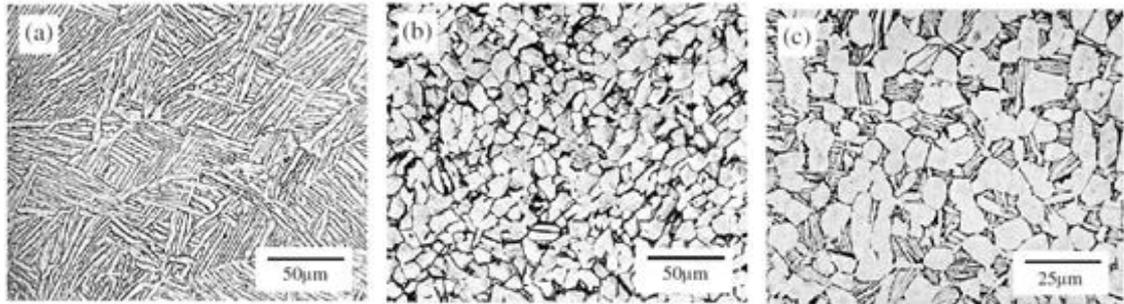
Fig. 2.7 – (a) Lamellar microstructure, (b) Equiaxed microstructure and (c) Bimodal microstructure [131].

The lamellar microstructure can be achieved by solution treatment, air cooling and aging. This microstructure brings excellent fracture toughness. The equiaxed microstructure can be obtained by solution annealing. This microstructure provides excellent strength and ductility but low facture toughness. The bimodal microstructure can be achieved by solution treatment, air cooling and aging. This microstructure has a good fatigue resistance. Generally, the finer the microstructure the higher the fatigue resistance [130, 131].

2.4.3 The β–titanium alloys

As noted in the last section, CP titanium and αβ-titanium alloys were the first generation of titanium alloys applied in the biomedical field. However, in the last 20 years, β titanium alloys have received attention by researches and scientists. These alloys were developed to achieve lower elastic modulus in comparison to αβ titanium alloys [3]. Examples of the first alloys created are Ti–29Nb–13Ta–4.6Zr (TNTZ), Ti–12Mo–6Zr–2Fe (TMZF) and Ti–35Nb–7Zr–5Ta. TNTZ alloys have 65 GPa, TMTF has 82 GPa and Ti–35Nb–7Zr–5Ta has 55 GPa of Young's modulus [133].

The β–titanium alloys have enhanced corrosion resistance in comparison to αβ-titanium alloys, because on αβ–titanium alloys there is a risk of galvanic corrosion. Also, β–titanium alloys exhibit improved ductility and lower elastic modulus than CP Titanium, α–titanium alloy and αβ–titanium alloy. The reason for that is that plastic deformation of hexagonal closed packed structures is more difficult than on body cantered cubic. Thus, β–titanium alloys show improved formability and ductility [12, 18].

Niobium, Tantalum, Zirconium, Molybdenum and Tin are the safest alloying elements to use to develop β–titanium alloys. Hence, the Titanium alloys with potential as biomaterials are: Ti–Ta system, Ti–Ta–Zr system, Ti–Nb–Hf system, Ti–Nb–Zr system, Ti–Nb–Sn system, Ti–Nb–Ta–Zr system, Ti–Fe–Ta system, Ti– Mo–Zr–Sn system, Ti–Sn–Nb–Ta system, Ti–Mo–Zr– Fe system, Ti–Mo–Nb–Si system, Ti–Mo–Ga system, Ti–Mo–Ge system and Ti–Mo–Al system [134, 135].

The most recent alloys developed for biomedical application are based on Ti–Mo, Ti–Nb, Ti–Zr, Ti–Ta alloys. Comparison of proprieties of α, αβ and β Titanium alloys are given in Table 2.2 [136].

Table 2.2 – Mechanical proprieties of different generations of Titanium–based alloys [12].

Material	Standard	Modulus (GPa)	Tensile strength (Mpa)	Alloy type
First generation biomaterials (1950–1990)				
Commercially pure Ti (Cp grade 1–4)	ASTM 1341	100	240–550	α
Ti–6Al–4V ELI wrought	ASTM F136	110	860–965	α + β
Ti–6Al–4V ELI Standard grade	ASTM F1472	112	895–930	α + β
Ti–6Al–7Nb Wrought	ASTM F1295	110	900–1050	α + β
Ti–5Al–2.5Fe	–	110	1020	α + β
Second generation biomaterials (1990-till date)				
Ti–13Nb–13Zr Wrought	ASTM F1713	79–84	973–1037	Metastabe β
Ti–12Mo–6Zr–2Fe (TMZF)	ASTM F1813	74–85	1060–1100	β
Ti–35Nb–7Zr–5Ta (TNZT)		55	596	β
Ti–29Nb–13Ta–4.6Zr	–	65	911	β
Ti–35Nb–5Ta–7Zr–0.40 (TNZTO)		66	1010	β
Ti–15Mo–5Zr–3Al		82		β
Ti–Mo	ASTM F2066			β

The parameter to evaluate the stability of β phase is called molybdenum equivalent and it is found by equation 2 [126].

$$Mo\ Eq = 1.0Mo + 0.67V + 0.44W + 0.28Nb + 0.22Ta + 1.6Cr + 1.0Al \quad \text{Eq. 2}$$

Generally, the β transus temperature goes down if the Mo equivalent increases, as can be seen in Fig. 2.8. A large Mo equivalent gives a stable alloy. For instance: Ti–13V–11Cr–3Al – B120VCA alloy or Ti–35V–15Cr – alloy C. Expansion of the number of β–titanium alloys started in the 1950s when the B120VCA alloy was created. After this, β titanium alloys like Ti–1Al–8V–5Fe (Ti185), Ti–8V– 8Mo–2Fe–3Al (Ti8823), and Ti–11.5Mo–6Zr– 4.5Sn (β 3) were created. Three significant β–titanium alloys were fabricated between 1969 and 1978. For instance: Ti–3Al–8V–4Mo–4Zr (β C), Ti–10V– 2Fe–3Al (Ti1023) and

Ti–15V–3Cr–3Sn–3Al (Ti153). The β–titanium alloys, Timetal alloys 21 and LCB, β CEZ, SP 700 and Ti–13Nb–13Zr were created 20 years ago [126].
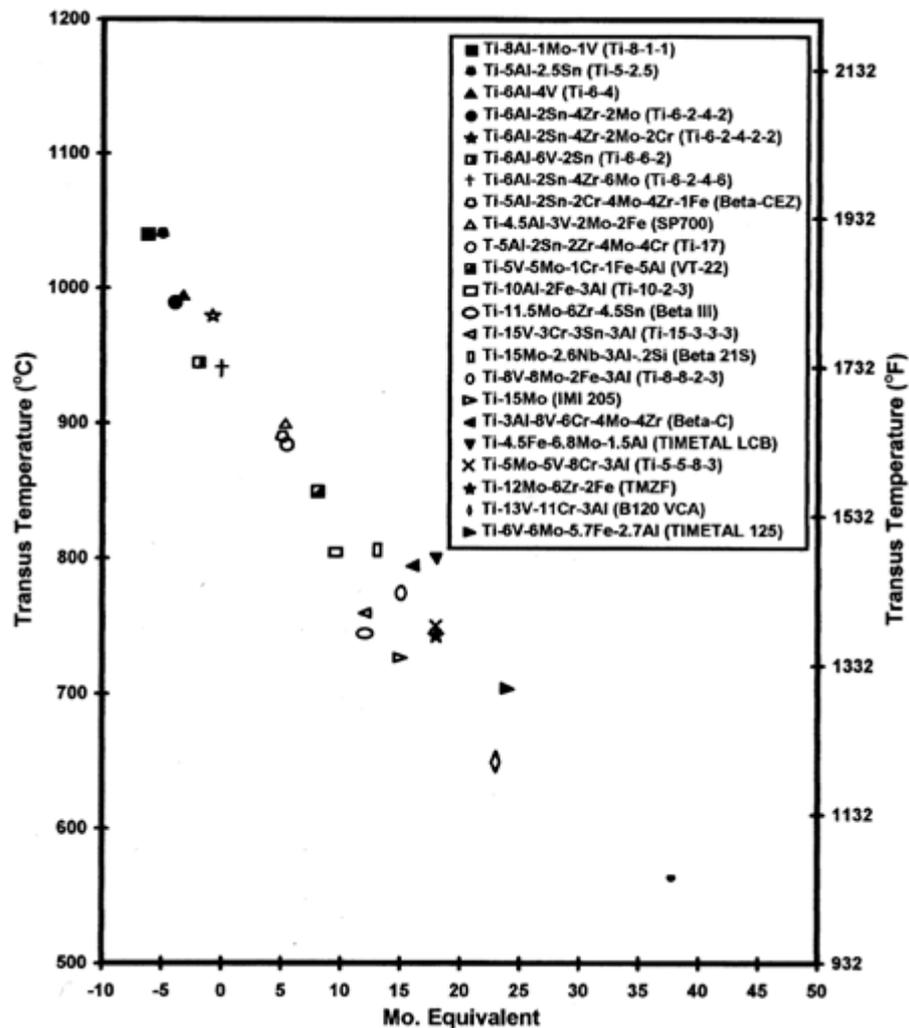
Fig. 2.8 – The β transus temperature vs Mo equivalent of commercial titanium alloys [126].

The necessity to hot work all these materials at low temperatures due microstructure controlling and desired properties frequently necessitates the use of isothermal or near–isothermal deformation processing. The classic hot working method for treating β–titanium alloys includes principally ingot breakdown in the β phase area by finishing it frequently at temperatures under the β transus temperature to acquire a final product, and secondary employing to create a precise form by hot rolling or hot forging exceeding or under the β transus temperature [126].

2.4.4 Tribological properties and elastic modulus of β titanium alloys

A layer of TiO_2 is formed when Titanium–based alloys are in contact with oxygen such as in air, (equation below). The layer is very hard and it is formed due to the diffusion of O_2 [5]. Oxygen is an α stabilizer and the existence of this phase on the surface enhances the hardness of Titanium–based alloys [137].

$$Ti + 2H_2O = TiO_2 + 4H^+ + 4e^-$$

One important factor that influence the performance of the oxide layer is the kinetic of repassivation of the oxide. Tantalum, a β stabilizer repassivates faster (96 ms) than Titanium (172 ms) and slower than CoCrMo (77 ms) [14, 138, 139].

Data from the wear behaviour on α–titanium alloys and β–titanium alloys is limited. β–titanium alloys exhibit strain hardening and this property is the reason for low resistance to deformation in the subsurface region on αβ-titanium based alloys. Thus, β–titanium alloys might offer the prospective for improved wear resistance [14].

The wear development is followed by these steps: debris generation and detachment by any wear mechanism (adhesion, abrasion, corrosion or fatigue); change of surface morphology and composition by third body effect, and finally the removal of these debris. Researchers found changes in the material's microstructure of Ti–based alloys after frictional contact. Those changes were the formation of β phase and growth of the ultra–fine grained of α phase [14].

For the β-titanium alloy Ti–13Nb–13Zr, the formation of ZrO_2 on the surface occurs and it results in an enhanced wear resistance. Thus, it suggests that the composition of the oxide layer may be made by the composition control of the alloy and enhancement of the wear resistance. Some researchers have found that the wear resistance of β–titanium alloys present improvements in comparison to αβ–titanium alloys, due to strain hardening [140, 141]. It is necessary for more improvements in the wear resistance of β–titanium alloys that will develop a better understanding of the tribological properties of these alloys [14].

2.4.5 Biocompatibility and corrosion of β–titanium alloys

There is no study that has shown a material totally free of adverse reaction in the human body related to implants. Titanium is a good choice for bio–application because it is well accepted in the body. Also, in some situations, Titanium can osseointegrate with the bone and the passive layer of Titanium can rebuild very fast [12].

Biocompatibility and corrosion resistance are two proprieties of biometallic materials that are closely related. Usually, β–titanium alloys exhibit good corrosion resistance and this characteristic relies on its composition and environment applied. Researchers have shown using the polarization test that Ti–12Mo–6Zr–2Fe (β) has the same corrosion resistance that Ti64 (α+ β). Also, Titanium, Niobium, and Zirconium develop extremely protecting passive layers and showing a lower potential electrochemical interaction than Ti64. Niobium and Zirconium show ideal passivity and these two elements form a protective passive film on titanium alloys [14].

2.4.6 Limitations of β–titanium alloys

The limitations of β–titanium alloys are: 1) There is still large gap between elastic modulus of β type and bone. The ω phase and α phase are important factors in controlling the elastic modulus. 2) The main β stabilizers alloying elements are Nb, Ta and neutral elements are Zr and Sn. Ti, Ta, Zr and Nb are problematic to melt in a homogeneous way because of large differences in melting point and specific gravity. It is common to observe coarse grain and macrosegregation on alloys made by traditional melting process, this degrades biocompatibility and mechanical properties [12]. 3) It is problematic to produce totally single β phase alloys. Usually, thermomechanical processing is used to enhance the microstructure. If β phase alloys are mechanically treated under the β transus and heat treated in the αβ region, the microstructure will be a mix of α and β phases in equiaxed form [12].

The best combination of high strength and low Young's modulus is seen from equiaxed grain structures in β alloys, which is superior to that from acicular

and lamellar structures. New β–titanium alloy having low elastic modulus, high strength and only a fine, equiaxed, single phase β phase alloy is a major research objective. This may be achieved through suitable alloy design and correct choice of production techniques [12].

2.5 Basic theories of corrosion and tribology

2.5.1 Corrosion principles and corrosion reactions

All materials are prone to aging and degradation when in use in different types of applications. These processes lead to time–dependent deterioration of their functionality. Material degradation in their surroundings can take place via different mechanisms such as thermal destruction, chemical dissolution, electrochemical corrosion processes, or mechanical wear [138].

The interaction of a material such as metals, ceramics and polymers, with the environment (liquids and gas) causes a degradation called corrosion [142]. Three factors are important to study corrosion: the metal, the environment and the interface metal–environment. This study focuses on the material degradation caused by the corrosion and wear of a material under tribological contact. The tendency for a material to corrode is studied by electrochemistry. To analyse equilibrium of a system, thermodynamics is used [143]. Metal in a form of ore has a low state energy and to get a pure metal (eliminate oxides), external energy is used to do it. So, they will have a state of high energy. The trend will be for the metal to return to a low state energy mode and will occur by corrosion [142]. Free energy (ΔG) is used to analyse the tendency of chemical reaction. If it is <0 there will be a high tendency to corrode, if it is >0 the metal is stable and if it is 0 the system is at equilibrium [144].

The relationship between free energy and potential is given by the following equation, where n is the number of electrons in the reaction and F is Faraday's constant:

$$\Delta G = -nFE \qquad \text{Eq. 3}$$

Large negative free-energy changes give rise to large positive potential differences, and large positive free-energy changes give rise to large negative potential differences. These terms are equivalent in that they both describe the magnitude of the driving force for a reaction to occur. Furthermore, at equilibrium, where there is no driving force for the reaction, both the free-energy change (ΔG) and the driving force in terms of potential (E) are equal to zero [145].

The corrosion process is based in two reactions called anodic and cathodic. Anodic reaction is the metal will dissolve and cathodic reaction the metal will reduce [146]. Corrosion equation can be generalised by

$M \rightarrow M^{n+}+ne^-$: oxidation
$M^{n+}+ne \rightarrow M$: reduction

For example following equations are the anodic reactions for iron:

$Fe \rightarrow Fe^{2+} + 2e^-$
$Fe^{2+} \rightarrow Fe^{3+} + 2e^-$

In case of passive metals, the oxidation reaction of the metal M results in the formation on the metal surface of an oxide film usually few nm thin (passive film) according to the reaction:

$M + nH_2O \rightarrow MO_n + 2nH^+ + 2e_-$

The oxygen reduction process is a cathodic reaction and it is expressed by the following equation:

$O_2 + 2H_2O + 4e^- \rightarrow 4OH^-$
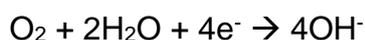
The hydrogen evolution occurs when a metal is in acidic condition. Electrons and Hydrogen ions form atomic Hydrogen at metal surface. Then a concentration of molecular hydrogen gas might be found.

$2H^+ + 2e \rightarrow H_2$

These reactions form corrosion products and passive films. The difference between them is that passive films are adherent to the metal surface and may promote protection [147].

The atoms from a metal in an electrolyte shows certain propensity to leave the metal lattice as a cation or to become part of the metal lattice. This propensity may be high or low and it depends on the nature of that metal and the electrolyte. When one of each process happens the surface will have some negative or positive space charge regions and this difference is compensated by the accumulation of ions with a opposite charge. Thus, a potential difference in the metal–electrolyte is seen and it is of great importance for the electrochemical reaction kinetics [148, 149].

The corrosion electrochemical reaction for Zn can be split into the two half-cell reactions of:

$Zn = Zn^{2+} + 2e^-$ (Oxidation)

$2H^+ + 2e^- = H_2$ (Reduction)
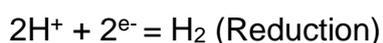
The two half-cell reactions often occur at separate locations on the metal and, because the metal is conductive, the electrons flow through the metal from the anodic to the cathodic region. The presence of water, a thin film of moisture or an electrolyte is all what is required to facilitate the movement of the ions [145].

The propensity of a metal to oxidise or reduce is given by the standard electrode potential of that metal (E^o). The standard electrode potential for hydrogen at standard conditions ($pH_2 = 1$, $a^{H+} = 1$, $T = 25$ °C) is zero, and other standard electrode potentials are given in reference to this electrode (SHE). Negative potentials show the tendency for the oxidation of the metal [147].

Oxidized species may be present in the system as solvated cations or in the form of corrosion product layers. An example is the formation of stable oxides of the passive metals; oxides form protective film on the surface, reducing the dissolution of the metal. The formation of the metal oxide may be a chemical reaction ($2Fe^{3+} + 3H_2O \rightarrow Fe_2O_3 + 6H^+$) or an electrochemical reaction ($3Fe^{2+} + 4H_2O \rightarrow Fe_3O_4 + 8H^+ + 2e^-$). For a thermodynamic analysis of the corrosion behaviour, it is not sufficient to consider only the electrode potentials of metals in the system, but the existence of different species in a system must be considered [138].

For a complete analysis of equilibrium reactions of a given metal and H_2O interface, thermodynamic calculations are summarized in potential–pH diagrams

or Pourbaix diagrams which were introduced by Pourbaix in 1963. These diagrams show the thermodynamic stability regions of metals in water in metallic state, dissolved species, or solid oxides. If the reaction product of metal oxidation is a stable oxide, the rate of the oxidation reaction decrease because a thin oxide film forms on the surface and the metal becomes passive. This is called passive potential region and the state of the metal under these conditions is called passivity [138].

The exact position of the lines and region depends on the concentrations of dissolved species in the equilibrium reactions according to the Nernst for electrochemical reactions and also according to the law of mass action for chemical equilibria for chemical reactions [138].

Metals and alloys form a film when in contact with air. This film is called passive film and it presents normally in the nanometrically range at room temperature. However, at high temperatures it is formed by thicker films. This passive film is not homogeneous for alloys and the passivity ability is not shown in all conditions. The oxidation reaction happens at the interface metal–oxide and the reduction reaction of oxygen occurs at the outer oxide surface. It means that the conductivity of the oxide layer has an important role in the kinetics of the oxide film development. The passive film can be broken uniformly or localized under specific conditions [142, 150].

Passivity is the state where the metal surface is covered by a protective layer, which decreases the metal dissolution. Generally, passive films consist of oxides of the alloying elements. The passive current is a measure of the protective quality of the passive film. The passive current densities are orders of magnitude lower than corrosion current densities. The passivation current density and the passivation potential are measures of the passivation ability of the metal [138]. Passivation occurs when its potential is more negative than the equilibrium potential of the coupled cathodic reaction. Thus, for metals that show spontaneous passivity in the absence of strong oxidizing species in the solution, the passivation potential should be as cathodic as possible. The presence of oxygen or other oxidizing species is required for passivation to occur [138].

Only when the passivation current is smaller than the absolute value of the cathodic current does spontaneous passivity occur. This is also a self-healing system where the mechanical destruction of the passive film leads to spontaneous repassivation. The smaller the passivation current, the fewer the

oxidizing species needed for spontaneous passivation. The passivation current density and passivation potential rely on the material and the environment [138].

Alloying elements also have an effect on passivation, such as the effect of Cr to Fe alloys. Cr content positively affects the passivation potential, the passivation current, and the passive current. So, high Cr-content in the alloy promotes spontaneous passivation in the absence of strong oxidizing agents in the solution and a protective film is formed on the metal surface. This is the basis of the high corrosion resistance of stainless steels [138].

For oxide growth, diffusion of metal cations or oxygen anions through the oxide layer is required. The ion movement in solid oxides depends on the non-stoichiometry of the oxide since diffusion through the defects requires lower activation energy than diffusion from lattice site to lattice site. Preferential ion transportation occurs by grain boundary diffusion. During oxide growth on the surface, the oxidation reaction occurs at the metal/oxide interface, while the oxygen reduction occurs at the outer oxide surface. Clearly, the electronic conductivity of the oxide layer is an important factor in the oxide growth [138].

Passivating layers are formed in aqueous solutions or in humid atmospheres, and that is why the layers may contain hydroxides. It is now believed that the barrier properties of passive films is due to the inner oxide layer, and the presence of hydroxide precipitate layers on top of the oxide film does not influence passivity. Also, it is known that amorphous passive films are less prone to breakdown with defects, such as chloride incorporation. Normally, the presence of grain boundaries is considered not good for passivation [138].

Surface analysis such as X-ray Photoelectron Spectroscopy (XPS) have been carried out to characterise the oxide films of biomedical alloys such as CoCr alloys. The outer layer of these alloys are mainly rich in Cr_2O_3 and CoO and MoO_3 and have a thickness of the order of a few nm. The total thickness of the passive film is about 4-5 nm. The inner layer of the passive film is rich in Cr_2O_3 and Co and Mo metal species [151].

The driving force for this corrosion reaction is the free-energy change or the overpotential. The rate of the reaction can be expressed as a current or the number of electrons generated per unit time [145].

$$i = A\left(\exp\left(\frac{\Delta G}{RT}\right)\right)$$
Eq. 4

An electrochemical reaction that behaves as described is referred to as being under the control of activation polarization. Activation polarization simply

means that the driving force for the reaction (overpotential) is proportional to the log of the reaction rate (current). The relationships for anodic and cathodic processes under activation polarization are as follows:

$$\eta a = \alpha a + \beta a \log i \text{ (anodic)} \qquad\qquad \text{Eq. 5}$$

$$\eta c = \alpha c + \beta c \log i \text{ (cathodic)} \qquad\qquad \text{Eq. 6}$$

Where η_a is the anodic over potential and η_c is the cathodic over potential. The constants α and β are the anodic and cathodic Tafel constants, respectively. Over the potential range where these equations describe the relationships between potential and current, reaction is under activation control [145].

The corrosion rate can be plotted versus potential and it is called a Tafel or polarization curve. The Tafel curve represented in Fig. 2.9. The current is obtained from from the Butler-Volmer equation:

$$i = icorr(\exp\left(\frac{2.3(E-Ecorr)}{\beta a}\right) - \exp(\frac{2.3(E-Ecorr)}{\beta c})) \qquad\qquad \text{Eq. 7}$$

Where i is the measured cell current density, i, is the corrosion current density from Figure 2.9. E is the electrode potential and Ecorr is the free corrosion potential. βa is the anodic Beta Tafel constant while βc is the cathodic Tafel constant [34].

From this plot, corrosion potential, corrosion rate and corrosion current can be found by extrapolating the linear portions of a log current versus potential plot back to their intersection. The positive side represents anodic reaction where corrosion happens and the negative side represents cathodic reaction where the cathodic current has a higher rate of flow [142].
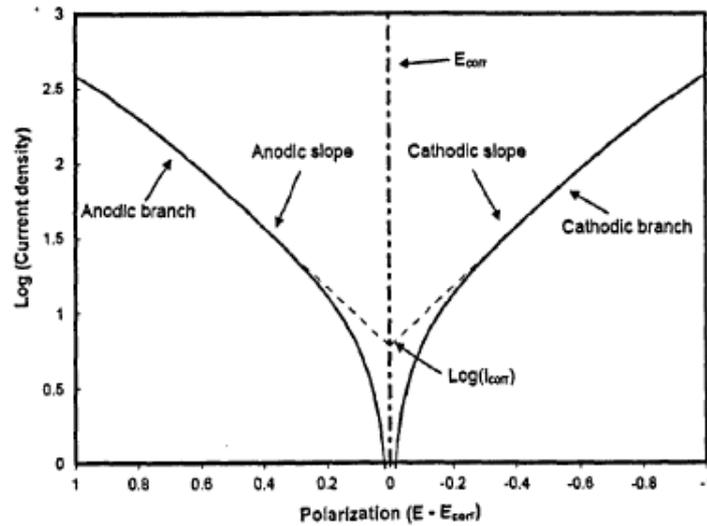
Fig. 2.9 – Hypothetical polarization curve and its relevant parameters [34].

The most common technique to find the corrosion resistance is called potentiodynamic polarization. In this technique the potential of the electrode is varied by applying a current through the electrolyte. Fig. 2.10 shows a Tafel curve for a metal and its different regions [34]. The polarization resistance (Rp) of a material is defined as the slope of the potential current density plot.

$$Rp = \frac{\Delta E}{\Delta i} = \frac{\beta a \; x \; \beta c}{2.3 \; x \; (\beta a + \beta c) \; x \; icorr} \qquad \text{Eq. 8}$$
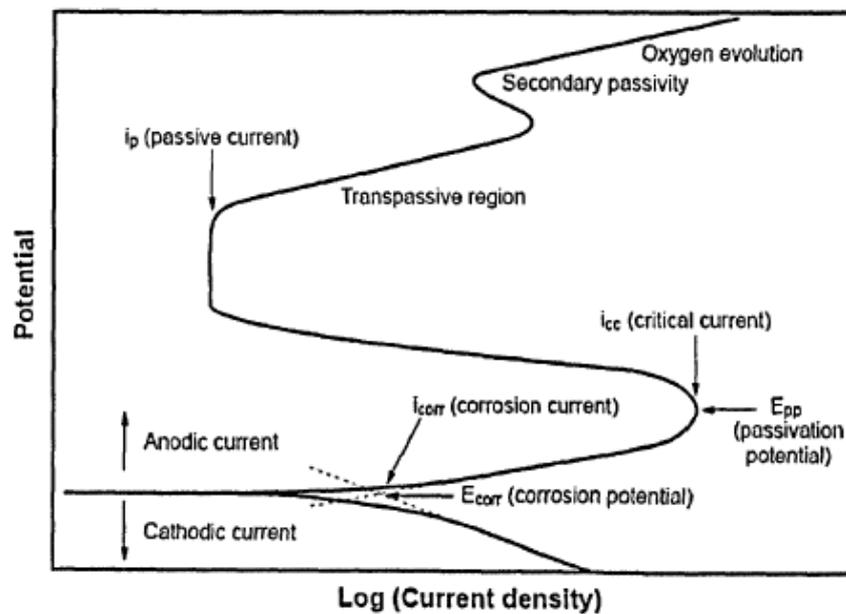
Fig. 2.10 – Hypothetical polarization curve for a passive metal and its regions.

Since the passive films from metals and alloys may show a breakdown, corrosion will occur, and it can be in different modes. The common characteristic of localized corrosion is the existence of an anodic area. The anodic area will couple with the cathodic area. If the anodic area is much smaller than the cathodic area, the corrosion rate is increased, and fast corrosion propagation is seen. Localized corrosion is normally linked to the presence of aggressive anions such as halide ions. Another important factor is the galvanic effect between dissimilar metals in contact. The driving force for galvanic corrosion is the difference of the corrosion potentials of the metals or alloys in contact. The corrosion potential of metals and alloys change as the environment is changed [152]. Localized corrosion mechanisms are identified as follows [142, 144, 146].

- Pitting Corrosion: localised corrosion happens when there is a heterogeneity such as a scratch and produces sharply defined holes. These holes may be small or large in diameter, but in most cases, they are relatively small. Pits may be isolated from each other on the surface or so close together that they resemble a roughened surface. The passivation in the pit is weak because ions migrate to the pit to balance the charges. Then the environment inside the pit will become aggressive and occurs when one area of a metal becomes anodic with respect to the rest of the surface or when highly localized changes in the corrodent in contact with the metal, as in crevices, cause accelerated localized attack. The penetration is high and the failure happens suddenly [153].

- Galvanic Corrosion: this corrosion happens when two dissimilar materials are in contact with an electrolyte. The difference of potential is the driving force to initiate the corrosion of the more active metal [153]. During galvanic coupling, corrosion of the less corrosion-resistant metal increases, and the surface becomes anodic, while corrosion of the more corrosion-resistant metal decreases, and the surface becomes cathodic. When a passive metal is submitted to mechanical depassivation, the passive film is removed and galvanic coupling occur between the depassivated area (anodic area) and the unworn area (cathodic area) [154, 155]. Another case of galvanic corrosion is the presence of different phases in an alloy. If the phases have different potentials, anodic and cathodic areas will be formed and the galvanic coupling occurs [156].

- Crevice Corrosion: this is a form of localized attack and happens when there are grooves or other kind of open spaces between metals surfaces. It occurs at narrow spaces between metal-to-metal or nonmetal-to-metal components. This type of attack results from a concentration cell formed between the electrolyte within the crevice, which is oxygen starved, and the electrolyte outside the crevice, where oxygen is more plentiful. The material within the crevice acts as the anode, and the exterior material becomes the cathode. Crevices may be produced by design or accident. Although crevice corrosion affects both active and passive metals, the attack is often more severe for passive alloys, particularly those in the stainless steel group [32, 144, 146].

- Fretting Corrosion: is a combined wear and corrosion process in which material is removed from contacting surfaces when motion between the surfaces is restricted to very small amplitude oscillations (often, the relative movement is barely discernible - micromotions). Usually, the condition exists in machine components that are considered fixed and not expected to wear. Oxidation is the most common element in the fretting process. [157, 158]. Example of this is rubbing bone to screw head [71]. When the motion is higher than fretting, the process is called wear corrosion [159, 160].

Since corrosion is a surface interaction, some techniques to protect the surface have been developed. They are: Coatings: one of the most common ways to protect the surface. They separate reactive elements from environmental corrosives [161]. Cathodic protection: this technique applies a cathodic current to the surface to minimize the anodic dissolution, which makes the surface cathodic. Another possibility is to connect another metal (sacrifice) which will act as an anode in a galvanic cell. Also, an external power can be applied to the current source. Anodic protection: this is less common than cathodic protection. It consists of an application of a anodic current on a metal in order to create a passive film [146].

2.5.1.1   Corrosion of metallic biomaterials

Corrosion has been considered as one of the major problems for metallic materials and when implanted in the human body they are not free of corrosion [162]. The biological fluid is not as aggressive as industrial fluids, but the presence of oxygenated saline solution and organic species make it corrosive to the implanted devices [163].

Metals with a high standard electrode potential are called noble metals. They are expensive in comparison to the other metals and lack of good mechanical proprieties. Due to this, those metals are rarely used for technical application. Gold and Iridium are examples of noble metals. Stainless materials have their resistance due to the formation of the oxide layer that is thin, dense and adhesive. The potential and rate of formation and repassivation important factors about the passive layer. Metals which show good passivation are Al, Ti and Cr. Metals such as Fe and Co do not show good passivation, but they can be alloyed with metals with good passivation such as Cr and Mo. The term corrosion resistance is more precise than stainless because depending of the circumstances all metals will show some corrosion [164].

Corrosion has a significance in material degradation [157] and it is not different for implants. The body fluids are corrosive to metals due to oxygen present in the organic species. The study of corrosion has great importance for biomaterials. Failure and surgery revision are the cause of non–adequate material used and that failure may be caused by corrosion and its products [163, 165]. One of the drawbacks of corrosion in a biomedical material is ion release. However, metals used as biomaterials form a passive film that may protect the surface to further corrosion and reduce the release of corrosion products [157, 166].

Mechanical depassivation such as wear removes the passive layer and releases debris in to the system. This event may also form localised corrosion such as pitting [167]. Cobalt Chromium Molybdenum alloys present a high corrosion resistance and stainless–steel presents a susceptibility to crevice and pitting corrosion. Both alloys are cytotoxic to the human body [168].

Metallic materials used for bearing surfaces in hip arthroplasties normally depend on the stability of the passive film, which forms spontaneously in air, for

their biocompatibility. The passive film can form a barrier which can efficiently the metal from further corrosion processes. The passive film inhibits corrosion and keeps current flow and the release of corrosion products at a very low level [142].

The link between the amount of metallic debris concentration in a human body and health issues are still topics of many studies [70] and it is certain that high level of ion concentration generated over the years, such as Co and Cr could be found in serum and urine, but It is not clear what level of these elements are acceptable [169-175].

Corrosion studies by electrochemical techniques are performed to better understand metallic biomaterials and their compatibility to the human body, and correlate to metallic levels [158, 160, 176]. Protein adsorption may imply corrosion behaviour of implanted materials. Thus, more research about the effect of an implanted material must be gained.

The Ti and CoCr alloys are known for their corrosion resistance while stainless steel suffers crevice and pitting corrosion. Hanawa [167] examined the surfaces of stainless steel, CoCrMo alloys and Titanium and the release of Co ion was observed for CoCrMo alloys and Fe ion for the stainless steel 316L. Also, an insignificant release of Mo in CoCrMo was identified [177]. Jacobs [178] found out that the Co released from the cast CoCrMo alloys was very small in the biological solution and it was found that Ni release from 316L decreased with increasing pH while Cr and Mo ions from CoCrMo were smaller at a pH of 4 or higher. Calcium phosphate was observed as precipitates on implant metals and on metal surfaces [179].

Brondner [169] studied retrieved CoCrMo metal-on-metal and observed that the Co and Cr concentration in blood serum and urine were high but decreased after 1 year. Black [172] showed that it is still unclear what constitutes a normal level for levels of these elements in an individual patient and what the consequences are of deviations from that level. This is clearly an important question for MoM implantation.

Visuri [173] showed that there was no increase in the risk of cancer in patients with CoCrMo MoM THR. Willert [174] found no proof that the release of metal is teratogenic but did show possibility of hypersensitivity to metals. Koegel [175] disagreed. An increased incidence of the heart muscle disease and tumours was found in animal tests. Because of the increase of the numbers of patients with a MoM TJR for 20 or longer years, it suggests that long-term studies are still

required to fully understand the relationship between ion release and associated diseases. Investigations to clarify the importance of toxicology are currently being carried out by scientist [168].

2.5.1.2   Corrosion of Titanium alloys

Titanium and its alloys naturally form a passive layer which has around a 3nm thickness and inputs good corrosion resistance in different environments. [180]. The passive film of Titanium alloys have good adherence to the bulk material and it repassivates when removed [181]. However, Titanium and its alloys are not corrosion resistant in the presence of fluoride ions [182].

In aqueous solution, Titanium behaves in 4 different ways: it can form Ti ions where the corrosion rate is high, it can form passive layer where the corrosion rate is low, it can show active–passive state and finally Titanium is corroded by hydrogen evolution [183].

Alloying elements used in Titanium alloys in order to improve corrosion resistance are Nb, Mo, Ta, and Zr. These elements form oxide layers such as Nb_2O_5, Ta_2O_5, and ZrO_2. Studies have demonstrated that these alloy elements form strong and adherent passive films [184-188]. However, it is not just the alloying elements that are important in order to improve corrosion resistance of Titanium alloys. The presence of α and β phases are an issue because it may reduce the corrosion resistance due to galvanic coupling between these two phases [156, 189, 190]. According to some studies, heat treatment plays an important role on corrosion resistance of these alloys. Water quenched samples were reported to have greater corrosion resistance than the sample submitted to solution treatment due to a less α–phase in the microstructure [191-196]. Geetha [190] studied Ti-13Nb-13Zr and showed that this alloy has a better corrosion resistance when submitted to sub transus heat treatment than that submitted to solution heat treatment.

Mohammed [195] studied the electrochemical behaviour of Ti-20Nb-13.6Zr-0.5V in Rigers solution at 37°C and found that the small amount of α phase present in this alloy after water quenching was the reason for the better corrosion resistance.

According to some studies, β phase alloys show better corrosion resistance than αβ –titanium alloys [156]. It is reported that the composition of the microstructure and the stability of the passive film are the main factors influencing the electrochemical behaviour of test alloys. Also, the corrosion resistance of these alloys may change in different electrolytes [197, 198].

In aqueous solution, Titanium shows four types of response, according to Kelly [183]: a) active response and high oxidation rate where Ti (III) is formed; b) Passive state where the passive film is formed; c) Passive/active state where the passive film only covers part of the surface; d) Finally, corrosion of Titanium due to Hydrogen evolution in negative potentials. According to some researches [184] Ti alloys has a higher corrosion resistance than CoCr alloys and 316L stainless steel.

Studies show that the lower ratio of α and β phases the higher corrosion resistance for Ti-6Al-4V. This is due to the galvanic coupling between these two phases [156]. Also, β phase alloys (Ti-12Mo-20Nb and Ti-12Mo-13Nb) are shown to be more corrosion resistant than Ti-6Al-4V in Riger's solution [197] and Atapour [156] found that β phase has better corrosion resistance than αβ microstructures and that composition and passive film stability are the main factors that influence the electrochemical behaviour of Ti-13Mo-27Zr-3Fe, Ti-35Nb-7Zr-5Ta and Ti-6Al-4V.

Chelariu [198] found that Nb addition plays an important role on corrosion resistance of Ti alloys. The best corrosion behaviour was observed in high Nb content alloys. Nb improves passivation and decrease dissolution of passive film formed.

Studies with Ti-60Ta, Ti-12Mo and CP Ti show that Ti-60Ta (β phase alloy) has a better corrosion resistance in fluoridated artificial saliva due to the presence of Ta [187]. Zhou [110] showed that the presence of Ta improves the corrosion resistance in Ti-Ta alloys in comparison to Ti-6Al-4V and Cp Ti. This was attributed to the formation of Ta_2O_5 oxide film which is more stable than TiO_2. Also, Mareci [187] showed that the passivation is improved by the presence of Ta.

The electrochemical resistance of the passive film depends on its composition, according to Nakagawa [139]. Potentiodynamic polarization test were carried out to study Ti-8Mo-6Nb-4Zr, Ti-8Mo-6Nb-3Zr, Ti-8Mo-4Nb-2Zr, and

Ti-8Mo-4Nb-5Zr in Hanks solution at 37°C. It was shown that the higher Nb content the better corrosion resistance.

2.5.2 Tribology

Tribology is defined as the area of science and technology interested with interacting surfaces in sliding contact. Sliding is characterized as the constant movement of two surfaces in contact when surfaces move against each other[93]. Even surfaces that have a mirror finish have imperfections larger than atomic scale and it is an important point for friction [138, 199]. Thus, lubrification, wear and friction are part of tribology [200]. Friction is the resistance to the movement between the two surfaces in contact [200].

Lubricants are used to reduce the friction by promoting a thin film between the surfaces [201].

The ratio of friction force and normal load is called coefficient of friction and it is the usual measure of the friction. Its range is from 0.001 to 10 that also depends on the system [202, 203].

Low values of coefficient of friction such as 0.01 are produced by the development of a thin film at the interface of the motion between the materials in contact and acts as a lubricant. If the film between the materials in motion are not homogeneous (in a mixed lubrication regime) over the contact area then the coefficient of friction will range from 0.01 to 0.1 [204].

The calculation of Hertzian contact theory for MoM THR shows that the elastic deformation is in the order of several micrometres. Also, the theoretical minimum film thickness is reported to be in order of nanometres. Then, the elastic deformation of the prothesis is larger than film thickness and water, serum, and synovial fluid are little affected by pressure. Therefore, it is concluded that MOM joints would work in elastohydrodynamic isoviscous regime [205].

The mixed lubrication regime in MOM THR is achieved by increasing the diameter and making the clearance low. It was observed that the lambda increases from less than unity for smaller diameter to up to 3 for the larger

diameter. This increment includes the transition from boundary lubrication to elastohydrodynamic EHL regime [205].

Lambda ratio (or film thickness ratio) is the minimum thickness and defines lubrication regime. Three lubricating regimes are know: boundary ($\lambda<1$), mixed ($1<\lambda<5$), and hydrodynamic or full film lubrication regime ($\lambda>5$). In animal or human joints and some hip replacements, the lubrication regime is in the boundary lubrication. However, for other hip replacements, the lubrication regime can be mixed lubrication. Fluid film lubrication is the most desirable form of lubrication. In this case the surfaces are not in contact and mixed regime lubrication is a mix of full film lubrication and some asperity contact [34].

$$\lambda = \frac{hmin}{\sqrt[2]{R_{a1}{}^2 + R_{a2}{}^2}}$$

Eq. 9

Where h_{min} is the minimum film thickness in relation to the composite surface roughness (R_{a1} and R_{a2}). There are three regimes as defined from the Stribeck curve, Fig. 2.11: boundary lubrication, mixed lubrication and hydrodynamic lubrication. The coefficient of friction is directly proportional to the viscosity of the lubricant and the difference in speed is inversely proportional to the pressure which is exerted on the contact surfaces [34].
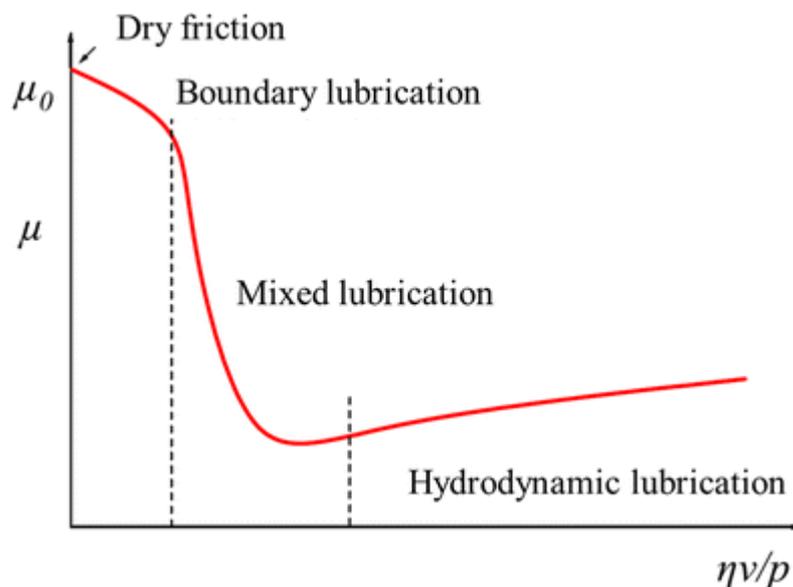
Fig. 2.11 - Stribeck curve and the lubrication regimes [206].

The surface oxide film formed on metals, polymers and ceramics acts by reducing the adhesion between the interfaces which leads to lower COF. Also, if

a material is brittle it will impact these values. Now, if a ductile material is in a vacuum or an inert gas atmosphere the coefficient of friction will range from 1 to 10 [207]. The values of coefficient of friction are due to the growth of the contact area due to the plastic deformation of the contact areas [138].

Friction and wear are responses to the system which relative motion, geometry, presence of contaminants, surface forces, load and its type, materials properties and environment [200]. Wear will be discussed in the next paragraphs.

Fig. 2.12 shows the conditions in which material degradation can happen, known as the wear processes. If the bodies slide over each other, the wear process is called sliding wear. If they roll over the other the wear process is called rolling wear and it is common for ball bearings. Fretting wear occurs when a reciprocating sliding wear is a small amplitude (smaller than sliding). When the surfaces have hard particles abrading the soft surface, it is called abrasion wear [208]. When a fluid carries those hard particles the wear process is called erosion and this process is characterized by a particle impact where combined mechanical and chemical attack occurs [209]. The movement of the surfaces can be unidirectional (pin–on–disk test) or it can be reciprocating. Nevertheless, the term tribocorrosion is normally attributed to sliding contacts [210].
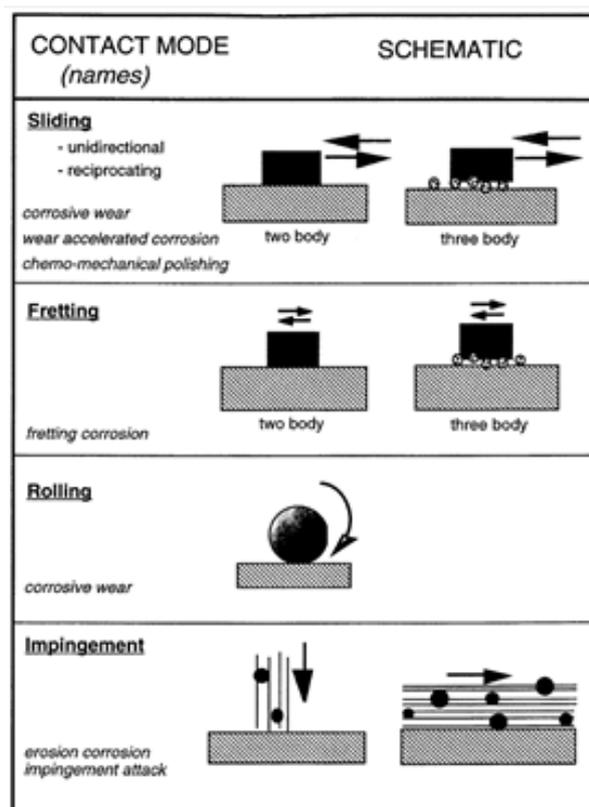
Fig. 2.12 – Tribological contact modes [210].

The relative motion will generate damage on the surface called wear [200]. Wear happens on both or one surface and loss of material can be see [93]. It often involves multiple wear mechanisms, the greatest of which is termed the dominant wear mechanism. It causes material transfer by producing surface plastic flow, scraping off soft surface fragments or breaking up and removing the surface layer due to the strong adhesive forces in the real contact area.

The equation below shows Archard's law, where V is the total material loss, A the real contact area and L is sliding distance, K is the Archard coefficient and it is measure wear severity. It was developed for adhesive wear.

$$V = K \, x \, A \, x \, L$$ Eq. 10

Another important factor is called specific wear rate (SWR) which is given by the volume loss / normal load multiplied by the sliding distance and its range is from 10^{-10} to about 10^{-2} mm^3/N m [211, 212]. The specific wear rate is around 10^{-9} mm^3/Nm when there is a thin film at the interface of the motion between the materials in contact and is irrelevant in practice when the film is well developed. If the film in mixed lubrication between the materials in motion is not homogeneous over the contact area then the specific wear rate will range from 10^{-8} to 10^{-2} mm^3/Nm [204] and if a ductile material is in a vacuum or in an inert gas atmosphere the specific wear rate will be above 10^{-3} mm^3/Nm [207].

The characteristics of the relative movement between two surfaces in contact express the wear processes. During sliding between two materials, three stages are seen: running in stage, steady stage and wear transition. The running in stage is discussed in the next paragraph. The steady stage is characterized by a steady wear rate and coefficient of friction. The last step occurs just when an increase or decrease in wear rate. This is caused by a change in the wear mechanism and coefficient of friction. This wear mechanism happens because of the surface temperature. If this temperature is about 50% of the melting temperature, a thermal softening at the contacting asperities is seen. Thus, the material is not able to support the oxide layer anymore [213].

The ''running in'' period in a point sliding contact has been seen in many metals [205]. The running in period in a point sliding contact relies on the tests system and geometry of contact [177, 214]. It can be 1 million cycles in *in vitro* test or 1 year *in vivo*. This phase is characterized by small wear debris and abrasive wear. The wear rate after reaching running in increases and failure may

occur [171, 177, 215]. Calcium phosphate is formed on Titanium surfaces in the steady state, after the running in period. It is not clear if calcium phosphate can reduce the wear rate [159, 216, 217]. This transition from running in period to steady state is associated to smother surface and change of mechanical proprieties [216].

2.5.2.1 Wear mechanisms

There are several wear processes in practice, but there are four central wear mechanisms: adhesive wear, abrasive wear, tribo–oxidative wear and fatigue wear. An understanding of these wear mechanisms is vital to correctly control each wear process. [204, 218-220].

Adhesive wear occurs when asperities from the worn surface bond to each other due to plastic deformation. The adhesive forces between the asperities on the surface have an important role in the formation of wear fragments. This mechanism is described by Archard's theory. After a few cycles, bonds break and cavities are seen, which can act as wear particles. The electron transfer makes the adhesion of those surfaces strong. Normally it happens with metal–on–metal [218, 221]. In ductile materials, plastic junctions form at the contact asperities when sliding. Adhesion occurs at the junctions that in some scenarios may be more resistant than the bulk material. Thus, the dislocation at some asperities may be due to fracture in the asperity bulk than by shearing at the interfaces. Such a fracture marks the development of loose wear debris [222]. Stopping the plastic deformation is a way to avoid adhesive wear. Metals with a hexagonal or body centred cubic crystal structure are more wear resistant than metals with a face centred cubic (FCC) crystal, since the FCC have a greater number of slip systems which make it more ductile. Other two ways to avoid this wear mechanism are improving the hardness, because it reduces the plasticity of the surface, and the presence of hard particles. [138].

The repeated plastic deformation at the asperities may induce local fatigue damage or a growth of plastic deformation. These processes include wide zones in the sub–surface contact regions and contribute to the material weakening.

Hereafter, it brings the formation of a wear debris once critical damage is attained [223, 224]

Tribo–oxidative wear is due to the interaction of the surfaces with an environment containing oxygen. Tribo–oxidative wear is thus given by a combination of oxidative and mechanical actions at the contacting asperities [204]. In general, it is accompanied by the formation of a surface oxide scale, which avoids the metal to metal contact at the asperities and may act as a sort of solid lubricant, thus reducing friction and wear. There are different situations that may lead to tribo–oxidative wear. Tribo–oxidative wear commonly occurs at high temperatures. The high temperature is reached by the environmental temperature or at high sliding speed [221]. The oxide grows at the asperity tips and detached once a critical thickness is reached. The oxide breaking thus produces wear fragments and generates a fresh surface that can oxidize again, thus continuing the process [218].

This wear process also occurs at low sliding speed and its steps are: at the contacting asperities, metallic fragments are generated by adhesive wear. Some may leave the tribological system and some may remain trapped between the mating surfaces. Such fragments are strain–hardened, fractured, oxidized (oxidation is activated by the very high surface area and the high density of surface defects) and agglomerated. If the load and sliding conditions are intense, a tribological layer made of compacted scales is formed. If the contact temperature is sufficiently high, the scales sinter and form a protective glaze layer on the top. Possible brittle fracture of the scales (orthogonally to the sliding direction) leads to the generation of fragments that may remain in the contact region or leave the tribological system [204, 225].

Abrasive wear happens when two materials are rubbed against each other and they have a similar hardness [204]. It is characterised by the indentation and grooving of a surface by a counter–body. This occurs only in cases when the counter–body, abrasive, have higher hardness than the rubbed material. It happens by microcutting, facture, ploughing or grain pull out. This wear mechanism also has two modes: two body and three body abrasive wear [204]. The existence of wear debris is inevitable, and they may come from the surrounding environment or from one of the materials involved, even if the surfaces are lubricated or not. The removal of those particles leaves grooves on the surface. The grooves are a result of plastic deformation due to contact from

the asperities on the counterpart. Plastic deformation and brittle fracture are present together in abrasive wear. The main way to avoid abrasion is to increase the surface hardness of the material and reinforce introducing hard phase is a solution for metals [93].

Also, several other minor mechanisms may occur. The table below summaries all wear processes [226].

Table 2.3 – Common observed wear mechanisms and descriptions [43].

Mechanism	Description
Adhesion	The transfer of material from one mating surface to another through atomic attraction. The bond formed is usually stronger than the shear strength of the softer material. Also defined as galling or scuffing.
Abrasion	Softer material is removed by ploughing or gouging by harder particles. These particles can be embedded into the mating counterface (2-body) or loose (3-body). Also defined as scoring.
Corrosion	A corrosive environment produces a reaction production on one or both sliding surfaces, which is subsequently removed by the relative motion between the two. Also includes metallic oxidation.
Fatigue	Repeated cyclic sliding stresses cause sub-surface cracks which eventually result in spalling of large material fragments.
Erosion	Can be also grouped into abrasion wear, but material is removed by the particles striking the surface, which are carried by a gas stream entrained in a flowing liquid.
Delamination	Removal of sheet-like wear debris due to the nucleation and propagation of sub-surface cracks parallel to the sliding surface.
Fretting	Wear of material due to oscillatory movement. Includes the generation of wear debris by adhesive and corrosive mechanisms.
Polishing	Wear by polishing operated by nearly the same mechanism as that of abrasion; however, the particles are blunted and schematised as spheres.
Impact Chipping	Small-scale spalling as though small chips knocked out of the hard material surface due to brittle fracture under high impact.
Tribochamical Wear	Very important to the wear of ceramics. Environmental factors influence plastic flow by affecting the mobility of near-surface dislocations, and also lead to the formation of transfer films.
Cavitation	Occurs via the collapse of vapour bubbles in the lubricant which causes acceleration and impingement of liquid at high velocity on the surface.

If all the plastically deformed material is removed, wear mode is by microcutting. If all the plastically deformed material flows to the sides of the

groove, wear is by microploughing. Conversely, in the presence of lubrication, flowing water included, the lubricant can remove the wear fragments of the abraded material, avoiding their accumulation that would block the abrasive action of the particles. In addition, lubricant reduces friction between the hard particle and the abraded surface, and this favours wear by microcutting [227].

The two–body abrasion mode is caused by the asperities of the counterpart. Three body abrasion mode is caused by the presence of free wear debris rolling between the surfaces in contact. If this particle is small or smooth the surface damage is small. This is similar to erosion wear, but in this later the particles need to be carried by liquid or gas [93].

Wear by contact fatigue is a typical fatigue failure: with the application of cyclic loading, a crack is nucleated and then it propagates up to the final fracture. This means that a wear fragment is produced after some cycles that correspond to the fatigue life of the loaded part. In addition, in most cases and depending on the intensity of the applied load, the overall damaging process takes place under small–scale plastic deformation, and the worn region appears macroscopically free from large plastic deformations [204, 221].

The wear rate is given by the ratio between the wear volume and the sliding distance. Archard's law is used to analyse the wear damage of worn surfaces and was developed by considering a single asperity deformation for adhesive wear [93, 228].

2.5.2.2   Mild wear severe wear

Wear is classified by two conditions: mild and severe. Large values of wear rate ($> 5 \times 10^{-3}$ mm^3/m) and specific wear rate ($> 10^{-4}$ m^2/N) wear is severe. Adhesion and abrasive wear are classified by severe while tribo oxidation is mild. Cracks and extremely rough surfaces are observed on severe wear. The transition between these two conditions is not clear and an intermediate region with a mix transitional behaviour exists. In this case it is useful to analyse a material by the so–called wear map which load and sliding speed varies in laboratory tests and plotted in a graph range to determine each condition. In metals, the higher the hardness the lower the specific wear rate because when

hardness is increased the capacity of a metal to support the oxide layer also increases. Also the presence of a lubricant film between two contact surface prevents the direct contact between the asperities reducing the sheer stress [213].

The wear material loss process has been investigated widely. However, this process *in vivo* is complex since not only wear exists but also corrosion is an important factor on material degradation [229].

2.5.2.3   Tribology of metallic biomaterials

While wear refers to material loss and it is a mechanical process; wear rate is the material loss volume over time. In the real implanted prothesis sliding wear is the process and wear and corrosion coexist. Materials with high wear rate in experiments such as ball on disk test are expected to have the same behaviour in replacements [143, 230].

Corrosion resistance and wear resistance are proprieties that do not rely only to the material. They depend on the dominating deuteriation mechanism and to the tribological system (counterpart, lubricant, load and electrolyte). It is not possible to improve the resistance of a material to one of the wear mechanisms in general but suitable materials have to be selected based on the information available of the conditions.

2.5.3 Tribocorrosion

The wear process has its own mechanisms as well as corrosion. However, when both occur at the same time, specific mechanisms are seen such as tribocorrosion, corrosion fatigue and fretting corrosion [231, 232].

The material loss in a tribological contact in a corrosive environment is called tribocorrosion (degradation due to the simultaneous action of chemical and mechanical effects) [210, 233]. In other words, tribocorrosion is the interaction of electrochemical and mechanical wear or a study of two different scientific

domains: tribology and corrosion. The degradation of materials used as implants were believed to degrade by only mechanically action due to tribological contact. Nevertheless, these materials are in a biological fluid that is a corrosive environment. Corrosion resistance in this case is not the only important propriety, since the passive film may be removed and the corrosion process accelerated. This process happen in several conditions and this transformation is permanent [234-236].

A common situation in a sliding condition is the wear due to two or three bodies. It is observed in fretting corrosion and also in ball bearing under contact. Another case that may results in tribocorrosion is particle impact that causes mechanical removal and chemical attack on the surface. A passive metal forms a protective layer that works as a shield from corrosion. However, this layer can be removed by mechanical repassivation. Normally, metals under this system show a corrosion acceleration, where wear enhances corrosion rate [160, 210].

In order to control the surface chemistry, it is necessary to understand the electrochemistry of the system in tribological contact. The connection between friction and electrochemistry processes is subject of many researches. The passive film has an important role on mechanical degradation and friction can change the corrosion resistance of metals [233, 237]. Corrosion is also enhanced due to the galvanic coupling between worn and unworn surfaces [199].

A passivated metal forms a layer who acts as a protection against the corrosive environment and corrosion. However, if there is a rubbing (real situation of a prosthesis) that removes partially or totally the passive layer, the corrosion rate will be enhanced (wear–accelerated corrosion), because the metal will depassivate leading to metal ion release, even if it subsequently re–passivates. Normally the degradation due to the mutual action of corrosion and wear are higher (synergetic effect) or lower (antagonistic effect or negative synergism) than that of adding separately the corrosion and wear. Many mechanisms of tribocorrosion are not yet fully understood. Fig. 2.13 shows tribocorrosion of passive metals [100, 238].
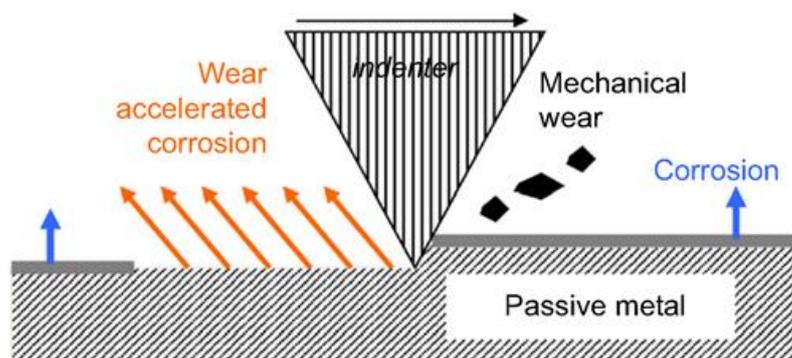
Fig. 2.13 – Tribocorrosion process of passive metals [232].

In the late 1970s and early 1980s several groups simultaneously studied the effect of wear on corrosion in abrasion-corrosion, erosion-corrosion and sliding-corrosion systems in different industrial applications. The open circuit potential (OCP), potentiostatic or potentiodynamic electrochemical techniques were used in an attempt to determine the synergies between wear and corrosion of Iron based alloys. Although similar trends in the synergistic effect of wear on corrosion rates were found, no systematic approach or model was proposed for understanding wear-corrosion (tribocorrosion) interactions [138].

Later, between the mid-1980s and early 1990s a group in the US Bureau of Mines proposed the first model for describing the interaction between wear and corrosion by elaborating a series of equations able to determine the extent of synergism existing in mining and mineral processing equipments. They based their experiments which determined the synergism between wear and corrosion of a high carbon steel using a jet impingement system by subtracting the pure abrasion rate and the electrochemical corrosion rate from the total material loss. The approach proposed by the US Bureau of Mines was later published in a standard guide for the determination of the synergism between wear and corrosion of metallic materials in liquid solutions or slurries [149].

The experiments proposed in the standard consist of measuring the individual contribution of corrosion (C_o) in a separate test where the mechanical part is eliminated; the individual contribution of wear (W_o) by applying a cathodic potential of 1 V versus OCP during wear to eliminate the corrosion component; and the concurrence of wear-corrosion by the total material loss (T). Thus the total material loss due to tribocorrosion can be expressed as the sum of the material loss due to pure wear, the material loss due to corrosion in absence of wear and the synergistic factor (S), which is the combined effect of wear and

corrosion [149]. Friction is highly dependent of potential applied due to the metal sensitivity to hydrogen embrittlement, that is why the standard fixes these potential values.

The synergism between corrosion and wear on tribocorrosion is mathematically expressed by equation 11 and it is known as the synergistic approach, proposed by ASTM G119.09 standard [22, 239, 240]:

$$T = W_o + C_o + S$$ Eq. 11

T: Total material loss

W_o: Material loss rate due to wear

C_o: Material loss rate due to corrosion

S: Material loss rate due to corrosion and wear

The synergistic term (S) is defined as the sum of the change in corrosion rate due to wear (wear-accelerated corrosion, ΔCw) and the change in wear rate due to corrosion (corrosion-accelerated wear, ΔWc). S is expressed by equation 9:

$$S = \Delta W_c + \Delta C_w$$ Eq. 12

ΔW_c: The increase of wear due to corrosion.

ΔC_w: The increase of corrosion due to wear.

The effect of wear on corrosion (ΔCw) is referred to in the standard as the 'additive effect'. The 'synergistic effect' is defined as the enhancement of wear due to corrosion (ΔWc) and the 'negative synergism' or 'antagonistic effect' is the protection of the surface against further wear due to the electrochemical formation of a protective layer [149].

Then, the equation 11 can be expressed:

$$T = W_o + C_o + \Delta W_c + \Delta C_w$$ Eq. 13

In addition, the total contribution of corrosion is given by Cw and the total contribuition of wear is given by Wc.

$$Cw = C_o + \Delta C_w \qquad\qquad \text{Eq. 14}$$

$$Wc = W_o + \Delta W_c \qquad\qquad \text{Eq. 15}$$

According to ASTM G119.09 standard [240], material loss rate is expressed by the following equation:

$$Material\ loss\ rate = \frac{8760\ x\ Wear\ track\ volume}{Wear\ track\ area} \qquad \text{Eq. 16}$$

It is expressed by mm/year [145, 240].

Yan [241] used this approach to identify the components of volume loss for high and low Carbon CoCrMo alloys and 316L stainless steel in 50% serum, Dulbecco's Modified Eagle's Medium (DMEM) and 0.36% NaCl solution; and identified that material loss in 50% serum is predominately due to wear and it changes with other electrolytes used.

Martin [242] studied the tribocorrosion behaviour of Ti-6Al-4V in NaCl solution and found that corrosion increased during wear and it was atribuited to the removal of the passive film. Mechanical wear was also increased when the surface was subjected to corrosive solution. It was atribuited to the formation of harder wear debris during anodic wear, which acts as an abrasive during sliding, and thus increases the mechanical wear. Other studies can also be found elsewhere [243, 244].

It is not possible to make a mechanistic interpretation of the tribocorrosion process using the synergistic approach because the current techniques are limited. The techniques measure separatedly the mechanical and corrosion contributions. Because of this limitation, the synergy is evaluated using external references such as application a cathodic potential to avoid metal dissolution and then determine the materal loss due to wear (Wo). Moreover, according to Akonko [245] and Espallargas [246] this method is dependent on the cathodic potential and electrolyte applied. Wear varies up to 1 order of magnitude when cathodic potential is changed to other values due to the metal sensitivity to hydrogen embrittlement [245]. Another important approach is called the

mechanistic approach. The mechanistic approach distinguishes two main contributions: anodic dissolution (wear-accelerated corrosion) and mechanical removal of metal particles (mechanical wear). A mechanistic approach for fretting-corrosion systems was first proposed by Uhlig in 1954, stating that the mechanism of fretting corrosion includes a chemical factor and a mechanical factor, with observed damage, in general, resulting from both. A methodology for quantifying the two contributions was developed at the Ecole Polytechnique Fédérale de Lausanne (EPFL, Switzerland) in the early 1990s. They observed on one hand that the electrochemical material removal rate is strongly influenced by mechanical parameters and, on the other hand, that the mechanical material removal rate depends on the prevailing electrochemical conditions [138]. This approach extensively used in erosion and abrasion-corrosion has been also applied to sliding systems of passive materials and coatings.

This approach is expressed by the equation [247, 248].

$$V_t = V_m + V_c \qquad\qquad \text{Eq. 16}$$

Where Vt is the total material loss, V_m is the material loss due to mechanical wear and V_c is the material loss due to corrosion in mm^3. Using Faraday's law, the materials loss due to corrosion is found using the following equation. The excess current can be related to the material loss through Faraday's law,

$$Vchem = \frac{Q \; x \; M}{n \; x \; F \; x \; \rho} \qquad\qquad \text{Eq. 17}$$

$$Q = \int_0^t idt \qquad\qquad \text{Eq. 18}$$

$$Vchem = \frac{i \; x \; t \; x \; M}{n \; x \; F \; x \; \rho} \qquad\qquad \text{Eq. 19}$$

Q is the electric charge flowing in the wear track (C), i is the average current (A) during rubbing for polarization tests (cathodic and anodic potentials) and for the OCP test i is the corrosion current (A) found by potentiodynamic test, t is the time (s) of rubbing, n is the charge number for oxidation reaction, F is the Faraday constant (96500 C/mol), ρ is density of alloy (g/mm^3), M is the atomic

mass of alloy (g/mol). This is the only way to analyse the tribocorrosion behaviour of a material and it is important to consider that material loss volume due to corrosion is related only to the worn surface [24, 249, 250].

Mischler [22] published a critical appraisal of the main electrochemical techniques and evaluation methods used in tribocorrosion research with special emphasis on sliding and fretting situations involving passive metals. They showed that the synergetic approach and mechanistic approach are one of the main methods used to quantitatively describe the synergistic effect between corrosion and wear.

Even though this approach has been used [210, 249, 250] there are some issues that still need to be considered. The volume is a result of the whole process, and there is no information generated as to differing electrochemical or chemical states on the surface of the material over the time during the progress of the process [22].

Many studies for investigations of wear and corrosion have used those equations [233, 251, 252] and their interactions in an environment where active biological solutions or saline solutions are used [70, 233]. Marques [253] studied the synergism biofunctional titanium oxide films and concluded wear as dominant mechanism. The contribution of wear and corrosion and their synergistic effect on the tribocorrosion process of TiC_xO_y thin films for decorative applications were analysed by Mathew [254]. It was observed that tribocorrosion process is dominated by wear process.

Khan [255] studied the synergism of corrosion and wear of Ti alloys for biomedical use. An increase weight loss due to the presence of corrosion is found in wear tests. However, with proteins, a weight gain was observed.

Tribocorrosion can be studied using different experimental procedures to control mechanical and electrochemical settings. Tafel test (polarization) can be applied to obtain an anodic environment and test a material under corrosion and rubbing. Normally, when a material is under anodic environment, its anodic current increases when rubbing starts due the removal of the passive film [256, 257]. Moreover, wear–accelerated corrosion relies on the material used, environment, force applied and the potential range. The manifestation of tribocorrosion is most common in industries such as marine, mining, aerospace, food, nuclear, chemical, and petrochemical. The fundamental mechanism and their overwhelming factors are not well understood. Examples of tribocorrosion

problems in industry are: the accelerated corrosion of steel conveyors exposed to ambient air of high relative humidity, the fall out of electrical connectors in the automotive industry, the degradation of orthopaedic prosthesis and dental fillings and the erosion wear of turbine blades. Finally, some researchers have realized a modification on surface proprieties of materials after tribocorrosion process [208, 210].

Tribocorrosion is an important factor in the damage caused to biomaterials used as joints and it is the principal contributor to the early deterioration of implants. Therefore, it is of extreme importance to understand the tribocorrosion behaviour of the materials used as replacements to avoid problems. The long–term durability of Metal–On–Metal (MOM) joints relies on control of both their corrosion resistance (relating to ion release) and wear behaviour (relating to creation of nanometre scale wear debris). A THR is illustrated on Fig. 2.14 where three interfaces are illustrated and it shows the femoral head and stem experience micromovements between the prosthesis and bone [210, 234].

The metals are used for femoral part of the implant are CoCr or Ti alloys. Usually, the anatomic medullary locking (AML) stem is made of CoCr alloys and the socket is made of Ti alloy. MoM hip implants were introduced in 2002 and are popular because they have a low wear rate. Ceramic-on-ceramic (CoC) implants are newer and a metal oxide is used as the ceramic for both the ball and socket. Although the release of wear debris is decreased, the concern with metal ions accumulating in the body from the MoM implants and the risk of the ceramic implants fracturing are design relevance to these types of implants. The metallurgy, diametric bearing clearance, sphericity, and surface finish of MoM implants may be the most important engineering factors for the success of the implants [258].

Current concerns regarding MoM implants are the higher release of CoCr as compared to their release in metal-on-polyethylene (MoP) articulation. Electrochemical issues MoM implants may present a problem because they release metal ions into the body. It has been well documented that patients with MoM hip replacements have increased the level of metal ions in blood and urine studies [259].

A difference in the cellular response to different types of metal-alloy particles of the same size has been demonstrated in several analysis. Even though CoCr particles are the most toxic to the body, particles from less toxic

alloys may be worse because of their ability to cause the release of inflammatory mediators. Although many studies have shown potentially adverse pathophysiological effects related to metal ions including Co, Cr, Ti, Al, and Ni in the human body, the definite effects have yet to be determined. Toxicity, carcinogenicity, and metal allergy are the most significant concerns. Compared to the other types of bearings, ceramics bearing surfaces have the lowest wear rates. Because of these low wear rates and the improvement in the quality of the ceramic material to reduce the risk of fracture, the use of ceramics in hip arthroplasties, especially for younger and more active patients, may provide the best opportunity for the long-term success of hip implants. CoC implants can be expected to last twenty years. Despite continuing research and improvements in components of hip implants, an ideal hip prosthesis has yet to be created [63].

The deposition of proteins on a surface under rubbing can form a layer called a tribolayer. Some researchers have found that it can enhance wear for some alloys. However, other researchers have found that the tribolayer can reduce the wear rate for other materials [209]. Raman spectroscopy is used to study the presence and nature of the tribolayer. Lindquist [260] studied the tribofilm formation of TiC and TiAlC coatings. The lower friction was attributed to the presence of only disordered amorphous Carbon on TiAlC surface. Namus [261] studied proteinaceous surface film formation of CoCrMo alloys in several normal loads. The lowest specific wear rates were found at 40N and 60N which is associated to the formation of proteinaceous film.
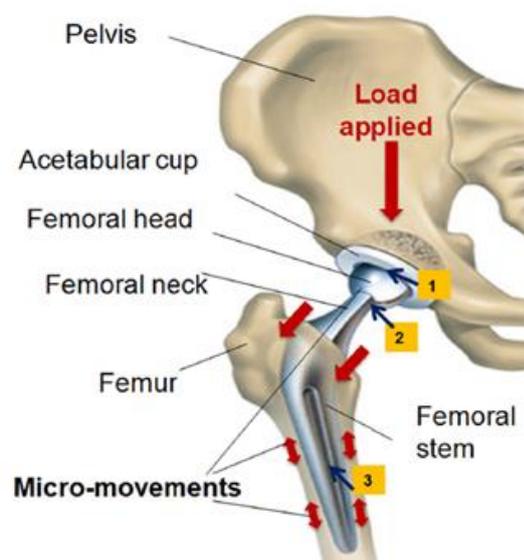
Fig. 2.14 – A total hip replacement and its interfaces [234].

The techniques that involve the study of corrosion and tribology have been developed recently and allow the study of tribocorrosion systems. One of the most common is the use of a potentiostat. It permits the control of the potential of the system and study the behaviour of a material over different conditions. It works by imposing a potential on a sample and then monitoring the current as a response of the sample during rubbing. When rubbing is taking place the system is perturbed which leads to the removal of the passive film which affects the corrosion rate. Also, the potentiodynamic test is used to measure the corrosion potential and corrosion current or a specific potential can be applied to analyse the behaviour of a material during rubbing. Potentiostatic and potentiodynamic tests combined with wear are common techniques used to study tribocorrosion [236, 238].

When OCP and wear tests are combined, the material shift to active from passive state because of the disturbance of wear on the surface [262]. This leads to galvanic coupling. If the passive film is removed during this test, a drop of the potential to the cathodic area is seen, called cathodic shift [263]. This change is only seen on passive metals and active metals show similar performance in OCP with or without rubbing [264].

The potentiostatic technique is characterized by the application of friction at just one potential. It records the material response to the current density and friction. It gives information about a material tested in the condition chosen such as passive or active areas [210]. The difference between potentiostatic technique and potentiodynamic technique in the latter potentiodynamic sweeps are applied. Current is also measured, but this test gives the chemical and electrochemical change during rubbing, and friction is also affected [183, 199].

A tribocorrosion cell set up is shown in Fig. 2.15. The corrosion cell has 3 electrodes: the reference electrode, working electrode (sample) and counter electrode in a solution that normally mimics the synovial fluid. This last is a complex body fluid that has proteins, organic molecules, cells and salt. It acts as a lubricant and as a corrosive fluid. In general, a tribometer measures the response of the material tested by applying frictional forces in an electrochemical environment and monitors the corrosion of the system [238]. It measures the current, potential and coefficient of friction and is useful for subsequent analysis and correlation with other information from the worn area. It can be used to test samples for orthopaedic and dental application, for example. Wear tests are

normally performed with electrochemical methods in order to test the tribocorrosion behaviour of a material. [8, 210].
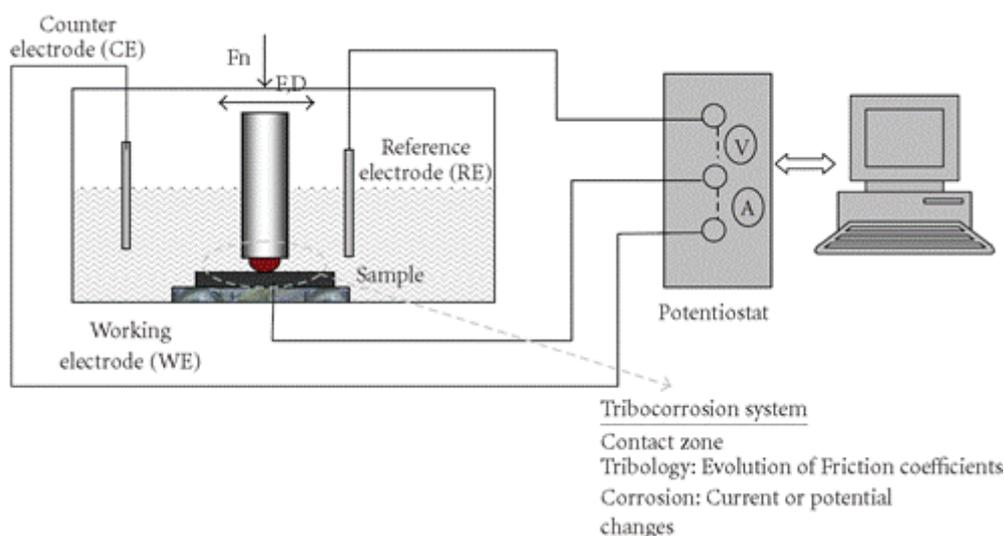
Fig. 2.15 – Tribocell and potentiostat [236].

It is important to understand the tribocorrosion behaviour of materials used as medical devices to avoid further revisions. Hip and knee simulators in laboratories are widely used to test materials and designs before they go to clinical trials. Such simulator tests and simple wear tests are always referred to as *in vitro* tests, while *in vivo* tests are experiments performed in the living organism.

Tribocorrosion experiments are used to study different conditions and their effects of parameters on passive film formation [265, 266]. Human synovial fluid is complex and the stability of the passive film may be modified by its action and the relative motion of implanted devices.

Another layer may be formed when two surfaces are in relative motion. This layer is called tribolayer (or tribofilm) a kind of fluid that contains proteins and it may be constituted by the debris generated, organic species and ions from the destroyed passive layer. The tribofilm has an important role on the performance of joints. However, its formation and proprieties are lacking studies [21, 267, 268].

The organic components may affect the wear performance of alloys used for hip replacement. The proteins in synovial fluid can form a proteinaceous film on the biomaterial surfaces immediately upon implantation. During the wearing process, there may be some kind of organic-metallic composite formed on the

surface. The tribofilm is carbonaceous its nature is specific to the sliding mechanisms [269].

Hallab [270] discussed the interfacial kinetics of the adsorbed biofilm composition and the released metal-protein complexes. The hypothesis that some interfacial properties such as metal-protein interactions are alloy and element-specific was demonstrated. These interfacial properties may influence long-term biological interactions of metallic biomaterials.

Wimmer [271] remarked that the carbonaceous film contains graphite. As graphite is a standard solid lubricant that is known to perform well in the presence of water, the existence of graphite has an important role in reducing friction as well as corrosion and wear. The detail of its formation is not fully understood. It could arise as a result of very high temperatures and shear stresses that are generated by the contacting asperities roughness in the artificial joints or the tribological effects of friction, lubrication and wear on the joint.

Liao [272] used several advanced techniques, such as FIB, SEM and Raman Spectroscopy to characterize the tribofilm on the surface of retrieved hip implants. They found that the tribofilm in MoM hip replacements is primarily graphitic carbon, which can reduce friction as well as wear and corrosion.

Yan [273] observed the surface of a retrieved hip implant as well as a hip components from a hip simulator by scanning electron microscopy (SEM), and found a tribofilm of about 15-80 nm thickness. It was reported that the formation of this tribofilm was attributed to the chemical reaction between organic species (proteins) and metal ions, and the tribofilm contains organometallic formations.

Electrochemical experiments showed the effect that the tribofilm has on the electrochemical character during the process of wearing. The total material loss and ion concentration after testing in serum and in NaCl were also measured. It was shown that due to the presence of the tribofilm, the total material loss and ion release in serum were less than that in NaCl. So the tribofilm can effectively limit the wear of MoM bearings. It can be concluded that a protective tribofilm can be formed by the interaction between proteins and released ions during the wearing process both in vitro and in vivo, and in turn reduces metal ion release. By applying a positive potential, under tribological contact with proteins, the tribofilm can form more quickly. The exact mechanism is still unknown and needs further investigation [274].

The studies of tribocorrosion focus on wear, corrosion and wear–corrosion of the most used metallic biomaterials alloys. These studies face challenges since simulating real conditions such as sliding movements, chemical environment, presence of proteins, contact conditions, pH and temperature is not an easy task, and the role of the proteins are not well understood. Another issue is the lack of standard test procedures because it is a relatively new field [275, 276].

Even though reciprocating wear tests cannot perfectly represent the real tribological contact of hip prosthesis *in vivo*, it has been accepted as a standard testing technique to describe the surface performance under simulated conditions [257].

2.6   Current status of tribocorrosion of Titanium

Surface treatment developments, performance and wear mechanisms and the effect of variables such as temperature, mechanical load, nature of electrolyte and speed are the main focus of recent studies of tribocorrosion of Titanium alloys [277, 278]. The repassivation capacity of a material under a wear process, microstructure, tribological and electrochemical proprieties have great importance in tribocorrosion proprieties of titanium alloys. Therefore, authors believe that this is a complex subject, but tribocorrosion plays the most important factor.

S.J. Li tested the wear behaviour of Ti–29Nb–13Ta–4.6Zr and Ti–6Al–4V in NaCl solution and concluded that oxidation treatment improves wear resistance of Ti–29Nb–13Ta–4.6Zr due to the formation of a hard, lubricating Nb_2O_5 oxide layer on the surface of the alloy during sliding wear test, whereas such a treatment has no effect on Ti–6Al–4V. In addition the increase of Nb content improves wear resistance of Ti–29Nb–13Ta–4.6Zr alloy [114] and Geetha found that low levels of Nb leads to high amount of alpha phase and inferior corrosion behaviour on Ti–13Nb–13Zr alloy in Ringer's solution [109]. Ti–29Nb–13Ta–4.6Zr showed COF of 0.4 in reciprocating sliding condition in Riger's solution [279] and Niinomi observed that Ti–29Nb–13Ta–4.6Zr presented lower material loss in Riger's solution than in air during wear test [280]. Diomidis tested Ti–29Nb–13Ta–4.6Zr in Hank's balanced salt solution and observed that the material loss is higher at passive potential than at OCP [236].

Buciumeanu found that the wear resistance of Ti64 tested in a Phosphate Buffered Saline (PBS) fluid relies on its manufacturing process, microstructure and hardness. This test presented COF 0.4 and the specific wear rate changed with manufacturing process where the cast material presented specific wear rate of $9x10^{-4}$ $mm^3N^{-1}m^{-1}$. Abrasive wear was identified as the main wear mechanism [129].

Abrasive wear was also identified as the main wear mechanism on Ti-13Nb-13Zr tested in Hank's solution and COF of 0.46 [83]. Ti–13Nb–13Zr alloy in Ringer's solution presented wear rate of 0.035 mm^3/m and wear resistance lower than Ti64 which is harder. The both alloys exhibit spontaneous passivity in naturally aerated Ringer's solution at 37°C [193].

Yang observed that the dominant wear mechanisms of Ti-12Mo-6Zr-2Fe in simulated body fluid are abrasive wear and tribo-chemical d and the COF in dry condition and in SBF was 0.8 [104]. Hacisalihoglu also used SBF to test Ti–13Nb–13Zr and found this alloy becomes more active when rubbed at OCP due to the removal of oxide layer and has a lower volume loss than other Titanium alloys such as Ti64 [281].

In 2002, Stryker developed two products called ABG II Modular and Rejuvenate Modular. These products were recalled by the US Food & Drug Administration (FDA) in 2011 due to the high levels of wear debris generated by the movement of the stem and neck at the contact point where they fit together. These products have a separated stem (Ti-12Mo-6Zr-2Fe) and a modular neck (CoCr alloy) and are made of alloys with different hardness, where CoCr alloy is harder and the wear debris are generated from the stem material under the conditions of articulating surfaces within the environment of the body [104]. However, Ti-12Mo-6Zr-2Fe alloy is a β alloy with low elastic modulus and has nontoxic elements.

The passivation and repassivation during rubbing, microstructure and alloying elements have an important role on tribological, electrochemical and tribocorrosion behaviour on Ti alloys. Understanding the tribocorrosion behaviour of Ti alloys for biomedical applications in body simulated fluid is vital for future alloys development because long lasting biomaterials are required. It includes synergy studies and identifying any link between tribocorrosion resistance, passivity and subsurface phase transformation. A study with this approach must

be performed since knowledge in this area is limited and Titanium alloys are promising biomaterials (low density, corrosion resistant and low elastic modulus).

This project studies wear and tribocorrosion behaviour of Ti–13Nb–13Zr, Ti-12Mo-6Zr-2Fe, Ti–29Nb–13Ta–4.6Zr aged at 300ºC and Ti–29Nb–13Ta–4.6Zr aged at 400ºC in bovine serum solution at 37ºC in order to obtain a better understanding of the effect of alloying elements and microstructure on these phenomena by analysing parameters such as COF, specific wear rate, volume loss, roughness, tribofilm formation, synergism and phase transformation.

2.7   Summary

This chapter gives an overview of biomaterials, wear, corrosion, tribocorrosion and synergism. Issues that led to surgery revision such as stress shielding effect and toxicity were discussed. Also an overview of current biomaterials used as biomaterials such as stainless steel, CoCr alloys and Titanium as well as their limitations was discussed.

The focus of this chapter was particularly Titanium alloys where their characteristics and properties were discussed as well as their use as biomaterials. β Titanium alloy show lower density and lower elastic modulus than stainless steel and CoCr alloys which makes them a good candidate for biomaterials application. However, Titanium alloy have poor wear resistance which leads to high ion realise to human body. Moreover, the tribocorrosion phenomena and mechanisms of titanium alloys in different electrolytes are not fully understood and studies are needed to contribute to this topic and for future alloys development.

The question then arises: what is the effect of microstructure and electrochemical condition on tribocorrosion behaviour of Ti alloys? Do they affect synergy? Up to now the synergistic and antagonistic effects between the effects of chemical and mechanical wear have not been properly investigated for different microstructures of titanium alloys in bovine serum solution.

Chapter 3 – Experiment methods and surface analysis techniques

3.1 Introduction

This chapter describes the main features of the experimental work. It presents the material preparation, alloy composition and processing, including melting, heating and rolling. Also it presents test conditions of tribocorrosion test and the electrochemical measurements. Finally surface analysis techniques are described such as XRD, nanoindentation, SEM, FIB, TEM, Raman spectroscopy and interferometry.

Figure 3.1 summarises the experiments used in this study to give the reader an overview of everything that was undertaken.

3.2 Materials preparation

The current investigation focused on the reciprocating sliding tribocorrosion testing and characterization of four different microstructures of Titanium alloys for artificial femoral head and stem hip–joint applications to compare their performance as a function of microstructure. Tribocorrosion tests were carried out at anodic potential, open circuit potential and cathodic potential for comparison. Section 5.1 focuses on tribocorrosion behaviour of the Titanium alloys chosen submitted to 0.5N normal load and Section 5.2 compares these results to 1N and 2N. The microstructure of each alloy will be detailed, and each alloy will be referred to by its microstructure. The Fig. 3.1 summarizes the processing and characterisation methods used on this project and the table 3.1 shows the composition of the samples (in % weight) used in this study.
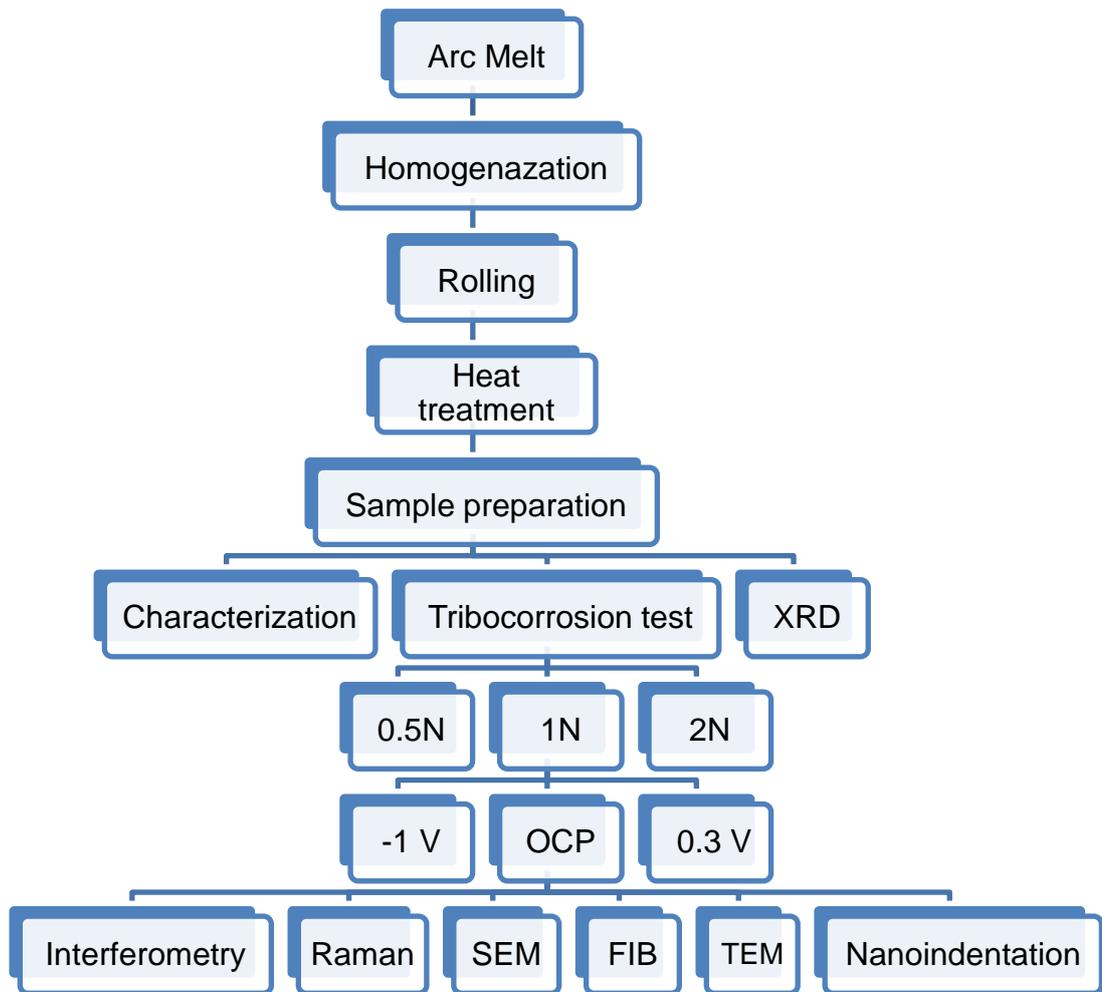
Fig. 3.1 – Summary of procedures of this project.

Table 3.1 – Composition of the alloys used in this study.

Alloys	Microstructure	Nb	Ta	Zr	Mo	Fe	Ti
1	Aβ	13	–	11	–	–	bal
2	Nβ	–	–	4	11	2	bal
3	B	30	13	3	–	–	bal
4	Bω	30	13	3	–	–	bal

These alloys were chosen in order to compare different microstructures and are based upon publication data for these materials for biomedical applications: ASTM F 1713, ASTM F 1813 and TNTZ alloy [5, 9, 12, 14, 18, 282]. The Titanium alloys were produced by a vacuum arc melting furnace using an Arc 200 arc melter supplied by Arcast. They were melted with DC transferred arc as the heat source. 100 grams of material was melted for each composition. The

machine was evacuated and flooded with argon. The machine was equipped with a water–cooled hemispherical bowl Copper crucible. The temperature of the electric arc is typically 3000°C (to guarantee complete dissolution of the Nb, Ta or Mo). All materials were melted for around 25 seconds, in order to obtain cast samples of optimal chemical and structural homogeneity. All specimens were remelted three times. After melting and stirring, each sample was completely solidified in the crucible, then turned about its cross axis using the in–furnace manipulator and subsequently reheated to remelt.

After the fourth remelting step the sample was finally cast into a round copper mould (6 mm of diameter). The Copper mould was at 25°C, which led to fast cooling, minimising segregation and suppressing dendrite development. Since Ti alloys undergo very strong chemical reactions with Oxygen, the samples were melted under an Argon atmosphere.

After melting and casting, all samples were heat treated at 1000°C (above the β transus temperature) for 4 hours in an Argon tubular furnace in order to homogenise to remove micro–scale concentration gradients and to obtain a uniform composition throughout the ingot. The ingots were immediately quenched in cold water at the end of the annealing period to avoid ω phase precipitation, which is formed at intermediate and slow cooling rates. The samples then subjected to different deformation process and heat treatments. The αβ alloy was subjected to a reduction of 67% by hot rolling at 680°C. After that, it was solution treated at 760°C for 1 hour and water quenched. The aim of this procedure was to get an αβ phase alloy. The β transus temperature of this alloy is 735°C, Fig. 3.2.
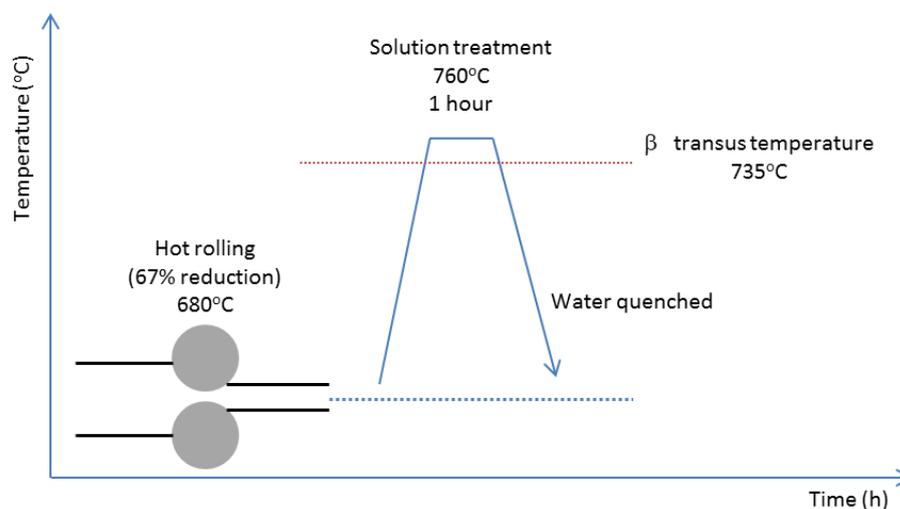
Fig. 3.2 – αβ alloy processing: rolling and heat treatment.

Nβ alloy was hot rolled (65% reduction), then aged at 600ºC for 4 hours and air cooled, as can be seen in Figure 3.3. The β transus temperature of this alloy is 743ºC. The aim of this procedure was to get a near β phase alloy.
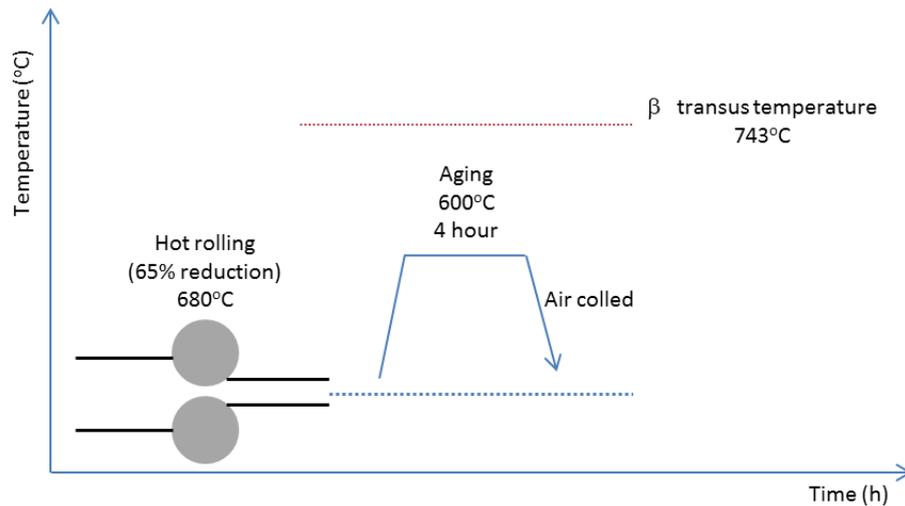
Fig. 3.3 – Nβ alloy processing: rolling and heat treatment.

β alloy was cold rolled to 87% of reduction. Then, it was solution treated at 790ºC for 1 hour, water quenched, aged at 400ºC for 72 hours and finally water quenched, to get the β phase alloy. The β transus temperature of this alloy is 740ºC, Fig. 3.4.

βω alloy was cold rolled to 87% of reduction. Then, it was solution treated at 790ºC for 1 hour, water quenched, aged at 300ºC for 72 hours and finally water quenched, to produce a βω phases alloy. The β transus temperature of this alloy is 740ºC, Fig. 3.5.

All samples were prepared by traditional metallography methods and washed in alcohol for 10 mins with ultrasonic agitation and blow–dried under compressed air immediately. The roughness of the samples was less than 20 nm for all starting surfaces.
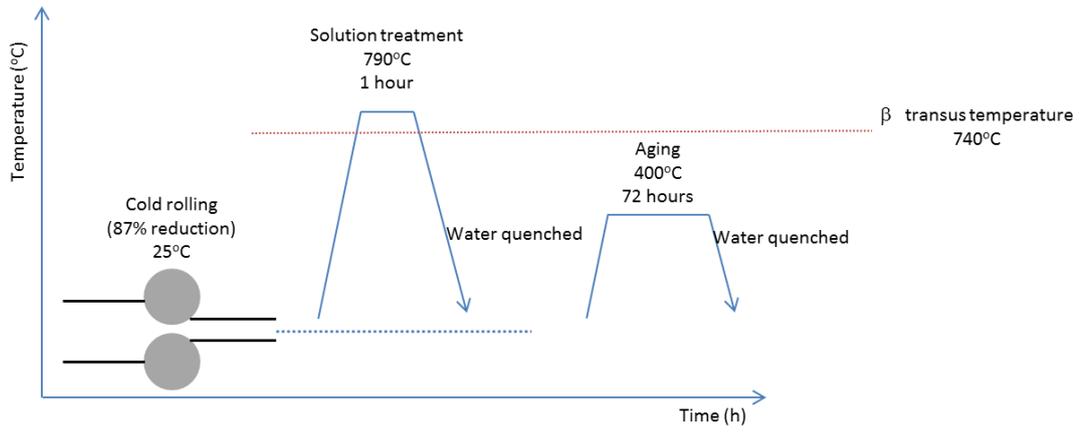
Fig. 3.4 – β alloy processing: rolling and heat treatment.
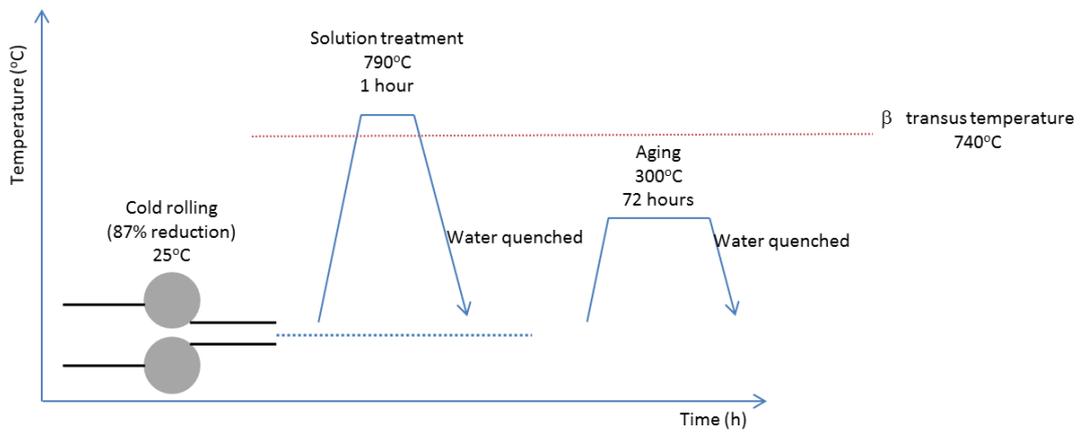
Fig.3.5 – βω alloy processing: rolling and heat treatment.

3.3 Test conditions

3.3.1 Surface processing

All samples were cut into 20x20 cm cubes using Struers Secotom 50 cutting machine. The samples were cold mounted in an Epoxicure^{Tm} – Epoxy Resin 20-3430-064 mix with Epoxicure 2 Hardener 20-3430-064 to avoid any transformation which might occur during hot mounting.

The exposed planar face was mechanically ground using SiC papers (P800, P1200, P2500 and P4000 grit for 60 seconds each), rotation 100 rpm and water (Buehler AUTO Met 250 Grinder-Polisher machine), and then followed by polishing using diamond suspensions (6 µm, 3 µm, and 1 µm for 5 mins each). Finally, polishing was carried out for 6 mins with colloidal silica suspension. Then washing with water for 2 min, and cleaned in ultrasonically bath in ethanol for 5 min.

3.3.2 Tribocorrosion tests

Reciprocating sliding wear tests were carried out using a Bruker UMT Multi Specimen Test System (Bruker, UK) connected to the CETR UMT software. A ball on plate configuration, which conformed to ASTM G133 and tribocorrosion synergistic approach conformed to a ASTM G119.09 standard.

The counterpart was an alumina ball with 4 mm diameter, 99% purity and roughness 5 – 8nm (Oakwase). An alumina ball was used as an inert counter face and to be able to compare the current tests with previous published work. This simulates the use of Titanium as tribological interface (Metal on Ceramic – MoC). The counter ball was installed in the upper holder, which is connected to a vertical linear motion system, which can take measurements to an accuracy of 50 nm. The test specimen was mounted in the lower liquid chamber, the tribocell. A precision spindle at the bottom rotates the lower tribocell at the chosen speed.

To simulate body fluids, new born calf serum (First Link) was diluted to 25 vol% in an aqueous solution of Phosphate buffer saline (Sigma–Aldrich). Ultra–pure water (Alfa Aesar) was used in the preparation of the solution. 1 wt% Sodium Azide (99% extra pure, ArcosOrganics) was added to the solution to avoid bacterial growth. This gave a solution a protein content of 15.5 g/L.

For reciprocating testing, a 2 mm stroke length and constant reciprocating speed of 5 Hz (0.02 m/s) was used. Although this speed is faster than in normal hip articulation it was chosen on the basis of previous Stribeck curve studies which showed that this speed allowed optimal lubrication conditions for this test rig. Also this speed was chosen to find out the possibility of enhancing the performance of these Ti alloys by simply changing the design. The test duration was 3h in all cases (equivalent to 54,000 cycles and 216 m sliding distance). The normal loads used were 0.5N, 1N and 2N. These parameters were chosen because this work aims to look at the worst scenario in the application and it has been reported that local contact pressure in the hips could reach different expected values [283].

The friction coefficients were measured by the ratio of tangential friction force and normal force in every second together with sliding time were recorded automatically by the machine during running. Tribocorrosion tests were performed under cathodic potential (−1 V vs OCP), open circuit potential and anodic potential (0.3 V vs OCP), according to ASTM G119.09 standard (Standard Guide for Determining Synergism Between Wear and Corrosion). Finally, the Tafel test was performed while rubbing. All samples were polished on colloidal silica and cleaned with alcohol for 10 min in ultrasonic bath 1 hour before the test. In order to guarantee reproducibility, these tests were repeated once and the results were consistent.

3.3.3 Specific wear and COF calculation

The wear rates of the materials in different lubricants were also studied. By using interferometry traces, the average cross–sectional wear loss area, A, can be calculated and it is possible to define the total wear volume loss, V, with the equation below:

$$V = A \times D \hspace{6cm} \text{Eq. 20}$$

The volume was also estimated by interferometry (Contour GT 3D Optical Microscope, vision64 software, Bruker, UK) and no difference was found. D, the

stroke length of the wear track. The average cross–sectional area of each wear track profile was achieved by taking five measurements at different locations.

According to the Archard theory [27, 284] for sliding wear of homogeneous materials, wear volume, V, can be assumed proportional to the normal load, Fn, and sliding distance, L. Therefore, the specific wear rate, (mm^3/Nm), was evaluated using:

$$SWR = \frac{V}{Fn \; x \; L}$$

<div align="right">Eq. 21</div>

The coefficient of friction (COF) is the ratio of tangential force and normal force and is measured by CETR UMT software. The normal force is a process input and the tangential force is measured.

3.4   Electrochemical measurements

The electrochemical properties (polarization behaviour) were measured in an electrochemical cell consisting of a container with a Ag/AgCl 1M KCl reference electrode (potential with respect to the standard hydrogen electrode is 0.235V) and a platinum wire as a counter electrode. This is known as a three-electrode cell. The Ag/AgCl 1M KCl was chosen due to its stability. The exposed areas were 1.54 cm^2. Polarization curves were measured using a VersaSTAT 3F Ametek potentiostat connected to the VersaStudio software. The potential scanning range was from –0.25V to 0.25V vs OCP at a sweep rate of 0.5 mV/s. After potential stabilization, the testing was ready to start. Corrosion potential and corrosion current were found and analysed by the extrapolation of the anodic and cathodic slopes of the potential dynamic test curve, dotted lines on Fig. 3.6, using the CView Software (Ametek Scientific Instruments). All samples were polished on colloidal silica and cleaned with alcohol for 10 min in ultrasonic bath 1 hour before the test.
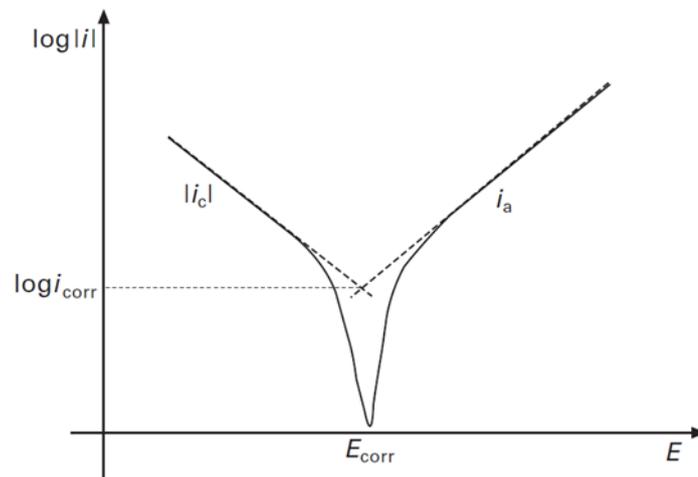
Fig. 3.6 - Determination of i_{corr} from a log|i| vs E curve [138].

3.5 Surface analysis techniques

In order to fully understand the wear mechanisms of the materials under investigation, the characterisation of unworn and worn surfaces is important. In this project, various surface characterisation techniques were employed, e.g. Scanning Electron Microscopy and Focused Ion Beam.

3.5.1 X–ray Diffraction Measurements

Structural characterization was performed, before tribocorrosion test by X–ray Diffraction Measurements (XRD) using a KristalloFlex 710D X–ray generator, Siemens Diffraktometer D5000 (Cu, GAXRD), with Cu Kα radiation (1.54178 Å wavelength), long, fine focus sealed tube source. The working conditions were: 40kV, 40mA. Data was collected using steps of 0.02°, ranging between 30° and 100°, and in fixed times of 2 s. The software used to obtain the data was DIFFRAC Plus measurement software. DIFFRAC.EVA phase analysis software package was used to index the peaks and analysis. The peaks were indexed by first selecting alloying elements and then indexing to the software data base available.

3.5.2 Nanoindentation

The reduced elastic modulus and nanohardness were measured by nanoindentation as a function of load and contact depth. Nanoindentation has become a common tool for surface mechanical properties measurement at extremely small scale. Nanoindentation was performed on a Hysitron, TI Premier, USA. A Berkovich three–sided pyramidal indenter was selected to examine the sample material in a wet environment. Calibration and determination of the tip area function was undertaken using a reference sample, fused silica (Hysitron, US), before and after the measurements on the test specimen surfaces. This material and the polished Titanium alloys samples were individually washed in alcohol for 10 mins ultrasonically and blow–dried under compressed air immediately.

Fig. 3.7 shows a typical curve for nanoindentation, a controlled loading-unloading cycle. Kick's law describes the the relation between P and h [285].
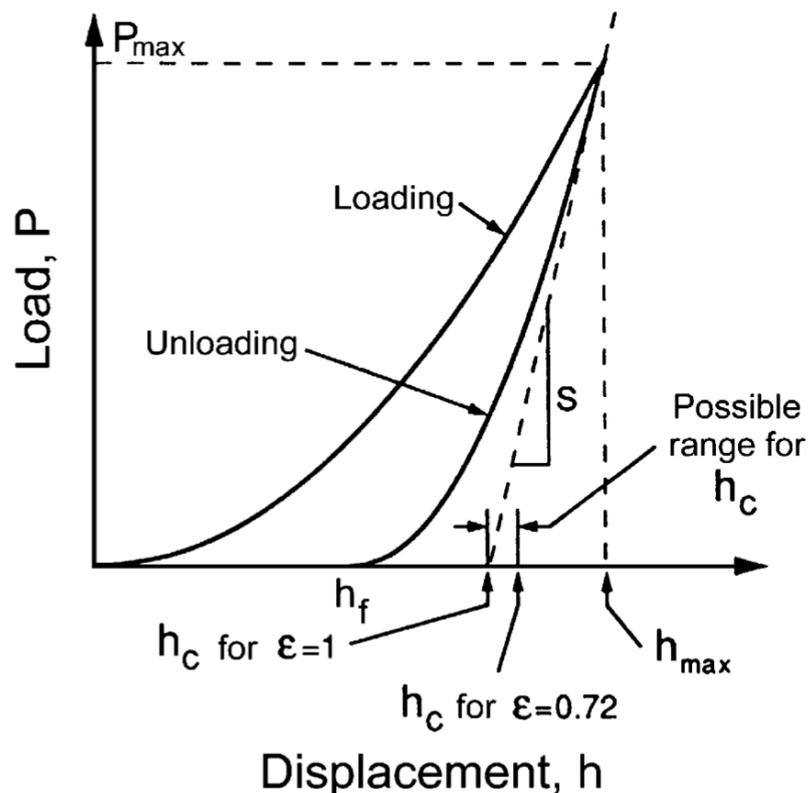
Fig. 3.7 – Nanoindentation curve [286].

$$P = C \, x \, h^2$$

Eq. 22

C is material constant that is independent on the indentation depth. The following equation shows how the contact is found [287].

$$hc = hmax - \omega \frac{Pmax}{S}$$ Eq. 23

Where ω is geometrical parameter, it is 1 for flat punch, 0.75 for cone and Berkovich tip. The hardness of the material can be found as [288]:

$$H = \frac{Pmax}{A}$$ Eq. 24

A is the projected area which is function of contact depth. For a Berkovich tip it is:

$$A = 24.5h_c{}^2$$ Eq. 25

The stiffness of the material S is extracted from loading-unloading curve as the initial slope of the unloading curve. Having both A and S one can determine the reduced modulus Er depending on the elastic part of deformation as following [288]:

$$Er = \frac{\sqrt{\pi} \, x \, S}{2\beta\sqrt{A}}$$ Eq. 26

Where β is constant depends on the indenter geometry, it is 1.034 for a Berkovich tip. Detailed calculations for elasto-plastic properties of the material by using nanoindentation can be found elsewhere [289].

Each indent had a load of 10,000 µN. 15 points were chosen on the central line of each wear track. Individual indent results were analysed, but also the average of all 15 indents were used to present the mechanical properties of the worn surface. The distance between each two indents were 5 µm to cover 75 µm of distance in total for each wear track. The software automatically calculates the relevant values after fitting the tip area function.

3.5.3 Scanning Electron Microscopy (SEM)

The general morphology of the wear track was characterised by SEM (FEI, InspectF, Netherlands) equiped with a Field Emission Gun (FEG) emitter using 5 kV, 10 kV and 20 kV for ordinary imaging as a balance between minimising the interaction volume (low voltage) and maximising resolution (high voltage). The samples were prepared by traditional micropreparation methods (section 3.3.1)

and were examined in the as–polished condition (control images) and after tribocorrosion test. The BSE images were used to quantify the grain structure (size and phase fraction) by ImageJ software.

3.5.4 Focused Ion Beam (FIB)

FIB system has the basic components similar to that of a SEM with the major difference being the additional use of a Gallium ions. Ions can strike the target with greater energy density, so can write milling patterns directly on hard materials. The use of dual beam FIB enables the area of interest to be determined using SEM and then the site–specific ion milling undertaken using the Ga+ beam.

FIB was undertaken to acquire images from the worn surfaces and to produce TEM samples, all samples and images were taken from the centre of wear track because it is where the maximum pressure is applied. FIB milling was undertaken using a FEI Quanta 200 3D (FEI, Netherlands). Carbon deposition was applied on the region of interest to prevent Ga+ implantation and sputter erosion of the top portion of the surface. the sample stage was tilted to 52° from the horizontal position to become perpendicular to the ion beam column. The Carbon deposit protection layers were 20 µm × 8 µm × 8 µm (length × width × thickness) and then two trenches (depths > 15 µm) were milled at one side of the deposition. The trench was milled using a range ion current from 5nA to 0.1nA of Ga+ ion beam for rough milling and with a 50 pA Ga+ ion beam finishing with a 52° angle between the electron beam and the sub surface cross–sectional planes. Then the sample was tilted back to 0°. The FIB cross section image (chanelling contrast image) was taken with 50pA Ga+ ion beam and at 1ms scan rate. FIB was undertaken to investigate the damage accumulation mechanisms below the worn surface for channelling contrast image. The FIB column was operated at 30kV and SEM at 10kV.

FIB can also provide a means to generate site–specific TEM samples, which is complicated using standard TEM foil preparation techniques. In this microscope, the sample stage was tilted to 52° from the horizontal position to become perpendicular to the ion beam column. The Carbon deposit protection layers were 15 µm × 2 µm × 2 µm (length × width × thickness) and then two trenches (depths > 7 µm) were milled at each side of the deposition. The trenches

were initially milled using a high ion current (5 nA), then reduced the current step by step (to 1 or 3 nA) as the regular cleaning steps moved closer to the deposition strap until sample material foil achieved with a thickness around 1µm. Then the sample was tilted back to 7 ° to allow the ion beam (current around 3 or 1NA) to cut the foil through at 45 ° and leave the other side visible with SEM. A little bit of material bridge was left on the right top corner position for holding the foil in place. Omniprobe (Omniprobe, US) was inserted into the microscope and driven to approach to the coincident point on the material foil until touching after the stage was tilted back to 0°. A small area (2 µm × 2 µm) of Carbon deposition was then sputtered at the connect point as glue to stick them together.

The remaining sample bridge was then cut through and then the Omniprobe was retracted so that sample foil was lifted out by the Omniprobe micromanipulator. A particular TEM Copper grid was placed in the chamber and the sample foil was then attached to the TEM grid by driving the Omniprobe to the coincident point and glued with Carbon and Platinum deposition layer. After that, the connecting point of the Omniprobe and the sample foil were milled by ion beam, in order to retract the Omniprobe. Final thinning was done using progressively smaller FIB currents, to slice the outer parts of the sample material until electron transparency was achieved. This final cleaning cross section was started with FIB current of 1000 pA for the front trench and then the back trench. The current was gradually decreased; 50 pA was selected for the final stage polishing. On the other hand, the stage had to be tilted to 53.2° for front trench cleaning and 50.8° for back trench cleaning to reduce the beam angle effect on the sample foil thickness. After the final thinning process, sample foil had a thickness of about 100 nm.

3.5.5 Transmission electron microscopy (TEM)

The Transmission Electron Microscope (TEM) uses a high energy electron beam transmitted through a very thin sample to image and analyse the microstructure of materials, such morphology, crystal structure, crystal phases and defects. with atomic scale resolution. TEM was performed using a Philips EM420 TEM operating at 120kV and a JEOL JEM-F200 Multi-purpose Electron Microscope operating at 200 kV accelerating voltage equipped with an Oxford Instruments Energy Dispersive X-ray spectrometer (EDX) with Aztec software

version 3.1, which was used for subsurface chemical analysis. Bright field, dark field and selected area diffraction patterns (SAED) were obtained. The images were obtained by software DigitalMicrograph (Gatan Inc.). The SAED were indexed using the following steps: software imageJ to measure the distance of each spot to the central spot to calculate d spacing values. d spacing is given by Bragg's equation ($n\lambda = 2d\sin\theta$) and then compared with the standard crystallographic diffraction patterns.

3.5.6 Raman spectroscopy

Light interacts with matter in different ways, transmitting through some materials, while reflecting or scattering off others. Both the material and the colour (wavelength) of the light affect this interaction. Spectroscopy is the study of this light. The Raman scattering process measures a very small fraction of the scattered light (frequency change). When light is scattered by matter, almost all of the scattering is an elastic process (Rayleigh scattering) and there is no change in energy. However, a very small percentage of scattering is an inelastic process, thus a scattered light has different energy from incident light. The frequency changes during the scattering process, its energy changed by interacting with molecular vibrations.

In this study Raman spectroscopy (inVia Renishaw, UK) with an exciting laser wavelength of 514 nm at a power of 20 mW was carried out on the wear tracks after wear tests. Raman spectra with a focused spot diameter of approximately 1 µm were performed from 1000 to 2000 cm^{-1}. Raman spectroscopy was used to identify the presence of a proteinaceous layer on the wear track. The measurements were repeated 5 times in different points of the worn area. A traditional fitting method was used: baseline correction, data smoothing, curve normalisation and Gaussian peak fitting, as recommended by Renishaw.

3.5.7 Interferometry

The wear track cross–sectional profile after reciprocating wear was assessed using an optical interferometry (Contour GT 3D Optical Microscope, Bruker, UK). This machine measured the surface roughness and wear track

profile of the samples. This profilometer permits accurate two–dimensional surface profiler measurements in a wide range of measurements using vertical scanning interferometry (VSI).

VSI uses a broadband (normally white) light source. It is effective for measuring objects with rough surfaces. VSI uses interferometric objectives consisting of an objective lens, a reference mirror and a beam-splitter. A source directs a light beam onto the sample surface through the interferometric objective, where the beam-splitter separates the light into two beams. One beam is reflected back by the reference mirror, while the other travels along the optical axis and interacts with the sample. This latter beam is reflected by the sample's surface. This results in an optical path difference between the two light beams and a pattern of interference fringes forms when the beams are recombined. This interference pattern is composed of light and dark bands: when the two beams are in phase their amplitudes are summed and a light band forms, whereas when the beams are out of phase their amplitudes are subtracted and a dark band of zero amplitude results. The interference fringes are sampled by a CCD (charge-coupled device) sensor and the signal is digitized and processed to obtain 3D topographical maps of the sample's surface [290].

VSI with 5X, 10X, and 50X objective lenses with 1x and 2x optical multiplier was used to measure the wear track profiles. The length, width, depth and volume loss of the wear track were measured using Vision64 software. Roughness values of the wear track of all alloys was found by the same software. Before the measurement, the sample surfaces were cleaned with methanol ultrasonically for 5 mins and dry the sample surfaces with compressed air. Five cross–section measurements were taken on each wear track.

3.6   Summary

The selected techniques used in this project makes possible to have a better analysis of corrosion behaviour, effect of wear on corrosion behaviour, effect of corrosion on tribological behaviour, synergism, wear mechanisms, surface analysis and tribofilm formation, subsurface deformation and phase transformation of Titanium alloys approaching factors not well investigated in the literature.

Chapter 4 – Materials characterization

4.1   Introduction

The Titanium alloys used in this project were characterized were carried in detail after melting, rolling and heat treatment. To identify the microstructure, backscattered electron images and X-ray diffraction were taken from the unworn surface to identify the nature of grains and phases. To investigate the electrochemical behaviour of the Titanium alloys, potentiodynamic tests were carried out in static conditions in bovine serum solution at 37°C in a three electrode cell as an attempt to understand the corrosion behaviour in absence of wear.

4.2   Starting surface

Backscattered electrons images were used to characterize the microstructure of the Titanium alloys of this study. Fig. 4.1 shows an SEM image of the αβ alloy. Grains of β phase and needles of a martensitic phase, α'' were observed and the average grain size was 140 μm. α phase was present in 47.2% and β phase 52.8% of this alloy. This microstructure is typical of an alloy heat treated in the β domain and water quenched.

Fig. 4.2 shows an SEM image of the Nβ alloy which consist of fine grains and average grain size 1.6 μm of α and β phases. The volume fraction of the phases was α: 39.1% and β: 60.9%. This microstructure resulted from the high reduction rolling process.

Fig. 4.3 shows an SEM image of the β alloy which has the average grain size of 20 μm, while Fig. 4.4 shows an SEM image of the βω alloy which has the average grain size of 12.8 μm, both of which had an equiaxed β grain structure. The small dark spots on the surface of the β and βω alloy are dislocation etch pits commonly detected on β phase alloys after metallographic sample preparation. The equiaxed grains are a product of heat treatment in the β domain, recrystallization and grain growth. Both alloys were 100% β phase. ω phase was not observed by BSE. ω phase transformation is induced by aging heat treatment

at low temperature and maybe present in a small volume fraction only visible in the TEM.
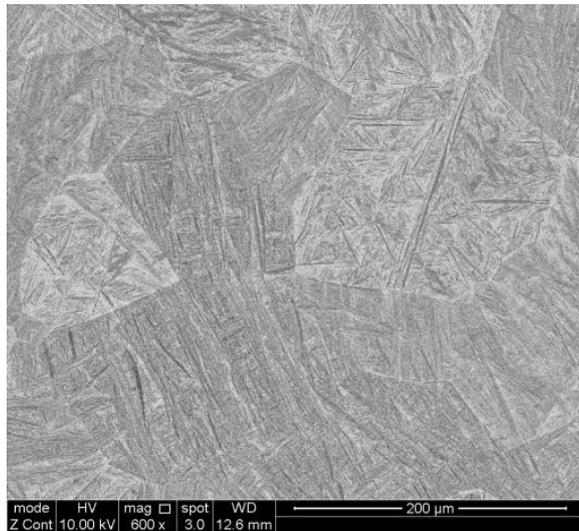
Fig. 4.1 - SEM backscatter electron image of the αβ alloy microstructure. The α phase is the lighter contrast and the needle like phase is martensite.
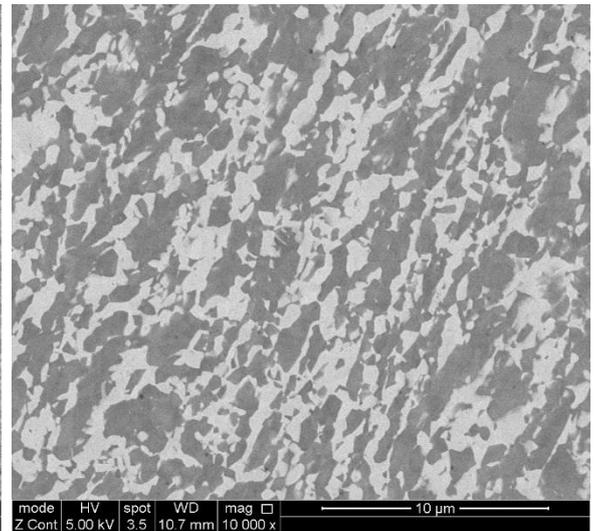
Fig. 4.2 - SEM backscatter electron image of the Nβ alloy microstructure. The α phase is the lighter contrast.
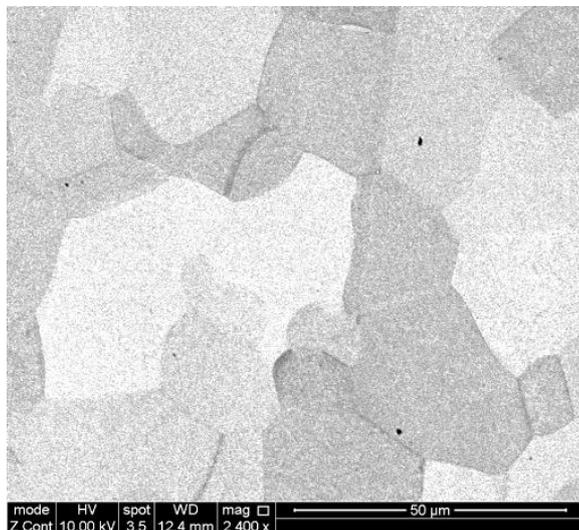
Fig. 4.3 – SEM backscatter electron image of the β alloy microstructure.
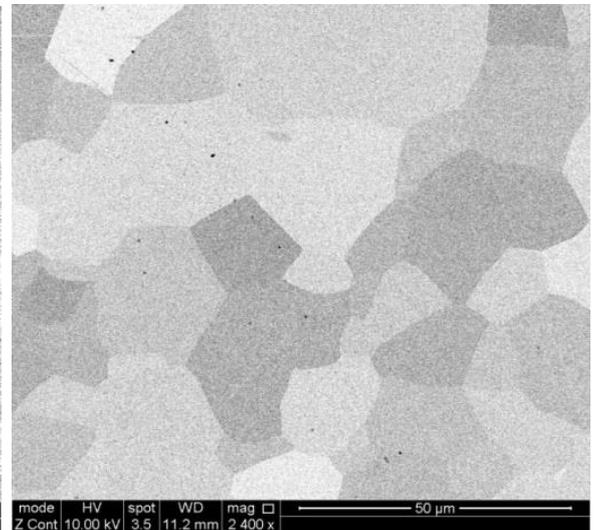
Fig. 4.4 – SEM backscatter electron image of the βω alloy microstructure.

The microstructure was confirmed by XRD, Fig. 4.5, where α, α'' and β phases were identified in the αβ alloy. For the Nβ alloy, β phase was identified as well as a low intensity (110) peak from the α phase. Only β phase was identified from the β alloy. For the βω alloy β phase was indentified as well as low intensity

(112) peak from the ω phase . The low intensity of ω phase is expected, since this phase appears in small fractions and after aging heat treatments. β phase is stabilized by elements such as Mo, Zr, Ta and Nb.
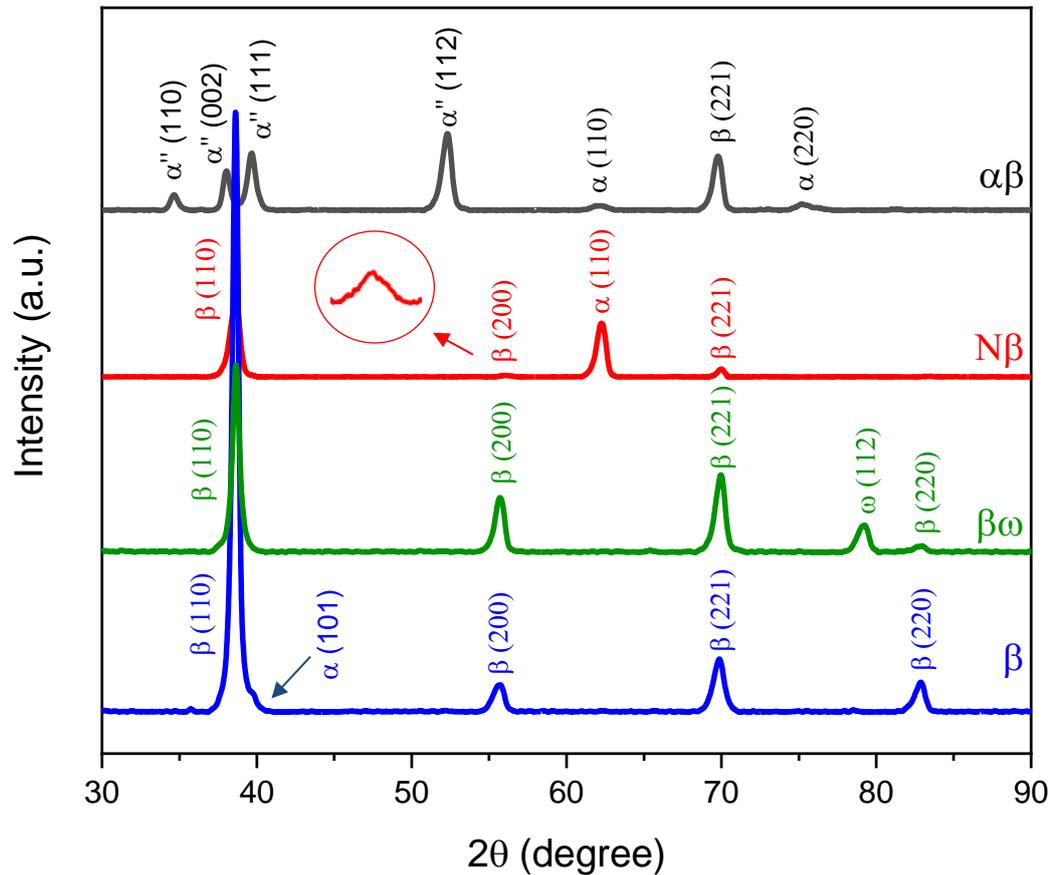
Fig. 4.5 – X–rays diffraction of the alloys studied in this project.

4.3   Corrosion proprieties of starting surface

To obtain further information on the influence of the phase composition and alloy additions on the electrochemical responses and the characteristics of the passive films of the titanium-based alloys, potentiodynamic polarization experiments were completed.

The potentiodynamic curves, also known as polarization curves, are presented in Fig. 4.6. These curves can give information about the effect of microstructure on the electrochemical behaviour and characteristics of the passive films. The curves are qualitatively similar in characteristic but with

different values to those from conventional Titanium alloys where the passive film is formed when these alloys are immersed in bovine serum solution.

These curves show three main domains: 1) the cathodic domain, which is below the corrosion potential and the rate of cathodic current is higher and the current is determined by the reduction of water and oxygen; 2) the domain where there is a transition between cathodic and anodic current where the cathodic and anodic current are equal; 3) the anodic domain where the passive film is created and the rate of anodic current is higher and it leads to metal dissolution.

The values of corrosion potential and corrosion current were found by Tafel extrapolation using both anodic and cathodic branches of the polarization curves, as explained in Fig. 2.9 and Fig. 3.6, and are presented in Fig. 4.7. The polarization curves for all alloys show corrosion characteristics, and essentially show a response that is characteristic of Titanium alloys. This is related to the natural passive film of titanium oxide which formed on the surface after immersion in the electrolyte at 37°C.

Nβ and βω show similar electrochemical behaviour with low corrosion current ($3nA/cm^2$ and $2.5nA/cm^2$) and higher corrosion potential (-0.52V and -0.51V). The βω alloy has the lowest corrosion current ($2.5nA/cm^2$) while the αβ alloy has the highest value ($8.2nA/cm^2$). The αβ is the noblest alloy, highest potential (-0.46V), and has highest corrosion current ($8.2nA/cm^2$). β alloy has the most active potential (-0.7V) and an intermediate corrosion current value ($4.1nA/cm^2$).
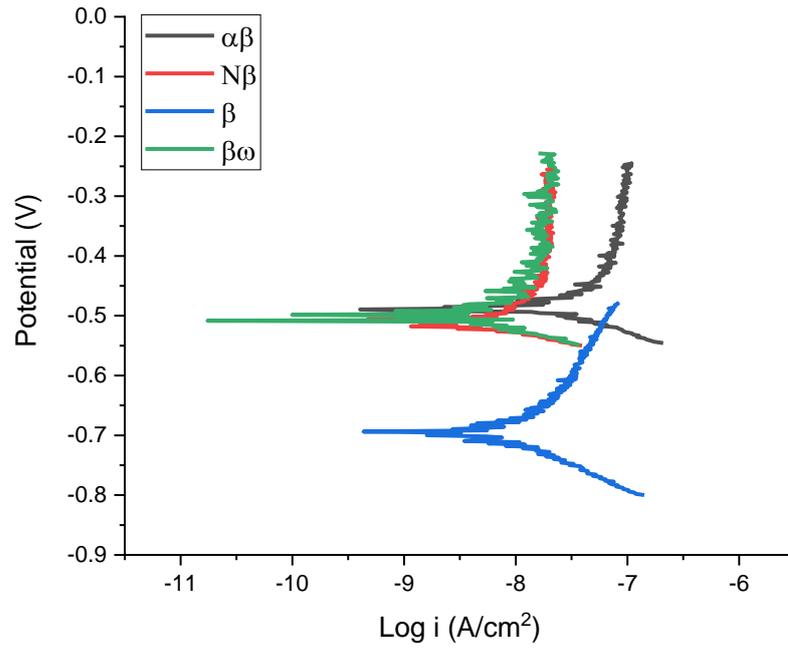
Fig. 4.6 – Polarization curves in bovine serum solution.
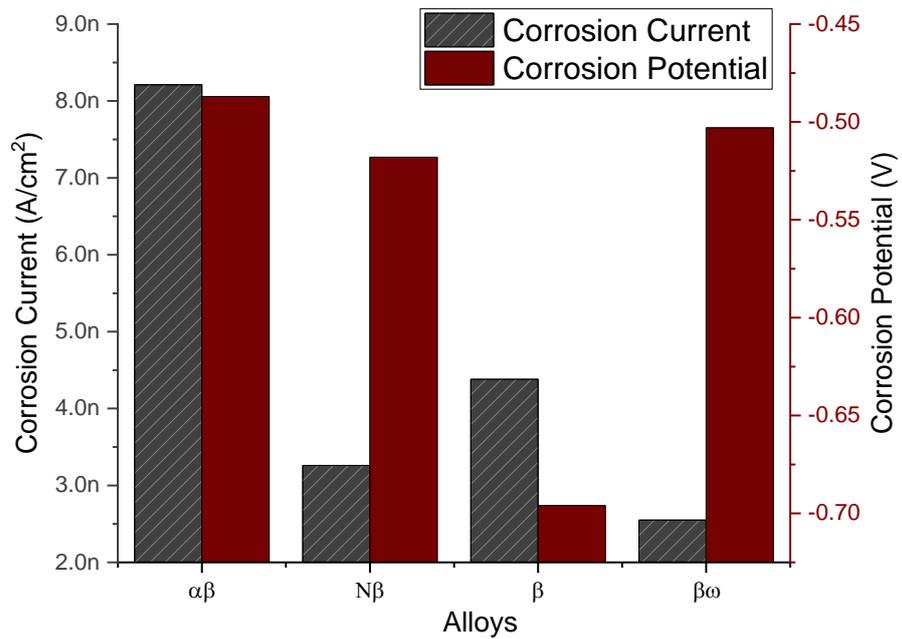
Fig. 4.7 – Corrosion potential and corrosion current extracted from polarization curves.

4.4   Summary

In this chapter, characterization of microstructure by image and X-ray diffraction in order to identify the crystal structure and potentiodynamic test to identify the corrosion behaviour in static conditions have been assessed. They are summarized as follow:

- Alloy 1 is an α and β phase alloy and show presence of martensite which is identified by α'' and has a grain size of 140 µm with 47.2% of α phase and 52.8% of β phase.
- Alloy 2 is an α and β phase alloy with fine grains of 1.6 µm and has 39.1% of α phase and 60.9% of β phase.
- Alloy 3 is a β phase alloy. The alloy was nearly 100% β phase although XRD identified a low intensity peak from the α phase. This alloy had a fine equiaxed grains of 20 µm.
- Alloy 4 is a β and ω phase alloy with fine equiaxed grains of 12.8 µm. XRD indicated 100% β phase ratio, with the volume fraction of ω phase too small to measure by XRD.
- αβ alloy has the lowest corrosion potential and therefore is the noblest alloy in this study
- β alloy has the highest corrosion potential and therefore is the most active alloy in this study.

These results show that these Titanium alloys are homogeneous and are good candidates for analysis to understand the tribological, electrochemical and tribocorrosion behaviour for biomedical applications. The next chapter shows their tribocorrosion behaviour and characterization of worn surface and subsurface.

Chapter 5 – Result: Tribocorrosion behaviour of Ti alloys

5.1   Introduction

The last chapter presented the characterization of the starting structure of the alloys. A better understanding of tribocorrosion phenomena and mechanisms are necessary for materials selection and development in biomedical applications.

In this chapter, the results are divided in two parts. The first part (section 5.2) shows the tribocorrosion behaviour of Titanium alloys at 0.5N analysing the effect of wear on polarization behaviour, current, potential and COF evolution during wear test, wear track morphology and its characterization, specific wear rate and changes in the subsurface structure. The second part (section 5.3) compares these results to tests at 1N and 2N and analyses the subsurface of all samples tested at 2N at anodic potential.

5.2   Tribocorrosion behaviour under 0.5N

5.2.1   Polarization during wear test

To characterize the electrochemical behaviour of the alloys in a solution that simulated the physiological media during rubbing, the Tafel extrapolation analysis method using both anodic and cathodic branches of the polarization curves was carried out over potential ranges relative to the OCP of -0.25mV vs OCP to 0.25mV vs OCP.

Figs. 5.1 to 5.4 show the polarization curve during wear (sliding) compared to the polarization curve from the starting surface (static) presented in the last section. This procedure reveals a combination of mechanical and electrochemical activities where the effect of wear on corrosion can be seen where the oxide film is removed and then repassivates. In other words, it represents the effect of wear on corrosion rate. The dotted lines in the graph represent the static condition potentiodynamic test and the red lines in the graph represent the potentiodynamic test taken when the sample was rubbed against alumina ball in bovine serum at 37°C.

Compared with static corrosion, the Tafel curves during rubbing had distinct and major fluctuations. A potential drop (more active) and an increase of

the corrosion current was observed for all alloys suggesting all alloys become more active to corrosion due to the constant mechanical wear. The constant depassivation enhanced the corrosion rate because of the repetitive depassivation and repassivation processes.

These results indicate that the wear accelerated the corrosion due to depassivation of worn areas, and friction was not stable. The passive layer acts as charge transfer and a diffusion barrier influencing the corrosion potentials.

The values of corrosion potential and corrosion current were found by Tafel extrapolation analysis using both anodic and cathodic branches of the polarization curves, as explained in Fig. 2.9 and 3.6. Fig. 5.5 and 5.6 compare corrosion current and corrosion potential respectively.

αβ alloy experienced a decrease of potential from -0.46V to -0.96 V and an increase of corrosion current from $8.2 \ 10^{-9}$ A/cm^2 to $6.66 \ 10^{-7}$ A/cm^2. Nβ alloy experienced a decrease of potential from -0.52V to -1.11 V and an increase of corrosion current from $3 \ 10^{-9}$ A/cm^2 to $6.22 \ 10^{-7}$ A/cm^2. The β alloy experienced a decrease of potential from -0.7V to -1.18 V and an increase of corrosion current from $4.1 \ 10^{-9}$ A/cm^2 to $1.14 \ 10^{-6}$ A/cm^2. Finally, the βω alloy experienced a decrease of potential from -0.51V to -0.97V and an increase of corrosion current from $2.5 \ 10^{-9}$ A/cm^2 to $9.72 \ 10^{-7}$ A/cm^2.

In order to compare these alloys, the β alloy shows the highest corrosion current ($1.14 \ 10^{-6}$ A/cm^2) and Nβ alloy shows the lowest corrosion current ($6.22 \ 10^{-7}$ A/cm^2), while αβ and βω alloys show intermediate corrosion current of $6.66 \ 10^{-7}$ A/cm^2 and $9.72 \ 10^{-7}$ A/cm^2. The αβ alloy show the highest corrosion potential (-0.96 V) during rubbing and the β alloy the most active potential (-1.18 V), while intermediate values are found for Nβ alloy -1.11 V and βω -0.97V.

Tribological contacts may enhance the charge transfer and increase the corrosion current density because the corrosion current reflexes the material loss caused by corrosion, therefore the current in this section can be used to observe of the tribology effect on corrosion.
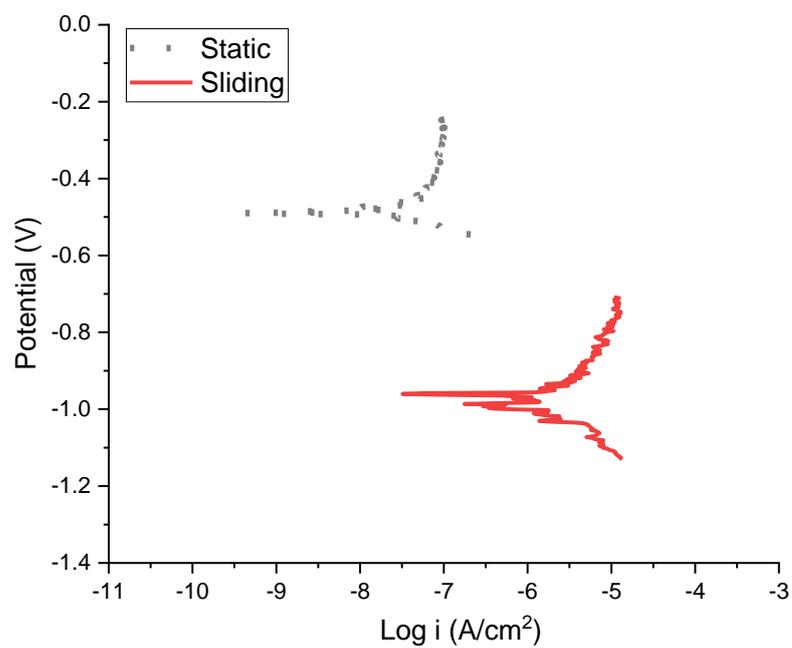
Fig. 5.1 – Polarization curves: static and during sliding of the αβ alloy.
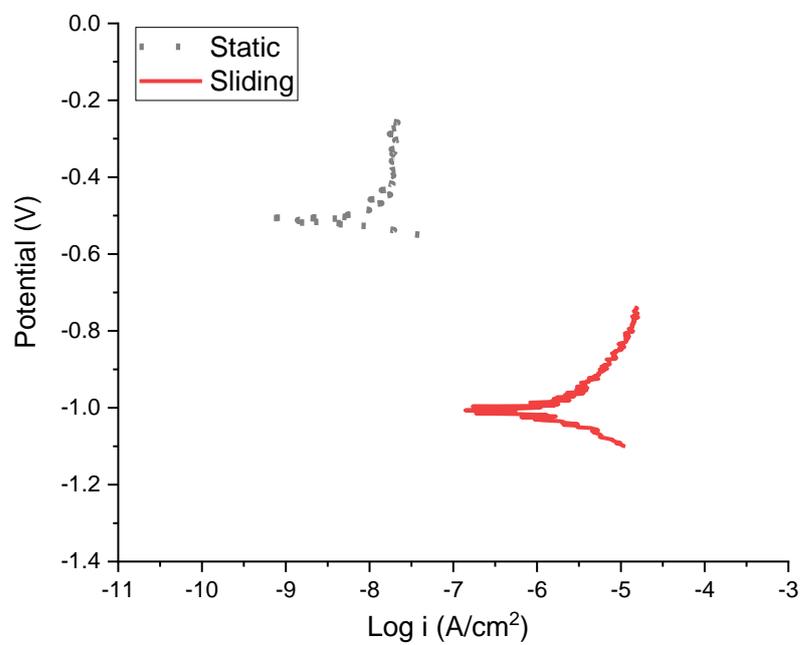
Fig. 5.2 – Polarization curves: static and during sliding of the Nβ alloy.
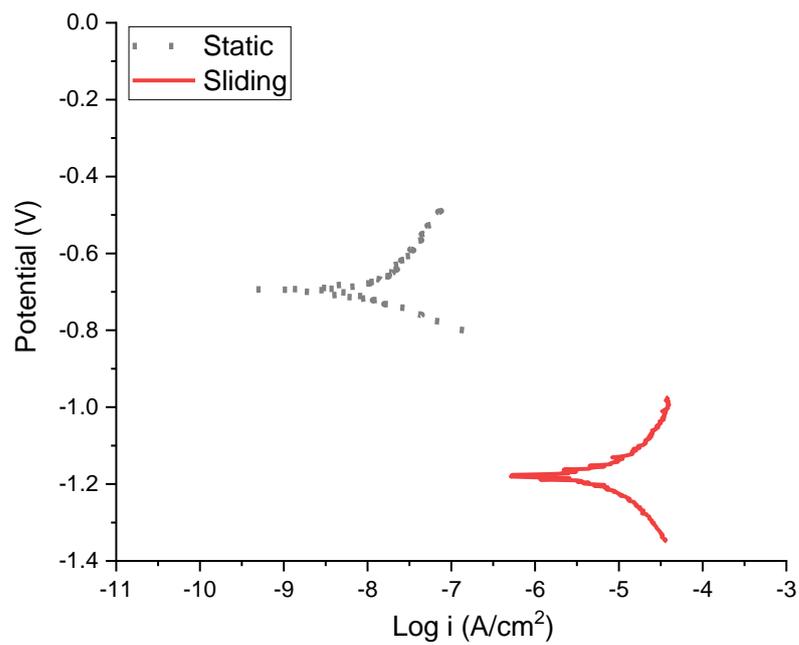
Fig. 5.3 – Polarization curves: static and during sliding of the β alloy.
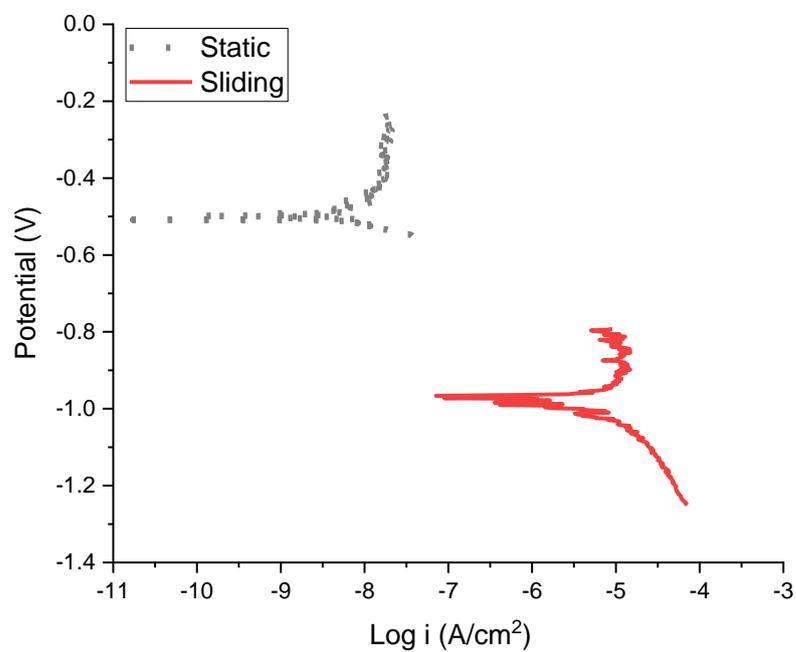
Fig. 5.4 – Polarization curves: static and during sliding of the βω alloy.
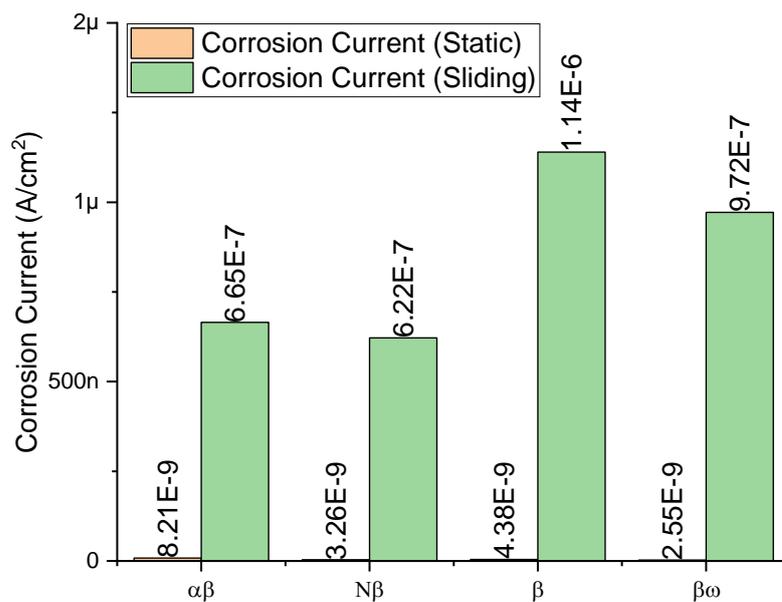
Fig. 5.5 – Corrosion current extracted from polarization curves static and during sliding.
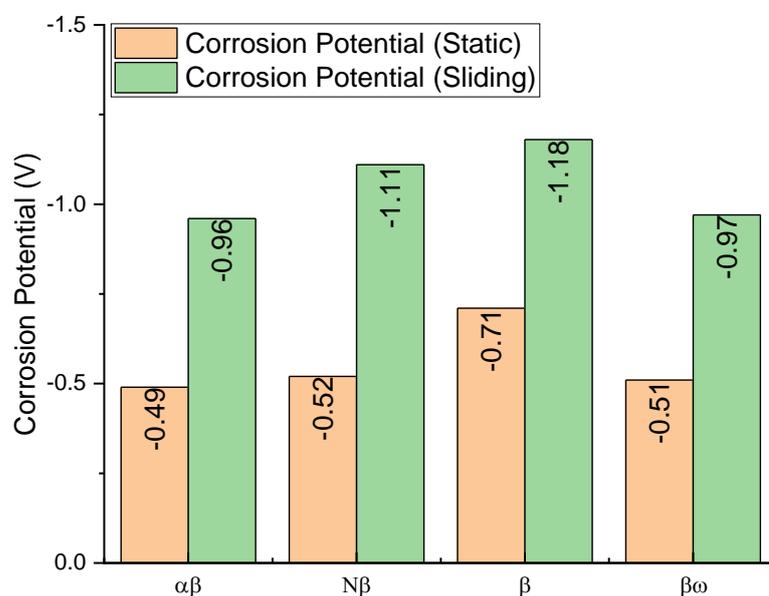
Fig. 5.6 – Corrosion potential extracted from polarization curves static and during sliding.

5.2.2 Current, potential and COF evolution.

5.1.2.1 Cathodic potential

Cathodic protection (CP) is a widely used technique to control corrosion and in this study sliding wear tests under CP enabled the wear material loss to be determined. This is an effective way of achieving isolation of the wear component to degradation and to stop any charge transfer at the working electrode surface.

The coefficient of friction and current evolution is presented as a function of time in Fig. 5.7 to Fig. 5.10 for cathodic potential (-1V vs OCP) in 25%vol bovine calf serum at 37°C under rubbing conditions. The graphs could be subdivided into three main zones. The first region is the waiting time under cathodic potential, with the expected negative current. The second zone corresponds to when rubbing was started. Finally, rubbing was stopped in the third region.

The current measured at cathodic potential dropped after applying normal load and motion. All alloys recorded negative current before, during and after wear tests. The current is negative because of the reduction of oxygen and water (oxidizing species) in the electrolyte and indicates no corrosion occurred. Depassivation promotes changes in the current. Theoretically, corrosion is not observed at cathodic potentials. However, the phenomenon is still not fully understood.

The αβ alloy showed an initial cathodic current -110μA which dropped to -170 μA when rubbing started, Fig. 5.7. The cathodic current kept dropping with fluctuations and the lowest value (-260μA) was measured just before rubbing stopped. When rubbing was stopped, the current increased to similar values that were observed before rubbing (-110μA). The COF was also measured and it showed values of 0.71 at the start of rubbing, but dropped until the end of the test to reach a value of 0.38.

The initial cathodic current measured for Nβ alloy was -95μA, but it dropped to -130μA when rubbing started, Fig. 5.8. A slight current increase was observed in the first minutes, but it continuously dropped until the end of the test where the lowest current was measured (-360μA). Then, the current increased (-200 μA), but to values lower than before rubbing. The COF was 0.45 at the

beginning of the test, but it increased at 2000 seconds to values of 0.57 and then it slightly decreased with fluctuations until the end of the test to values of 0.43.

The same behaviour was observed for the β alloy, Fig. 5.9. The initial current was -0.25 µA and dropped to -0.75 µA when rubbing started. It kept dropping with time and the lowest value of -130 µA was measured at the end of rubbing. The current increased again to -80 µA, lower than at the initial stage. At the same time, the COF measured showed initial values of 0.6 but it dropped with time to 0.4 with some oscillations observed.

The βω alloy showed an initial current of -0.27 µA and then a drop to -0.34 µA when rubbing started, Fig. 5.10. The current experienced an increase up to -20 µA but it dropped again up to the end of the test where the lowest value was registered (-0.54 µA). When rubbing stopped, the current increased to -0.42 µA. The COF evolution was higher at the beginning of the test (0.55) and dropped to 0.37 at the end of the test.

All alloys show an unstable behaviour since no steady state was observed and the current keeps dropping with time. These alloys do not recover passivity during the wear tests. At the end of rubbing the current increased to the initial value. The main cathodic reactions proposed at this potential may be the oxygen reduction:

$$O_2 + 2H_2O + 4e^- \rightarrow 4OH^-$$
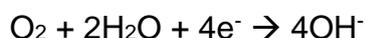
At the beginning of the COF measurements, a running in and subsequent a steady state is seen, except for the Nβ alloy. However, the running in period changes as the microstructure and potential change. The Nβ alloy has the highest average COF (0.46), but the average COF are in the same range of 0.4 and the lowest average COF is for the βω alloy (0.4), αβ alloy (0.41) and then β alloy (0.42), Fig. 5.11 which also presents the standard deviation of 10,816 COF measurements.
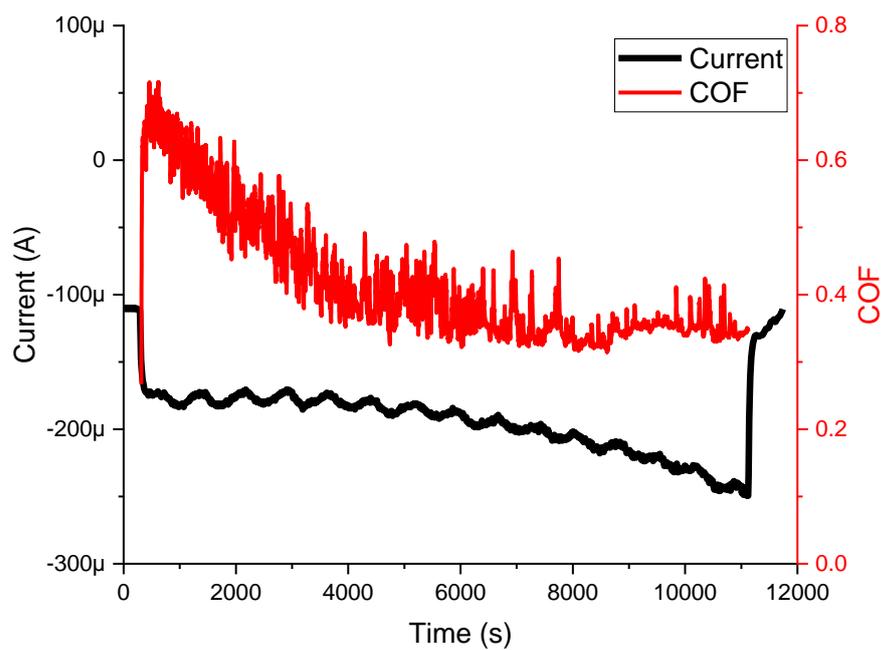
Fig. 5.7 – Current and COF evolution αβ alloy at cathodic potential at 0.5N.
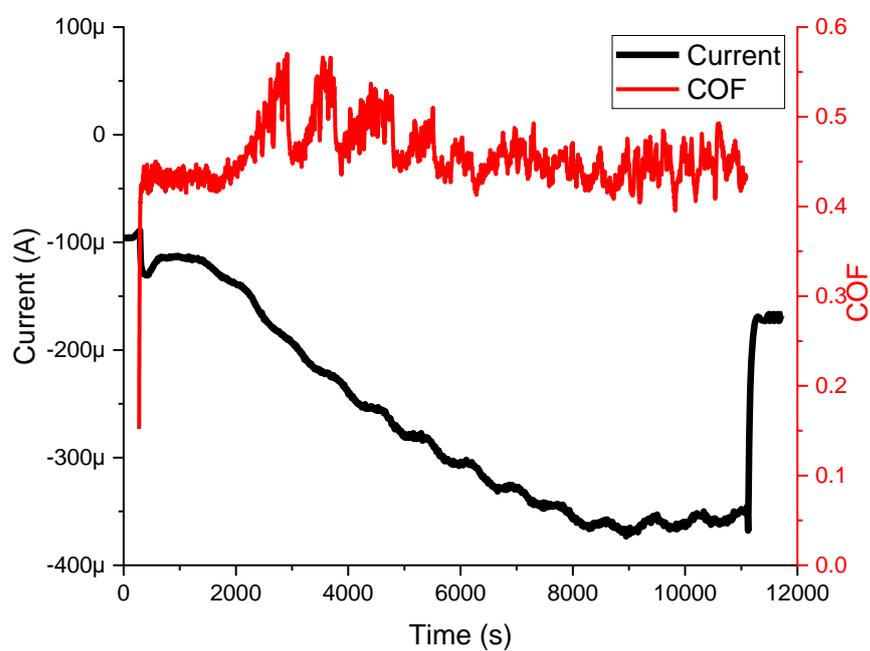
Fig. 5.8 – Current and COF evolution Nβ alloy at cathodic potential at 0.5N.
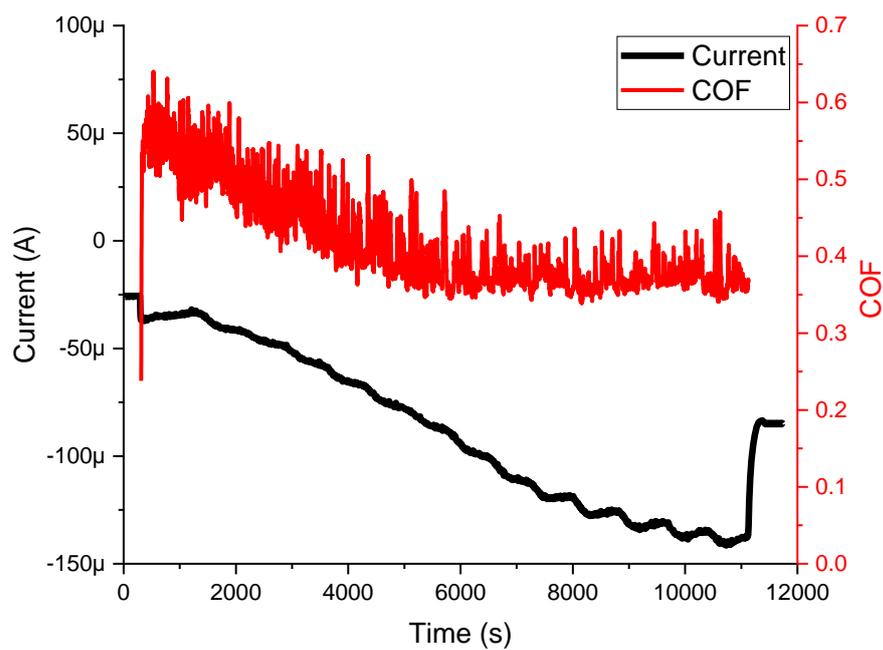
Fig. 5.9 – Current and COF evolution β alloy at cathodic potential at 0.5N.
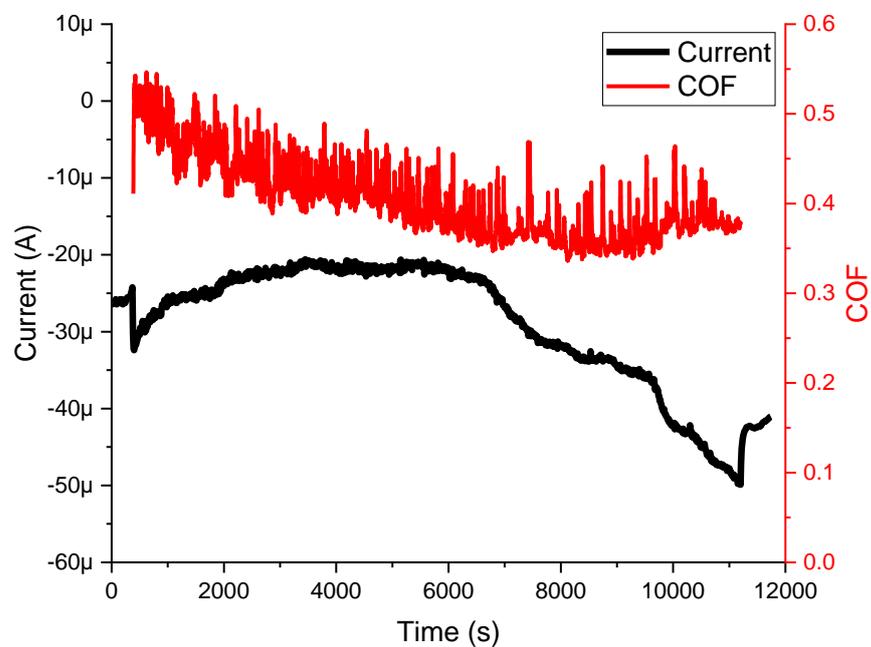
Fig. 5.10 – Current and COF evolution βω alloy at cathodic potential at 0.5N.
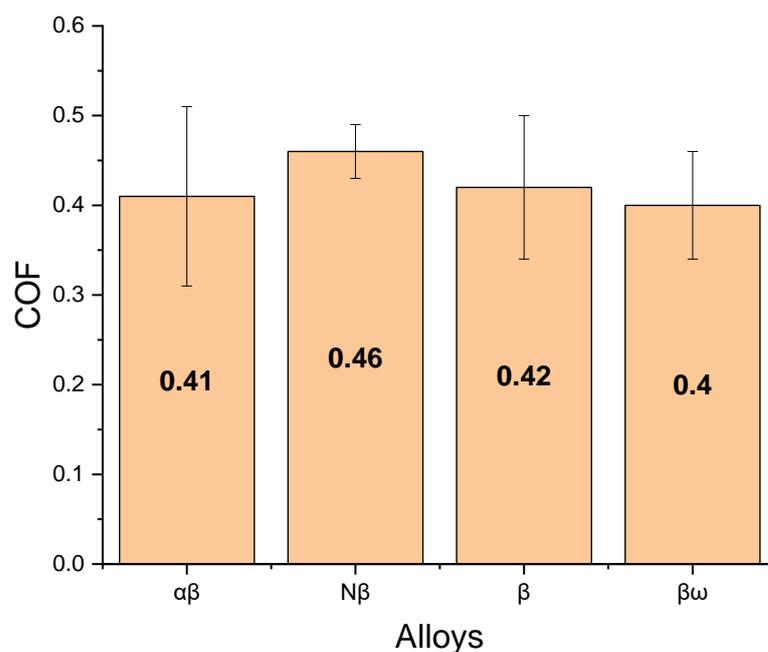
Fig. 5.11 – Average COF measured during wear test at cathodic potential at 0.5N.

5.1.2.2 Open circuit potential

The evaluation of the friction coefficient and open circuit potential as a function of testing time in 25%vol bovine calf serum at 37°C are shown in Fig. 5.12 to Fig. 5.15. The coefficient of friction and potential evolution as a function of time for the OCP are presented. A cathodic drop was observed for all alloys when rubbing started, as expected when the charge transfer barrier is removed. This cathodic shift observed is typical of passive metals. Also, plastic deformation occurred on the sample surface, which may contribute to the shift of potential.

The noblest material before rubbing was Nβ alloy (-0.1V) and the most active β alloy (-0.54V), while αβ alloy shows an initial OCP value of -0.25V and βω alloy -0.2V.

When rubbing started, the OCP value dropped to -0.85V (ΔE = -0.6V) for αβ alloy and this value increased to -0.75V and then dropped again to -0.85V, Fig. 5.12. When rubbing was stopped, the potential rose again to -0.4V, a value

lower than that before rubbing, indicating repassivation. Higher values of COF (0.45) were observed when rubbing started and it kept dropping with fluctuations up to 0.27 when rubbing stopped.

The potential also dropped for the Nβ alloy when rubbing started, indicating depassivation, to -0.9V (ΔE = -0.8V) and shows slightly fluctuations until the end of rubbing which the potential registered was -1.05V. The potential rose again to -0.8V when rubbing stopped. The initial values of COF were around 0.5 and increased to 0.6 when at 2000 seconds it suddenly dropped to 0.35 and then remained steady until the end of the test.

The β alloy showed a potential drop to -1V (ΔE = -0.45V), Fig. 5.13. The potential remained steady and isolated peaks were seen. Then, when rubbing stopped the potential rose (-0.65V) , but to values lower than measured before rubbing. The COF evolution showed an initial value of 0.47 and final values of 0.27.

The potential dropped to -1V for the βω alloy (ΔE = -0.8V) due to the depassivation caused by rubbing, Fig. 5.14. The potential evolution was steady and decreased slightly to -1.1V at the end of rubbing. This alloy also experienced a potential increase to -0.6V when rubbing was stopped. The COF evolution started at 0.47 and was 0.3 at the end of the test.

The Nβ alloy shows the highest and β alloy the smallest cathodic drop. The potential dropped to around –1V for all alloys. After dropping, the potential does not recover during rubbing and it remained stable.

The constant value of OCP with slight fluctuations indicates that those alloys did not repassivate. The least transient curve is seen for the βω alloy. The αβ alloy was the noblest during rubbing and the Nβ was the most active during the same period. When rubbing stops, the potential rose again but to values lower than before rubbing. In addition, the potential evolution showed different variation for all alloys, which may suggest that microstructure does influence this condition. Also, the ionic species released due to the charge transfer at the interface may interact with the bovine serum constituents and affect the friction and wear response of that interface.

The COF has values around 0.3, with the lowest value found for the αβ alloy (0.29), β alloy (0.31), βω (0.32) and Nβ (0.36), Fig. 5.16, which also presents the standard deviation of 10,816 COF measurements. These values are lower than those from cathodic potential test.

The reproducibility of these tests is presented from Fig.5.17 to Fig. 5.19, which shows the wear test at OCP of αβ alloy at 0.5N. Test 1 showed an initial OCP of -0.25V and a cathodic drop to -0.85V (ΔE = -0.6V) and an OCP increase to -0.4V. Test 2 showed an initial OCP of -0.21 and a cathodic drop to -0.78 (ΔE = -0.57V) and an OCP increase to -0.35V. Also, the COF evolution started at 0.47 and ended around 0.27 for both curves.
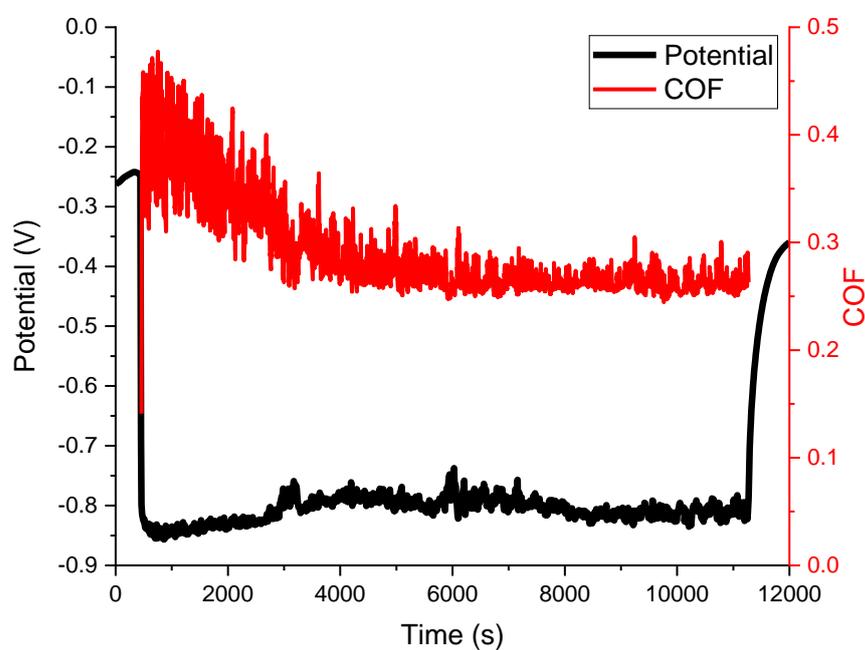
Fig. 5.12 – Potential and COF evolution αβ alloy at OCP at 0.5N.
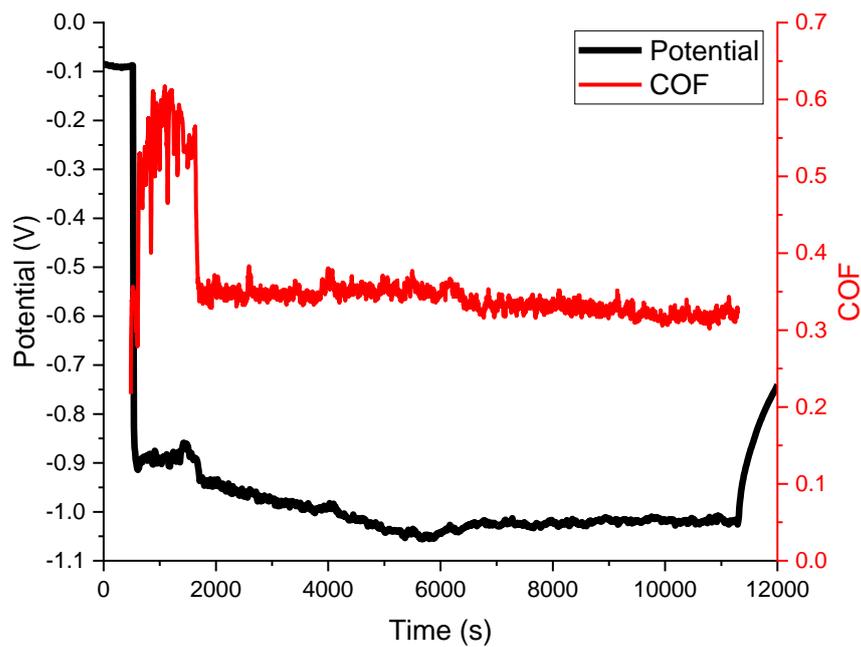
Fig. 5.13 – Potential and COF evolution Nβ alloy at OCP at 0.5N.
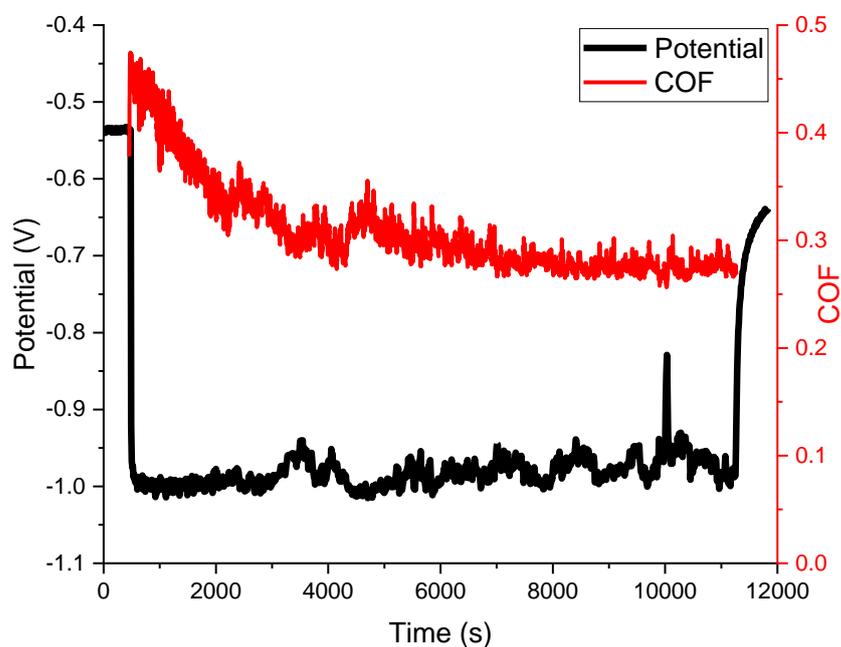
Fig. 5.14 – Potential and COF evolution β alloy at OCP at 0.5N.
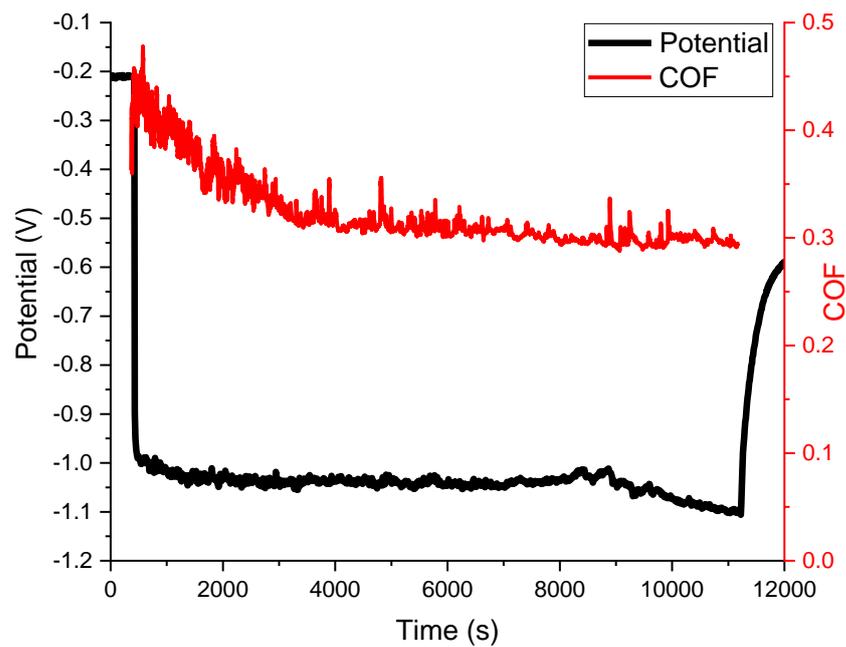
Fig. 5.15 – Potential and COF evolution βω alloy at OCP at 0.5N.
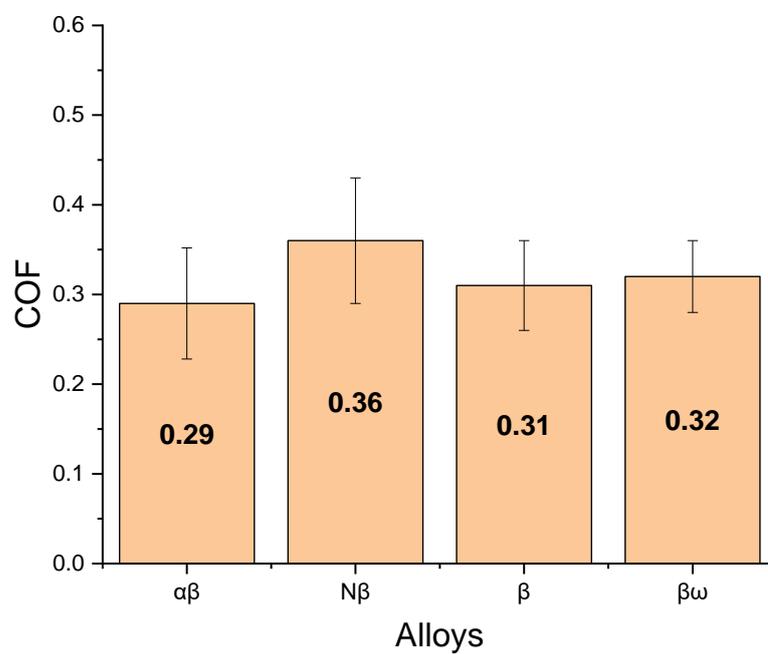
Fig. 5.16 – Average COF measured during wear test at OCP at 0.5N.
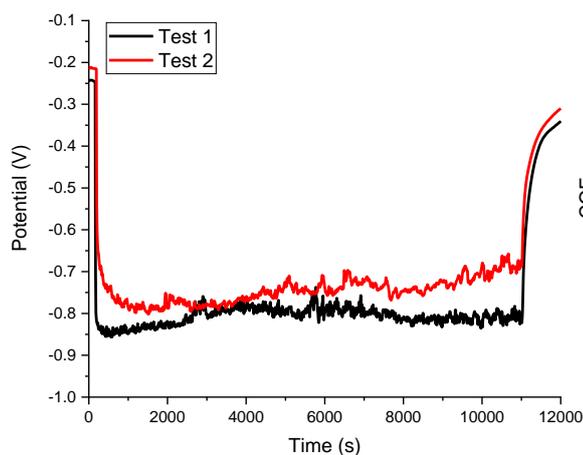
Fig. 5.17 – Reproducibility of OCP test of αβ alloy at 0.5N.
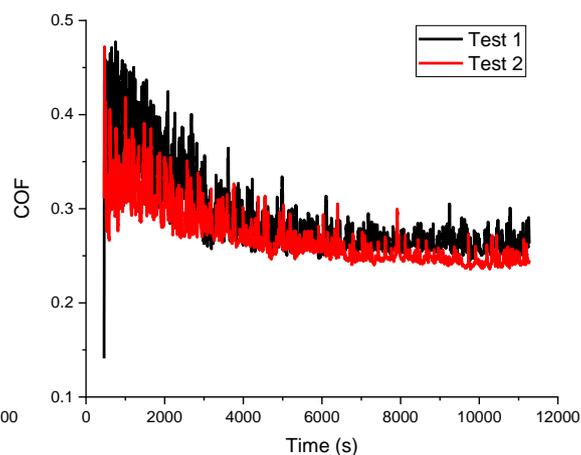
Fig. 5.18 – Reproducibility of COF evolution of αβ alloy at 0.5N.
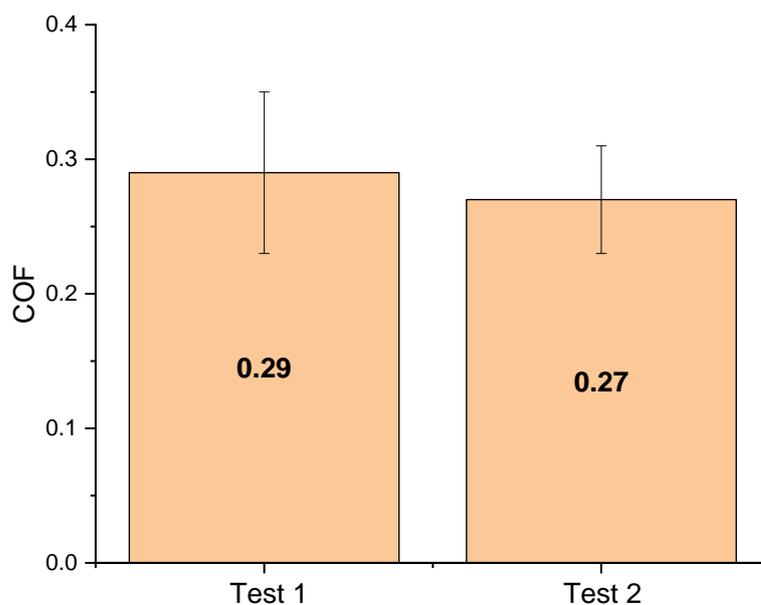
Fig. 5.19 – Reproducibility of average COF of αβ alloy at 0.5N.

5.1.2.3 Anodic potential

Fig. 5.20 to 5.23 presents the coefficient of friction and current evolution as a function of time for the anodic potential (0.3V vs OCP). At anodic potential,

the initial current measurement was 1×10^{-7} A. The current shifts to more positive values when rubbing starts. The continuous metal ion release was due to the tribological contacts and the electrochemical driving force. The charge transfer rate is controlled by activation energy since the passive film is removing during rubbing, and it acts a barrier for charge transfer. It leads to a release of ions which start the interaction with the bovine serum.

The reactions for all Titanium alloys were suggested as follows:

$Ti = Ti^{2+} + 2e^-$
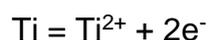
In addition, for the Nβ alloy the Fe loses electrons through Fe^{2+}/Fe^{3+} reactions.

αβ and Nβ alloys showed an increase in current up to 70μA when rubbing started and a current peak of 50μA was seen up to the end of the test. Similarly, the β and βω alloys show an increase of current up to 60 μA and 50 μA when rubbing started and the current peaks at the end of the test. Some current peaks occurred at the same position as the peak in COF which might be due to the release of entrapped debris and the high values of COF and current at the beginning of the test represents the removal of the passive layer.

All alloys presented a stabilization of the anodic current after 4,000 s, although fluctuations were seen throughout the test. This may be due to the reaction of proteins and released Ti^+, as the wear process accelerated ion release. Then it may form a layer which acts to block charge transfer at the metal/solution interface. Also, this layer acts reducing friction and indicates that this layer is an efficacious solid lubricant.

The current drops to 1×10^{-6} A when rubbing stopped indicating the restoration of passivity where the passive film is a barrier to charge transfer.

The COF evolution of αβ alloy and β alloy was high (0.6) at the beginning of the test and after 3000 s, it dropped to 0.3 and remained constant with few isolated peaks. The Nβ alloy also showed a high COF at the beginning of the test (0.45) and then dropped to 0.3 after 3000 s and then remained constant with a few isolated peaks. Finally, the COF evolution of βω alloy was 0.55 at the beginning of the test and after 6000 s, the COF remained stable around 0.3.

The COF curves at anodic potential are less transient and the average COF is the lowest at that potential, around 0.29, for all alloys. The αβ alloy recorded the lowest average COF, 0.28, Fig. 5.24 which also presents the standard deviation of 10,816 COF measurements. Overall, these alloys will experience wear accelerated corrosion if the passive film is damaged.

It is important to remember that these alloys might have different oxides such as TiO_2, Nb_2O_5, Ta_2O_5, MO_3 and ZrO_2 on their surface, which may affect the repassivation and mechanical proprieties.

It has been reported that corrosion accelerates wear for passive metals, but wear is not always enhanced by corrosion because corrosion may change friction and contact stress fields. Also, COF is higher at cathodic potential and lower at anodic potential, indicating that it is affected by the composition and potential.
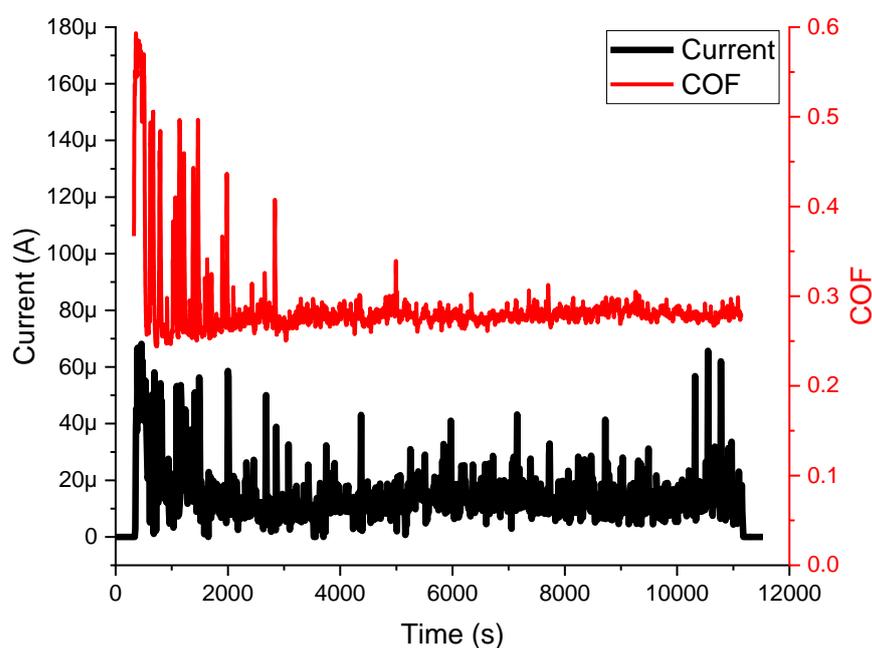
Fig. 5.20 – Current and COF evolution αβ alloy at anodic potential at 0.5N.
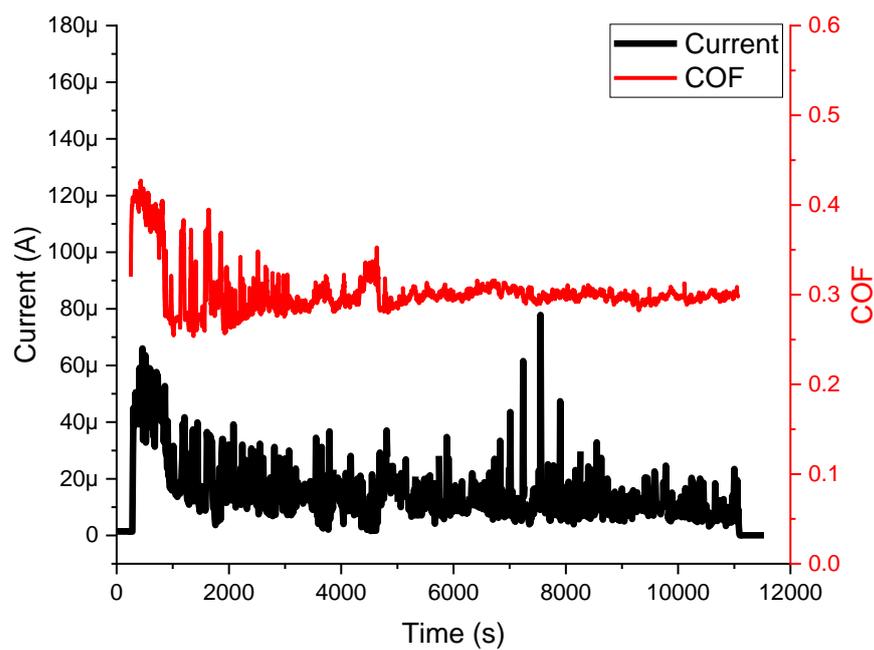
Fig. 5.21 – Current and COF evolution Nβ alloy at anodic potential at 0.5N.
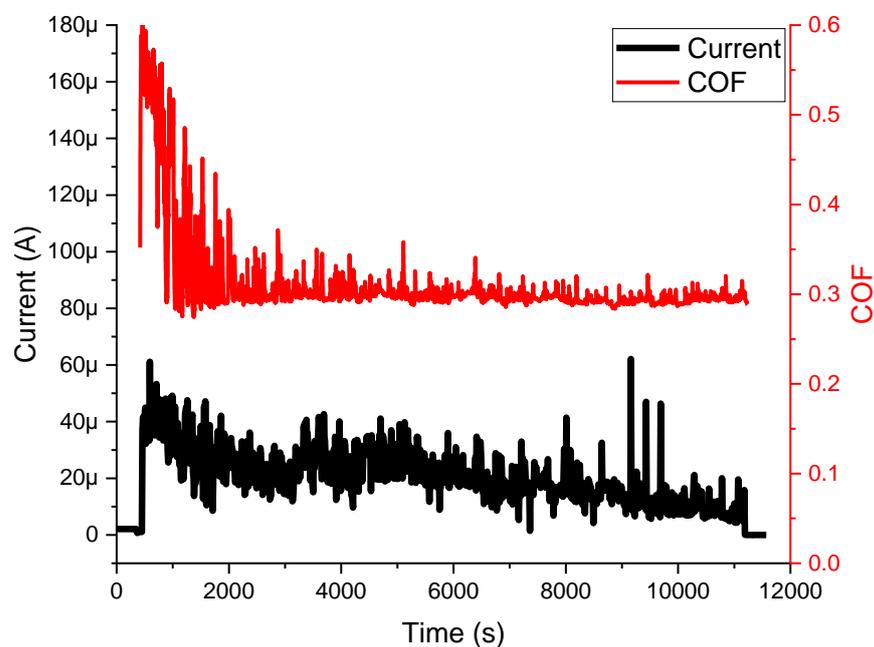
Fig. 5.22 – Current and COF evolution β alloy at anodic potential at 0.5N.
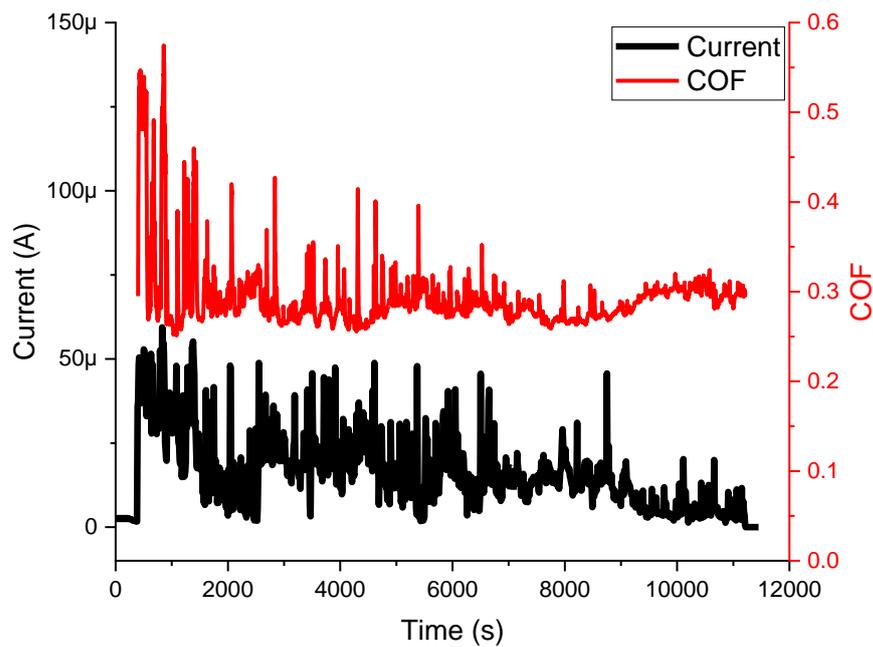
Fig. 5.23 – Current and COF evolution βω alloy at anodic potential at 0.5N.
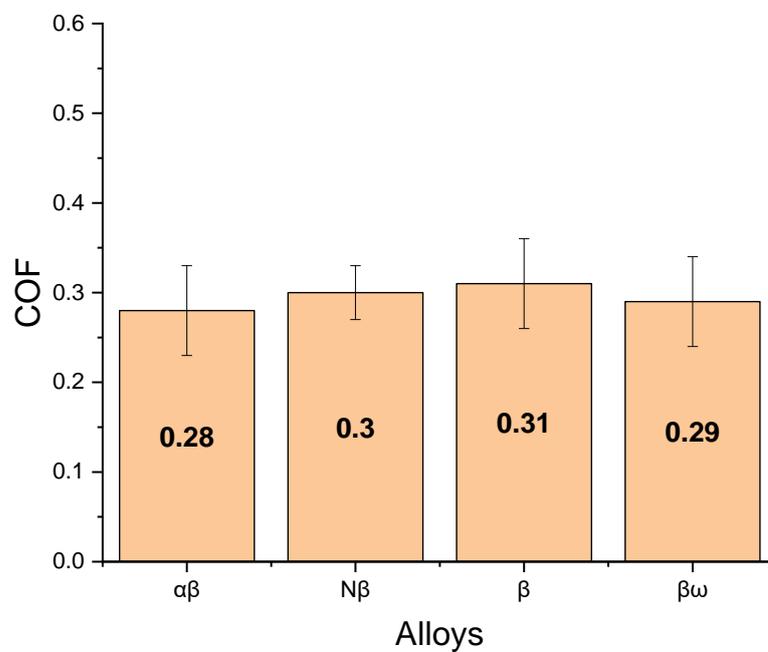
Fig. 5.24 – Average COF measured during wear test at anodic potential
at 0.5N.

5.2.3 Wear track profile

The wear track profile is seen from Fig. 5.25 to Fig. 5.28 and the 3D image of each wear track is presented in Table 5.1. It is clear that the αβ alloy has a shallower wear track than the other alloys.

The αβ alloy had a depth of 35µm and a width of 0.71mm at anodic potential, a depth of 49µm and a width of 0.8 at OCP and a depth of 60µm and a width of 0.95mm at cathodic potential.

The Nβ alloy had a depth of 40µm and a width of 0.89mm at anodic potential, a depth of 45µm and a width of 0.8 at OCP and a depth of 67µm and a width of 1mm at cathodic potential.

The β alloy had a depth of 45µm and a width of 0.95mm at anodic potential and OCP and a depth of 68µm and a width of 1mm at cathodic potential.

The βω alloy showed a depth of 41µm and a width of 0.8mm at anodic potential, a depth of 55µm and a width of 0.9 at OCP and a depth of 59µm and a width of 0.95 at cathodic potential.

The wear track was shallower for all alloys at anodic potential. Comparing alloys, the αβ alloy had the shallowest wear track in all electrochemical conditions. The αβ alloy had a depth of 35µm and a width of 0.71mm at anodic potential which is the shallowest wear track and Nβ alloy show the deepest wear track with depth of 67µm and a width of 1mm at cathodic potential. This indicates that the wear track depth depends on the potential and it is lower when anodic potential is applied.
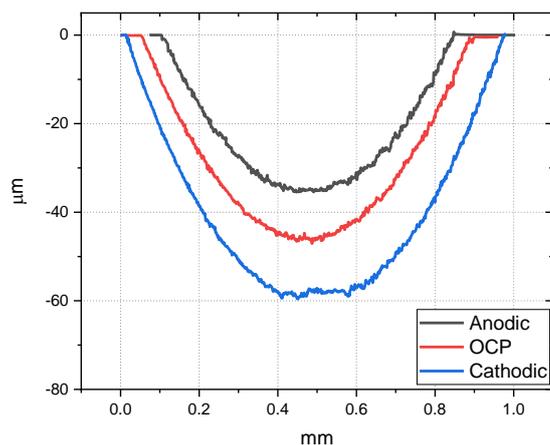
Fig. 5.25 – Comparison of wear track profile of αβ alloy at anodic potential, OCP and cathodic potential at 0.5N.
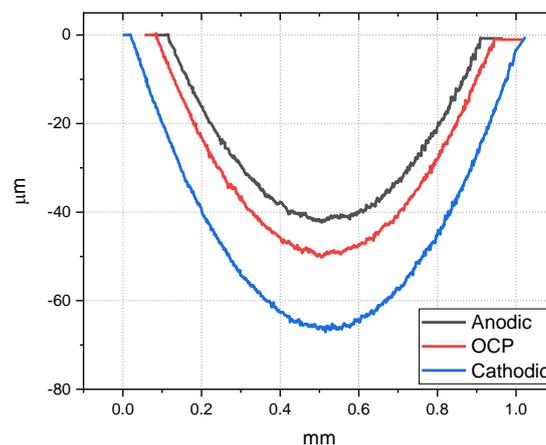
Fig. 5.26 – Comparison of wear track profile of Nβ alloy at anodic potential, OCP and cathodic potential at 0.5N.
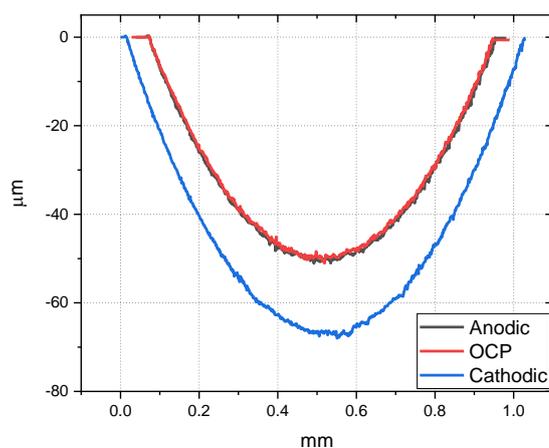
Fig. 5.27 – Comparison of wear track profile of β alloy at anodic potential, OCP and cathodic potential at 0.5N.
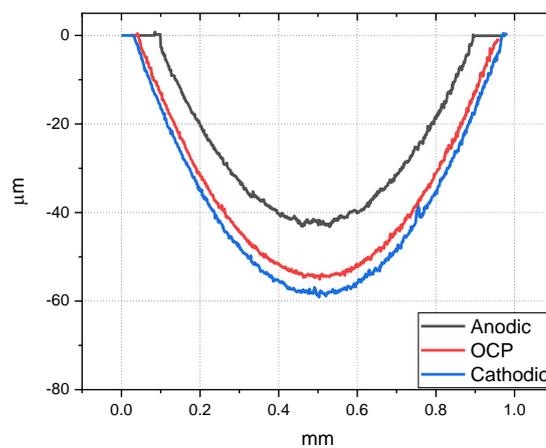
Fig. 5.28 – Comparison of wear track profile of βω alloy at anodic potential, OCP and cathodic potential at 0.5N.

Table 5.1 – 3D wear track images at 0.5N.

Alloys	Cathodic	OCP	Anodic
αβ	31.4 / -32.8 μm	27.2 / -32.1 μm	17.6 / -26.6 μm
Nβ	32.4 / -38.1 μm	23 / -31.2 μm	17.6 / -26.6 μm
β	31.7 / -39.9 μm	24.1 / -32.8 μm	21.5 / -31.4 μm
βω	36.6 / -35 μm	26 / -33.6 μm	19.6 / -22 μm
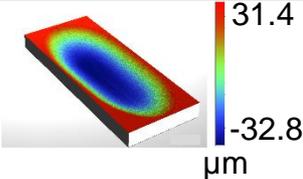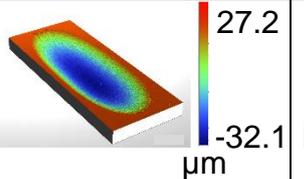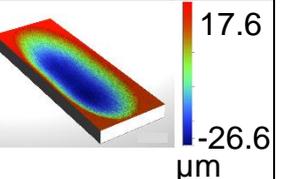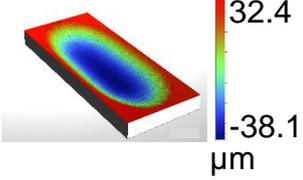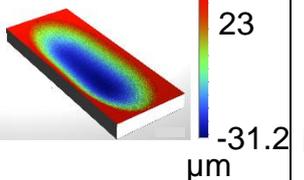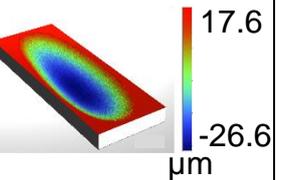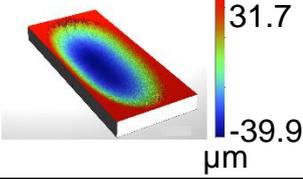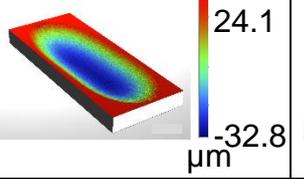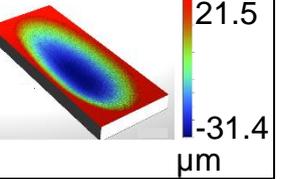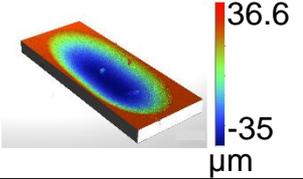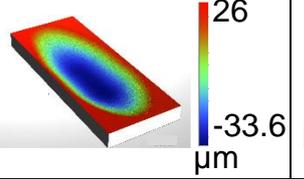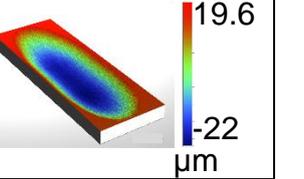
5.2.4 Wear track volume, surface roughness and specific wear rate

The wear track volume is presented in Fig. 5.29. The wear track volume is the total material loss during the tribocorrosion test due to mechanical wear and corrosion.

The αβ alloy had a wear track volume of 5.37×10^{-2} mm^3 at cathodic potential, 3.67×10^{-2} mm^3 at OCP and 2.47×10^{-2} mm^3 at anodic potential. The Nβ alloy had a wear track volume of 5.85×10^{-2} mm^3 at cathodic potential, 4.27×10^{-2} mm^3 at OCP and 3.2×10^{-2} mm^3 at anodic potential. The β alloy had a wear track volume of $7.24 \ 10^{-2}$ mm^3 at cathodic potential, 4.33×10^{-2} mm^3 at OCP and 4.17×10^{-2} mm^3 at anodic potential. The βω alloy had a wear track volume of 6.16×10^{-2} mm^3 at cathodic potential, 4.58×10^{-2} mm^3 at OCP and 3.22×10^{-2} mm^3 at anodic potential.

The lowest values of wear volume were observed at anodic potential and highest values observed at cathodic potential. The β alloy exhibited the highest volume loss and the αβ presented the lowest values in all electrochemical

conditions. The smallest material loss was found for the αβ alloy at anodic potential (2.47×10^{-2} mm^3) and the highest material loss was found for the β at cathodic potential (7.24×10^{-2} mm^3).

Therefore, the material loss depends of the potential, and it is smaller when anodic potential is applied. The highest material removal was found at cathodic potential, and the lowest at anodic condition and the wear track volume increases by the following order: anodic potential, OCP and cathodic potential.

The surface roughness of the centre of the wear track is shown in Fig. 5.30. It is clear that the potential had an influence on roughness.

The αβ alloy had a surface roughness of 0.85μm at cathodic potential, 1.13 μm at OCP and 1.17μm at anodic potential. Nβ alloy had a surface roughness of 1.09μm at cathodic potential, 1.15μm at OCP and 1.3μm at anodic potential. The β alloy had surface roughness of 1.06μm at cathodic potential, 1.11μm at OCP and 1.35μm at anodic potential. The βω alloy had a surface roughness of 1.08μm at cathodic potential, 1.15μm at OCP and 1.18μm at anodic potential.

Overall, the roughness was slightly lower at cathodic potential and higher at anodic potential. The αβ alloy at cathodic potential exhibited the lowest surface roughness (0.85μm) and the β alloy at anodic potential the highest value (1.35μm).

The specific wear rates are presented on Fig. 5.31. The αβ alloy had a specific wear rate of 4.97×10^{-4} mm^3/Nm at cathodic potential, 3.4×10^{-4} mm^3/Nm at OCP and 2.29×10^{-4} mm^3/Nm at anodic potential. The Nβ alloy had a specific wear rate of 5.42×10^{-4} mm^3/Nm at cathodic potential, 3.96×10^{-4} mm^3/Nm at OCP and 2.96×10^{-4} mm^3/Nm at anodic potential. The β alloy had a specific wear rate of 6.7×10^{-4} mm^3/Nm at cathodic potential, 4.01×10^{-4} mm^3/Nm at OCP and 3.86×10^{-4} mm^3/Nm at anodic potential. The βω alloy had a specific wear rate of 5.7×10^{-4} mm^3/Nm at cathodic potential, 4.24×10^{-4} mm^3/Nm at OCP and 2.98×10^{-4} mm^3/Nm at anodic potential.

The β alloy had the highest specific wear rate (6.7×10^{-4} mm^3/Nm at cathodic potential) with the αβ alloy exhibiting the lowest values (2.29×10^{-4} mm^3/Nm at anodic potential). The wear rate and specific wear rate varied with the applied potential. When anodic potential is applied, the wear rate and specific wear rate reduce. In addition, the αβ alloy had lower specific wear rate than the other alloys.
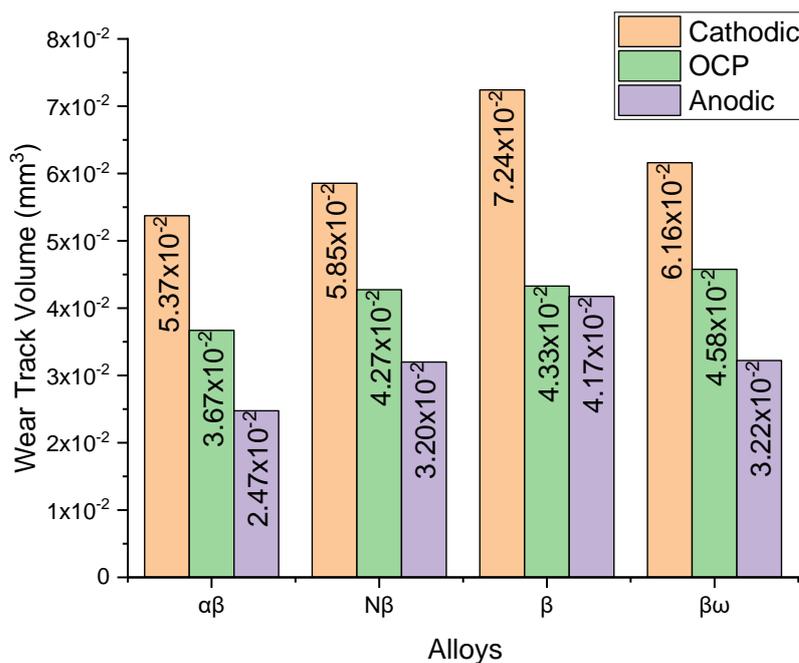
Fig. 5.29 – Comparison of wear track volume at cathodic potential, OCP and anodic potential at 0.5N.
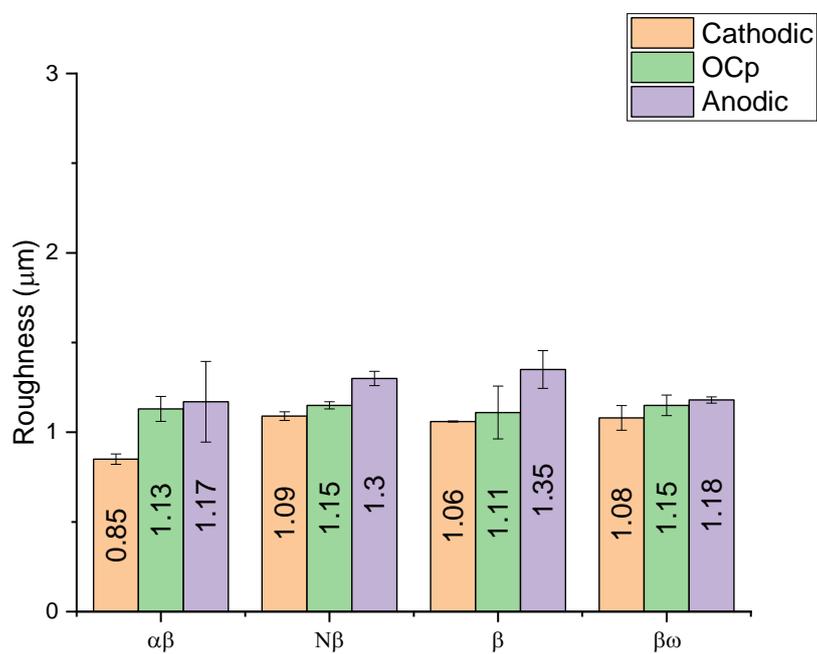
Fig. 5.30 – Comparison of roughness at cathodic potential, OCP and anodic potential at 0.5N.
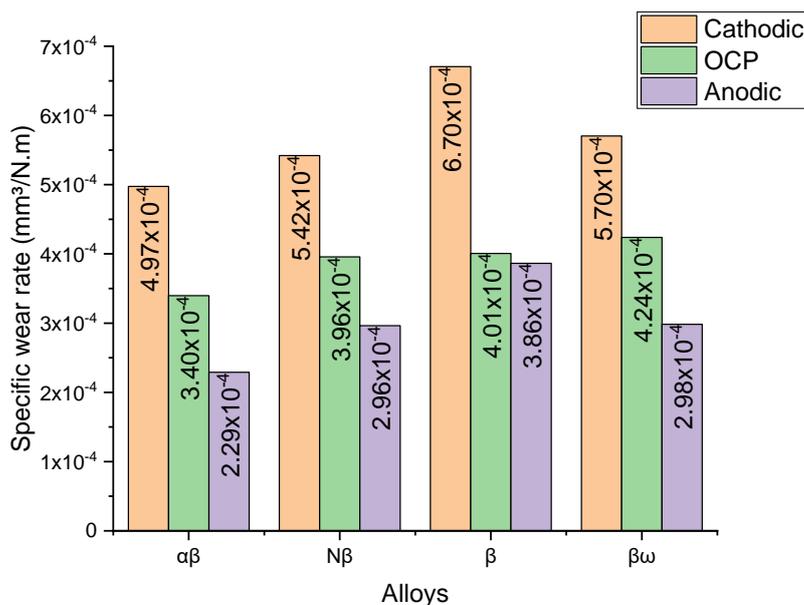
Fig. 5.31 – Comparison of specific wear rate at cathodic potential, OCP and anodic potential at 0.5N.

5.2.5 Surface characterization

Details of the topography of the materials tested on backscattered and secondary electrons images of the wear track are presented in Figs. 5.32 to 5.55. Cracks were not found, but isolated debris, wide grooves, scratches were observed, which is characteristic of ploughing and delamination. The ploughing appearance on the worn surface indicates poor resistance of these alloys to plastic deformation. There is no difference among all surfaces when the electrochemical conditions change and the surfaces are free of corrosion product.

Delamination is higher at cathodic potential with the Nβ alloy being less rough surface. The β and βω alloys are the roughest surfaces at OCP and cathodic potentials.

Dark areas were observed on backscattered images in all alloys, which are an indication of the presence of an organic layer, which must be confirmed by Raman spectroscopy.

Overall, worn surfaces at cathodic potential are less rough than OCP and anodic potential which are rougher. All Titanium alloys show the same wear mechanism despite variation of electrochemical conditions.
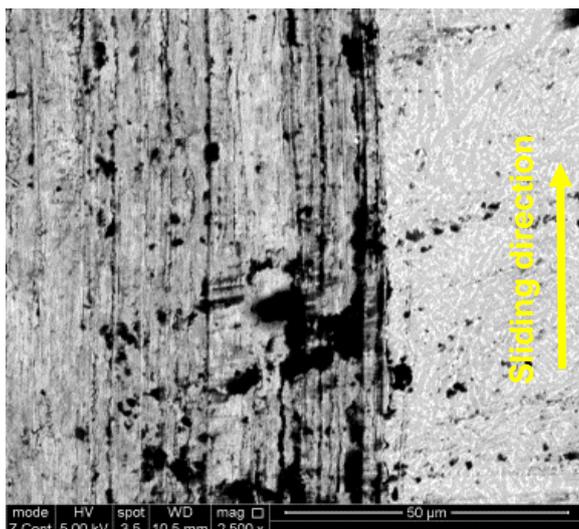
- **αβ alloy at 0.5N**

Fig. 5.32 – BSE image of the worn surface of αβ alloy at anodic potential at 0.5N.
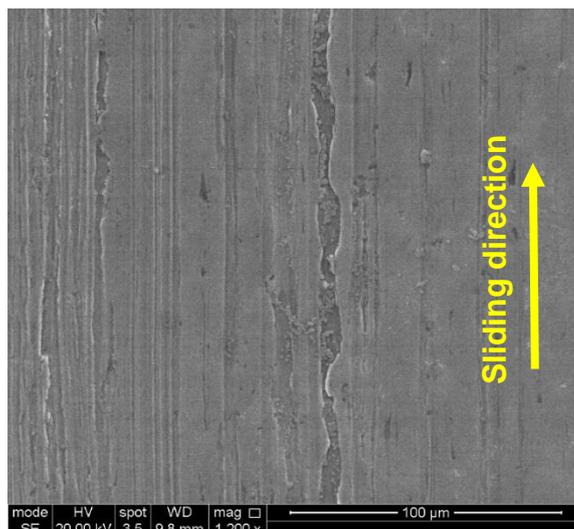
Fig 5.33 - SE image of the worn surface of αβ alloy at anodic potential at 0.5N
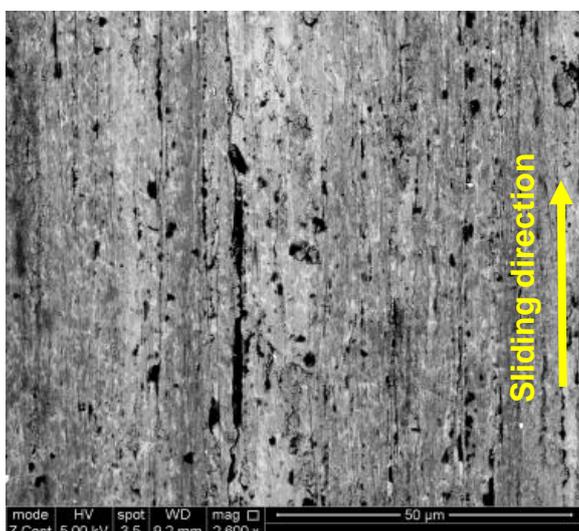
Fig. 5.34 – BSE image of the worn surface of αβ alloy at OCP at 0.5N.
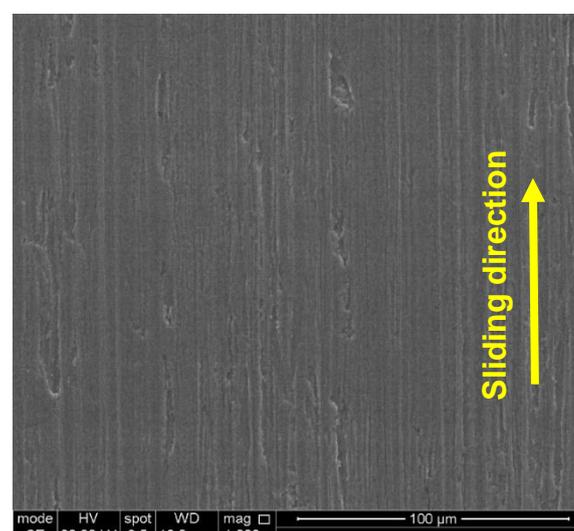
Fig. 5.35 – SE image of the worn surface of αβ alloy at OCP at 0.5N.
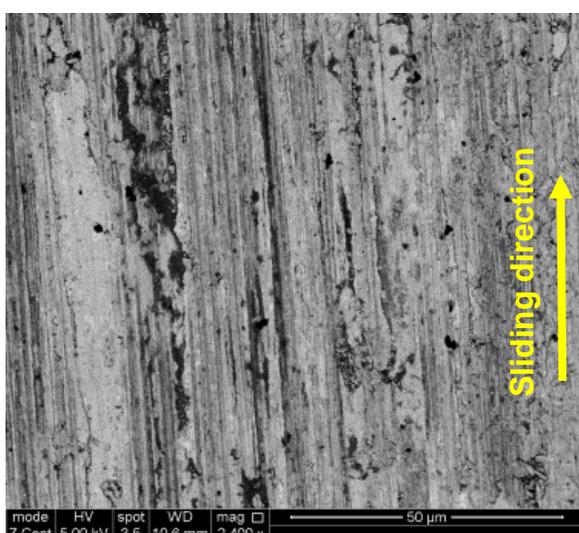
Fig. 5.36 – BSE image of the worn surface of αβ alloy at cathodic potential at 0.5N.
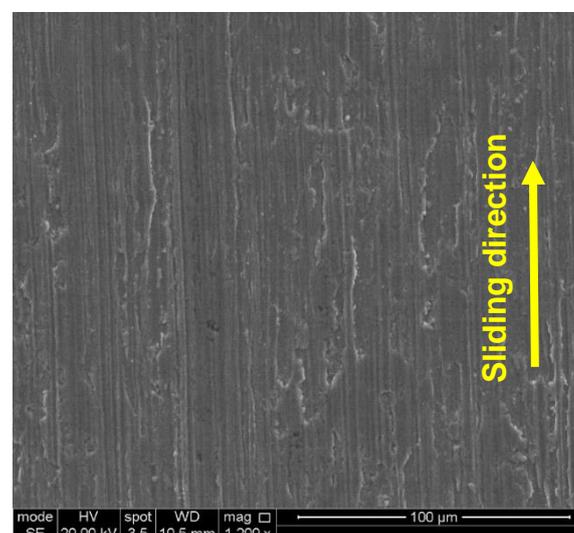
Fig. 5.37 – SE image of the worn surface of αβ alloy at cathodic potential at 0.5N.

- **Nβ alloy at 0.5N**
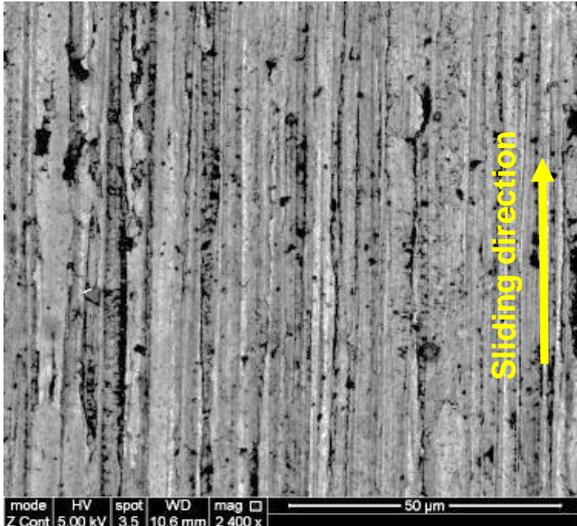
Fig. 5.38– BSE image of the worn surface of Nβ alloy at anodic potential at 0.5N.
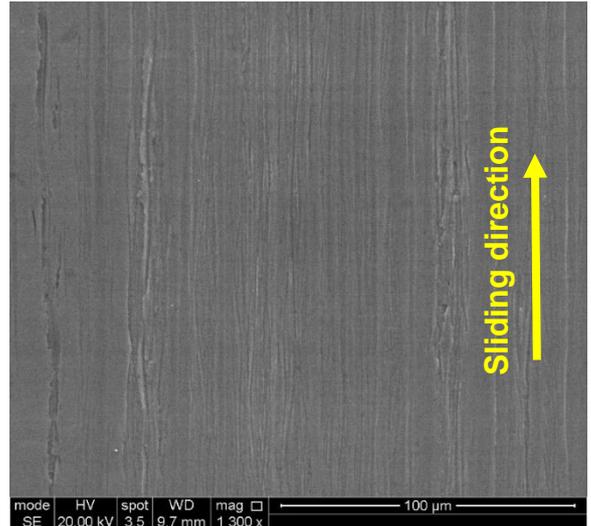
Fig 5.39 - SE image of the worn surface of Nβ alloy at anodic potential at 0.5N
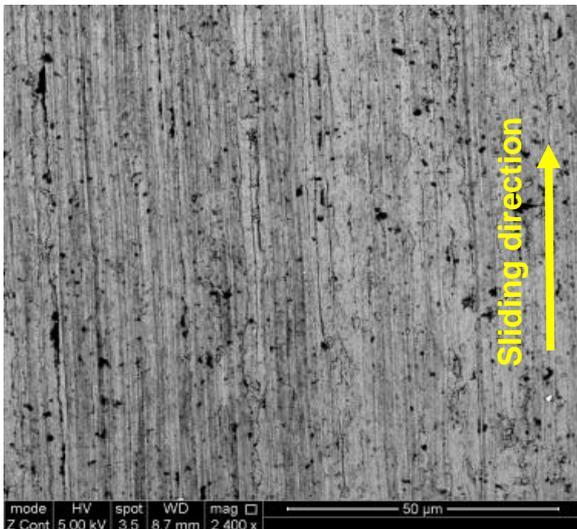
Fig. 5.40 – BSE image of the worn surface of Nβ alloy at OCP at 0.5N.
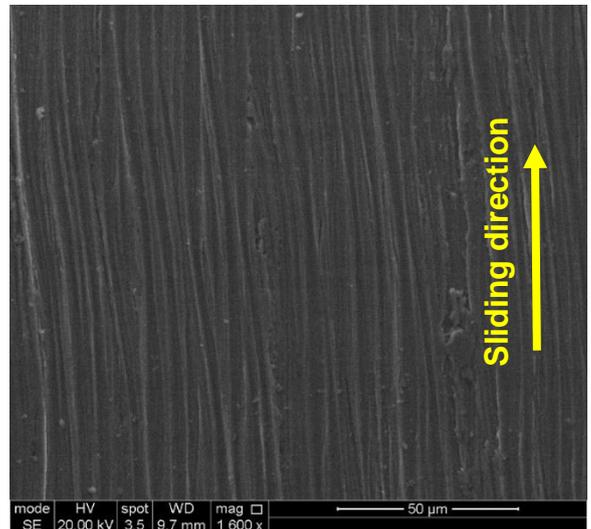
Fig. 5.41 – SE image of the worn surface of Nβ alloy at OCP at 0.5N.
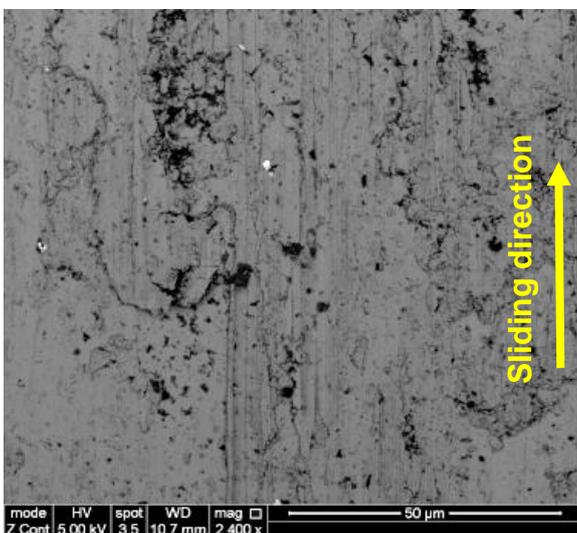
Fig. 5.42 – BSE image of the worn surface of Nβ alloy at cathodic potential at 0.5N.
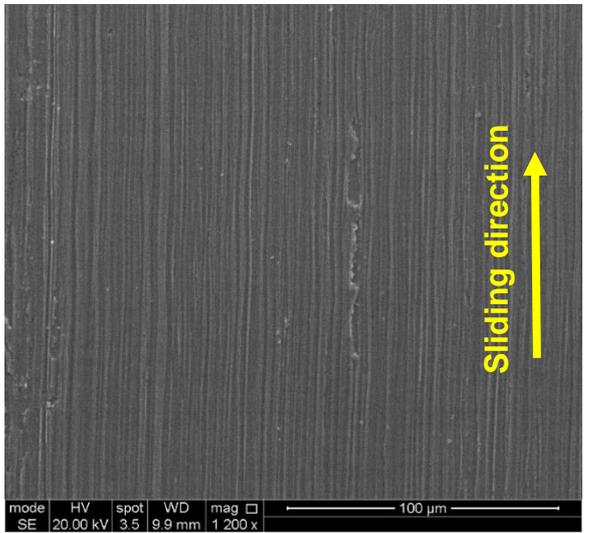
Fig. 5.43 – SE image of the worn surface of Nβ alloy at cathodic potential at 0.5N.

121

- **β alloy at 0.5N**

Fig. 5.44 – BSE image of the worn surface of β alloy at anodic potential at 0.5N.
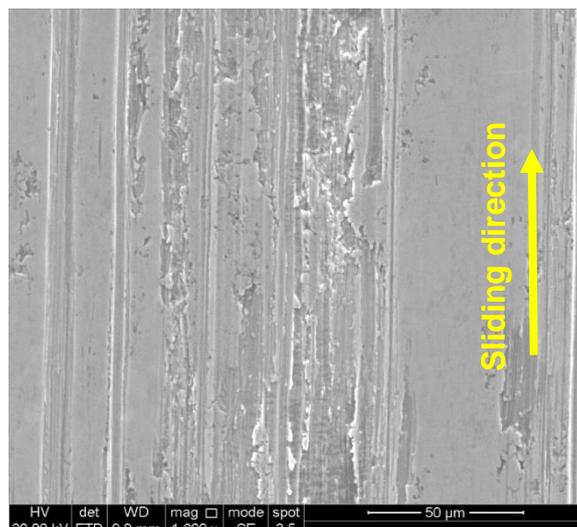
Fig 5.45 - SE image of the worn surface of β alloy at anodic potential at 0.5N
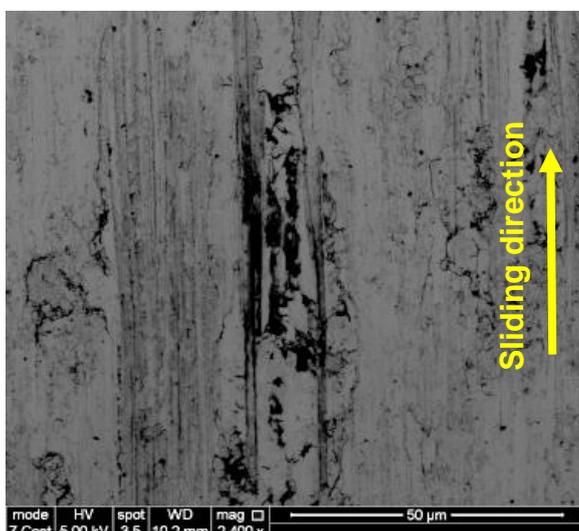
Fig. 5.46 – BSE image of the worn surface of β alloy at OCP at 0.5N.
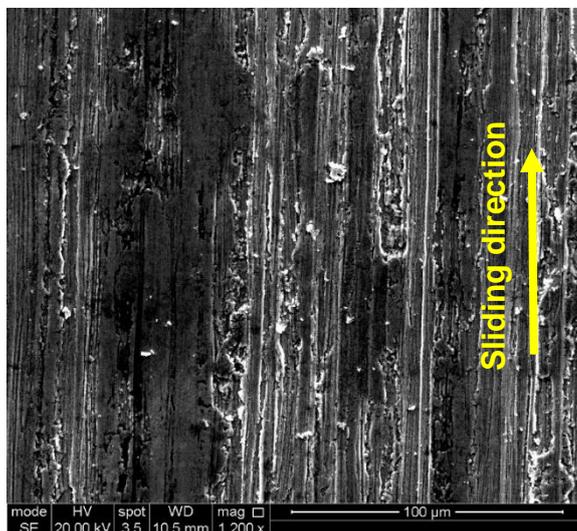
Fig. 5.47 – SE image of the worn surface of β alloy at OCP at 0.5N.
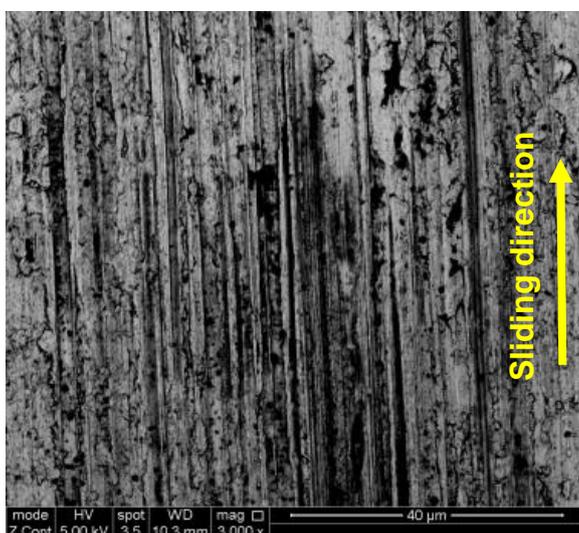
Fig. 5.48 – BSE image of the worn surface of β alloy at cathodic potential at 0.5N.
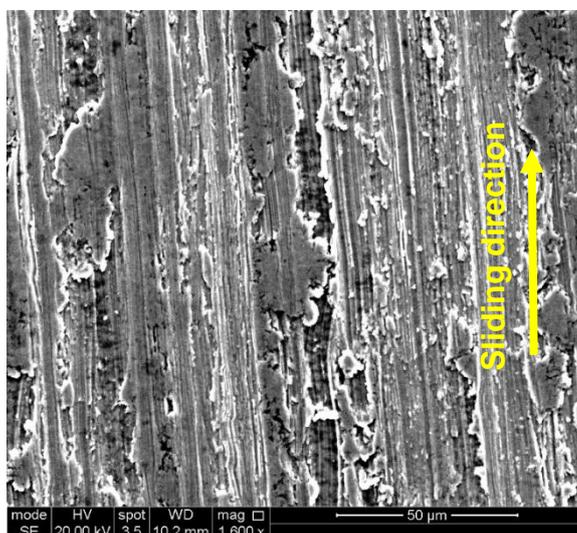
Fig. 5.49 – SE image of the worn surface of β alloy at cathodic potential at 0.5N.
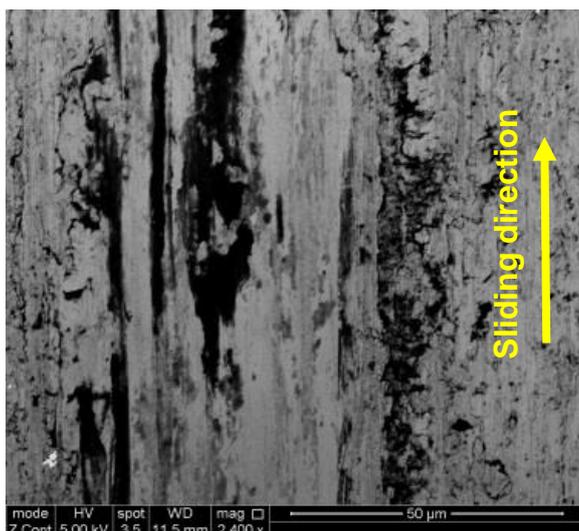
- **βω alloy at 0.5N**

Fig. 5.50 – BSE image of the worn surface of βω alloy at anodic potential at 0.5N.
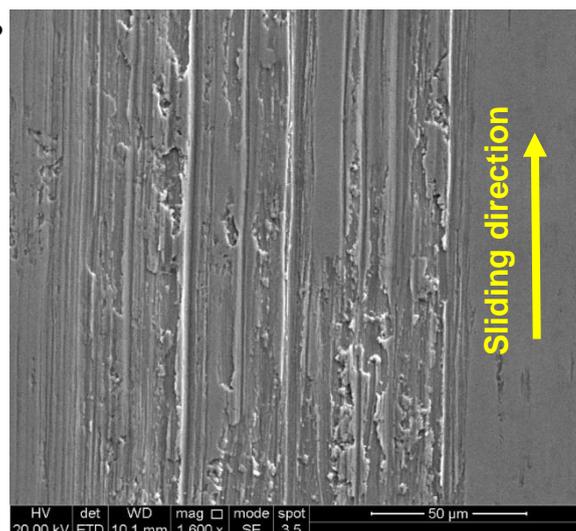
Fig. 5.51 - SE image of the worn surface of βω alloy at anodic potential at 0.5N
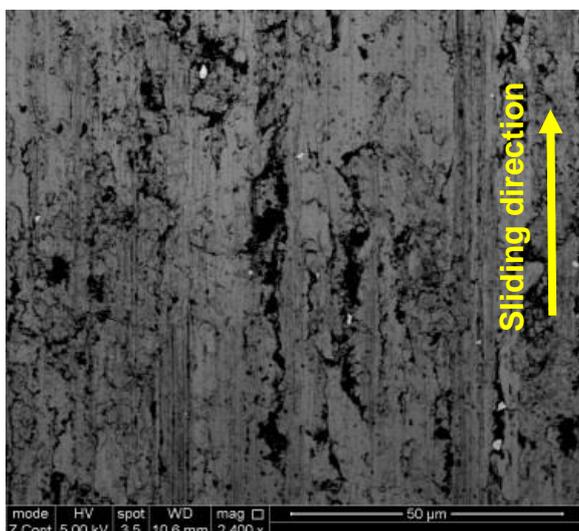
Fig. 5.52 – BSE image of the worn surface of βω alloy at OCP at 0.5N.
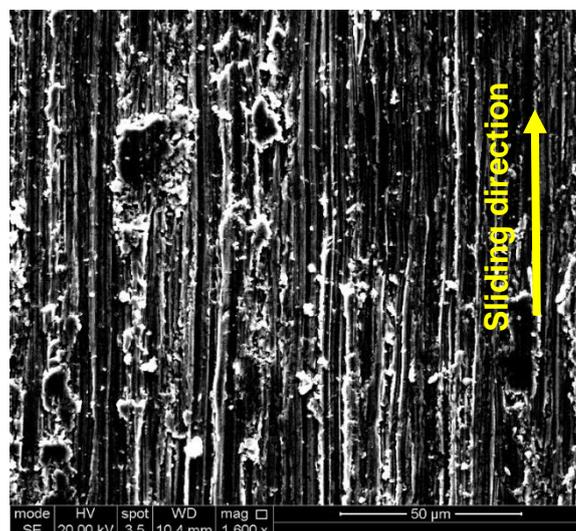
Fig. 5.53 – SE image of the worn surface of βω alloy at OCP at 0.5N.
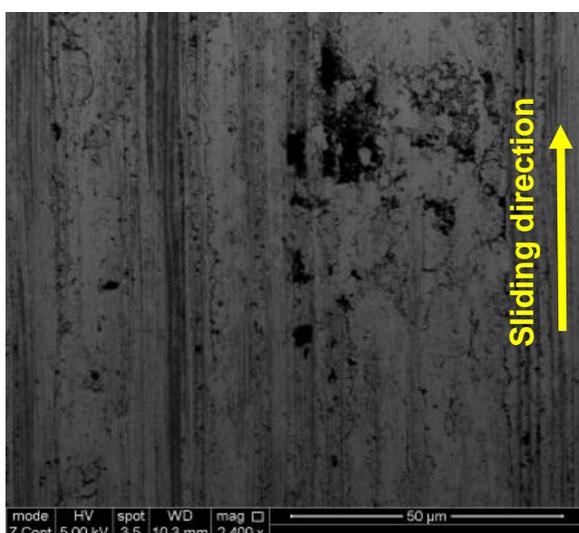
Fig. 5.54 – BSE image of the worn surface of βω alloy at cathodic potential at 0.5N.
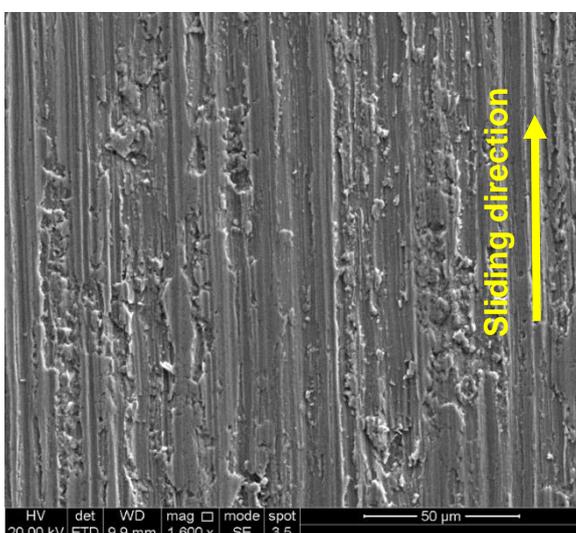
Fig. 5.55 – SE image of the worn surface of βω alloy at cathodic potential at 0.5N.

123

5.2.6 Presence of tribolayer and mechanical properties of the surface

Raman spectra with Gaussian peak fitting, presented in Fig. 5.56 to 5.59, have peaks at 1332 cm^{-1} and 1545 cm^{-1}. Carbon has two crystalline forms, graphite and diamond. For both structures the Raman spectra are well known. Thus, these peaks can be related to the spectra of disordered graphite or disorder mode (D band) and single crystalline graphite or tangential stretch mode (G band), which relates to the presence of Carbon, with all alloys tested having these peaks.

In the D band the bond-angle disorder in the sp^2 graphite-like microdomains, induced by linking with sp^3 atoms, as well as the finite crystalline sizes of sp^2 microdomains, while the G band is ascribed to sp^2 trigonal bonding related to the graphite phase [291]. In this sense, the results from the Raman spectra show that the worn area was composed of sp^2-carbon and sp^3-carbon.

In general, the intensity ratio of D and G peaks is related to the relative content of sp^2 and sp^3 bonds. The sp^2 bond could effectively reduce the shearing resistance on the contact surface and the sp^3 bond with diamond-structure could enhance the hardness of material.

The αβ and βω alloys show higher and lower peaks at cathodic potential (175.05 and 150.43) and anodic potential (114.54 and 106.33). G peaks are always more intense than the D peak, exept for βω at OCP, where the D peak is 113.07 and G peak is 107.73.

The Raman curves are similimar for Nβ alloy despite the electrochemical condition, where G peaks are higher than D peak. β alloy show higher and lower peaks at anodic potential (D = 142.03 and G = 127.26) and cathodic potential (D = 30.31 and G = 42.22) where G peak is lower at cathodic potential and D peak is higher at OCP and anodic potential.

The highest G band (175.05) intensity was observed for the αβ alloy at cathodic potential. The lowest D band (30.31) intensity was observed for the β alloy at cathodic potential.

Raman shift defines the vibration modes of the chemical bond as a result of the laser beam. Any change of the Raman shift position will indicate a change in the physical or chemical structure of the molecule being analysed. These peaks confirm the presence of tribolayer being generated during the motion of the surfaces in contact.The tribolayer is rich in protein and it may be beneficial for the

tribocorrosion process which is formed by the interaction of ions released by the passive film and proteins. However, published data on this it is scarce.

Of the five measurements taken per wear track not all of them registered the presence of a tribolayer and it is presented only the results that show the presence of C. This indicates the tribolayer is present in all alloys, but it is not continuous or uniform on the whole surface.

Fig. 5.60 and Fig. 5.61 show the reduced elastic modulus and nanohardness of the worn surfaces in comparison to the unworn surface as function of the contact depth. The αβ and β alloys exhibited the highest (96.6 GPa) and lowest (70.3 GPA) reduced elastic modulus of the unworn surface respectively. β also had the highest material loss (7.24 10^{-2} mm^3 at cathodic potential). There could be a relationship between the material loss volume and mechanical proprieties of the worn surfaces, however, it must be investigated further on other normal loads. The depth of penetration ranged from 201 nm to 355 nm.

αβ alloy experienced an increase of reduced elastic modulus after wear test and higher elastic modulus at cathodic polarized surface than anodic polarized surface (unworn surface: 96.6 GPa; cathodic potential: 101 GPa; OCP: 99.1GPa and anodic: 98GPa). Similar observations were made for the βω alloy for which the cathodic polarized surface had the highest reduced elastic modulus (104 GPa) and OCP surface had the lowest reduced elastic modulus (87.2 GPa). The Nβ alloy and β alloy show the highest elastic modulus for the anodic polarized surfaces (104 GPa) and the lowest elastic modulus at cathodic polarized surfaces (88.7 GPa and 93.1 GPa).

All alloys showed an increase of nanohardness of the surfaces after the wear test where αβ alloy showed the highest values (unworn surface: 3.5 GPa; cathodic potential: 4.3 GPa; OCP: 4.4 GPa and anodic: 4.6GPa) and βω alloy showed the lowest values (unworn surface: 2.8 GPa; cathodic potential: 3.3 GPa; OCP: 3.1 GPa and anodic: 3.3GPa).

Fig. 5.62 show the force, displacement and reduced nanohardness for the unworn Nβ alloy. With the exception of the αβ alloy, all other alloys show an increase in the reduced elastic modulus after rubbing, although there was a high degree of scatter in the results. All alloys exhibited an increase in the nanohardness of the worn surfaces after rubbing, but again the degree of scatter was large making it difficult to discern statistically meaningful differences. The

worn surfaces at anodic potential were slightly harder. These results can be correlated with the subsurface analysis, presented in section 5.2.10.
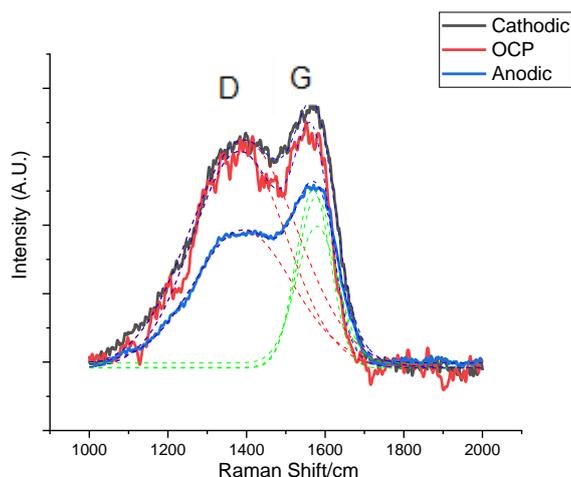
Fig. 5.56 – Raman spectroscopy of worn surface of αβ alloy at 0.5N.
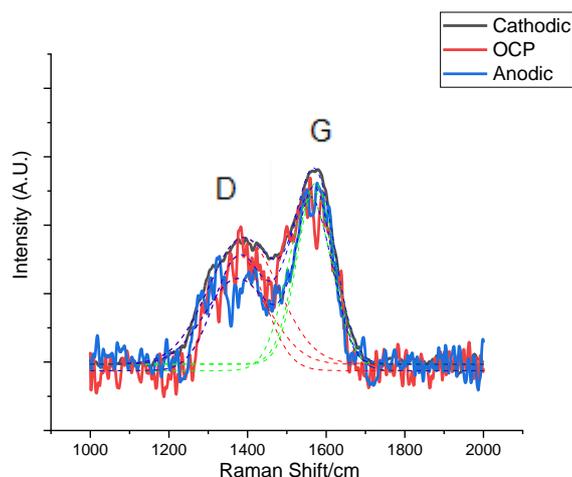
Fig 5.57 – Raman spectroscopy of worn surface of Nβ alloy at 0.5N.
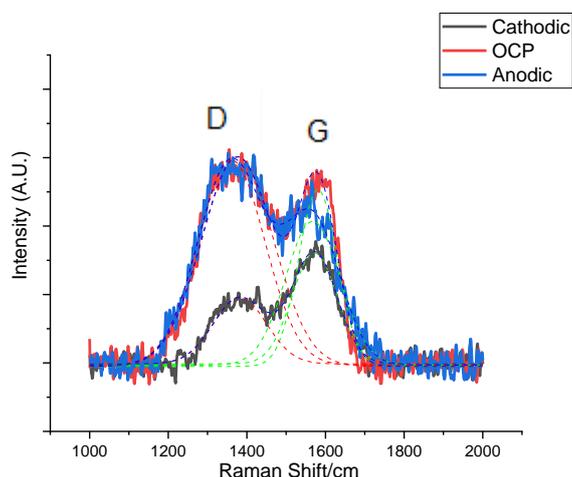
Fig 5.58 – Raman spectroscopy of worn surface of β alloy at 0.5N.
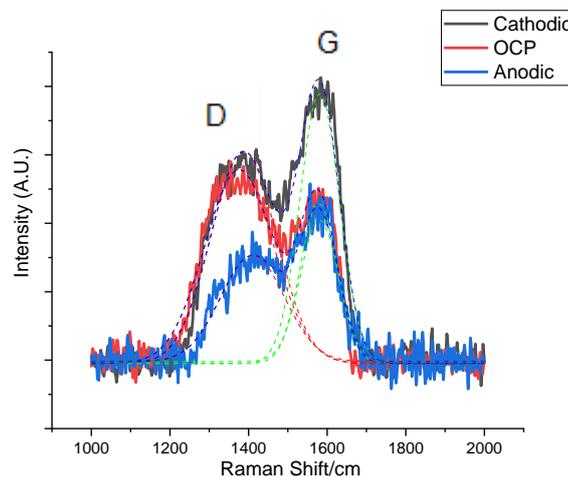
Fig. 5.59 – Raman spectroscopy of worn surface of βω alloy at 0.5N.
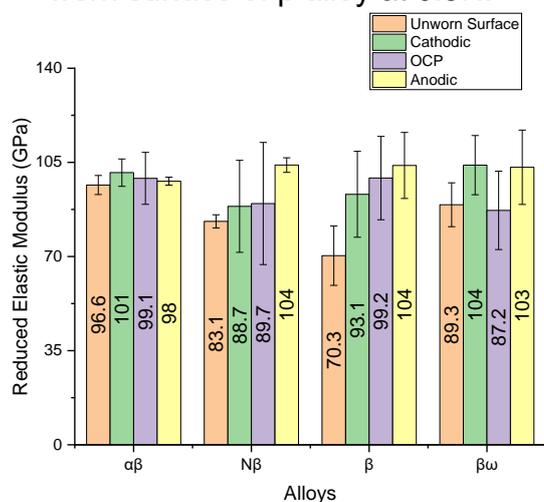
Fig. 5.60 – Reduced elastic modulus
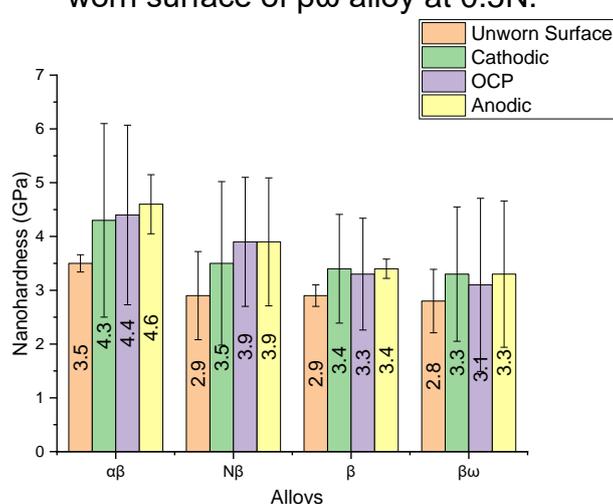
Fig. 5.61 – Nanohardness
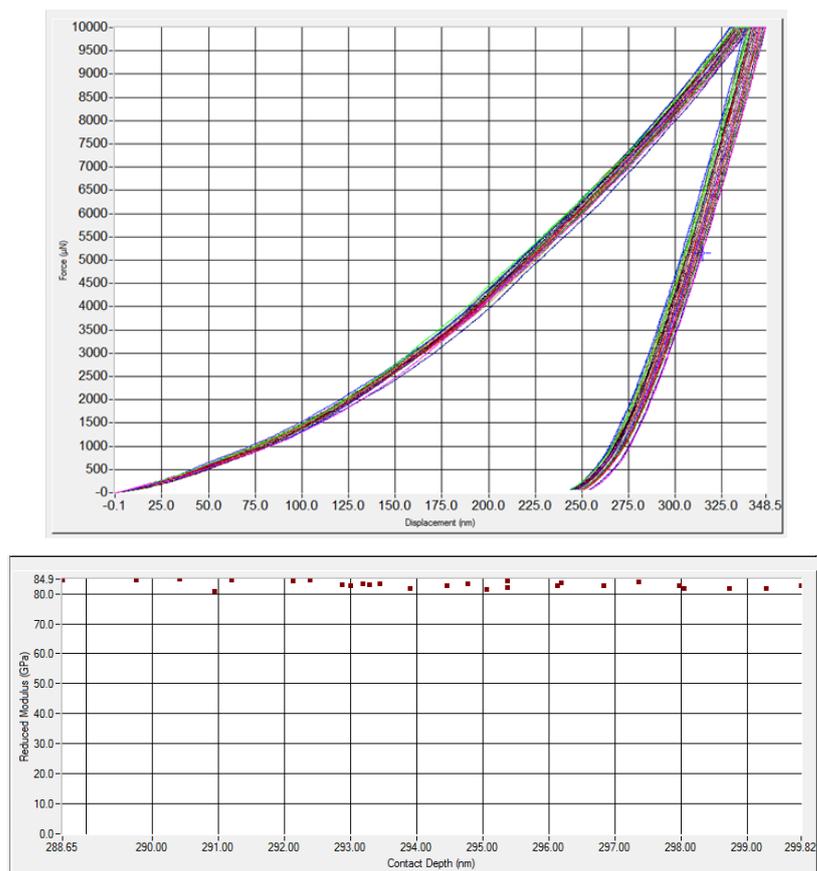
Fig. 5.62 – Force, displacement and reduced nanohardness of Nβ unworn surface nanoindentation test.

5.2.7 Subsurface deformation

Tribocorrosion resulted in changes in the structure at the worn surface when compared to the unworn surfaces in section 4.1. This changed the mechanical proprieties of the surface and induces surface hardening.

The worn surface structure was investigated using FIB. Figs. 5.63 to 5.74 show the subsurface area of the wear track imaged using ion channelling contrast. Generally, 3 regions were observed at the subsurface deformed area: the bulk material, the plastically deformed area and a nanocrystalline layer. These images show the presence of a refined grain area close to the surface, with the grains becoming larger with depth.

Comparing the subsurface to the bulk material, the αβ and βω alloys present a thin layer of refined grain at all potentials, which is clearer at OCP and cathodic potentials. However, the β and βω alloys do not show the presence of refined grains and there is no evidence of twinning. The boundary between the nanocrystalline and microcrystalline zone was not clear.

The presence of deformed areas in the subsurface is influenced by constant movement and load of tribological systems and by the presence of any lubricant.

The formation of the subsurface areas depended on the electrochemical conditions, with different behaviour seen for different alloys. For the β alloy, the greatest depth of deformation was seen under anodic conditions. For the αβ alloy, the least deformation was observed for the anodic condition, with similar deformation seen for the OCP and cathodic conditions. Virtually no deformation was observed for the βω alloy under all conditions. It should be noted that the depth of deformation may well have varied from one place on the surface to another and so these results need to be considered in that context.

However, comparing the grain size of this images to those from Fig. 4.1 to 4.4 (BSE images of unworn surface) the subsurface damage was identified. Large grains were observed in the bulk material by channelling contrast images of β and βω alloys which cannot be measured due to the area shown. However, the grains for αβ (2μm) and Nβ (1μm) alloys were smaller than those presented at BSE images of unworn surface (140 μm average grain size of αβ alloy and 1.6μm average grain size of Nβ alloy). Therefore, Fig. 5.63 to 5.68 are in the subsurface damaged area.
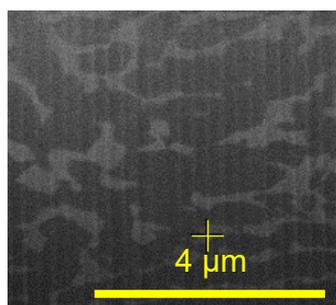
Fig. 5.63 – Subsurface image of the worn surface of αβ alloy at anodic potential at 0.5N.
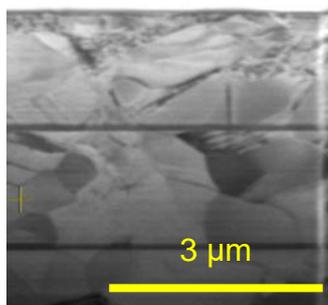
Fig. 5.64 – Subsurface image of the worn surface of αβ alloy at OCP at 0.5N.
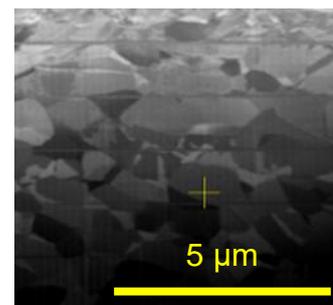
Fig. 5.65 – Subsurface image of the worn surface of αβ alloy at cathodic potential at 0.5N.
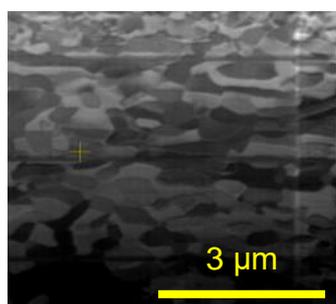
Fig. 5.66 – Subsurface image of the worn surface of Nβ alloy at anodic potential at 0.5N.
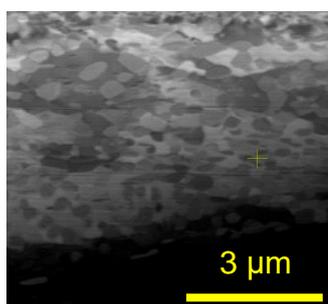
Fig. 5.67 – Subsurface image of the worn surface of Nβ alloy at OCP at 0.5N.
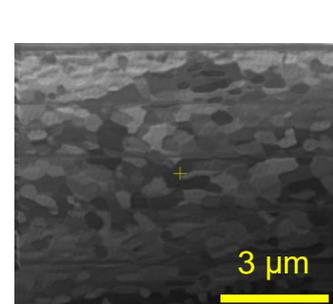
Fig. 5.68 – Subsurface image of the worn surface of Nβ alloy at cathodic potential at 0.5N.
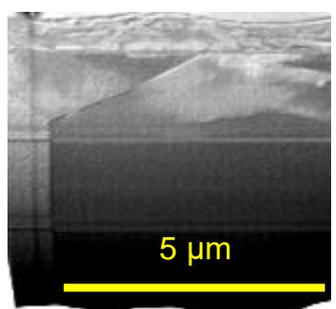
Fig. 5.69 – Subsurface image of the worn surface of β alloy at anodic potential at 0.5N.
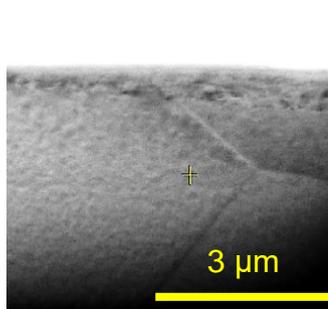
Fig. 5.70 – Subsurface image of the worn surface of β alloy at OCP at 0.5N.
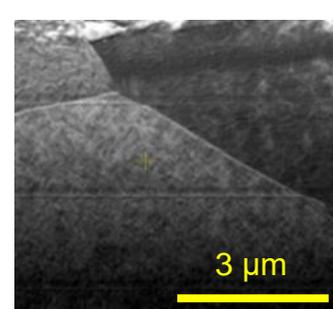
Fig. 5.71 – Subsurface image of the worn surface of β alloy at cathodic potential at 0.5N.
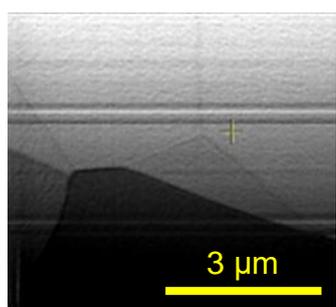
Fig. 5.72 – Subsurface image of the worn surface of βω alloy at anodic potential at 0.5N.
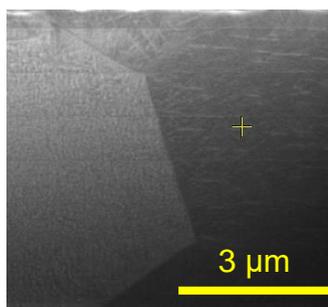
Fig. 5.73 – Subsurface image of the worn surface of βω alloy at OCP at 0.5N.
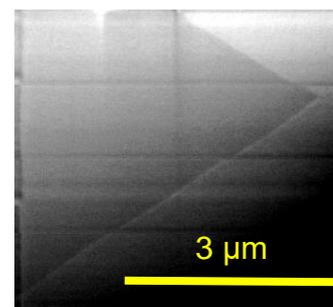
Fig. 5.74 – Subsurface image of the worn surface of βω alloy at cathodic potential at 0.5N.

5.2.8 Transmission Electron Microscopy

Bright field TEM micrographs and associated diffraction patterns taken from FIB specimens of the subsurface of the worn areas tested at 0.5N are given in Figs. 5.75 to 5.82. Figs. 5.75 to 5.77 show the αβ alloy at anodic potential, OCP and cathodic potential respectively. Figs. 5.78 to 5.80 show the Nβ alloy at anodic potential, OCP and cathodic potential respectively, while Fig. 5.81 shows the β alloy at OCP and Fig. 5.82 shows βω alloy at OCP.

The presence of α and β phases was observed in αβ alloy for all electrochemical conditions, as expected. For anodic conditions, there was evidence of surface deformation, consistent with the ion channelling image in Fig. 5.63. Under OCP conditions, there was evidence of a nanocrystalline layer formed, again consistent with the ion channelling image in Fig. 5.64. Under cathodic conditions, TEM showed little evidence of surface microstructure change, which is consistent with the ion channelling images.

For the Nβ alloy, there was major microstructural change at the worn surface. Under anodic conditions, Fig. 5.78, a nanocrystalline surface layer was observed. Moreover, phase transformations had occurred with the presence of α, α'' and ω phases observed. Similar observations were made under OCP conditions, although the nanocrystalline layer was very thin at the surface, Fig. 5.79. Major changes were observed under cathodic conditions, where there was extensive precipitation of a second phase, Fig. 5.80, which was believed to be α phase. The transformation to ω could have occurred through the deformation mechanism, but also may have been derived from frictional heating leading to precipitation.

Fig. 5.81 shows the near surface structure of the β alloy under OCP conditions. The TEM image shows that a phase changed had occurred and what appears to be α and ω phases precipitated out.

The surface of the βω alloy at OCP is shown in Fig. 5.82. The ω appears to have partly transformed to α phase, but the structure was difficult to image.
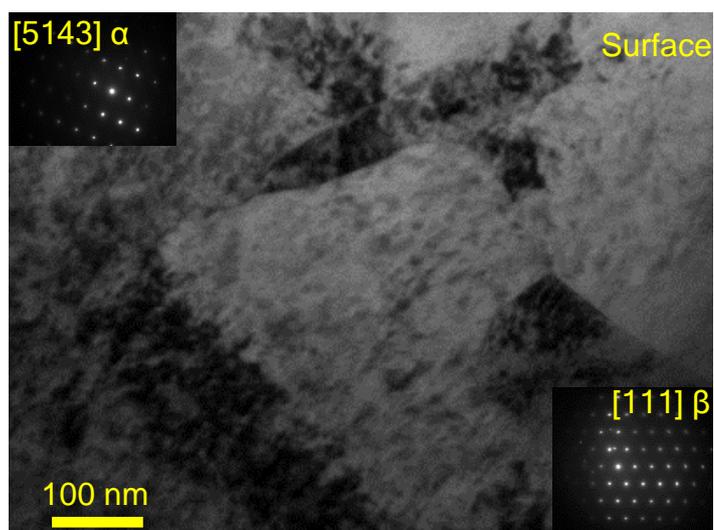
αβ alloy at 0.5N load

Fig. 5.75 – TEM image and difraction pattern of the worn area of αβ alloy at anodic potential at 0.5N load.
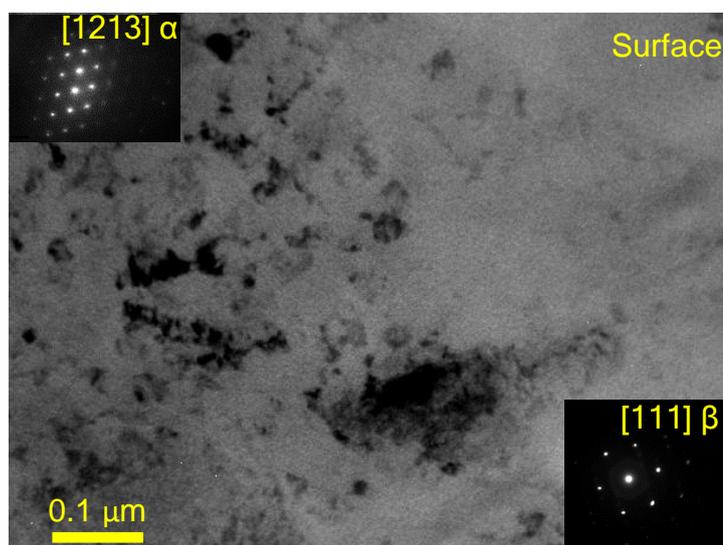
Fig. 5.76 – TEM image and difraction pattern of the worn area of αβ alloy at OCP at 0.5N load.
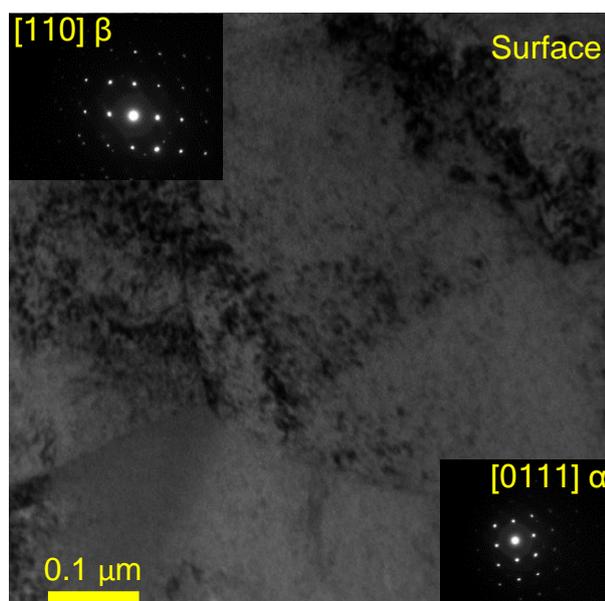
Fig. 5.77 – TEM image and difraction pattern of the worn area of αβ alloy at cathodic potetial at 0.5N load.
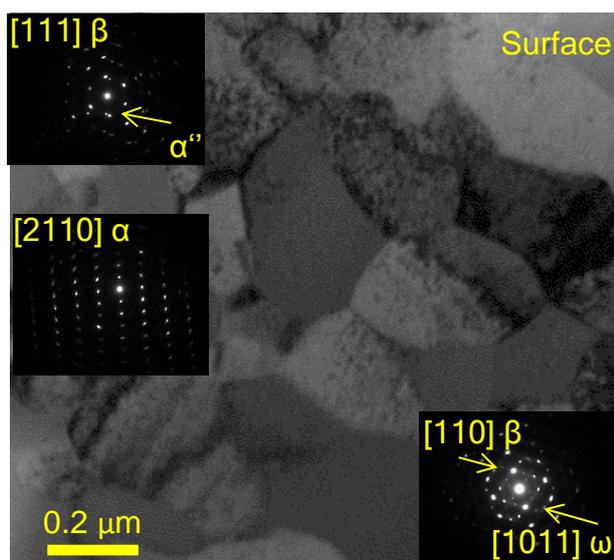
- **Nβ alloy at 0.5N load**

Fig. 5.78 – TEM image and difraction pattern of the worn area of Nβ alloy at anodic potential at 0.5N load.
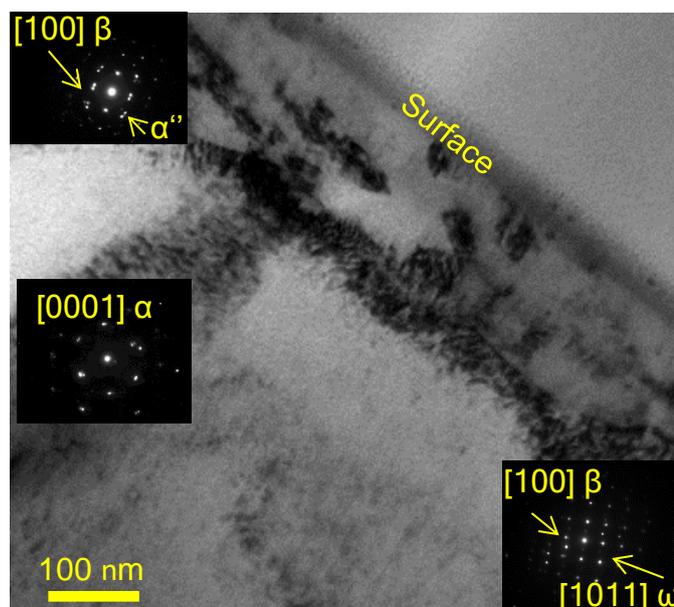
Fig. 5.79 – TEM image and difraction pattern of the worn area of Nβ alloy at OCP at 0.5N load.
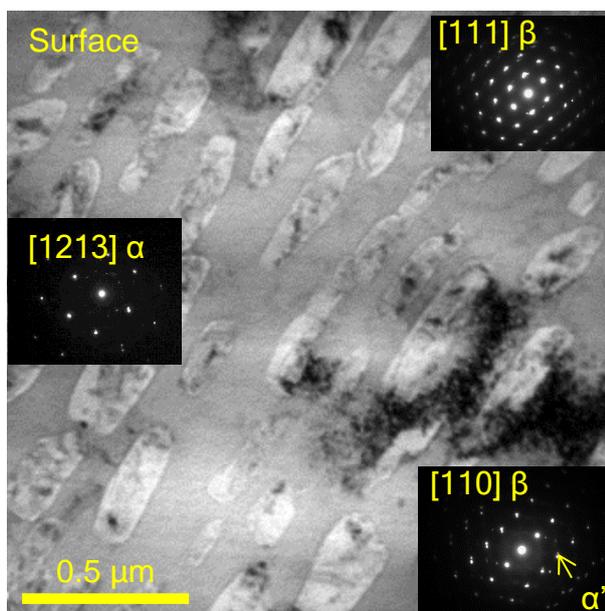
Fig. 5.80 – TEM image and difraction pattern of the worn area of Nβ alloy at cathodic potetial at 0.5N load.
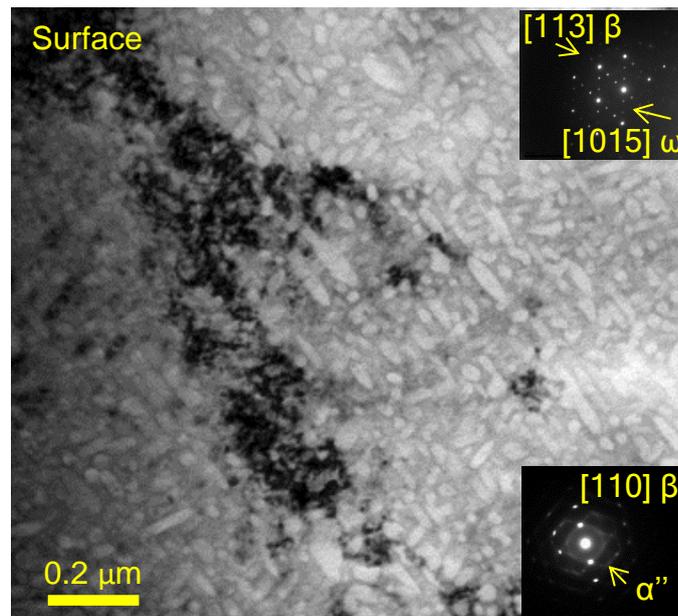
- **β alloy at 0.5N load**

Fig. 5.81 – TEM image and difraction pattern of the worn area of β alloy at OCP at 0.5N load.
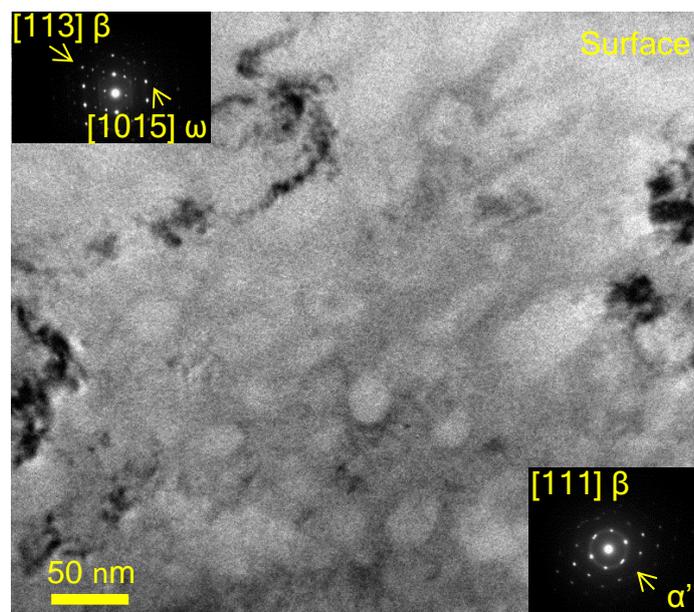
- **βω alloy at 0.5N load**

Fig. 5.82 – TEM image and difraction pattern of the worn area of βω alloy at OCP at 0.5N load.

5.3   Influence of normal load on tribocorrosion properties

The last section presented the effect of microstructure on tribocorrosion behaviour of Ti alloys at 0.5N in bovine serum solution. This section aims to study the effect of normal load (1N and 2N) on tribocorrosion behaviour of Ti alloys and compare these results to those from the last section. The tests were also carried out in bovine serum at 37°C.

5.3.1 Tribocorrosion behaviour

5.3.1.1   Cathodic potential

Figs. 5.83 and 5.84 show the current evolution of Titanium alloys versus time at cathodic potential (-1V vs OCP) for 1N and 2N respectively. All alloys show a decrease in current after rubbing started.

The αβ alloy had a similar behaviour at both loads showing a current drop and after 600 seconds a steady state was observed. The initial cathodic current measured was -60μA for 1N. Then it dropped to -95 μA and experienced an increase to -80μA and remained stable until the end of the rubbing where the current increased to -40μA at 1N. Similar behaviour was observed at 2N, where the initial cathodic current was -50μA and when rubbing started the current dropped to -75μA and decreased up to -100μA at the end of rubbing where the current increased to -55 μA.

Similar behaviour was seen in the β alloy. However, the current drop was not as large as in αβ alloy. The initial cathodic current measured for β alloy at 1N was -30μA then it dropped to -60 μA when rubbing started. An increase of current was observed at 1000s to -35 μA and remained stable up to the end of test where the current increased to -25 μA. At 2N the initial cathodic current measured was -30μA then it dropped to -50 μA when rubbing started. An increase in current was observed at 1000s to -40 μA and remained stable up to the end of test where the current increased to -30 μA.

The current evolution for the Nβ alloy during rubbing decreased at both loads. The initial cathodic current measured was -50 μA at 1N. It decreased when rubbing started to -65 μA and kept decreasing until -165 μA when the test was ended. Then an increase of current to -123 μA was observed. The similar

behaviour was observed at 2N, however the current drop was higher. The initial cathodic current measured was -60 µA and it decreased when rubbing started to -50 µA and kept dropping until -440 µA when the test was ended. Then an increase of current to -180 µA was observed. It showed that wear and normal load enhance the cathodic reaction.

Finally, the βω alloy showed different behaviour at each load. At 1N this alloy showed a current drop to -50 µA after rubbing started and then an increase to -30 µA. However, at 100s the current started to decrease again until the end of the test where the current was -80 µA and increased to -70 µA. This alloy at 2N showed the steady state showing a current of -50 µA during rubbing.

After rubbing, all alloys showed an increase in the current. The lowest current recorded was for Nβ (-123 µA and -440 µA) and the highest was for the β alloy (-25 µA and -30 µA) during rubbing at both loads. The current and COF evolution show a clear link. In fact they are influenced by the removal of the passive film at the beginning of the test, by the formation for tribolayer and by the plastic deformation that occurred at the sample surface. The isolated peaks may be the removal of entrapped debris. Wear enhanced by cathodic reaction due to the removal of original oxide layer (ceramic) and exposure of bare metal.

The COF is shown in Fig. 5.85 and Fig. 5.86 at 1N and 2N respectively. A high COF was recorded for the αβ (0.7), β (0.82) and βω (0.81) alloys at 1N at the start of the test. However, the COF reduced and a steady state was reached after 7000 seconds for αβ (COF 4.4) and βω (3.2) alloys and after 9000 seconds for the β alloy (COF 0.4). A different behaviour was observed for the Nβ alloy which did not show large variations of COF (0.49). The average COF is presented on Fig. 5.87 and Fig. 5.88 for 1N and 2N respectively. The lowest COF was observed for the αβ alloy (0.44) and the highest for the β alloy (0.53). However, they are in the same range as the Nβ (0.49) and βω (0.47) alloys. At 2N, the steady state was seen for the αβ (COF 0.7 to 0.5), β (COF 0.84 to 0.4) and βω (0.8 to 0.43) alloys from 7000 seconds and these alloys show a similar behaviour to 1N. However, the Nβ alloy showed an increase of COF up to 7,000 seconds from 0.48 to 0.6 and then steady state was observed. This alloy also shows the least transient curve at both loads.

The average COF at cathodic potential increased with load for all alloys, except the β alloy, Fig. 5.87 and 5.88 which also present the standard deviation

of 10,816 COF measurements. In comparison to 0.5N, the COF increased with load.
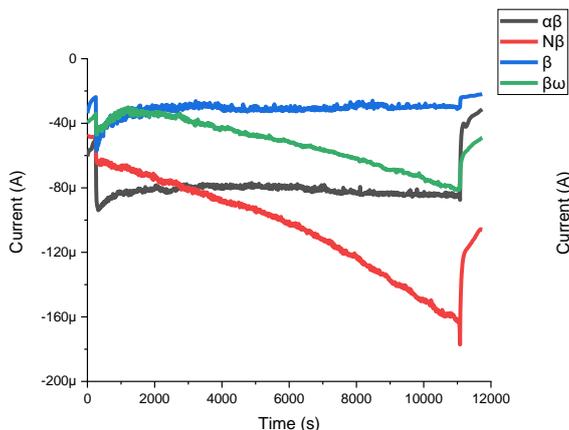
Fig. 5.83 - Current evolution all alloys at cathodic potential on 1N.
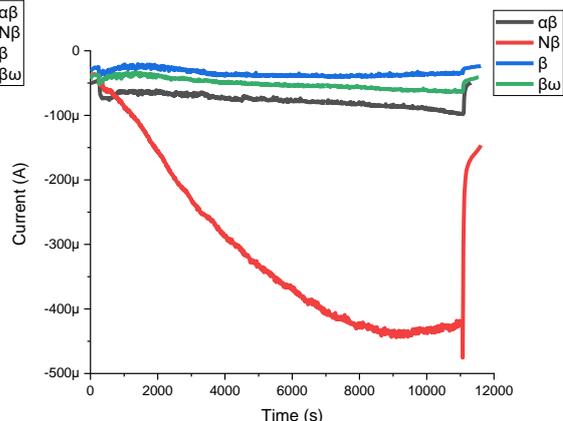
Fig. 5.84 - Current evolution all alloys at cathodic potential on 2N.
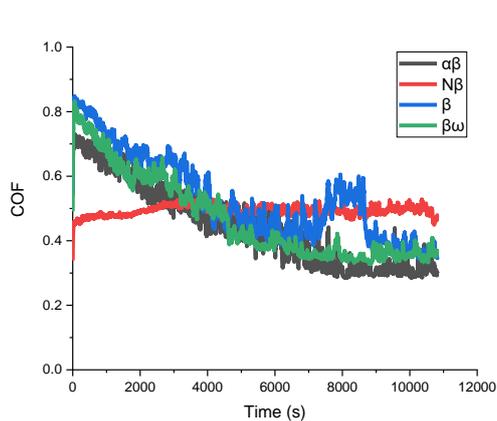
Fig. 5.85 - COF evolution all alloys at cathodic potential on 1N.
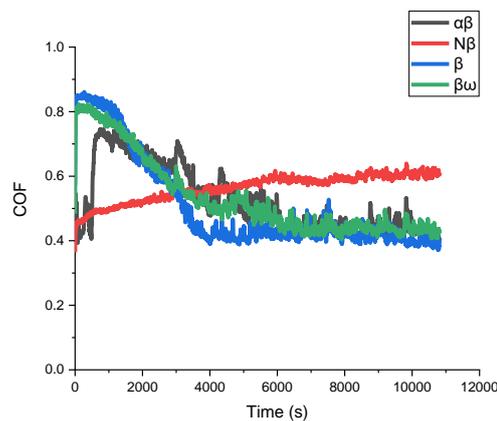
Fig. 5.86 - COF evolution all alloys at cathodic potential on 2N.
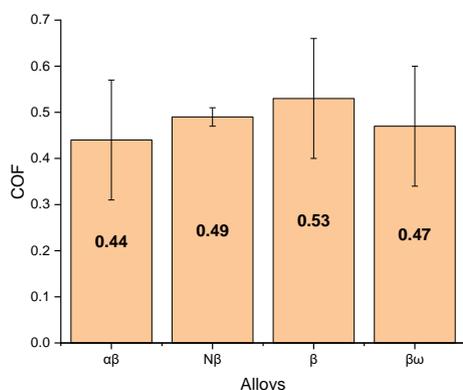
Fig. 5.87 – Average COF of all alloys at cathodic potential on 1N.
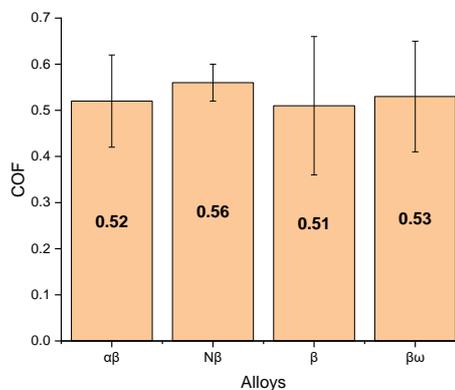
Fig. 5.88 – Average COF of all alloys at cathodic potential on 2N.

5.3.1.2   Open circuit potential

Figs. 5.89 and 5.90 show the potential evolution of these alloys versus time for 1N and 2N respectively.

The Nβ alloy was the noblest alloy (-0.09V) and the β alloy was the most active (-0.52V) before rubbing, but all alloys showed a cathodic drop as expected when there is a removal of the charge transfer barrier. Also, plastic deformation occurred on the sample surface, which may contribute to the shift in the potential.

The βω alloy showed the highest (ΔE = -1.1V and -0.8V) and the β alloy the lowest cathodic drop (ΔE = -0.5V both loads). The potential evolution for all alloys was not transient and constant. The βω alloy recorded the lowest (-1.1V) and β alloy the highest (-0.97V) value of OCP during rubbing for 1N load and the β alloy recorded the lowest (-1.1V) and the αβ alloy the highest (-0.98V) value of OCP during rubbing for 2N. The OCP increased again when rubbing was stopped to values lower than those of starting surface.

The ionic species released due to the charge transfer at the interface may interact with the bovine serum constituents and affect the friction and wear response of that interface.

Figs. 5.91 and 5.92 show the COF evolution of these alloys versus time for 1N and 2N respectively. The COF at OCP exhibited similar behaviour to that at 0.5N. All alloys registered high COF during the start of the test (αβ: 0.69 at 1N and 0.7 at 2N; β: 0.72 a 1N and 0.76 at 2N; βω: 0.75 at 1N and 0.8 at 2N), except Nβ alloy (0.45) that showed a steady and not transient curve. The αβ alloy shows a steady curve from 2,000 seconds and 4,000 seconds at 1N and 2N respectively.

The β alloy and βω alloy achieved steady state after 3,000 seconds and 4,000 seconds at 1N and 2N respectively. The average COF is presented in Fig. 5.93 and 5.94 which also present the standard deviation of 10,816 COF measurements. The lowest COF registered was 0.32 for the αβ alloy, while the highest was 0.45 for the Nβ alloy at 1N; 0.36 for the αβ alloy and 0.48 for the β alloy at 2N. However, the values are all in the same range. The reproducibility of these tests is presented in Figs. 5.95 to 5.100, which show a ΔE = -0.9V and -0.85V. Also, COF is 0.45 and 0.4 for Nβ alloy and ΔE = -0.55V for both tests. Also, COF is 0.48 and 0.1 for β, which show good reproducibility of the wear tests at OCP of Nβ and β alloys at 1N and 2N respectively.
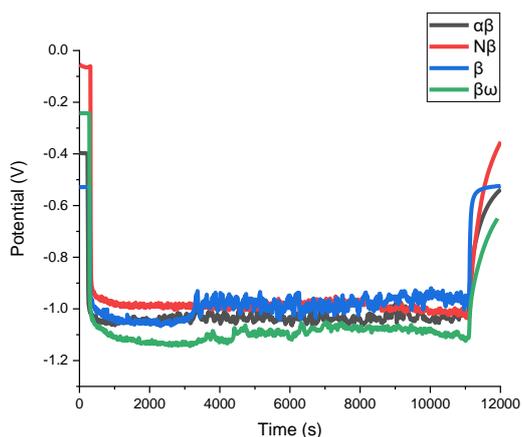
Fig. 5.89 - Potential evolution all alloys at OCP at 1N.
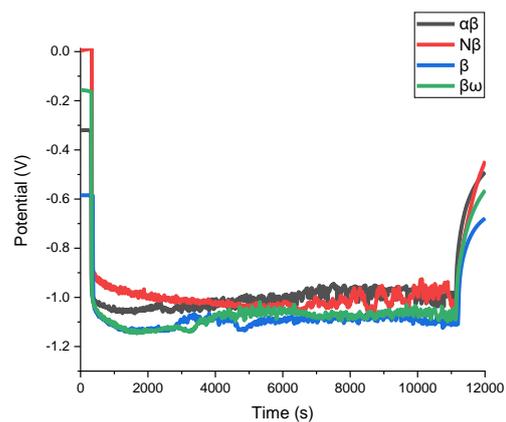
Fig. 5.90 - Potential evolution all alloys at OCP at 2N.
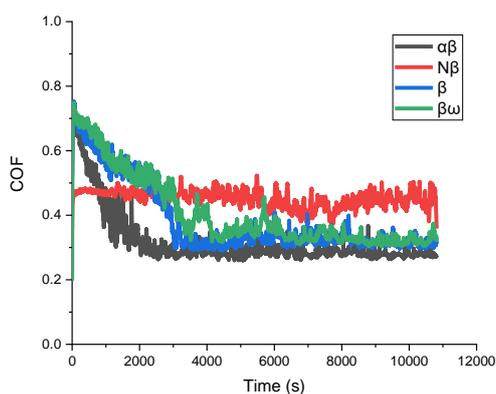
Fig. 5.91 - COF evolution all alloys at OCP at 1N.
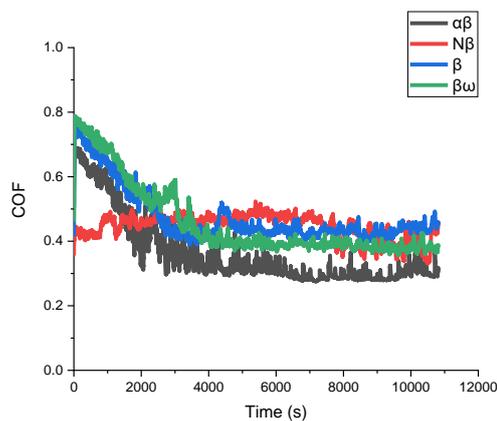
Fig. 5.92 - COF evolution all alloys at OCP at 2N.
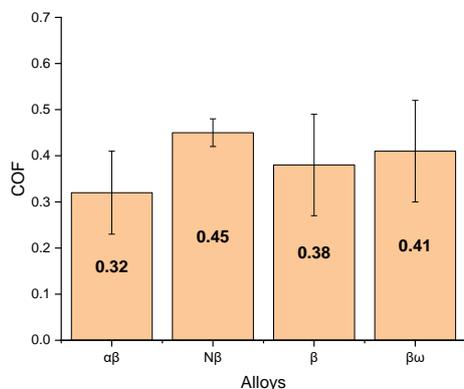
Fig. 5.93 – Average COF of all alloys at OCP at 1N.
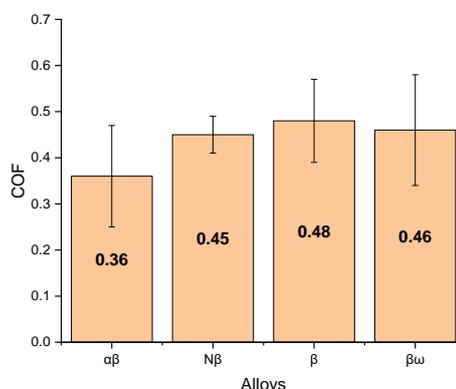
Fig. 5.94 – Average COF of all alloys at OCP at 2N.
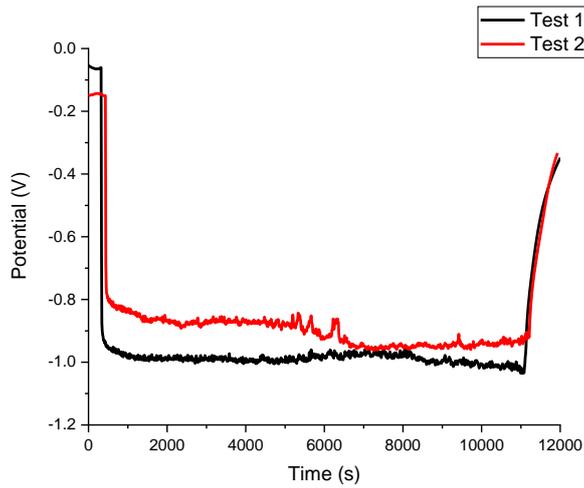
Fig. 5.95 – Reproducibility of the
OCP test of the Nβ alloy at 1N.
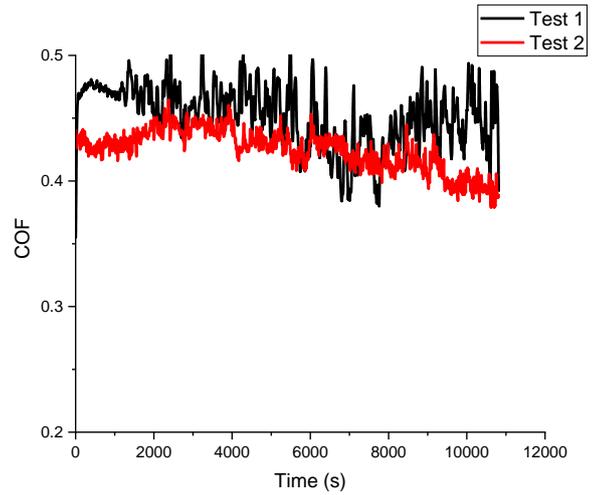
Fig. 5.96 – Reproducibility of the
COF evolution of the Nβ alloy at 1N.
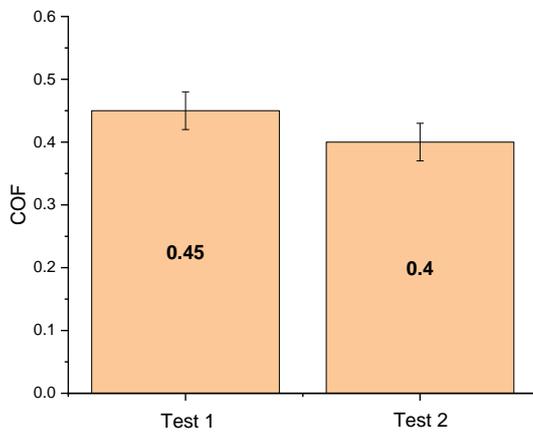
Fig. 5.97 – Reproducibility of average
the COF of the Nβ alloy at 1N.
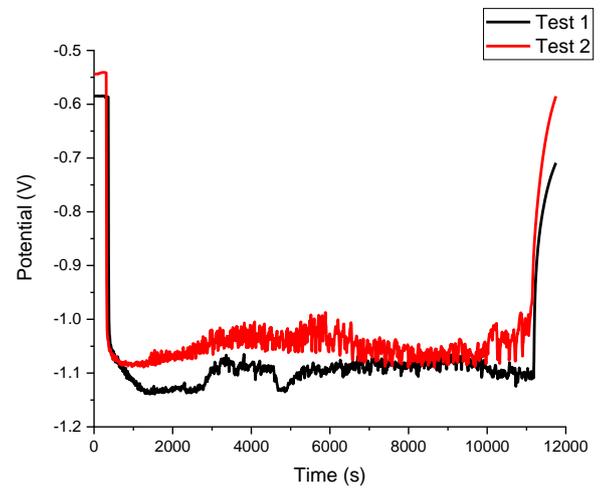
Fig. 5.99 – Reproducibility of the
COF evolution of the β alloy at 2N.
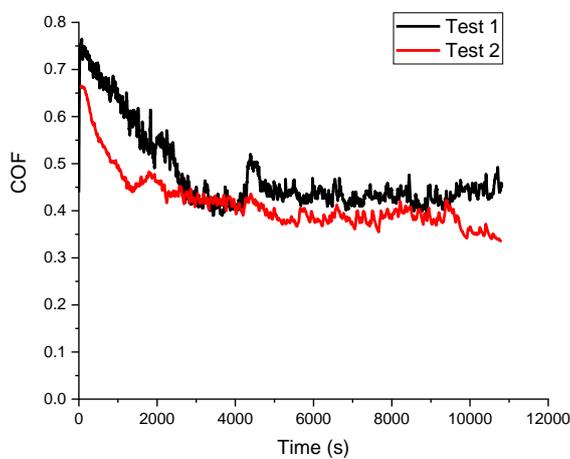
Fig. 5.99 – Reproducibility of the
COF evolution of the β alloy at 2N.
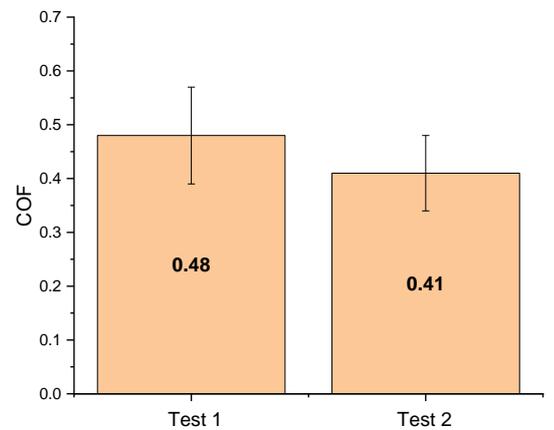
Fig. 5.100 – Reproducibility of
average the COF of the β alloy at 2N.

5.3.1.3   Anodic potential

Fig. 5.101 and 5.102 show the evolution of the anodic current versus time for 1N and 2N respectively at anodic potential (0.3V vs OCP). Before running, all the measured currents were 1 x 10^{-7} A and they increased when rubbing started. The βω alloy showed the highest corrosion current (185μA at 1N and 284 μA) when rubbing started due to the increase in the worn area.

The continuous metal ion release was due to the tribological contacts and the electrochemical driving force. The charge transfer rate is controlled by activation energy since the passive film is removed during rubbing, and it acts a barrier for charge transfer. It leads to a release of ions which starts the interaction with the bovine serum.

The curves were similar for all alloys at 1N and 2N. After an initial increase, the current drops and stays stable at ~5,000 seconds and 4,000 seconds for 1N and 2N respectively. This may be due to the reaction of proteins and released Ti^+, as the wear process accelerates release ions. Then it may form a layer which blocks charge transfer at the metal/solution interface. Also this layer reduces friction and indicates that this layer is an efficacious solid lubricant.

Steady state was observed earlier at 2N than at 1N. The current remained low and stayed the same after the conclusion of rubbing indicating the restoration of passivity where the passive film is a barrier to charge transfer. When rubbing ended, the current measured was 1x 10^{-7} A. The observed peaks in the current evolution and COF were due to wear debris generation.

The COF evolution is presented on Fig. 5.103 and Fig. 5.104 for 1N and 2N respectively. αβ, β and βω alloys show a high COF (0.7) at the beginning of the test and then a dropped to 0.28 at 1000s and a steady curve up to the end of the test. Nβ alloy also show high values (0.4) when the test started and a drop to 0.29 for 1N and 2N.

The average COF is presented on Fig. 5.105 and Fig. 5.106 which also presents the standard deviation of 10,816 COF measurements. The αβ alloy had the lowest COF for both 1N and 2N of 0.26 and 0.24 respectively. The β alloy had the highest COF of 0.29 and 0.31 for 1N and 2N respectively. It is clear that the

COF was higher at the cathodic potential and lower at the anodic potential. The COF was similar for all alloys in each electrochemical condition.
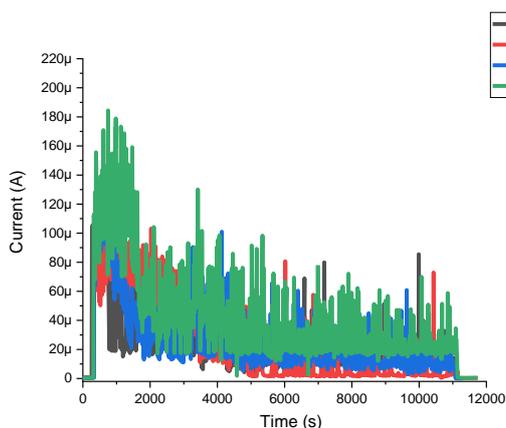

Fig. 5.101 - Current evolution all alloys at anodic potential at 1N.
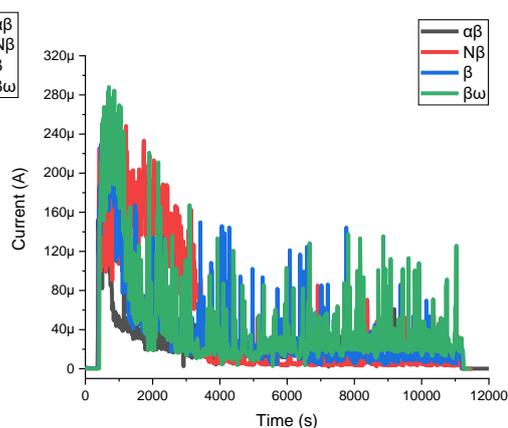
Fig. 5.102 - Current evolution all alloys at anodic potential at 2N.
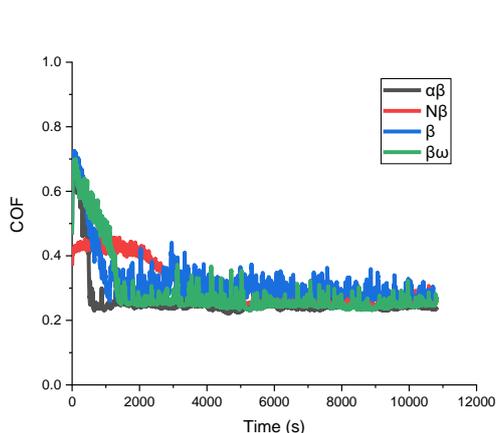
Fig. 5.103 - COF evolution all alloys at anodic potential at 1N.
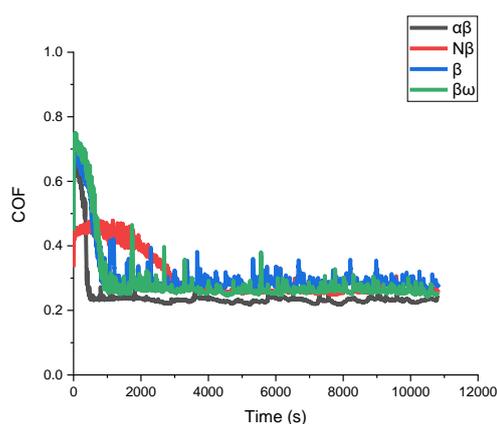
Fig. 5.104 - COF evolution all alloys at anodic potential at 2N.
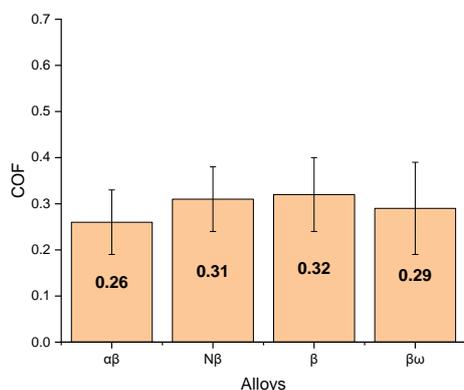
Fig. 5.105 – Average COF of all alloys at anodic potential at 1N.
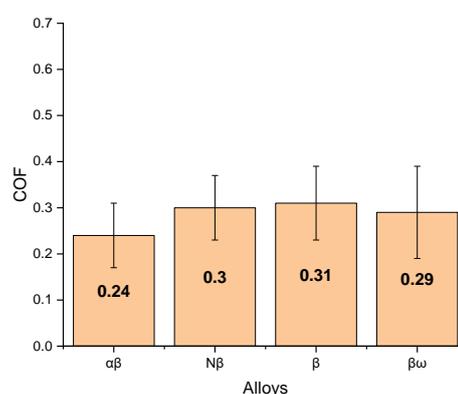
Fig. 5.106 – Average COF of all alloys at anodic potential at 2N.

5.3.2 Wear track profile

Fig. 5.107 to 5.112 gives the wear track profile for cathodic potential, OCP and anodic potential at 1N and 2N. The 3D images from the wear tracks are presented on table 5.2.

At cathodic potential, the αβ alloy has the shallowest (90μm and 130μm) and the Nβ alloy the deepest (145μm and 195μm) wear track for both loads. In addition, the wear tracks at 2N are deeper than those at 1N. The αβ alloy has the width of 1.2mm, Nβ alloy 1.25mm, β alloy 1.45mm and βω alloy 1.4mm at 1N; and αβ alloy 1.5mm, Nβ alloy 1.65mm, β alloy 1.66mm and βω alloy 1.5mm at 2N.

For OCP, the αβ alloy again has the shallowest wear track (50μm and 110μm) for both loads but at 1N the Nβ alloy has the deepest (107μm) and at 2N the βω alloy has the deepest (165μm). The αβ alloy presents the width of 1.1mm, Nβ alloy 1.2mm, β alloy 1.3mm and βω alloy 1.3mm at 1N; and αβ alloy 1.5mm, Nβ alloy 1.6mm, β alloy 1.5mm and βω alloy 1.5mm at 2N.

At anodic potential, the αβ alloy has the shallowest (50μm) and the β alloy the deepest (81μm and 100μm) wear track for both normal loads. αβ alloy shows the width of 0.9mm, Nβ alloy 1.1mm, β alloy 1.15mm and βω alloy 1.25mm at 1N; and αβ alloy 0.95mm, Nβ alloy 1.2mm, β alloy 1.3mm and βω alloy 1.5mm at 2N.

These results show that the αβ alloy had the shallowest wear track for all electrochemical conditions at both loads. The same trend at 0.5N was seen: the wear tracks at cathodic potential were the deepest and those at anodic potential were the shallowest. Also, the depth of the wear track for each alloy follows different trends, for instance, at OCP, the Nβ alloy presents the deepest wear track at 1N (107μm) but when the load is increased to 2N, the βω alloy produces the deepest wear track (165μm) followed by the β alloy (150μm).
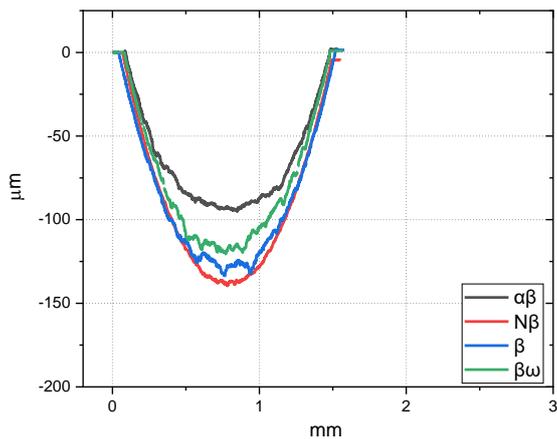
Fig. 5.107 – Comparison of wear track profile of all alloys at cathodic potential at 1N.
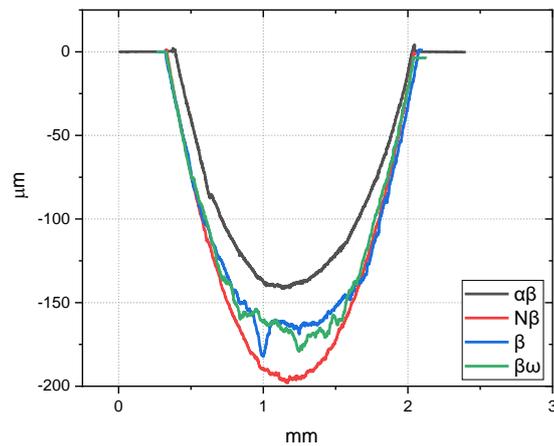

Fig. 5.108 – Comparison of wear track profile of all alloys at cathodic potential at 2N.
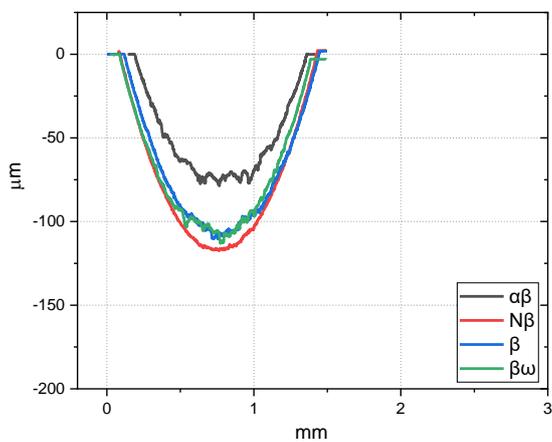

Fig. 5.109 – Comparison of wear track profile of all alloys at OCP at 1N.
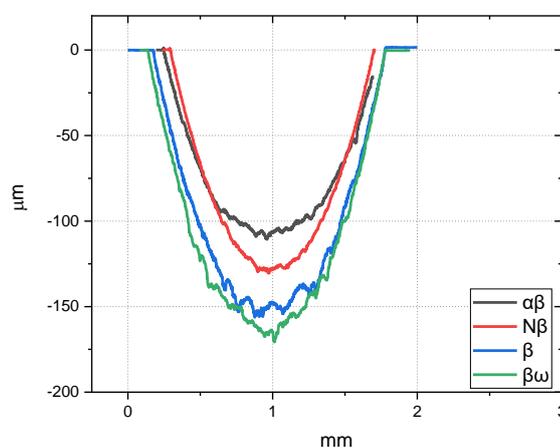
Fig. 5.110 – Comparison of wear track profile of all alloys at OCP at 2N.
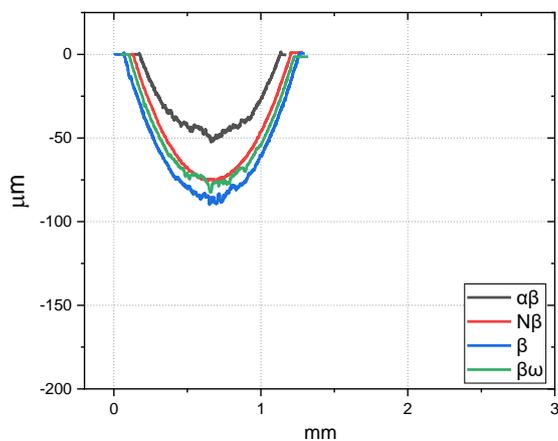
Fig. 5.111 – Comparison of wear track profile of all alloys at anodic potential at 1N.
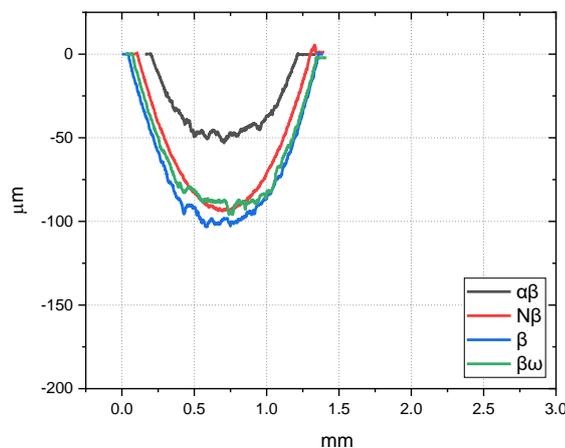
Fig. 5.112 – Comparison of wear track profile of all alloys at anodic potential at 2N.

Table 5.2 – 3D wear track images at 1N and 2N.

Alloys	Load	Cathodic	OCP	Anodic
αβ	1N	49 / -56 μm	36.5 / -48.2 μm	23.9 / -33.3 μm
	2N	39 / -114 μm	62 / -63 μm	52.8 / -33.6 μm
Nβ	1N	74 / -82 μm	53 / -73 μm	35 / -49.1 μm
	2N	88 / -117 μm	59 / -83 μm	45 / -60 μm
β	1N	59 / -82 μm	52 / -71 μm	43 / -57 μm
	2N	84 / -109 μm	58 / -114 μm	47 / -65 μm
βω	1N	48 / -76 μm	44 / -72 μm	57 / -54 μm
	2N	72 / -112 μm	70 / -107 μm	53 / -61 μm

5.3.3 Wear track volume, surface roughness and specific wear rate

The wear track volume is presented in Fig. 5.113 and Fig. 5.114 for 1N and 2N respectively. The wear track volume was higher for all alloys at 2N.

At cathodic potential and OCP at 1N, the Nβ alloy presented the highest volume loss (1.95 10^{-1} mm^3 and 1.54 10^{-1} mm^3) and the αβ alloy the lowest (1.28 10^{-1} mm^3 and 8.91 10^{-2} mm^3). The αβ alloy was also the smallest material loss at anodic potential but the highest material loss in this case was exhibited by the β alloy (1.09 10^{-1} mm^3 and 1.2 10^{-1} mm^3) for both load. The wear track volume at OCP show intermediate values, where αβ has 8.9 10^{-1} mm^3, Nβ 1.54$10^{-1}$ mm^3, β1.35 10^{-1} mm^3 and βω 1.49 10^{-1} mm^3.

At 2N, the αβ alloy had the lowest (2.23 10^{-1} mm^3) and the Nβ alloy the highest (3.05 10^{-1} mm^3) material loss at cathodic potential, which was similar to at 1N. However, the Nβ alloy presented the lowest (1.59 10^{-1} mm^3) and the βω alloy the highest (2.3 10^{-1} mm^3) material loss at OCP. Finally, similar to 1N, the αβ alloy had the lowest (5.14 10^{-1} mm^3) and the β alloy the highest (1.21 10^{-1} mm^3) material loss at anodic potential.

The same trend was observed regarding the effect of the electrochemical condition on material loss. At anodic potential the material loss was lower than at cathodic potential and OCP exhibited intermediary values. At 0.5N, the αβ alloy presents a better performance than the other alloys. When the load was increased to 1N and 2N, the same trend was observed.

The specific wear rates are presented in Figs. 5.115 and 5.116 for loads of 1N and 2N. At both loads the specific wear rate decreased in the order cathodic, OCP and anodic for all alloys.

The specific wear rate for αβ alloy increased from anodic (2.09 10^{-4} mm^3/Nm) to cathodic (5.93 10^{-4} mm^3/Nm), for the Nβ alloy it increased from anodic (3.44 10^{-4} mm^3/Nm) to cathodic (9.03 10^{-4} mm^3/Nm), for the β alloy it increased from anodic (5.07 10^{-4} mm^3/Nm) to cathodic (7.92 10^{-4} mm^3/Nm) and for the βω alloy it increased from anodic (3.92 10^{-4} mm^3/Nm) to cathodic (8.35 10^{-4} mm^3/Nm) at 1N.

For 2N, the specific wear rate for the αβ alloy increased from anodic (1.5 10^{-4} mm^3/Nm) to cathodic (5.16 10^{-4} mm^3/Nm), for the Nβ alloy it increased from anodic (2.33 10^{-4} mm^3/Nm) to cathodic (7.05 10^{-4} mm^3/Nm), for the β alloy it increased from anodic (2.8 10^{-4} mm^3/Nm) to cathodic (6.9 10^{-4} mm^3/Nm) and for

the βω alloy it increased from anodic (2.610^{-4} mm^3/Nm) to cathodic ($6.39\ 10^{-4}$ mm^3/Nm) and intermediate values were observed at OCP.

The αβ alloy exhibited the lowest and Nβ alloy and the β alloy the highest values specific wear rates. These values are high when compared to other metals for biomedical applications, such as CoCr and stainless steel.

The surface roughness of the centre of each wear track is shown in Fig. 5.117 and Fig. 5.118. The effect of potential and normal load on roughness was the same as observed at 0.5N.

At 1N and 2N, the surface roughness was higher at anodic potential, lower at cathodic potential and intermediate values were seen at OCP. At cathodic potential, the αβ alloy showed the lowest roughness (0.95 and 0.88) and the βω alloy (1.55 and 2) showed the highest roughness at both loads. At OCP, the β alloy showed the lowest roughness (1.18) and the βω alloy (1.66) showed the highest roughness at 1N and the Nβ alloy showed the lowest roughness (1.34) and the βω alloy (2.5) showed the highest roughness at 2N. Finally, at anodic potential, the Nβ alloy showed the lowest roughness (1.3 and 1.52) and the βω alloy (1.95 and 2.54) showed the highest roughness at both loads.

The roughness increases with load for all alloys. This property has higher values at anodic potential and lower values at cathodic potential. In general, the αβ alloy exhibited lower values and βω alloy higher values of roughness.
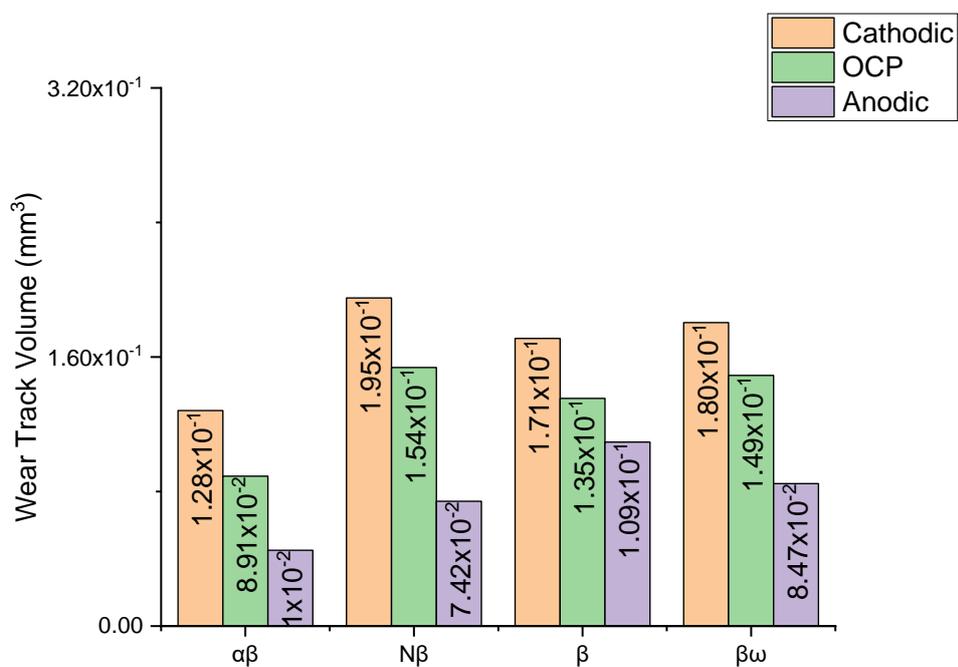
Fig. 5.113 – Comparison of wear track volume of all alloys in all electrochemical conditions at 1N.
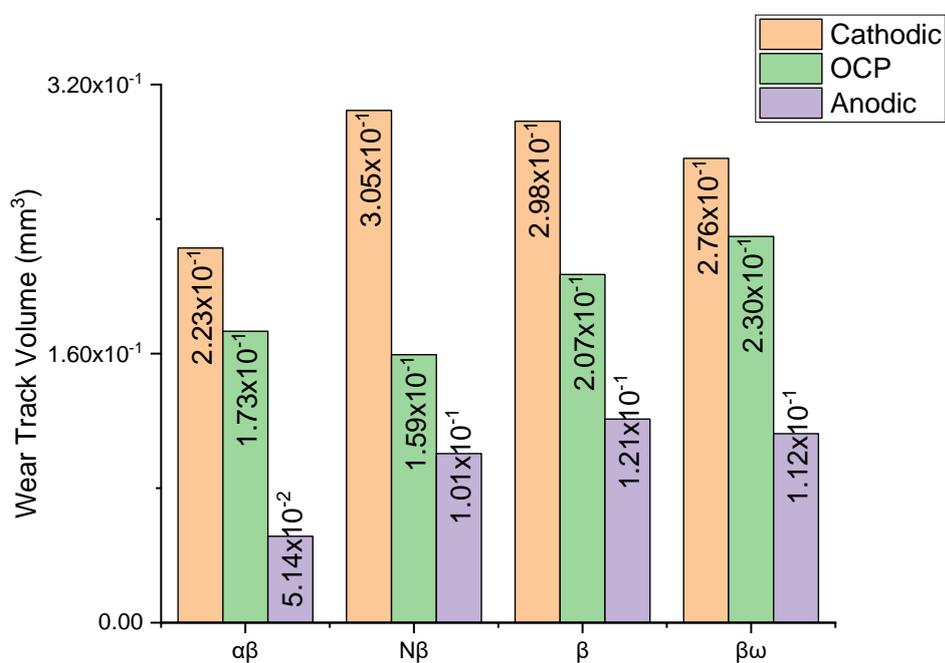
Fig. 5.114 – Comparison of wear track volume of all alloys in all electrochemical conditions at 2N.
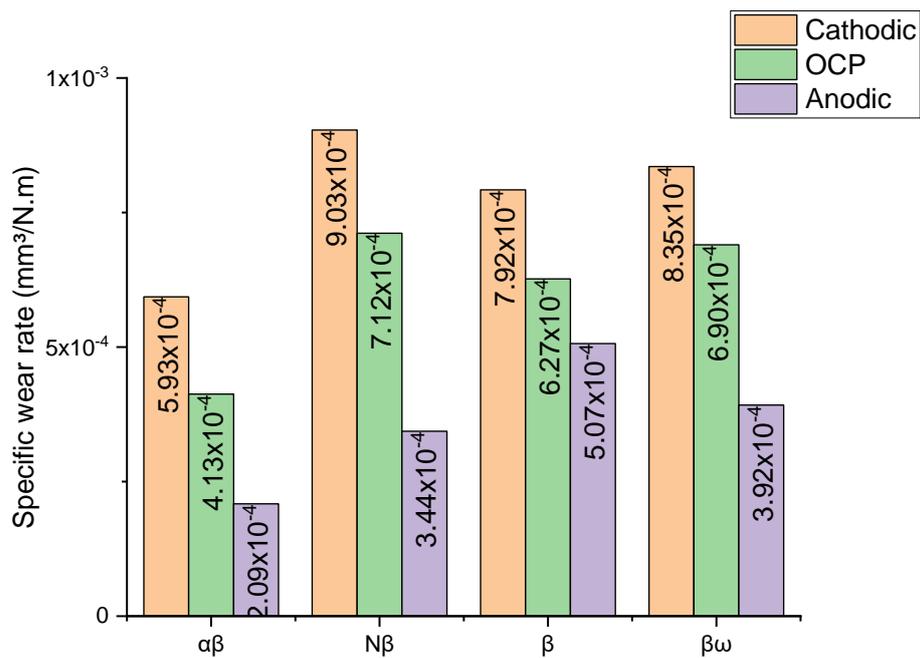
Fig. 5.115 – Comparison of specific wear rate at cathodic potential, OCP and anodic potential at 1N.
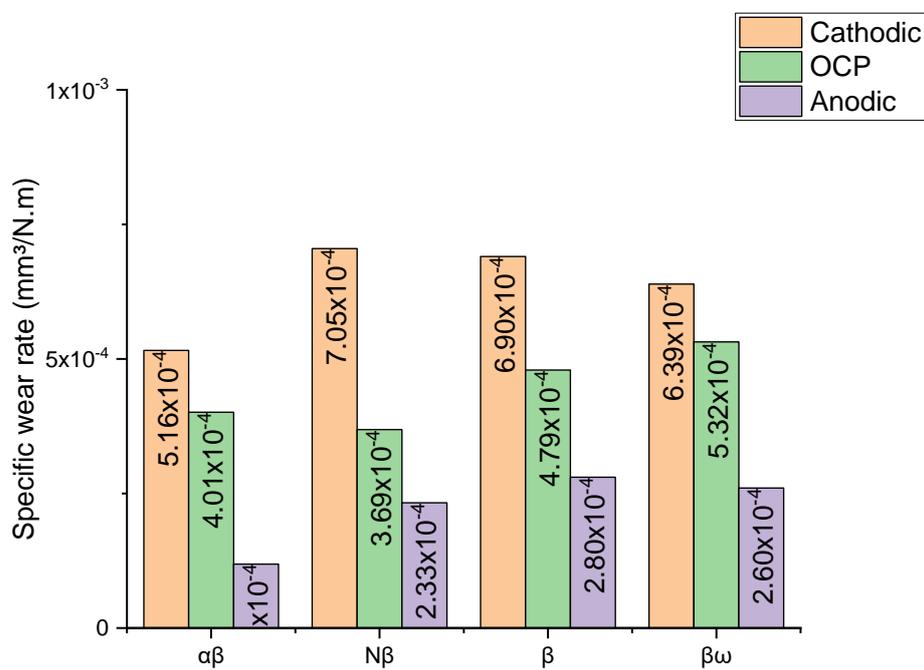
Fig. 5.116 – Comparison of specific wear rate at cathodic potential, OCP and anodic potential at 2N.
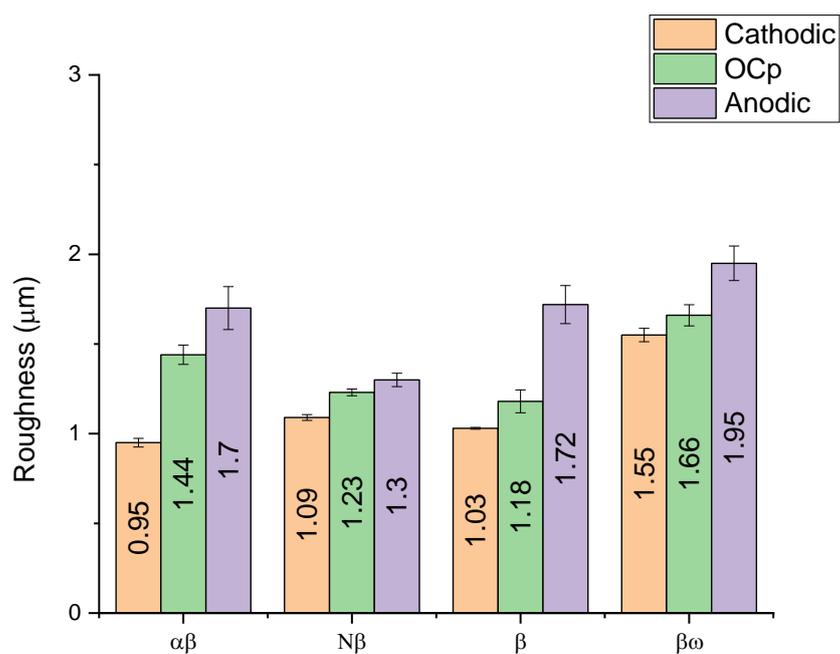
Fig. 5.117 – Comparison of roughness at cathodic potential, OCP and anodic potential at 1N.
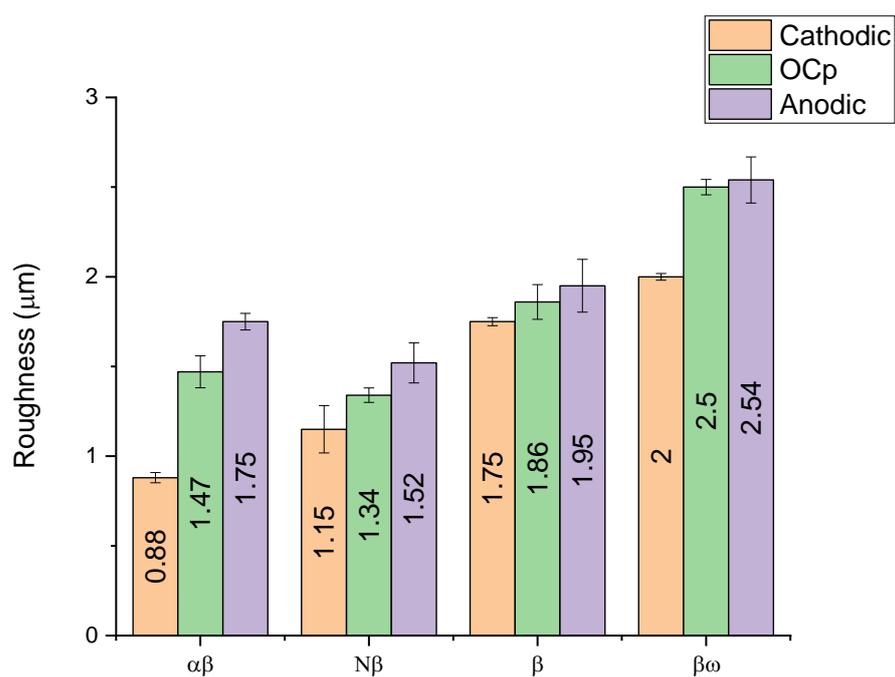
Fig. 5.118– Comparison of roughness at cathodic potential, OCP and anodic potential at 2N.

5.3.4 Surface characterization

The topography of the worn surfaces are presented in Figs. 5.133 to 5.180, using both backscattered and secondary electrons images in the following order: αβ alloy at 1N, αβ alloy at 2N, Nβ alloy at 1N, Nβ alloy at 2N, β alloy at 1N, β alloy at 2N, βω alloy at 1N and βω alloy at 2N.

Extensive surface roughening had occurred with isolated debris but no cracking was identified. These isolated debris might have acted as a third body. Features of ploughing and delamination such as wide grooves and scratches were observed throughout the worn surface. These are features of abrasive wear, similar to that at 0.5N.

There was no difference among all surfaces when the electrochemical condition was changed and the surfaces were free of corrosion product. The same features were also observed when the normal load and electrochemical conditions were changed. However, the surface roughness was higher when the load was increased.

The surface features is also similar to other ductile metals, which suggests that the electrochemical condition does not affect the wear mechanism.

An observation in all alloys was a dark area in backscattered images which indicates the presence of tribolayer (for 0.5N as well) which was not homogeneously distributed and later confirmed by Raman.
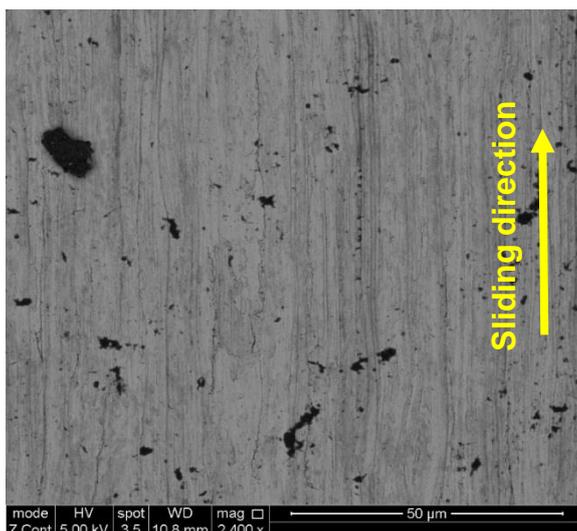
- **αβ alloy at 1N**

Fig. 5.119 – BSE image of the worn surface of αβ alloy at anodic potential at 1N.
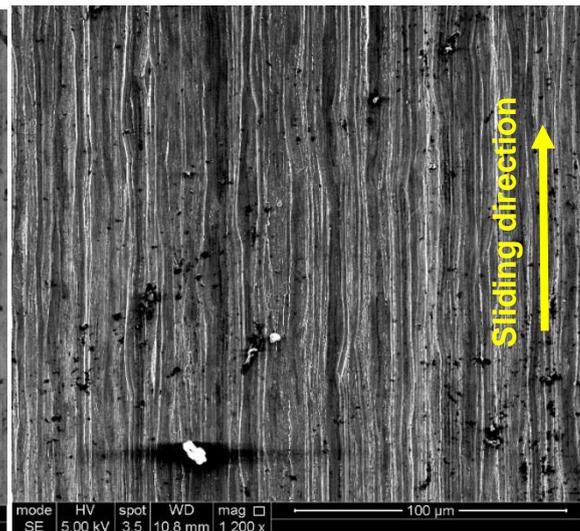
Fig. 5.120 - SE image of the worn surface of αβ alloy at anodic potential at 1N.
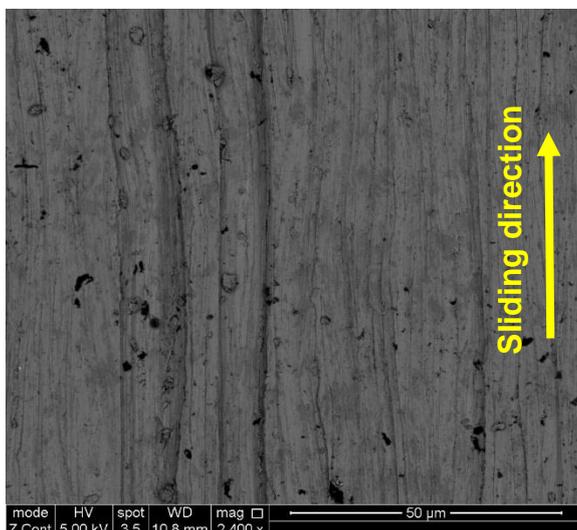
Fig. 5.121 – BSE image of the worn surface of αβ alloy at OCP at 1N.
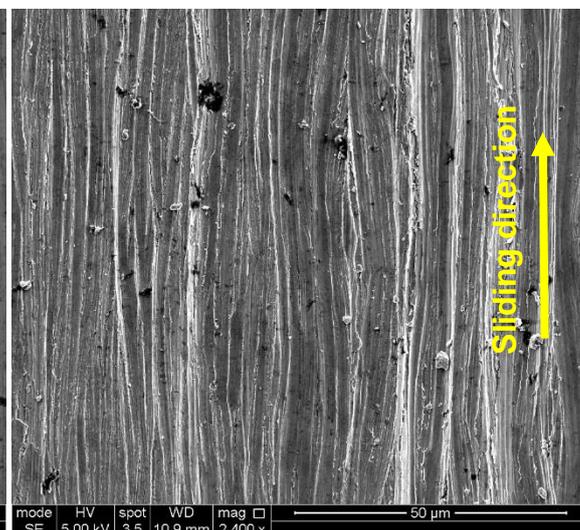
Fig. 5.122 – SE image of the worn surface of αβ alloy at OCP at 1N.
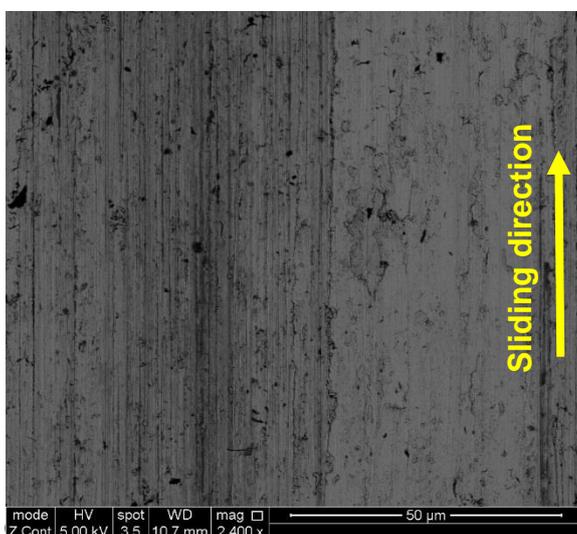
Fig. 5.123 – BSE image of the worn surface of αβ alloy at cathodic potential at 1N.
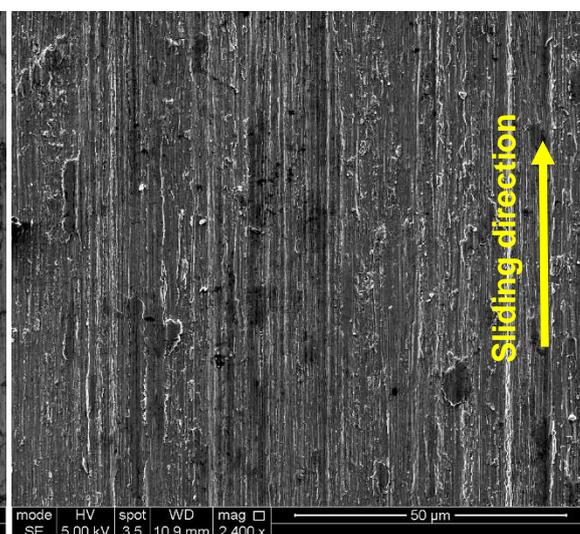
Fig. 5.124 – SE image of the worn surface of αβ alloy at cathodic potential at 1N.

152
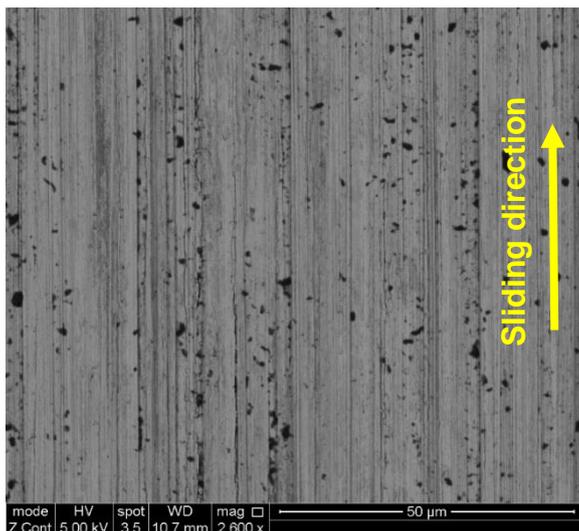
- **αβ alloy at 2N**

Fig. 5.125 – BSE image of the worn surface of αβ alloy at anodic potential at 2N.
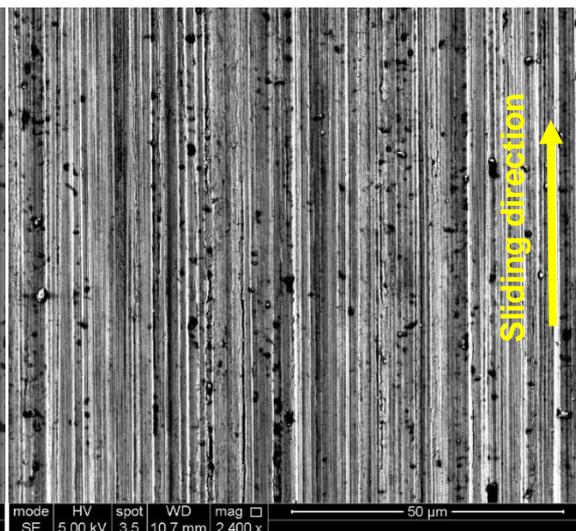
Fig. 5.126 - SE image of the worn surface of αβ alloy at anodic potential at 2N.
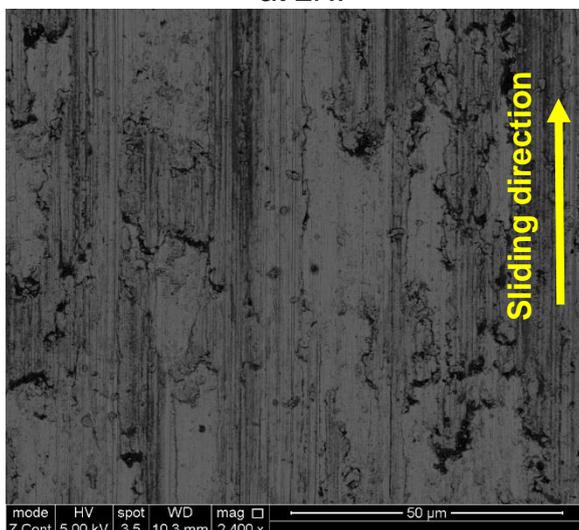
Fig. 5.127 – BSE image of the worn surface of αβ alloy at OCP at 2N.
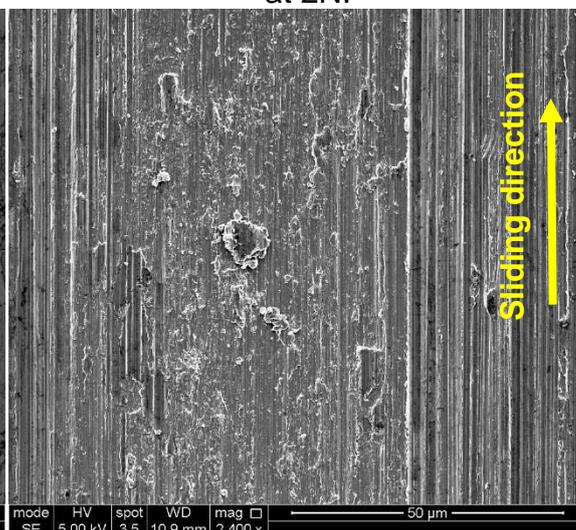
Fig. 5.128 – SE image of the worn surface of αβ alloy at OCP at 2N.
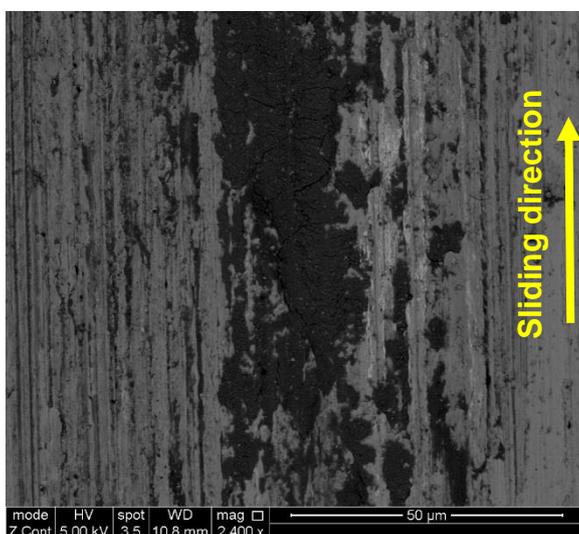
Fig. 5.129 – BSE image of the worn surface of αβ alloy at cathodic potential at 2N.
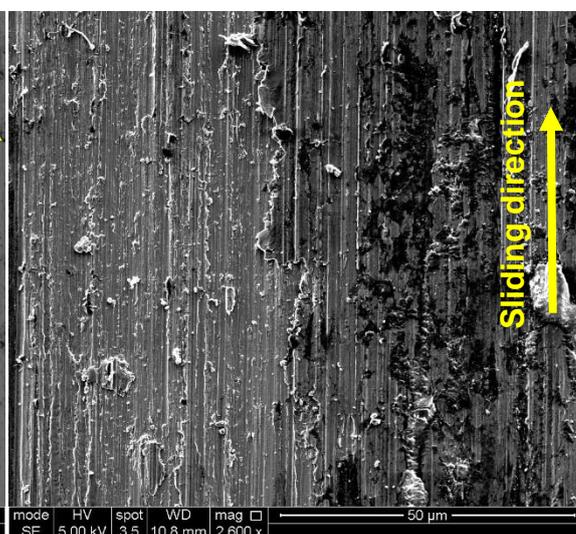
Fig. 5.130 – SE image of the worn surface of αβ alloy at cathodic potential at 2N.

153
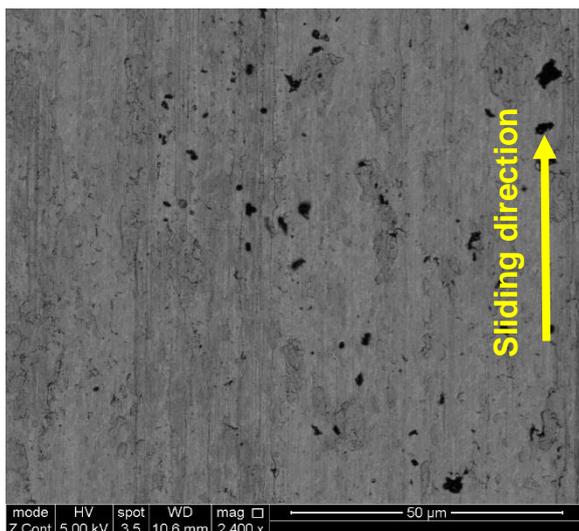
- **Nβ alloy at 1N**

Fig. 5.131 – BSE image of the worn surface of Nβ alloy at anodic potential at 1N.
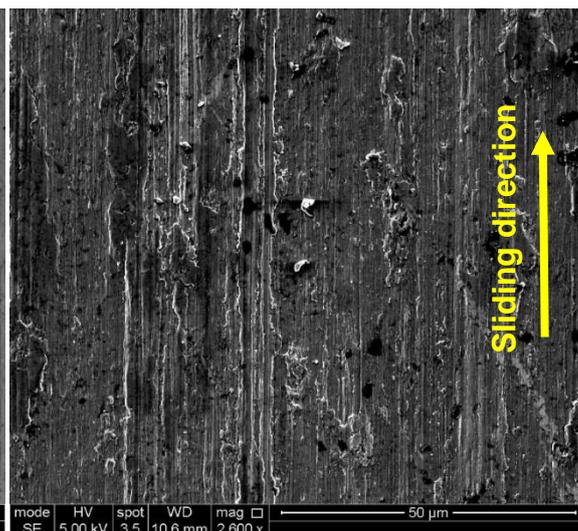
Fig. 5.132 - SE image of the worn surface of Nβ alloy at anodic potential at 1N.
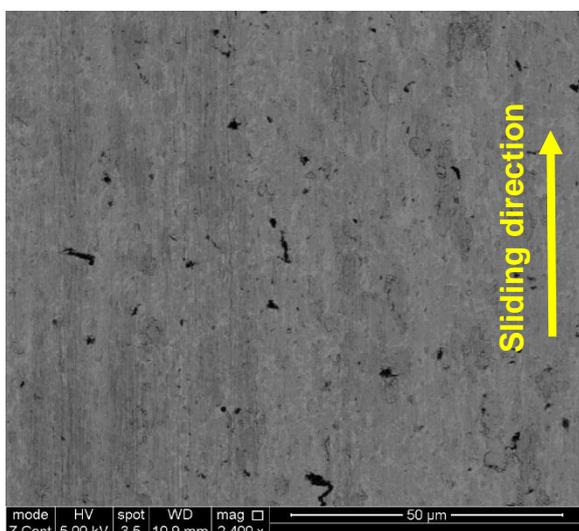
Fig. 5.133 – BSE image of the worn surface of Nβ alloy at OCP at 1N.
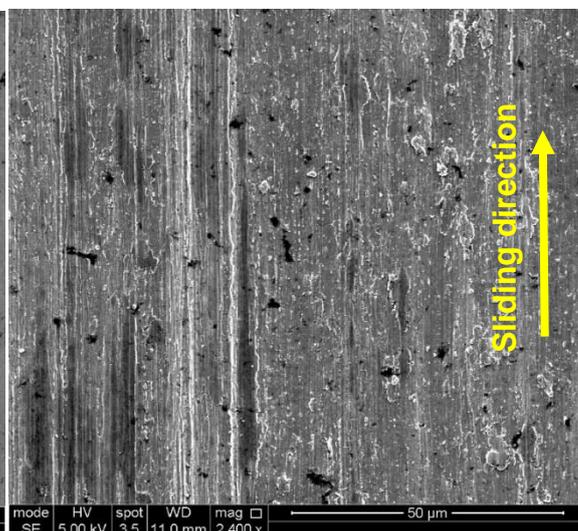
Fig. 5.134 – SE image of the worn surface of Nβ alloy at OCP at 1N.
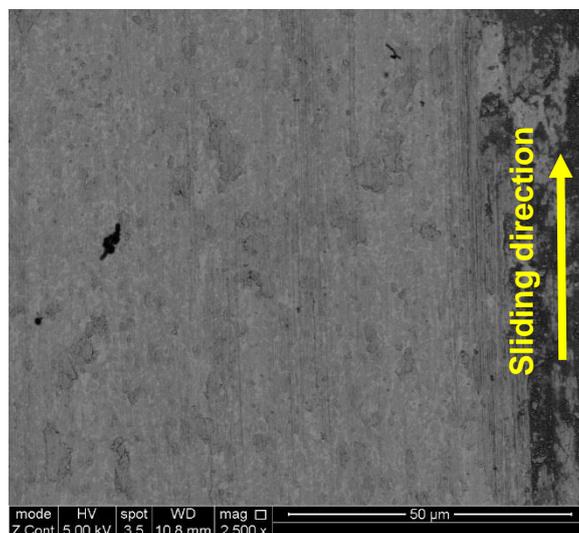
Fig. 5.135– BSE image of the worn surface of Nβ alloy at cathodic potential at 1N.
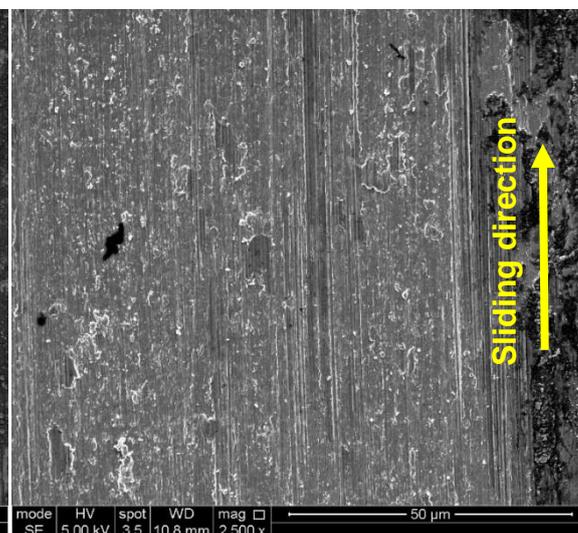
Fig. 5.136 – SE image of the worn surface of Nβ alloy at cathodic potential at 1N.

154
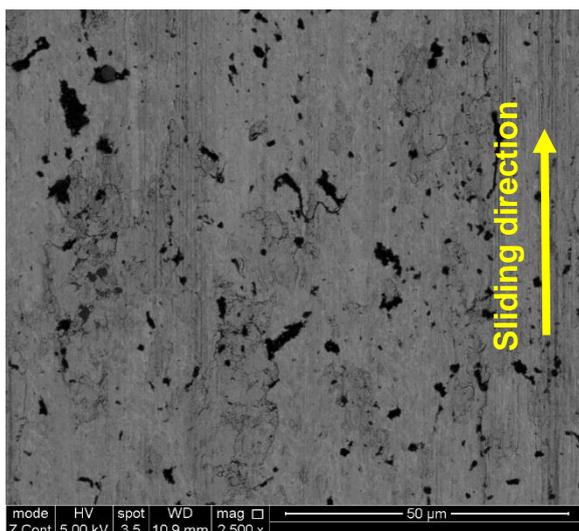
- **Nβ alloy at 2N**

Fig. 5.137 – BSE image of the worn surface of Nβ alloy at anodic potential at 2N.
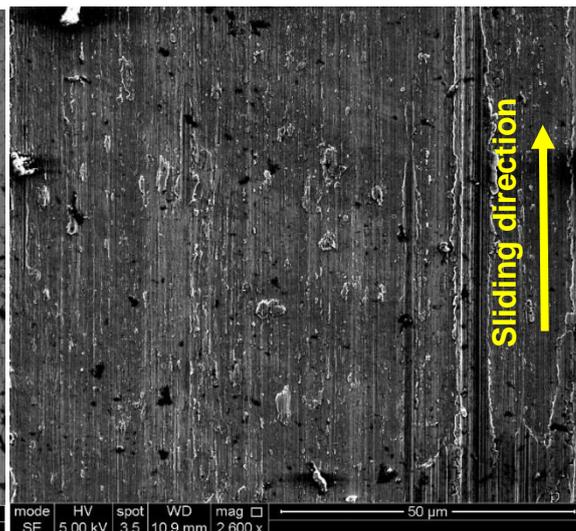
Fig. 5.138 - SE image of the worn surface of Nβ alloy at anodic potential at 2N.
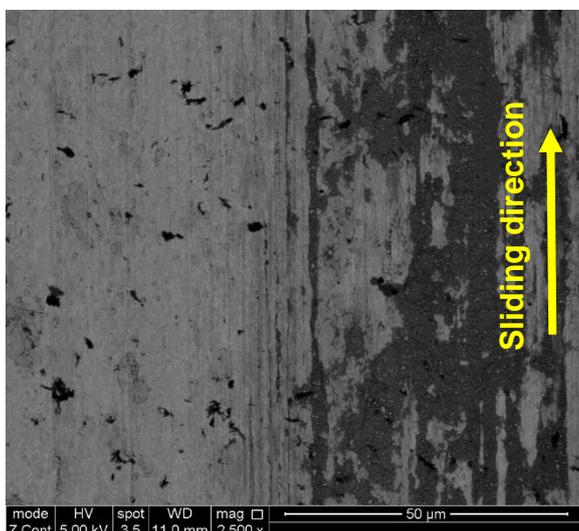
Fig. 5.139 – BSE image of the worn surface of Nβ alloy at OCP at 2N.
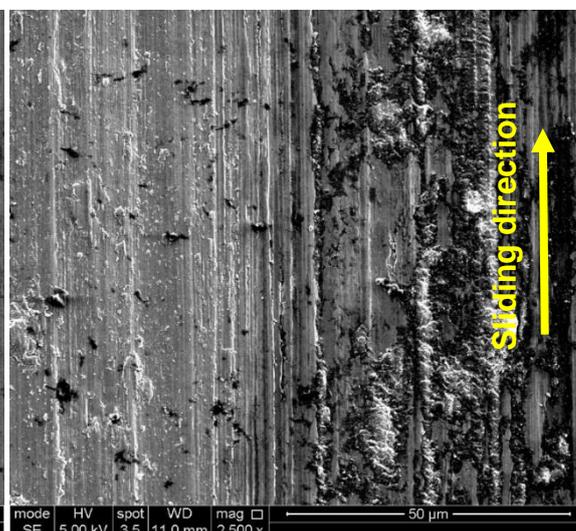
Fig. 5.140 – SE image of the worn surface of Nβ alloy at OCP at 2N.
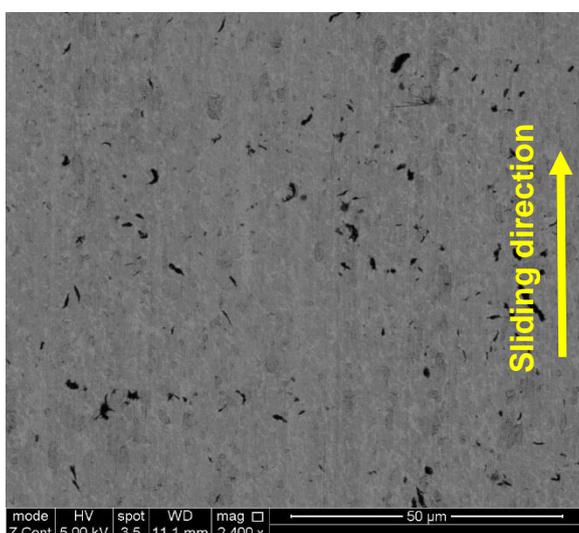
Fig. 5.141 – BSE image of the worn surface of Nβ alloy at cathodic potential at 2N.
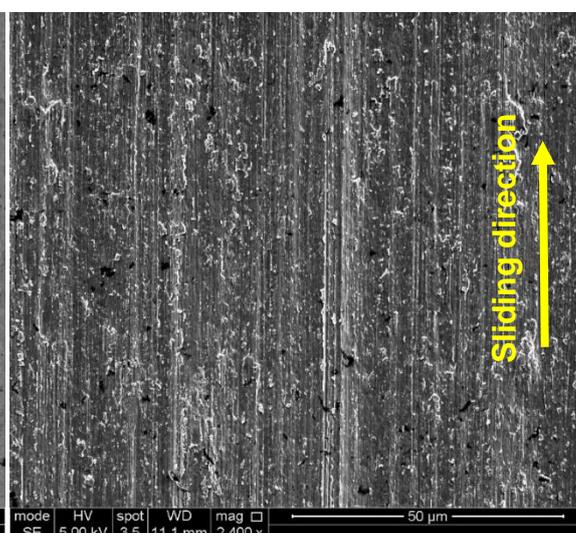
Fig. 5.142 – SE image of the worn surface of Nβ alloy at cathodic potential at 2N.

155
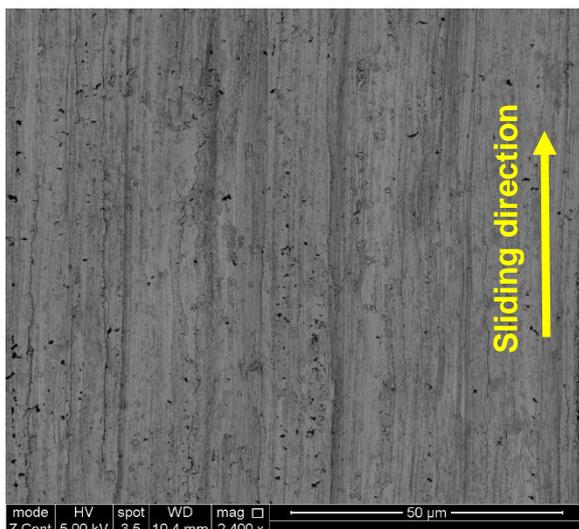
- **β alloy at 1N**

Fig. 5.143 – BSE image of the worn surface of β alloy at anodic potential at 1N.
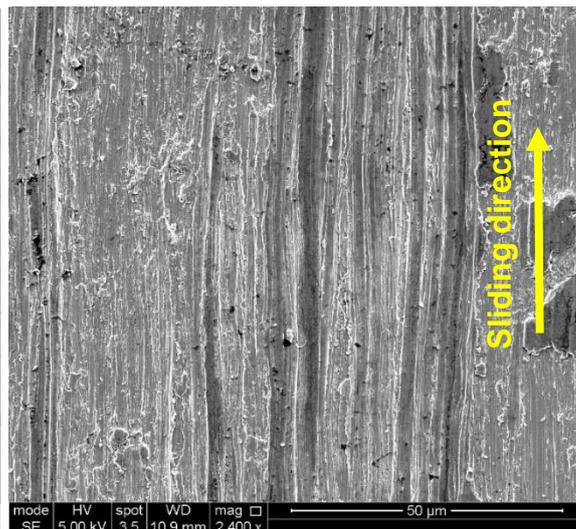
Fig. 5.144 - SE image of the worn surface of β alloy at anodic potential at 1N.
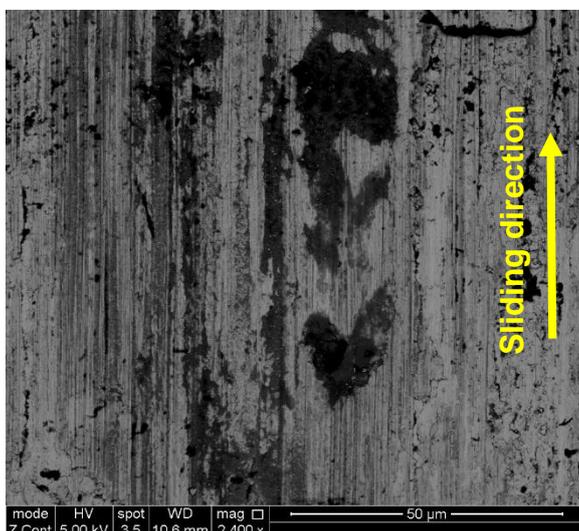
Fig. 5.145 – BSE image of the worn surface of β alloy at OCP at 1N.
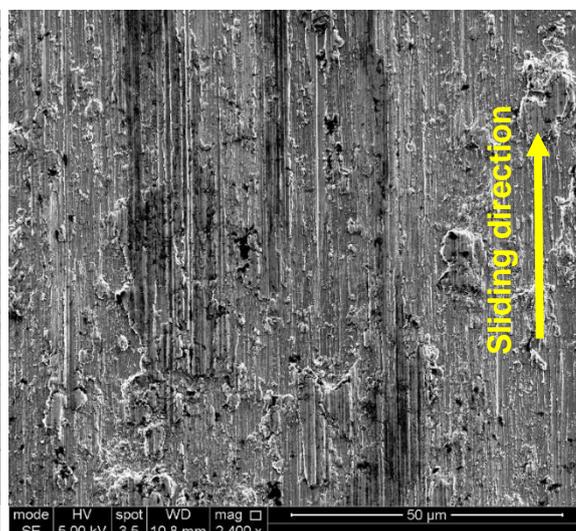
Fig. 5.146 – SE image of the worn surface of β alloy at OCP at 1N.
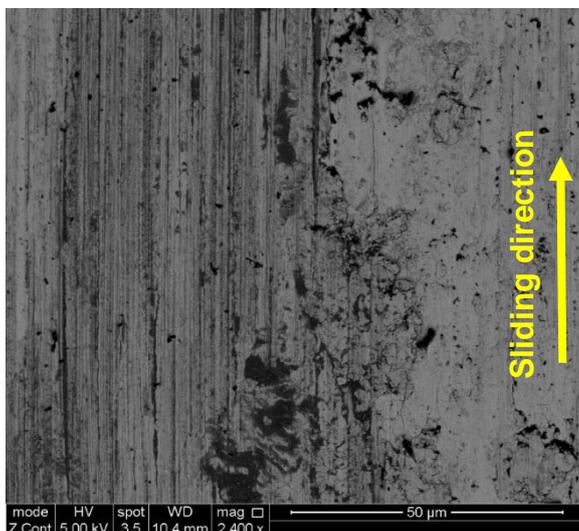
Fig. 5.147 – BSE image of the worn surface of β alloy at cathodic potential at 1N.
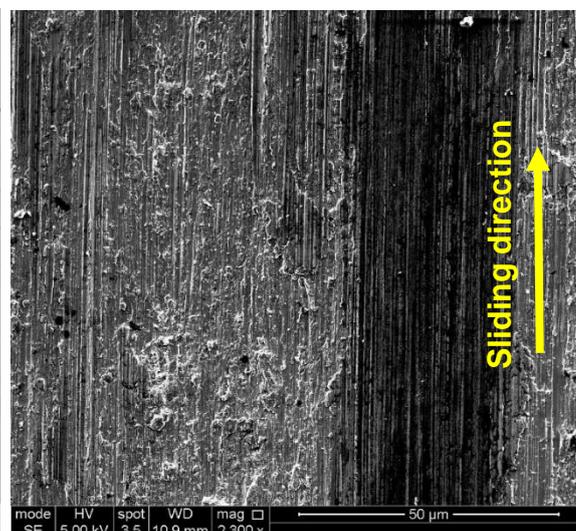
Fig. 5.148 – SE image of the worn surface of β alloy at cathodic potential at 1N.
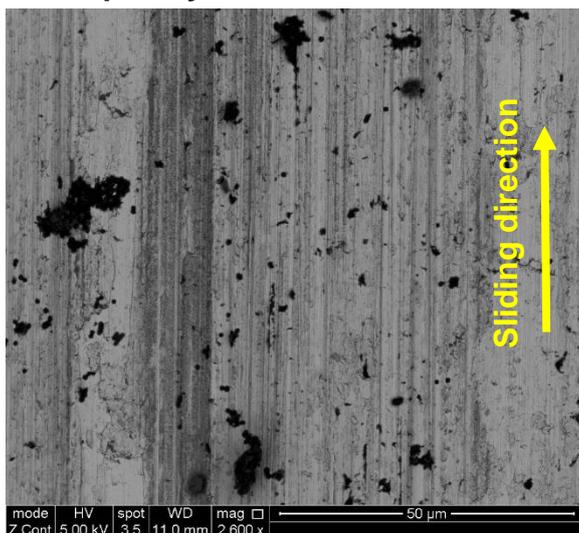
- **β alloy at 2N**

Fig. 5.149 – BSE image of the worn surface of β alloy at anodic potential at 2N.
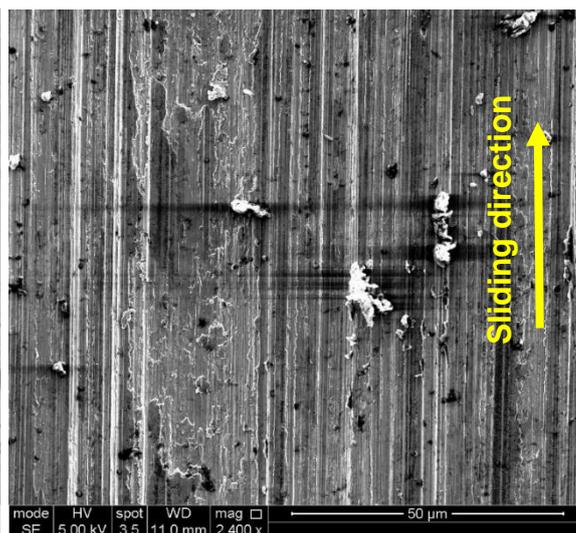
Fig. 5.150 - SE image of the worn surface of β alloy at anodic potential at 2N.
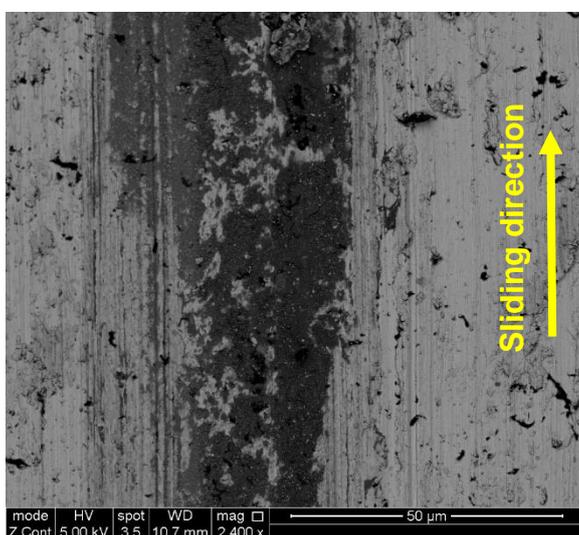
Fig. 5.151 – BSE image of the worn surface of β alloy at OCP at 2N.
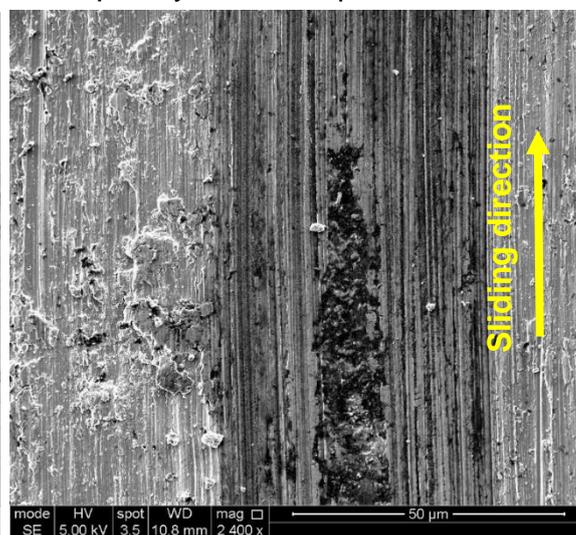
Fig. 5.152 – SE image of the worn surface of β alloy at OCP at 2N.
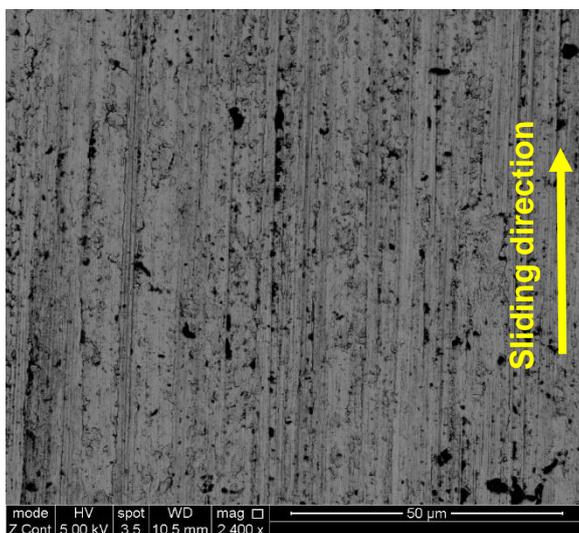
Fig. 5.153 – BSE image of the worn surface of β alloy at cathodic potential at 2N.
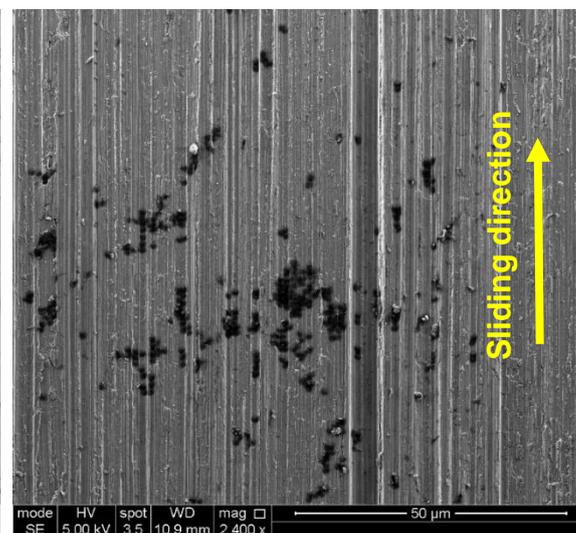
Fig. 5.154– SE image of the worn surface of β alloy at cathodic potential at 2N.
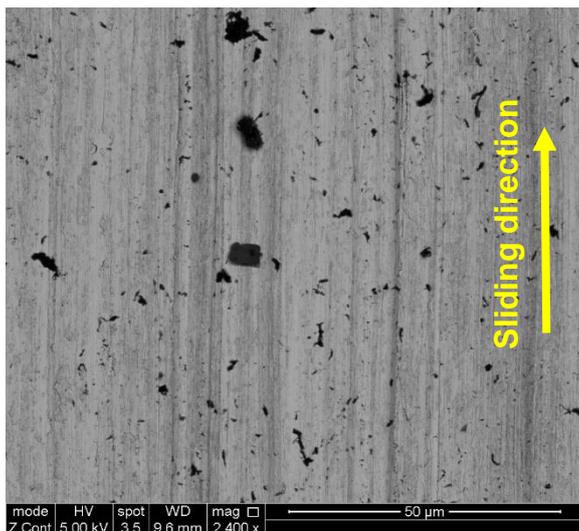
- **βω alloy at 1N**

Fig. 5.155 – BSE image of the worn surface of βω alloy at anodic potential at 1N.
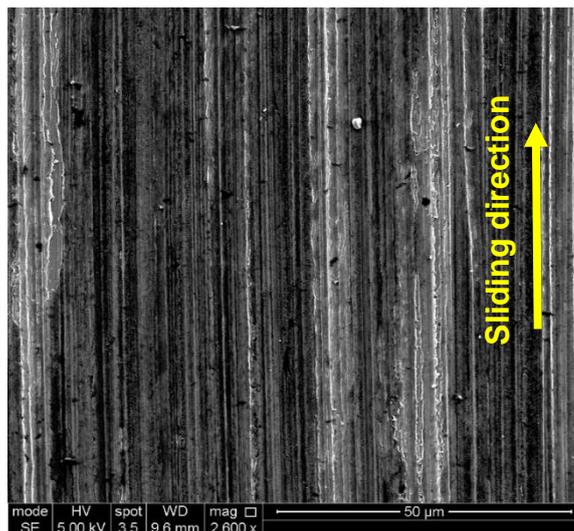
Fig. 5.156 - SE image of the worn surface of βω alloy at anodic potential at 1N.
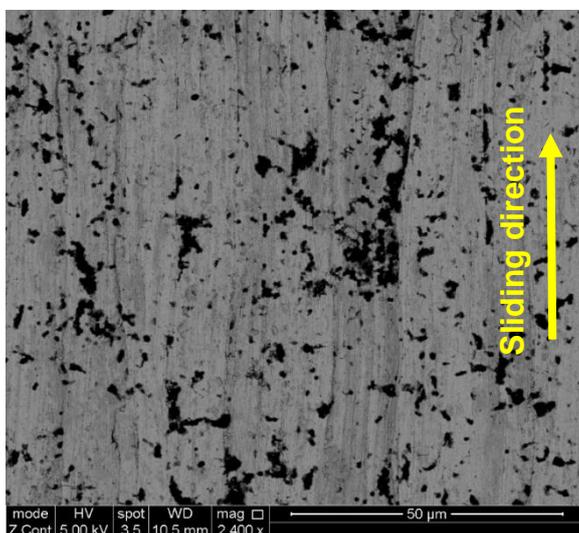
Fig. 5.157 – BSE image of the worn surface of βω alloy at OCP at 1N.
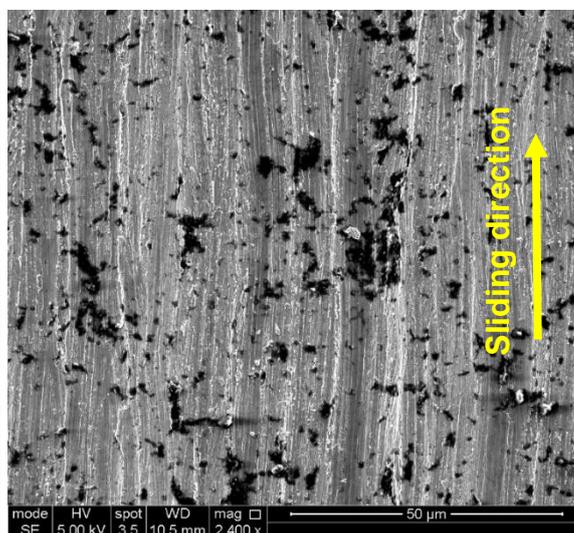
Fig. 5.158 – SE image of the worn surface of βω alloy at OCP at 1N.
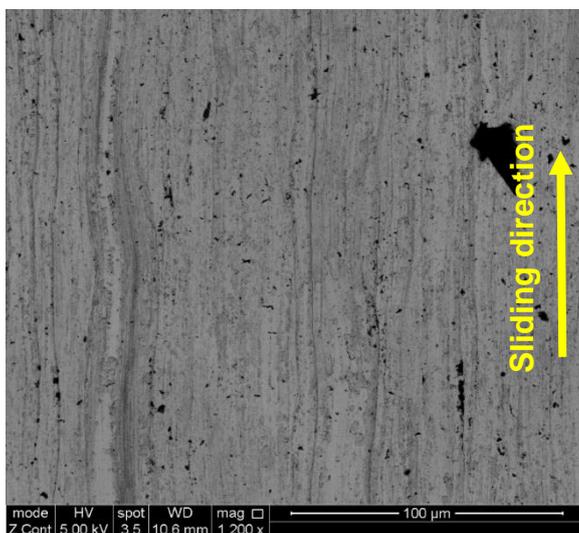
Fig. 5.159 – BSE image of the worn surface of βω alloy at cathodic potential at 1N.
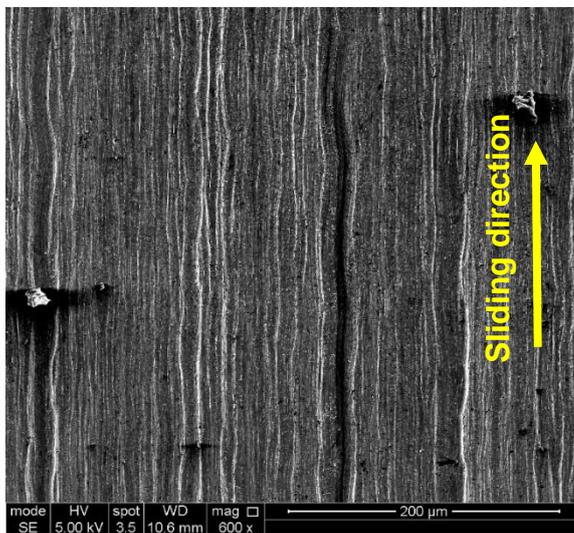
Fig. 5.160 – SE image of the worn surface of βω alloy at cathodic potential at 1N.
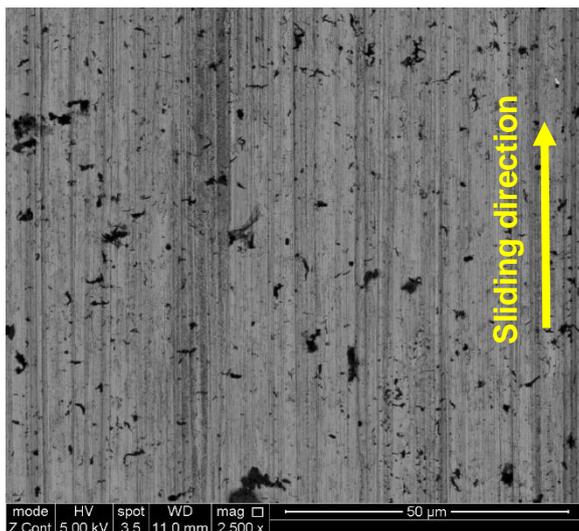
- **βω alloy at 2N**

Fig. 5.161 – BSE image of the worn surface of βω alloy at anodic potential at 2N.
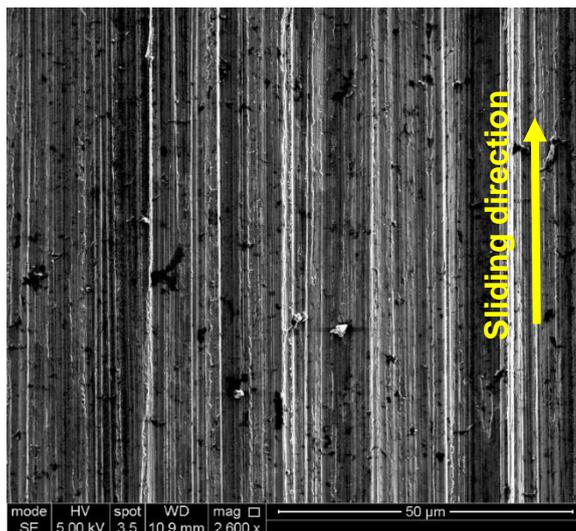
Fig. 5.162 - SE image of the worn surface of βω alloy at anodic potential at 2N.
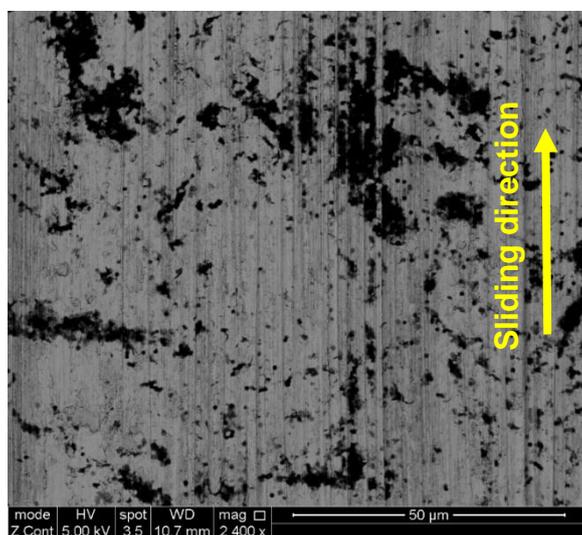
Fig. 5.163 – BSE image of the worn surface of βω alloy at OCP at 2N.
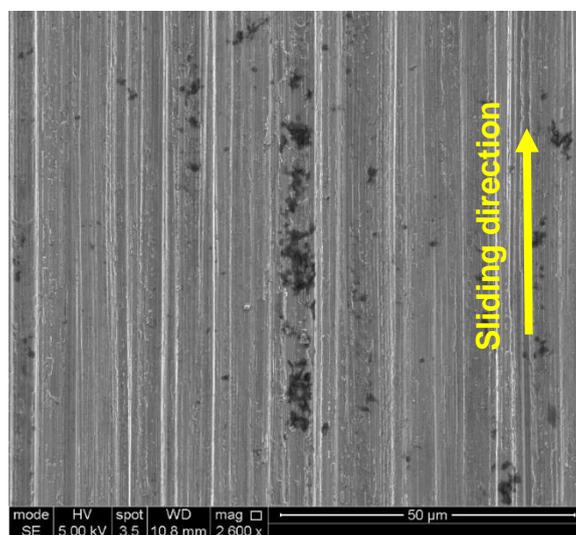
Fig. 5.164 – SE image of the worn surface of βω alloy at OCP at 2N.
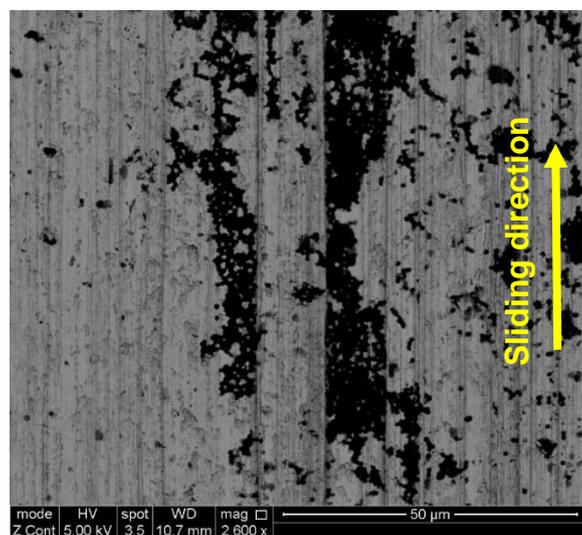
Fig. 5.165 – BSE image of the worn surface of βω alloy at cathodic potential at 2N.
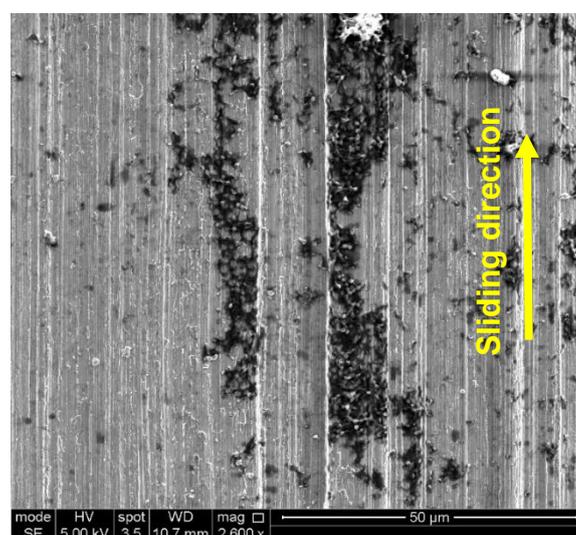
Fig. 5.166 – SE image of the worn surface of βω alloy at cathodic potential at 2N.

5.2.10 Presence of tribolayer

Raman spectra with Gaussian peak fitting, presented in Figs. 5.167 to 5.172, for 1N and 2N have peaks at 1332 cm^{-1} and 1545 cm^{-1}, similar to that observed at 0.5N. These peaks are related to graphite and diamond. These peaks arise from disordered graphite or disorder mode (D band) and single crystalline graphite or tangential stretch mode (G band), which relates to the presence of Carbon, with all alloys tested having these peaks.

In the D band the bond-angle disorder in the sp^2 graphite-like microdomains, induced by linking with sp^3 atoms, as well as the finite crystalline sizes of sp^2 microdomains, while the G band is ascribed to sp^2 trigonal bonding related to the graphite phase [291]. In this sense, the results from the Raman spectrum show that the worn area was composed of sp^2-carbon and sp^3-carbon.

In general, the intensity ratio of D and G peaks is related to the relative content of sp^2 and sp^3 bonds. The sp^2 bond could effectively reduce the shearing resistance on the contact surface and the sp^3 bond with diamond-structure could enhance the hardness of material.

The G peak was higher in all conditions, except for Nβ alloy at 1N and at anodic potential (159.34) and at 2N at anodic (156.57) and cathodic (123.42) potentials. At anodic potential the intensity of the peaks was higher with the highest intensity observed on the αβ alloy at this potential for G band (145.42 and 134.04 for 1N and 2N). The lowest intensity was seen on αβ at OCP (D band: 46.63) at 1N and the highest intensity observed was at anodic potential at 1N and Nβ alloy (D band: 159.34). The presence of high intensity G peak may have influenced wear due to the lubricating properties.

These peaks confirm the presence of tribolayer being generated during the motion of the surfaces in contact. The tribolayer is rich in protein and it may be beneficial for the tribocorrosion process which is formed by the interaction of ions released by the passive film and proteins. However, published data on this it is contradictory.

The same number of measurements were taken from these samples as 0.5N (5 measurements). Not all of them registered the presence of a tribolayer; the results shown here are only from where C was detected. This indicates the tribolayer was present in all alloys, but it was not continuous and was not uniform across the whole surface. At 0.5N the intensity of the peaks was higher but for

1N and 2N this trend was not observed. However, the αβ alloy showed the most intense peaks at cathodic potential at 1N, similar to 0.5N. This alloy shows the lowest material loss at 1N and 2N in all electrochemical conditions.
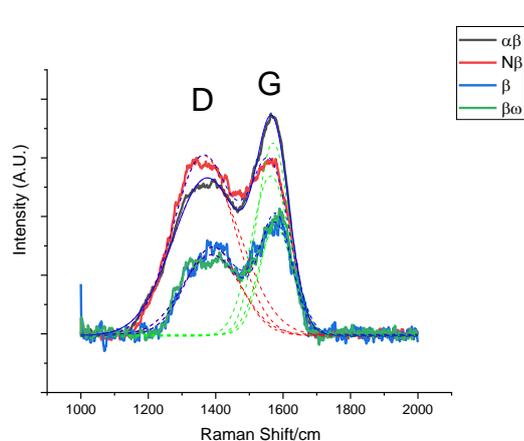
Fig 5.167 – Raman spectroscopy of worn surface of all alloys at cathodic potential at 1N.
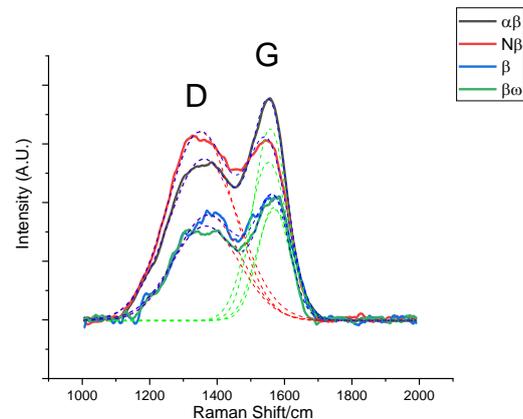
Fig 5.168 – Raman spectroscopy of worn surface of all alloys at cathodic potential at 2N.
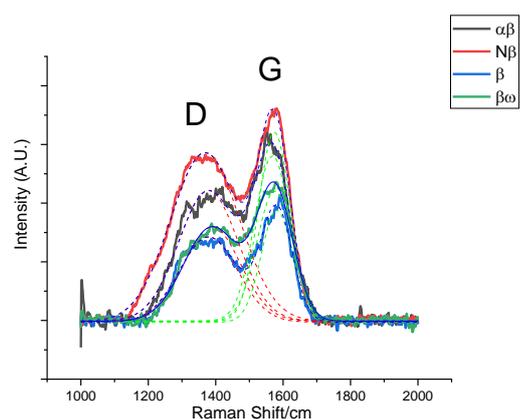
Fig 5.169 – Raman spectroscopy of worn surface of all alloys at OCP at 1N.
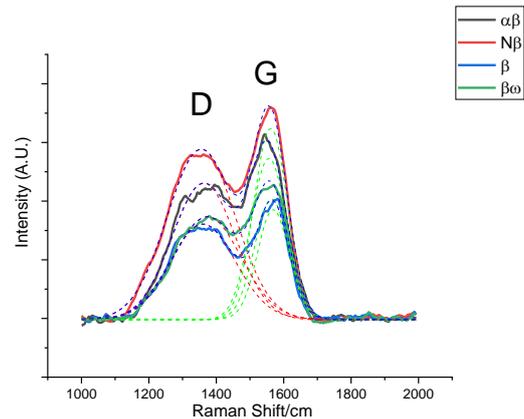
Fig 5.170 – Raman spectroscopy of worn surface of all alloys at OCP at 2N.
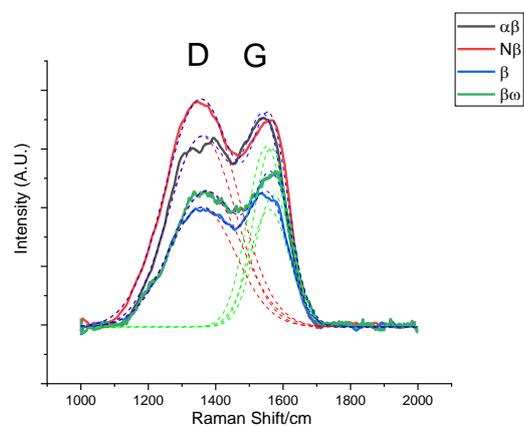
Fig 5.171 – Raman spectroscopy of worn surface of all alloys at anodic potential at 1N.
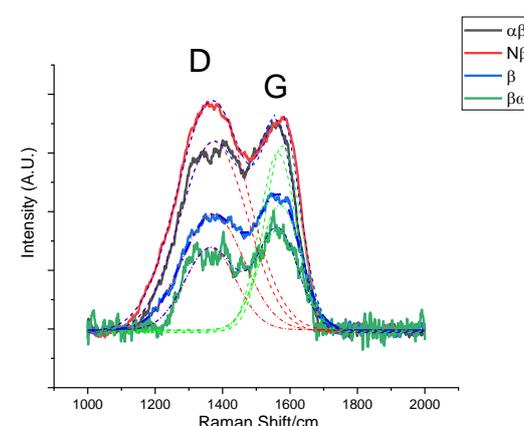
Fig 5.172 – Raman spectroscopy of worn surface of all alloys at anodic potential at 2N.

5.2.11 Characterization of subsurface at anodic potential

The subsurface of the alloys tested at 2N with an anodic potential were analysed by TEM from FIB specimens to characterize the tribolayer and surface deformation. This potential was chosen since it showed the lowest material loss.

Figs. 5.173 to 5.175 show TEM and STEM cross section images, EDX spectra and diffraction pattern from the αβ alloy. Figs. 5.176 to 5.178 show TEM and STEM cross section images, EDX spectra and diffraction patterns from the Nβ alloy. Figs. 5.179 to 5.181 show TEM and STEM cross section images, EDX spectra and diffraction patterns from the β alloy. Figs. 5.182 to 5.184 show TEM and STEM cross section images, EDX spectra and diffraction patterns from the αβ alloy. In all cases the worn surface was protected by Pt deposition, which also served to label the original worn surface.

Surface deformation was observed with flow of material following the sliding direction for all cases. For the αβ alloy, Fig. 5.173, the surface strained layer was around 200nm thick and contained a fine nanocrystalline layer. EDX showed the presence of a thin oxide layer, Fig. 5.174.   Diffraction of the surface strained layer suggested it was predominantly β phase, Fig. 5.175.

The Nβ alloy exhibited a thick (300nm) relatively uniform nanocrystalline surface layer in comparison to the αβ alloy, Fig. 5.176. Some oxide was present on the surface, but impacted wear debris was clearly an oxide, Fig. 5.177. Electron diffraction suggested the surface was predominantly β phase, Fig. 5.178.

The β alloy exhibited a variable nanocrystalline layer at the surface, with the depth ranging from about 100 to 600nm, Fig. 5.179. There was also evidence of surface wear debris, which was nanocrystalline in structure. EDX again showed an oxide layer on the surface and that the wear debris had become oxidised, Fig. 5.180. Electron diffraction of the surface region indicated that it had remained β phase, Fig. 5.181.

The surface of the the βω alloy was largely featureless, Fig. 5.182. Again, a surface oxide layer was present, Fig. 5.183. Electron diffraction indicated that the surface was predominantly β phase, but some faint circular diffraction suggested some amorphous phase might be present, Fig. 5.184.
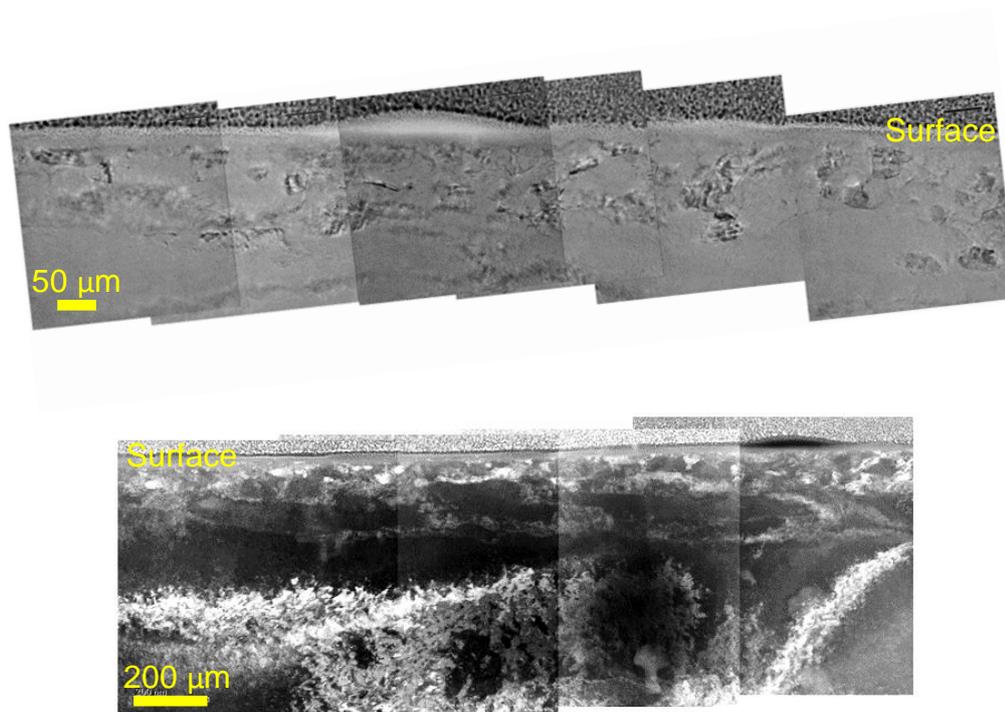
Fig. 5.173 – TEM and STEM cross section images of worn surface of the αβ alloy.
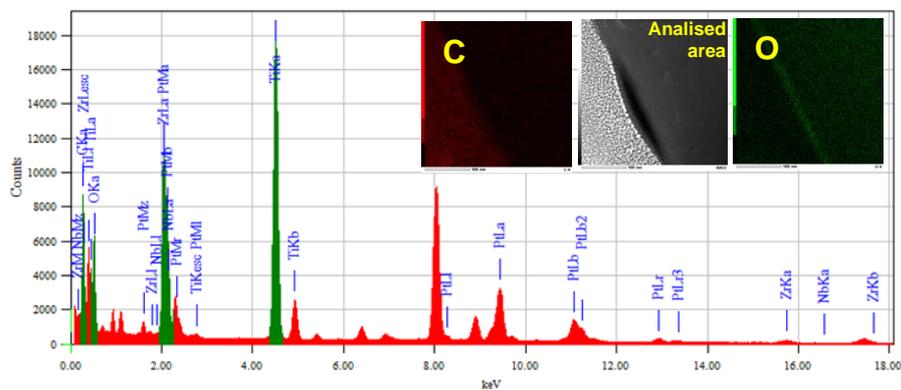
Fig. 5.174 – EDX spectra of cross section inside worn surface of the αβ alloy.
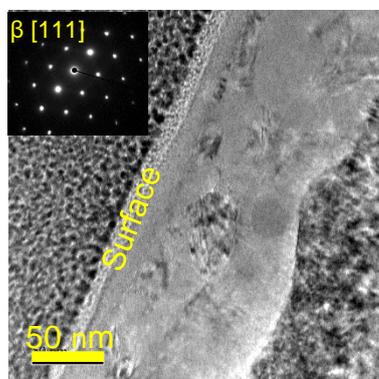
Fig. 5. 175 – Diffraction pattern of cross section inside worn surface of the αβ alloy.
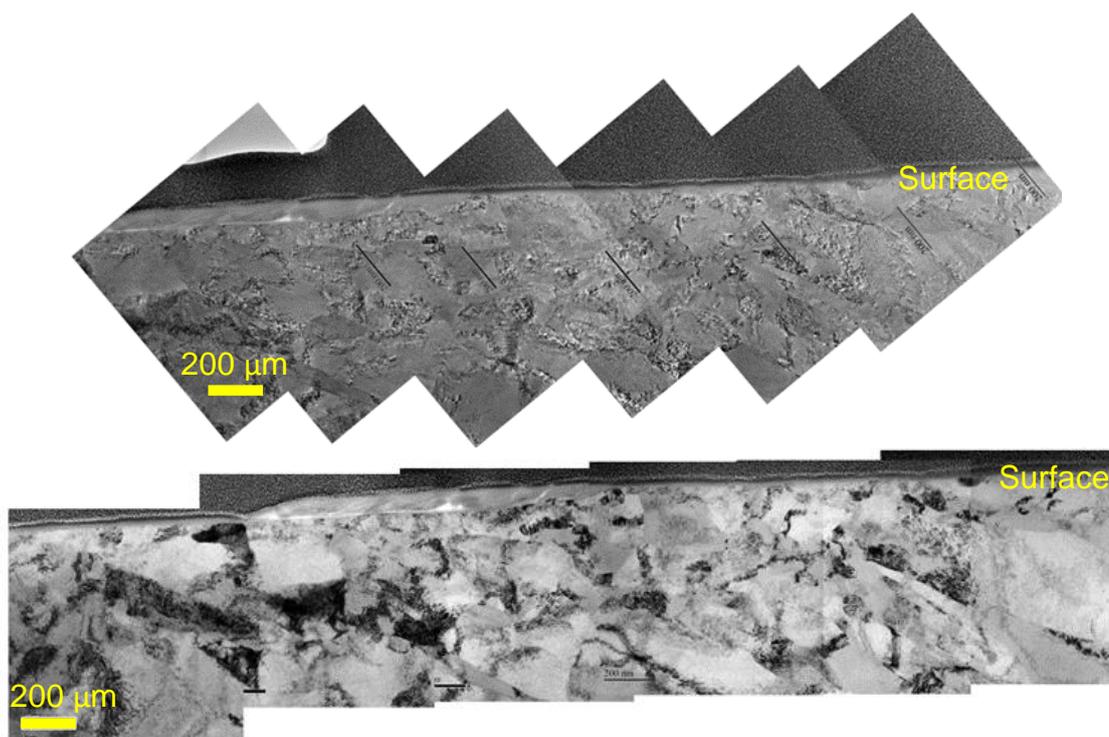
Fig. 5.176 – TEM and STEM cross section images of worn surface of the Nβ alloy.
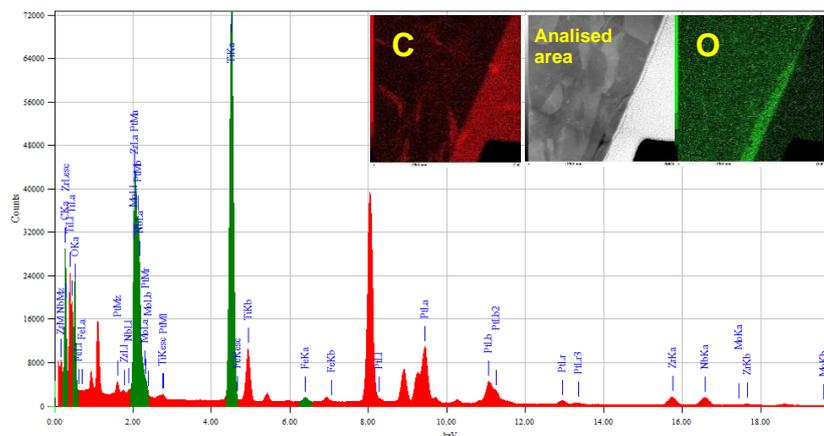
Fig. 5.177 – EDX spectra of cross section inside worn surface of the Nβ alloy.
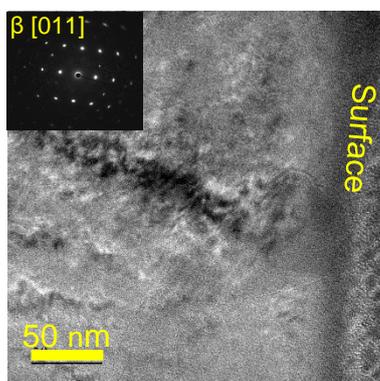
Fig. 5. 178 – Diffraction pattern of cross section inside worn surface of the Nβ alloy.

Fig. 5.179 – TEM and STEM cross section images of worn surface of the β alloy.

Fig. 5.180 – EDX spectra of cross section inside worn surface of the β alloy.

Fig. 5. 181 – Diffraction pattern of cross section inside worn surface of the β alloy.
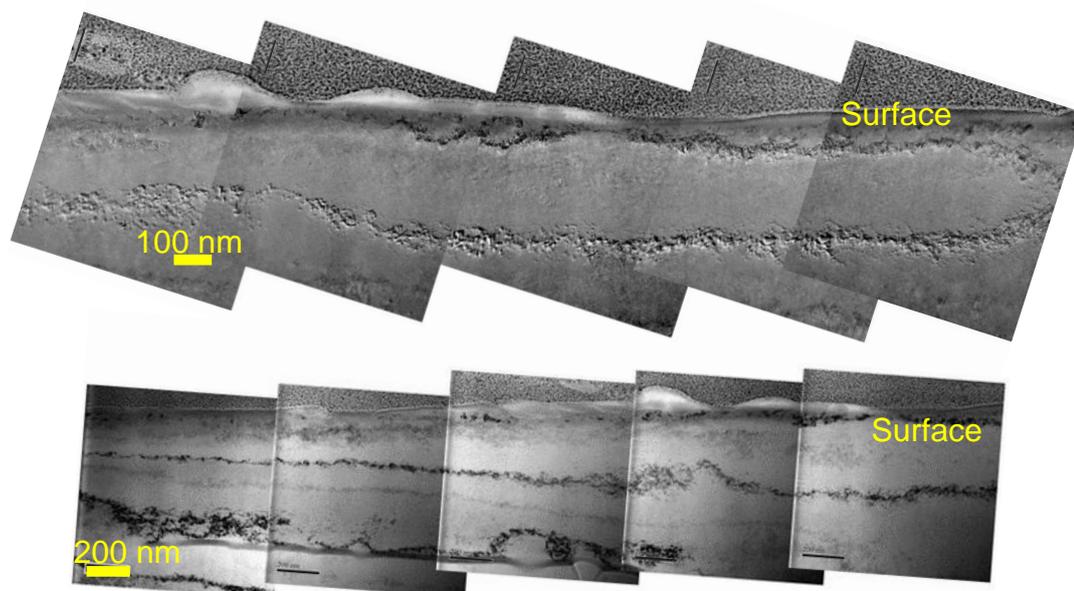
Fig. 5.182– TEM and STEM cross section images of worn surface of the βω alloy.
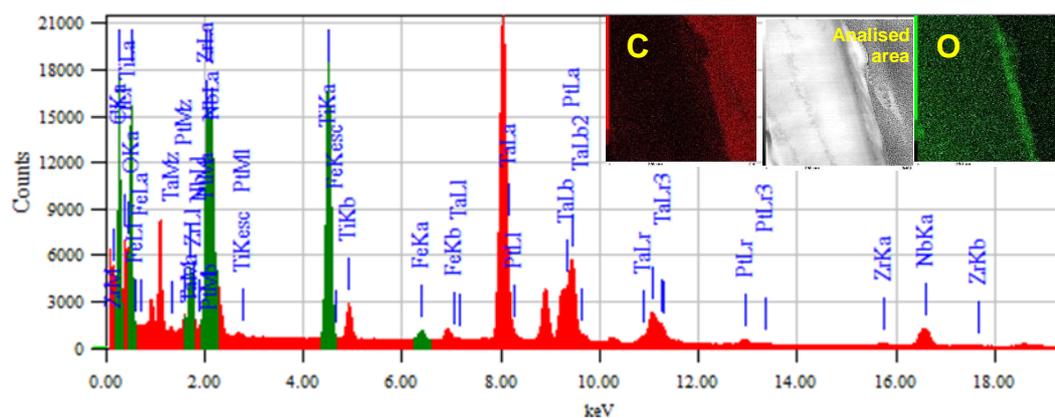
Fig. 5.183 – EDX spectra of cross section inside worn surface of the βω alloy.
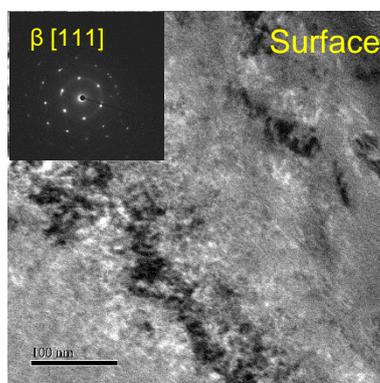
Fig. 5. 184 – Diffraction pattern of cross section inside worn surface of the βω alloy.

5.2.12 Summary

In this chapter, the tribocorrosion behaviour of αβ, Nβ, β and βω alloys were analysed. Some major points can be summarized:

- All alloys become more active when subjected to mechanical wear, characterized by the drop of the polarization curves to a more negative potential and higher current.
- COF evolution curves show a running in and steady state for all alloys, except for Nβ alloy.
- The cathodic current drops during the wear test but rose again when the sliding movement stopped for all conditions.
- A cathodic drop is observed on potential when wear test starts and an anodic shift is observed on potential when wear test stops. However, the potential reaches lower values than before the wear test.
- Anodic current increases during the wear test and drops when it is stopped.
- Charge transfer occurs at OCP due to the removal of the passive layer which acts as a barrier of ion movement.
- At anodic potential, charge transfer occurs due to the continuous metal ion release due to the tribological contacts and the electrochemical driving force. The charge transfer leads to a layer formation due to the reaction of the released ions and bovine serum components, which act as charge transfer barrier and solid lubricant.
- COF, wear track volume and specific wear rate increase with normal load and are lower at anodic potential and higher at cathodic potential. Thus, corrosion played an important role and affected wear extensively.
- Roughness is higher at anodic potential and lower at cathodic potential.
- The αβ alloy shows the lowest COF, wear track volume and specific wear rate.
- The worn surfaces are characterized by wide grooves, scratches, isolated debris and there is no difference on the worn surfaces when potential, load and microstructure is changed. Cracks were not observed.
- An organic film is detected on the worn surfaces in all electrochemical and normal load conditions.

- Nanohardness and reduced elastic modulus are higher for all worn surfaces with a high degree of scatter in the results.

- Channelling contrast images identified subsurface deformation in all alloys, except β alloy, but TEM results show the presence of α'' and ω on its subsurface.

- The presence of α, α'', β and ω phases was observed in worn subsurface.

- Analysis of the subsurface of the alloys tested at 2N at anodic potential show material flowing on the sliding direction, the presence of nanocrystalline layer, the presence of a thin oxide layer and presence of β phase.

Chapter 6 – Discussion

6.1 Introduction

It is possible to conclude from the literature review, chapter 2, that the tribocorrosion mechanisms and phenomena of Titanium alloys are not fully understood and a contribution in this topic is needed.

This discussion chapter brings together the results presented in the last chapter: the tribocorrosion behaviour at cathodic potential, OCP and anodic potential, the wear track morphology and properties, the wear rate, the presence of a tribofilm, surface and subsurface characterization and the effect of normal load on these properties. This summarises the main findings and discusses their relevance in relation to the key contribution made by this thesis.

Firstly the effect of electrochemical condition is analysed, then the effect of normal load, the microstructure and chemical composition effect and finally the interaction between wear and corrosion.

6.2 Effect of electrochemical condition

All alloys in this study present a qualitatively similar polarization behaviour, although the values differed, where αβ alloy is the noblest alloy. There are differences among polarization curves, such as the corrosion current and corrosion potential, which defines the best corrosion resistance. These alloys present good corrosion resistance, which is due to the presence of alloying elements such as Nb, Zr, Ta and Mo. These alloying elements form stable oxides on Titanium alloys such as MoO_3, ZrO_2, Ta_2O_3 and Nb_2O_5 [156]. Gnanavel [292] studied the corrosion behaviour of Ti64 and Ti-13Nb-13Zr in Hank's solution at 37°C and compared these alloys with coated surfaces. The results show Ti-13Nb-13Zr has a better corrosion resistance. In the study of More [24], Ti–29Nb–13Ta–4.6Zr alloy showed a better corrosion resistance than Ti-13Nb-13Zr alloy and Ti64. Also, Wang [293] compared the corrosion behaviour Ti64 in different electrolytes and show that in bovine serum Ti64 showed the noblest behaviour due to the presence of protein Contu [294] found that the higher concentration of serum, the higher corrosion resistance of Ti alloys.

The orthopaedic implants suffer of local removal of the protective layer and this process leads to a polarization of the surface depending on the extent of scratching. These alloys become more active when subjected to rubbing due to the effect of wear on corrosion, i.e. the capability of repassivation of these alloys is affected by friction. It shows that rubbing plays an important role on corrosion behaviour of these alloys. The depassivated areas (worn areas) react with the passivated areas and form a galvanic couple leading to an increase of metal dissolution and material loss [232].

The rubbed areas experience an increase in metal oxidation rate because of the loss of passivity. Therefore, their theoretical corrosion potential is expected to move towards more cathodic values, Fig. 6.1. Rubbing affects the metal anodic reaction, which increases the current and decreases the potential [232].

Huang [295] studied the effect of wear on potentiodynamical behaviour of Ti–25Nb–3Mo–3Zr–2Sn Alloy in Simulated Physiological Solution and observed that this alloy became more active when rubbing.

Titanium alloys corrode easily under the synergy of corrosion and wear, and the passive film is easily damaged which removes the protection for the alloy and accelerates the corrosion rate. This suggests that wear enhanced the thermodynamic corrosion potential.
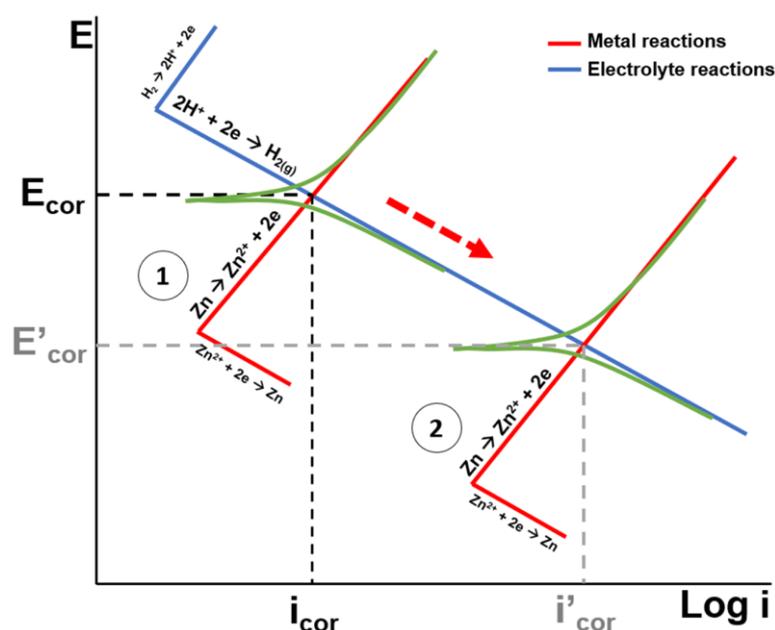
Fig. 6.1 – Effect of wear on potentiodynamical test (adapted) [232].

All alloys are expected to have a passive film on their surfaces and the composition of each film relies on the composition of the respective alloys. High COF is observed when the wear test starts and the contact between these alloys with the counterpart, alumina, leads to damage or removal of the passive film. Steady state is reached when a tribofilm is formed and repassivation of the surface occurs. The COF does depend on the potential applied, being lower at anodic potential and higher at cathodic potential. This is explained due to the formation of a thicker tribolayer at anodic potential, which changes the contact mechanism and acts as lubricant. Wear debris were generated, possibly removed as oxide, and the peaks observed on the COF evolution are a result of debris entrapped between the surfaces.

Wimmer [296] studied the effect of contact load on tribofilm formation on CoCr alloys and concluded that the tribofilm formation was beneficial in reducing wear because it is linked to the wear rate plateau observed when normal load increased.

The reason for the higher COF at the beginning of the test is because a tangential force is required to start the motion between the two bodies in contact. It occurs because, before starting the motion, a large stress relaxation at the junctions may occur due to increase in temperature, which leads to an increase of the real area of contact [213]. In addition, the wear rate is very high because the surfaces in contact are unlikely to be nonconformal, and so the local Herztian contact pressure is high leading to high wear rates. As the contact becomes more conformal through wear, the Hertzian contact stress decreases and the wear rate decreases. The wear mechanism may change at this stage.

At cathodic potential the current drops after rubbing starts due to proton reduction. This is caused by mechanical action and the enhancement of the cathodic reaction rate caused by the stirring of the electrolyte in the tribocell which affects the kinetics of mass transport. The current increases after rubbing stops, due to the stirring effect of the alumina counterpart, which enhances mass transport and the mechanical removal of the passive film, which is known to inhibit the cathodic reaction [231]. Friction is highly dependent on the potential applied due to the metal sensitivity to hydrogen embrittlement, that is why the synergism standard fixes these potential values for tests.

A cathodic drop is observed when rubbing starts due to the removal of the passive film and exposure of bare metal to the electrolyte. A potential difference

is stabilised between the worn (anodic area) and unworn (cathodic area) areas and it reflects the galvanic coupling of these two distinct surfaces states. This enhances the active dissolution of the metal and modifies the potential of the passive area [297].

All alloys show a constant value of OCP with slight fluctuations, which is attributed to a dynamic equilibrium achieved between mechanical depassivation (passive film removed) and electrochemical passivation (recovery mechanism) [229].

The parabolic anodic shift (increase) to values lower than before rubbing that was observed at all applied loads is due to the modified surface, which suggests that all alloys show the ability to regrow the passive film but not instantaneously. Finally, the potential evolution varies for each alloy and it may suggest that microstructure influences it. Again, the COF changes with load and electrochemical condition.

Zavieh [298] studied the effect of friction on tribocorrosion behaviour of stainless steel. It was found that at OCP, the potential drops when rubbing starts suggesting high depassivation rate and galvanic coupling between the unworn (passivated) area outside the wear track and the fresh (depassivated) area due to rubbing of the counterpart. This is a typical behaviour of passive alloys.

At anodic potential, the current shifts to more positive values when rubbing starts due to the oxidation of the exposed bare material to the electrolyte with progressive wear. It indicates that wear enhances corrosion rate. This change is due to the removal of the passive film and exposure of bare and active material to the media in the contact region. It leads to a reaction between the active exposed surface and the electrolyte accelerating the electrochemical reaction and anodic metal oxidation. The initial current shift increases with normal load. All alloys present a stable current and the isolated peaks represent a local repassivation that rapidly depassivated. This is due to the repassivation of all alloys during rubbing. This steady state indicates that all alloys have the ability to regain they passivation even under sliding at anodic potential and depassivation has ceased. Overall, these alloys experience wear accelerated corrosion when the passive film is damaged, confirmed by the synergistic approach. This indicates that the tribofilm is formed more effectivity at anodic potential, it acts as a lubricant and changes the contact mechanism reducing friction.

Guadalupe [299] applied anodic polarization on CoCr alloys with different carbide content and observed that the wear test at anodic potential showed an increase of current when rubbing started. Guadalupe attributed it to enlargement of the wear track with progressing wear. The lowest values of COF is observed at anodic potential, but it increased at OCP and cathodic potential. The only reason for this is that the anodic condition had the thickest oxide layer which appears to have affected the friction coefficient. In addition, the formation of a thicker tribofilm at anodic potential may have acted as a solid lubricant and changes the contact mechanism, reducing friction. Diomidis [300] studied the surface state behaviour of complex metallic alloys in sliding contacts and observed the dependence of COF to electrochemical condition in PBS. Also, it has been reported that COF is lower at anodic potentials than at cathodic potentials for CoCrMo and 316L stainless steel in bovine serum and H_2SO_4 [301, 302].

The lower values of specific wear rate at anodic potential show the role of the passive film reducing friction and material loss. This is the first indication of the positive effect of corrosion on wear rate. This is confirmed by the synergistic approach. Also, it may be explained by the formation of a thicker tribofilm at this potential.

The poor wear resistance of these alloys is the reason for the highest material removal found at cathodic potential where the bare metal is exposed to wear, while the wear volume was lower at anodic condition at all applied normal loads because the material surface was protected by a stable and adherent corrosion film that reduces the contact stresses. The exact adhesion strength of proteins on metallic surface is not known to date [303] and the film formation is affected by ion release. This suggests that the potential applied in the system has an effect on the tribological properties. All alloys suffer from wear–accelerated corrosion but benefit from corrosion–decelerated wear. This is called antagonistic or negative synergy effect (beneficial effect). Khan [255] shows that the material loss of Ti alloys from wear test is lower in the presence of protein. It suggests that the presence of protein and released ions form a stable and adherent tribofilm that acts as solid lubricant and reduces the contact stress field.

This shows that the passivation performance of all alloys has a positive effect on the tribocorrosion behaviour at passive applied potentials. The alloys have the ability to recover their passivity (even in a short period of time) on the

worn area even under mechanical disturbance and they show a wear–accelerated corrosion resistance. The recovery of the passive state is effective in reducing material loss with the formation of tribofilm which changes the contact mechanisms and acts as a barrier to friction. The mechanical wear seems to be dominant in material loss and the capacity of passivity recovery during sliding contact is a key characteristic when developing new alloys for THR, as it can reduce friction.

Delamination was extensive and at anodic potential the surfaces were rougher. The high roughness at this potential is also attributed to the formation and presence of a thicker tribolayer. Raman spectra identified an organic layer in all alloys for all conditions. However, the intensity was higher at anodic potential in most cases and it is consistent with the smaller material loss and higher roughness at anodic potential due to a thicker tribolayer. The effect of the applied potential is also observed where the refined area is clearer at cathodic potential. The load applied might have an effect too. It suggests that the subsurface transformation in this system is dependent of the alloy composition and electrochemical condition applied. Several workers have reported the subsurface modification due to the wear test at anodic potential for CoCr alloys [299, 304] and at OCP for stainless steel [298].

Under cathodic potential, corrosion was prevented by an imposed current. No ions were released from the surface. The material loss was totally controlled by mechanical factors. At anodic potential, a passive film and organic layer was forced to form and due to its protective characteristics, the release of ions was prevented. Therefore, the material degradation mechanism was influenced by both mechanical and electrochemical conditions. It clearly shows that by forcing the passive film and organic film to form the tribocorrosion behaviour of Ti alloys can be improved.

The applied potential plays a crucial role on corrosion behaviour of Ti alloys in bovine serum solution. All alloys become active when the surface is rubbed due to the galvanic coupling between the unworn and worn areas. This indicates why material loss is lower at anodic potential. The lowest properties values are observed at anodic potential which is attributed to the formation of a thicker tribofilm which changes and contact stress field and act as solid lubricant.

6.3   Effect of normal load applied

Fig. 6.2 and table 6.1 show the material volume loss for each alloy at 0.5N, 1N and 2N with the volume loss increasing with load. In general, material loss was lower at anodic potential and higher at cathodic potential. The αβ alloy had the lowest and Nβ alloy the highest material loss. Normally, the studies show higher material loss at cathodic potential, which is attributed to the synergism between wear and corrosion.

The same comparison is made for specific wear rate, Fig. 6.3 and table 6.2 with 0.5N displaying the lowest values and 1N the highest values. In addition, the highest and lowest values of this propriety were seen at cathodic and anodic potentials. In general, the lowest and highest values were seen on the αβ and Nβ alloys. The enhancement of the specific wear rate of cathodic polarized surfaces compared to surfaces tested at OCP and at anodic potential was quite noticeable. For instance, the specific wear rate of αβ alloy at cathodic potential ($5x10^{-4}$ mm^3/Nm) is more than twice higher than that at anodic potential ($2x10^{-4}$ mm^3/Nm). This clearly shows the role of oxide layer on the worn surfaces.

Finally, the COF is shown in Fig. 6.4 and table 6.3 at cathodic potential and OCP, which increases slightly with load, but for the anodic potential it remained stable when the normal load was increased. The αβ alloy had the lowest COF for all conditions, and the β alloy had the highest at 0.5N and Nβ alloy at 1N and 2N respectively.

In fact, the lower COF at anodic potential has also been identified in an study of tribocorrosion behaviour of Ti6Al4V in artificial seawater at low contact pressures [305] and for stainless steel in H_2SO_4 solution [306].
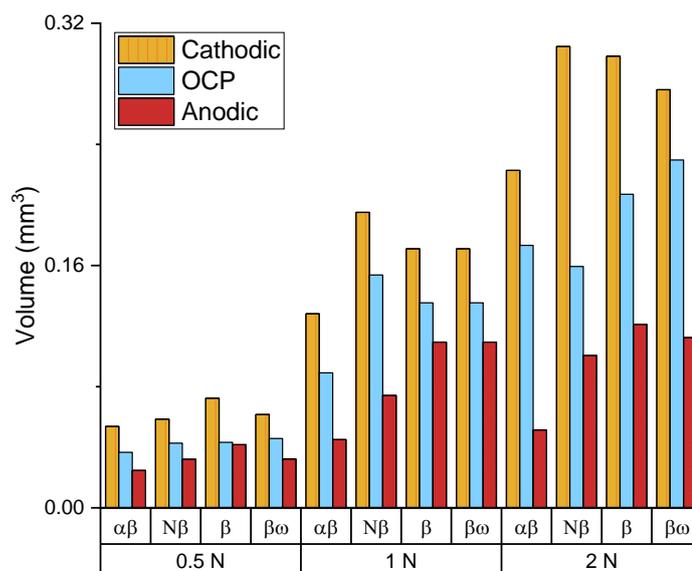
Fig. 6.2 – Comparison of wear track volume at cathodic potential, OCP and anodic potential at 0.5N, 1N and 2N.

Table 6.1 – Comparison of wear track volume (mm^3) at cathodic potential, OCP and anodic potential at 0.5N, 1N and 2N.

Alloy	Load	Cathodic	OCP	Anodic
Aβ	0.5N	0.05	0.04	0.02
	1N	0.13	0.09	0.05
	2N	0.22	0.17	0.05
Nβ	0.5N	0.06	0.04	0.03
	1N	0.2	0.15	0.07
	2N	0.3	0.16	0.1
B	0.5N	0.07	0.04	0.04
	1N	0.17	0.14	0.11
	2N	0.3	0.21	0.12
βω	0.5N	0.06	0.05	0.03
	1N	0.17	0.14	0.11
	2N	0.28	0.23	0.11
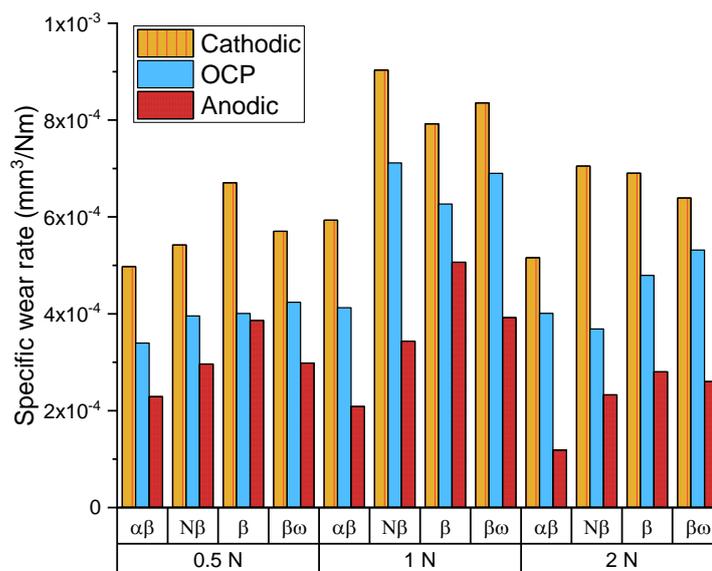
Fig. 6.3 – Comparison of specific wear rate at cathodic potential, OCP and anodic potential at 0.5N, 1N and 2N.

Table 6.2 – Comparison of specific wear rate (mm^3/Nm) at cathodic potential, OCP and anodic potential at 0.5N, 1N and 2N.

Alloy	Load	Cathodic	OCP	Anodic
Aβ	0.5N	4.97E–04	3.40E–04	2.29E–04
	1N	5.93E–04	4.13E–04	2.09E–04
	2N	5.16E–04	4.01E–04	1.19E–04
Nβ	0.5N	5.42E–04	3.96E–04	2.96E–04
	1N	9.03E–04	7.12E–04	3.44E–04
	2N	7.05E–04	3.69E–04	2.33E–04
B	0.5N	6.70E–04	4.01E–04	3.86E–04
	1N	7.92E–04	6.27E–04	5.07E–04
	2N	6.90E–04	4.79E–04	2.80E–04
Bω	0.5N	5.70E–04	4.24E–04	2.98E–04
	1N	8.35E–04	6.90E–04	3.92E–04
	2N	6.39E–04	5.32E–04	2.60E–04
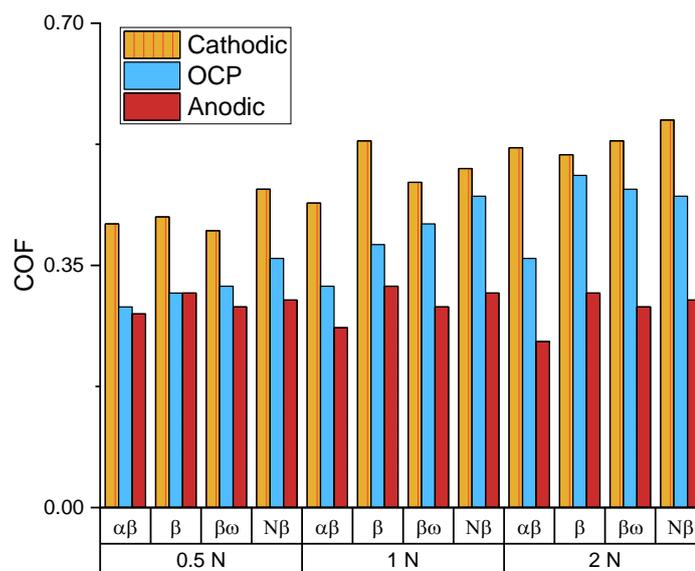
Fig. 6.4 – Comparison of the average coefficient of friction at cathodic potential, OCP and anodic potential at 0.5N, 1N and 2N.

Table 6.3 – Comparison of the average coefficient of friction at cathodic potential, OCP and anodic potential at 0.5N, 1N and 2N.

Alloy	Load	Cathodic	OCP	Anodic
Aβ	0.5N	0.41	0.29	0.28
	1N	0.44	0.32	0.26
	2N	0.52	0.36	0.24
Nβ	0.5N	0.46	0.36	0.3
	1N	0.49	0.45	0.31
	2N	0.56	0.45	0.3
B	0.5N	0.42	0.31	0.31
	1N	0.53	0.38	0.32
	2N	0.51	0.48	0.31
Bω	0.5N	0.4	0.32	0.29
	1N	0.47	0.41	0.29
	2N	0.53	0.46	0.29

The specific wear rate increases from 0.5N to 1N and then slightly decreases from 1N to 2N, which may suggest a change of the wear mechanism. The αβ alloy presents the lowest and Nβ alloy and β alloy the highest values of specific wear rate, due to the presence of α phase.

The normal load also shows an effect on the current and potential evolution of wear test. The higher the contact pressure the higher is the cathodic drop at OCP due to a larger exposed generated area. The higher the contact pressure the higher is the current increase at anodic potential also due to the exposed generated area by higher normal load and it suggests that wear enhances the anodic current. The increase of normal load leads also to an increase of the ploughing effect and this is reason why the surface roughness increases with normal load.

As expected, normal load increase leads to higher COF, specific wear rate and volume loss. This is attributed to the enhancement of the ploughing effect. It shows that the higher normal load the higher is the material degradation. The process of ion release is accelerated by tribological contact and the polarization resistance decreases, which indicates that the protective film in the wear scar is influenced by tribology and tribocorrosion.

6.4   Microstructure and chemical composition effect

Preferential corrosion of α or β phase was not observed, despite the fact that β phases normally have better corrosion resistance due to the presence of high corrosion resistant alloying elements. Also, other electrochemical tests are required to fully assess the corrosion behaviour of these alloys and point out which alloy has the best corrosion resistance.

Steady state is observed on COF evolution at cathodic potential for the αβ, βω and β alloys. The Nβ alloy does not show any large variations on COF evolution, which shows a good stability of this alloy and it might be explained by the presence of Fe which does not promote passivation.

The αβ alloy experienced the least material loss at all electrochemical conditions, due to the presence of α phase. This indicates that the material loss depends of material composition, normal load and electrochemical condition.

The low COF of the αβ alloy is attributed to the presence of α phase which is harder than the β phase. The limited plastic deformability of α phase is explained by its number of slip systems. In fact, α phase is a hexagonal close packed phase and it has only 3 slip systems, while β phase (bcc) has 12 slip systems [297]. According to von–Misses criterion, at least 5 slip systems is

required for homogeneous plastic deformation [298]. A larger number of slip planes are energetically most favourable for plastic deformation.

Wear occurred in these alloys because alumina counterpart (harder) penetrated their softer surface and grooved it. The material is mainly removed by microploughing because the particles of the wear track flowed to the sides of the track and the surface is severely damaged, but microcutting may also have occurred simultaneously in lower intensity because it is favoured by the presence of a lubricant.

That ploughing appearance on the worn surface indicates the poor resistance of these alloys to plastic deformation [213]. Every abrasive interaction is characterized by an intense plastic deformation that is accumulated by repeated interactions. This indicates that abrasive wear with delamination is the dominant wear mechanism and it started in the steady state stage, but tribo–oxidative wear may have occurred due to the repassivation of these alloys in the running in period. This is a typical two body abrasion, which is a severe form of wear [138]. The same wear mechanism occurred in all alloys despite the variation of the electrochemical condition, composition and microstructure.

Studies show that abrasive and adhesive wear have been seen in artificial joint replacements and they may cause failure of TJR [36, 214].

The wear resistance of an alloy relies on the mechanical properties of the passive film and contact pressure [277]. The contact pressure is the same for each condition, but the mechanical proprieties of the passive film is different for each alloy because it depends on the alloy composition and microstructure. This microstructure may change with mechanical wear and electrochemical action on the active area.

All alloys exhibited the formation of a tribolayer on the surface in all conditions. Wimmer [91, 296] observed that the tribolayer formation only occurred at high loads for CoCr alloys and that the dissolution of Mo is crucial for tribofilm formation. Liao [272] studied the graphitic tribological layers and concluded that transition metals remove water and ammonia from albumin which leads to a formation of a tribofilm which reduces friction. Thus, the oxide layer must be removed for the formation of a tribofilm. Liao [229] and Yan [302] suggested that the tribofilm is composed of a mix of released metal and protein.

The αβ alloy presented the highest Raman peaks intensity from the organic layer, which may be linked to the low wear rate, demonstrating the

effectiveness of the tribolayer of reducing the friction. The high intensity indicates a thicker film. The intensity of the organic layer signal was higher at a load of 0.5N. The tribofilm may be formed by the released ions from the passive layer and proteins from the bovine serum. However, information about this is scarce [229]. The presence of the tribolayer was not homogeneous as shown by the variation in five measurements from each surface, which is agreement with the literature [307]. The presence of the tribolayer does not seem to be linked with the microstructure, but potential and normal load influence its formation. Other metallic alloys only form tribolayer in specific loads and potentials.

Table 6.4 shows the ratio of D and G bands and the graphite size domain (Lα). Raman spectroscopy results showed that the tribofilm formed on the worn surfaces at all electrochemical conditions is a composed of amorphous and nanocrystalline carbon. It is possible to roughly correlate the relative intensity (ID/IG) to the graphite cluster, where the relative intensity is equal to Cλ/Lα [308]. Cλ is 4.4nm for the used laser (515.5nm). It shows that the graphite domain size ranges from 3.9nm (β alloy at 0.5N at anodic potential) to 8.7nm (Nβ at 0.5N at anodic potential). Results from other researches show that the graphite domain size is 4.5nm [272]. Studies with CoCr show that the formation of an organic nanostructure composite may occur in the outermost layer of the surface [309].

Table 6.4 – Ratio of D and G bands.

Alloy	Load (N)	Potential	I(D)/I(G)	Lα (nm)
αβ	0.5	Anodic	0.8	5.7
αβ	0.5	OCP	1.0	4.6
αβ	0.5	Cathodic	0.9	4.8
αβ	1	Anodic	0.9	5.0
αβ	1	OCP	0.6	7.8
αβ	1	Cathodic	0.7	6.3
αβ	2	Anodic	0.9	5.0
αβ	2	OCP	0.7	6.1
αβ	2	Cathodic	0.7	6.2
β	0.5	Anodic	1.1	3.9
β	0.5	OCP	1.1	4.0
β	0.5	Cathodic	0.7	6.4
β	1	Anodic	0.9	5.0
β	1	OCP	0.7	6.0
β	1	Cathodic	0.7	6.5
β	2	Anodic	0.9	4.9
β	2	OCP	0.8	5.6
β	2	Cathodic	0.9	5.0
βω	0.5	Anodic	0.7	5.9
βω	0.5	OCP	1.0	4.2
βω	0.5	Cathodic	0.8	5.6
βω	1	Anodic	0.8	5.5
βω	1	OCP	0.8	5.8
βω	1	Cathodic	0.7	6.5
βω	2	Anodic	0.9	4.8
βω	2	OCP	0.8	5.8
βω	2	Cathodic	0.7	5.9
Nβ	0.5	Anodic	0.5	8.7
Nβ	0.5	OCP	0.6	6.9
Nβ	0.5	Cathodic	0.7	6.7
Nβ	1	Anodic	1.1	4.2
Nβ	1	OCP	0.8	5.5
Nβ	1	Cathodic	1.0	4.4
Nβ	2	Anodic	1.1	4.1
Nβ	2	OCP	0.8	5.6
Nβ	2	Cathodic	1.0	4.3

The αβ alloy had the lowest material loss which could be linked to the highest nanohardness and reduced elastic modulus of this alloy. Interestingly, at anodic potential, the nanohardness showed its highest values, the volume loss exhibited its lowest values and roughness its highest values, which suggests a hard and wear resistant surface and rougher due to the thicker tribolayer.

The increase in the mechanical properties of the worn surfaces occurred due to the subsurface change during the wear test. This is due to the applied stress that is larger than the elastic shakedown limit and the materials experienced strain hardening due to the steady state cyclic plasticity that leads to an accumulation of plastic strain. Plastic yielding was achieved at the asperities contact points. These asperities experienced a cyclic load due to the repeated contact and with the continuous accumulation of plastic deformation and local compressive state of stress, which leads to plastic deformation [213]. It may influence hardness due to strain hardening and it may increase with load. However, this relationship has not yet been proved.

Studies shows that small grains of CP Ti leads to an increase of mechanical properties but no effect on wear properties was observed [310]. In addition, ultra fine grains have been reported to reduce wear properties [311]. Also, it is an indication that ductility of these alloys reduces after wear test since it is inversely proportional to hardness. However, other studies concluded that fine grain size enhance the wear resistance of CP Ti [312].

The elastic modulus for the body centre cubic phase is lower than hexagonal and orthorhombic phases, but it is also affected by the volume fraction of each phase. HCP phase has a low ability to deform plastically. Thus, during sliding the asperity junctions deform with lower intensity and the adhesion forces at the junctions are not able to develop fully [93].

The subsurface characterization by FIB and TEM demonstrate that microstructural changes occurred during the wear test and it changes with the electrochemical condition. These are signs of dynamic recrystallization since the constant flow of electrolyte at 37°C and the smooth surface finishing reduce the probability of reaching high temperatures necessary for a recrystallization process by heat treatment. This may be started during running in stage since the wear rate is higher. Therefore, the mechanical effect is more dominant in grain size reduction than thermally induced recrystallization.

The formation mechanisms of this microstructural subsurface change is not yet clear, but it is formed by strain accumulation at the contact subsurface due to repetitive loading (cyclic nature of friction) during sliding, which leads to dislocation cell formation and its movement (severe plastic deformation) evidenced by mechanical milling and dynamic recrystallization [138].

The presence of a surface strain region indicates that the oxide layer was continuously broken by the asperities. This allows ion release, such as Ti, that was sufficient promote the formation of this layer.

Studies with stainless steel NaCl electrolyte show that subsurface deformation was observed at all electrochemical conditions (cathodic, OCP and anodic potential). It was attributed to due to shear strain in the contact. High shear stress resulted in a very fine grain structure. The reduction in grain size is attributed to dynamic recrystallization. Interestingly there was no difference in grain refinement at the different potential applied [313], which is different in this project and is in agreement with other authors [314].

The presence of a tribofilm may be the reason for a clearer area of refined grains at some potentials, since it may act as a barrier leading to an accumulation of dislocation favouring dynamic recrystallization or promoting dislocation annihilation [315]. This refined grain area might explain changes in mechanical properties since the increase of hardness might be a result from the mix of hard particles and chemical changes. Also, it may affect the COF.

The changes in contact mechanism and contact stress field inside the wear track, due to the formation of a tribofilm from the higher protein absorption at anodic potential, affects the changes in microstructure because these changes in the contact mechanisms affects the compression stress where the contact begins and a tensile stress at the end of contact. It will affect sub-surface shear stresses, Fig. 6.5, and the formation of subsurface strain and dislocation accumulation due to repetitive loading, which is needed for dynamic recrystallization. The contact mechanics is also affected by these factors at OCP because there is metal dissolution and at cathodic potential the contact mechanics is not affected by metal dissolution.
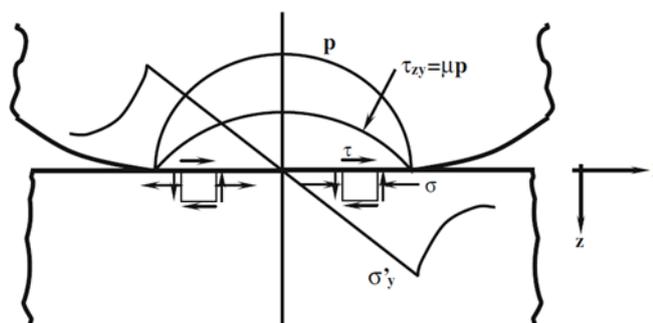
Fig. 6.5 - Stress distribution on the flat surface in the area of contact [213].

The analysis of subsurface area for alloys tests at 2N at anodic potential show the presence of tribolayer but not homogeneously distributed. Grain refinement took place and β phase was found near to the surface.

Martensitic transformation (α' and α'') and ω phase were not found in the αβ alloy indicating this alloy only exhibited grain refinement. However, the Nβ alloy experienced limited transformation to α'' phase in all electrochemical conditions and ω phase transformation at anodic potential and OCP. Martensitic α'' and ω phase transformation were identified in the β and βω alloys at OCP. The formation of α'' phase can be linked to the presence of Ta in these alloys [94]. Also, it suggests that α'' and ω transformation may occur simultaneously [118]. Therefore, it is clear that the tribocorrosion process in Nβ, β and βω alloys induces ω phase transformation.

The ω phase is formed by the collapse of one pair of $(111)_{bcc}$ planes while keeping the neighbouring one $(111)_{bcc}$ plane not modified in the bcc lattice [121, 122]. In fact, ω phase is found is many β titanium alloys due to the presence of high concentration of β stabilizers which affect its formation. This phase has high elastic modulus and this is the reason that this phase is not desired in biomaterials applications [12]. However, no difference in mechanical proprieties was found for these alloys when compared to the unworn surface. It is important to note that the reflections of ω phase on diffraction pattern are not strong and it indicates low phase volume fraction of this phase. Also, the ω phase found on the worn surface is athermal and has the same crystal structure than that formed during aging. Correa [316] observed that the β alloy Ti-15Zr-7.5Mo experienced the same ω phase transformation in the subsurface after wear test at OCP.

In conclusion, the αβ alloy has the lowest and the Nβ alloy has the highest material loss. It has been discussed why the αβ alloy presents a better tribocorrosion performance. This alloy presented a better performance regarding material loss than the other alloys in all electrochemical conditions. The presence of α phase plays the most important factor in this regard and it is attributed to the nature of HCP crystal.

6.5 The Interaction between wear and corrosion

Mechanistic approach

It is possible to roughly estimate the electrochemical and mechanical contributions of material loss using Faraday's law (equation 17). These contributions are presented in Figs. 6.6 to 6.8 and Table 6.5 and represent the material loss only of the worn area. The material volume loss due to mechanical wear was identified by the difference between total volume loss and chemical wear. The material loss volume due to corrosion was low in comparison to the material loss due to pure wear and it slightly changed with load. At anodic potential, the difference between Vchem and Vmech is up to two order of magnitude, such as αβ at 0.5N which Vchem is $2.0 \ 10^{-3}$ mm3 and Vmech is $2.3 \ 10^{-2}$ mm^3. However, this difference at OCP rises up to four orders of magnitude, such as Nβ alloy at 1N which Vchem is $7.5 \ 10^{-5}$ and Vmec is $1.5 \ 10^{-1}$.

In all conditions, the αβ alloy presented the highest and the β alloy the lowest material loss due to corrosion. In addition, material loss increased with load and in the following order anodic potential (0.3V vs OCP), OCP and cathodic potential (-1 V vc OCP)

.
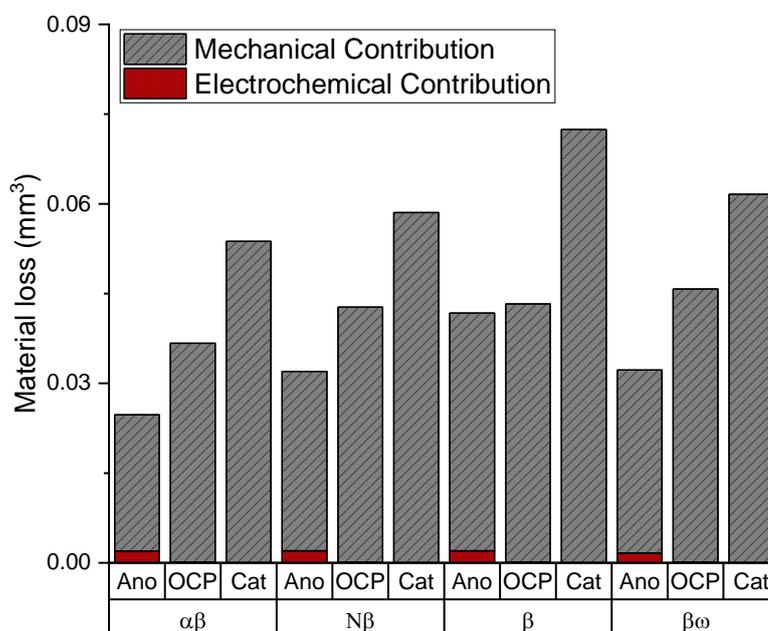
Fig. 6.6 – Electrochemical and mechanical contribution on material loss at 0.5N.
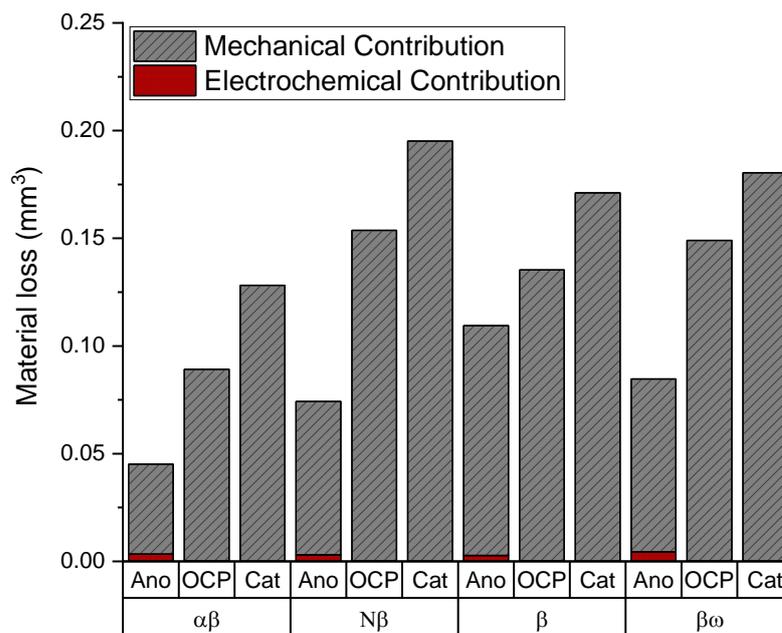
Fig. 6.7 – Electrochemical and mechanical contribution on material loss at 1N.
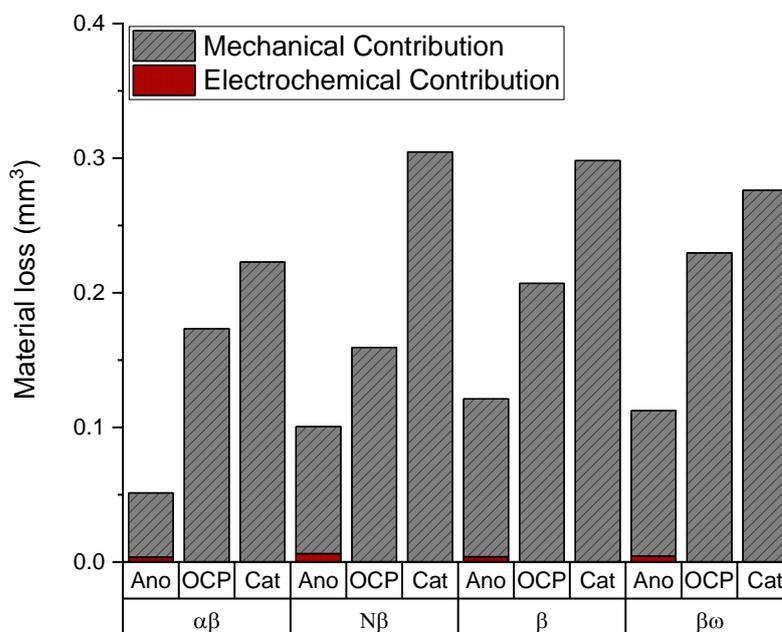
Fig. 6.8 – Electrochemical and mechanical contribution on material loss at 2N.

Table 6.5 – Electrochemical and mechanical contribution on material loss at
0.5N, 1N and 2N.

Alloy	Load (N)	Potential	V_{chem}	V_{mech}
Aβ	0.5	Anodic	2.0E–03	2.3E–02
Nβ	0.5	Anodic	2.0E–03	3.0E–02
B	0.5	Anodic	2.0E–03	4.0E–02
Bω	0.5	Anodic	1.6E–03	3.1E–02
Aβ	1	Anodic	3.3E–03	4.2E–02
Nβ	1	Anodic	3.0E–03	7.1E–02
B	1	Anodic	2.8E–03	1.1E–01
Bω	1	Anodic	4.4E–03	8.0E–02
Aβ	2	Anodic	3.6E–03	4.8E–02
Nβ	2	Anodic	6.2E–03	9.4E–02
B	2	Anodic	3.9E–03	1.2E–01
Bω	2	Anodic	4.6E–03	1.1E–01
Aβ	0.5	OCP	8.9E–05	3.7E–02
Nβ	0.5	OCP	7.5E–05	4.3E–02
B	0.5	OCP	1.1E–04	4.3E–02
Bω	0.5	OCP	9.6E–05	4.6E–02
Aβ	1	OCP	8.9E–05	8.9E–02
Nβ	1	OCP	7.5E–05	1.5E–01
B	1	OCP	1.1E–04	1.4E–01
Bω	1	OCP	9.6E–05	1.5E–01
Aβ	2	OCP	8.9E–05	1.7E–01
Nβ	2	OCP	7.5E–05	1.6E–01
B	2	OCP	1.1E–04	2.1E–01
Bω	2	OCP	9.6E–05	2.3E–01
Aβ	0.5	Cathodic	0	5.4E–02
Nβ	0.5	Cathodic	0	5.9E–02
B	0.5	Cathodic	0	7.2E–02
Bω	0.5	Cathodic	0	6.2E–02
Aβ	1	Cathodic	0	1.3E–01
Nβ	1	Cathodic	0	2.0E–01
B	1	Cathodic	0	1.7E–01
Bω	1	Cathodic	0	1.8E–01
Aβ	2	Cathodic	0	2.2E–01
Nβ	2	Cathodic	0	3.0E–01
B	2	Cathodic	0	3.0E–01
Bω	2	Cathodic	0	2.8E–01

This identified the material loss was predominantly due to mechanical
wear for all alloys in all conditions. V_{chem} corresponds to the amount of oxidized
metal during the process of repassivation – depassivation during rubbing. In fact,

V_{chem} increases with load, but the overall percentage of material loss does not show any variation. In addition, V_{chem} is zero at cathodic potential and it has low values at OCP. The electrochemical contribution is also low at anodic potential. Overall, the Nβ and β alloys suffer more from the mechanical contribution. In all conditions the αβ alloy presents the highest and β alloy the lowest material loss due to corrosion. The reason for the high material loss due to corrosion of αβ alloy is the effect of galvanic coupling due the two phase structure. Mechanical contributions to material loss only depend on the normal load, material composition and microstructure. In addition, material loss increases with load and in the order of anodic potential, OCP and cathodic potential.

Synergistic approach

The experimental way to find components of equation 13 is:

T = material loss rate from OCP test

Wo = material loss rate from cathodic potential test (-1V vs OCP)

Co = Penetration corrosion rate from potentiodynamical test

ΔCw = Penetration corrosion rate from potentiodynamical test during wear test

ΔWc = Difference.

Material loss rate for T and Wo is obtained by equation 10.3; and corrosion rate from ΔCw is obtained by the extrapolation of potentiodynamical test during wear test. ΔWc is the difference, according to ASTM G119.09 standard [217].

Fig. 6.9 and table 6.6 show each component of equation 13 related to the synergistic approach. It is clear that material loss due to pure wear (Wo) was larger than total material loss (T). In addition, the material loss due to pure corrosion (Co) was nearly zero; in fact, all the alloys studied in this project are passive and show a very low passive dissolution rate. The effect of wear on corrosion (ΔCw) was larger than the material loss due to pure corrosion, but still not comparable to the total material loss (T) and material loss due to pure wear (Wo). Finally, the effect of corrosion on wear (ΔWc) had a negative value. Each component increased with normal load.

The total contribution of corrosion (Cw) and wear (Wc) are presented in Fig. 6.10 and table 6.7. There is a contribution of corrosion to material loss, but it is irrelevant when compared to the contribution of wear. The total contribution of corrosion (Cw) does not change with normal load, but the total contribution of wear (Wc) increases with normal load.
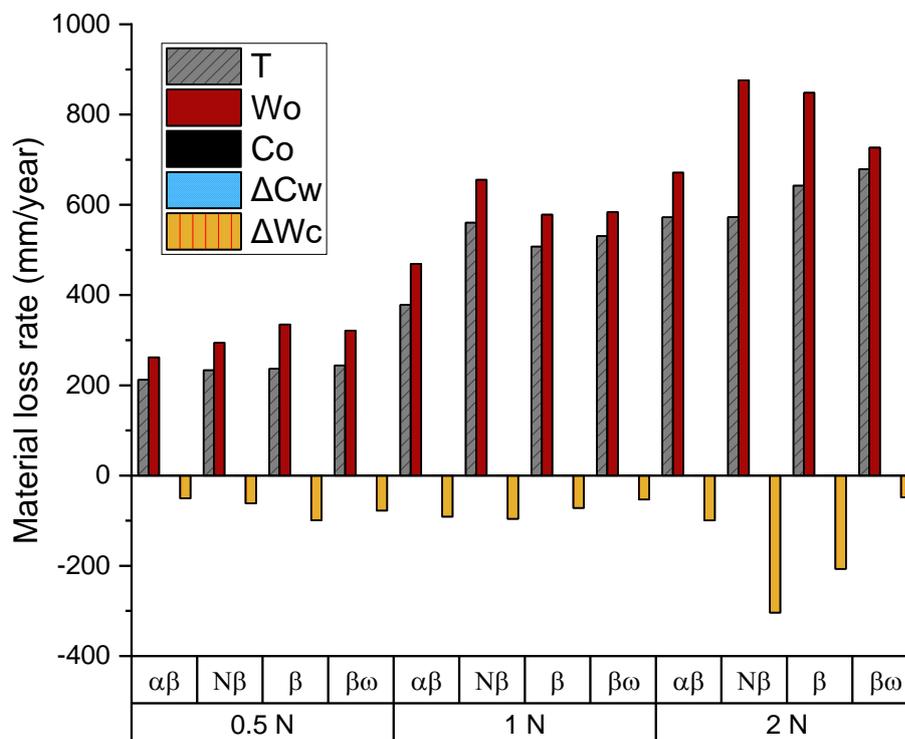
Fig. 6.9 – Total and synergism material loss rate.

Table 6.6 – Total and synergism material loss rate in mm/year.

Alloy	Load (N)	T	W_o	C_o	ΔC_w	ΔW_c
αβ	0.5	212	262	1.1E–04	0.70	–51
Nβ	0.5	234	294	1.7E–05	0.58	–61
β	0.5	237	335	3.4E–05	0.73	–99
βω	0.5	244	321	1.8E–05	0.40	–78
αβ	1	378	469	1.1E–04	0.63	–91
Nβ	1	560	656	1.7E–05	0.60	–96
β	1	507	578	3.4E–05	0.74	–72
βω	1	531	584	1.8E–05	0.45	–53
αβ	2	573	671	1.1E–04	0.68	–100
Nβ	2	573	876	1.7E–05	0.59	–304
β	2	642	848	3.4E–05	0.77	–207
βω	2	679	727	1.8E–05	0.44	–48
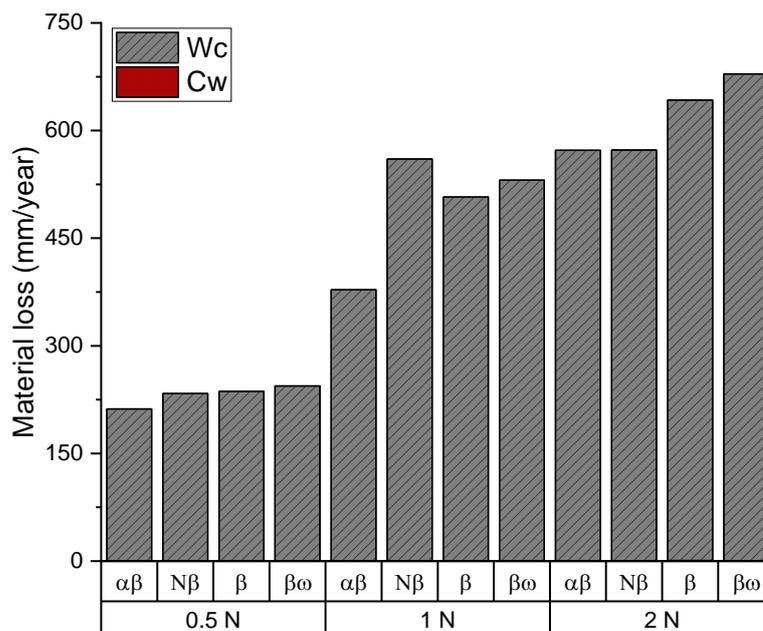
Fig. 6.10 – Total contribution of corrosion (Cw) and wear (Wc) on material loss.

Table 6.7 – Total corrosion (Cw) and wear (Wc) on material loss.

Alloy	Load (N)	Cw	Wc
αβ	0.5	0.7	212
Nβ	0.5	0.58	233
β	0.5	0.73	236
βω	0.5	0.4	244
αβ	1	0.63	378
Nβ	1	0.6	560
β	1	0.74	507
βω	1	0.45	531
αβ	2	0.68	572
Nβ	2	0.59	572
β	2	0.77	642
βω	2	0.44	678

This approach confirms that the main cause of material loss is due to mechanical wear. The corrosion rate enhanced by wear (ΔCw) is bigger than material loss due to pure corrosion, but still not comparable to the total material loss (T) and material loss due to pure wear (Wo). The effect of corrosion on wear rate (ΔWc) has a negative value, which confirms that corrosion does not enhance wear rate, but also it reduces wear rate. It is in an erosive dominated regime.

191

Thus, corrosion has a positive effect on reducing wear rate, antagonistic effect. Overall, each component increases with normal load. It is explained by the good corrosion resistance of these alloys, but also by the formation of tribofilm on all alloys during tribocorrosion process that acts as lubricant and changes the contact field. The total contribution of corrosion (Cw) is much lower than the total contribution of wear (Wc) and that does not change with load, but Wc does change with load. This confirms that mechanical wear is the main cause of material loss on these Titanium alloys. The reason for this behaviour might be the excellent corrosion resistance of these alloys, the presence of tribofilm acting as a lubricant, poor mechanical properties of the passive film which is removed easily and poor wear resistance of Titanium alloys.

Numerous studies have found systems to have negative synergistic effects or antagonistic effect even under a relatively small set of parameters. This could be a result of wear particles embedding themselves in the surface of the material where corrosion has etched away the binder, effectively creating a self-healing surface. Protein may also play a role on lubrication and protein absorption may be different at each potential applied.

Mathew [317] compared the tribocorrosion behaviour of CP Ti and Ti64 in artificial saliva (pH 6.5) with different concentration of lipopolysaccharide (LPS). It was observed that only Ti64 in 150µg/ml LPS concentration show the antagonistic behaviour.

Albayrak [264] compared the tribocorrosion behaviour of CP titanium to duplex treated CP titanium and nitrided CP titanium in simulated body fluid. It was found that all alloys tested have an antagonistic effect behaviour and it was stronger on the nitride specimens. It was attributed to solution formed oxide layer on the surface of the alloys.

Sadiq [318] studied the behaviour of CoCrMo alloy in calf serum solution in a wide range of normal load and potentials. It is observed that CoCr alloys show an antagonistic effect when SiC particles are present in the electrolyte. The antagonistic effect was attributed to the accumulation of organic material on the alloy surface. Also, it was pointed out that the antagonistic effect may result from an increased solution viscosity, which improves the lubrication regime and thus inhibits corrosion–wear due to the mixed protein molecules and particles. Also, the hard SiC particles are likely to have embedded on the surface of the softer UHMWPE ball.

Hodge [319] studied the tribo-corrosion mechanisms of 316L stainless steel in soft drinks. It was observed that medium loads and higher viscosities produce synergistic conditions whilst combinations of either high loads and low viscosities or low loads and high viscosities produce antagonistic conditions. It was stated that 316L stainless steel in both milk and soda experience antagonistic and transition regimes for the majority of loads tested due to the formation of protective passive films in the anodic regime. Also, it was noted that corroded metals ions may alter the solution viscosity which will in turn have an effect on the contact friction coefficient.

Purandare [320] studied the effect of velocity on erosion–corrosion behaviour of uncoated M2 H.S.S tool steel and M2 H.S.S tool steel coated with CrN/NbN superlattice coating in buffer solution. It was found that uncoated steel shows a synergistic effect and the coated material shows an antagonistic effect at +400 mV. Tests under cathodic, passive and anodic potentials showed an antagonistic effect for passive +300 mV and to a lesser extent for anodic +700 mV attributed to the protective nature of the passive layers of Cr and Nb at +300 mV and a cushioning effect due to preferential dissolution of Cr phase. It was concluded that this behaviour depends on the electrochemical potential and impact velocity.

Bozzini [321] showed that annealed carbon steel has a more active corrosion potential before it was work hardened and shows a reduction in overall corrosion rate (antagonistic effect) with erosion present.

Bello [322] found out that UNS S31603 and S32760 stainless steels have an antagonistic effect while S30403 does not in NaCl solution. It was attributed to a reflection of the differences in repassivation kinetics or composition of the passive films reducing the overall level of two-body abrasion with S30403 having weaker repassivation/passive oxide film structure. Sinnett-Jones [323] analysed the micro-abrasion–corrosion of a CoCrMo alloy in Ringer's solution and antagonistic effects were also observed for the MoM and anodically polarised contacts.

The antagonistic effect observed in this study can be characterized as corrosion inhibited abrasion and not abrasion inhibited corrosion. In fact, wear enhances corrosion rate. The mechanism for this effect is explained by the creation of an oxide layer which acts as a solid lubricant, increases surface compliance and decreases point stresses due to the metal dissolution, thus

reducing mechanical wear. The formation of a tribofilm due to the absorption of protein may also act as a solid lubricant and may change the fluid viscosity due to the ion release, which will change the lubrication regime. These effects may have changed the contact mechanisms and real contact area/contact stress field inside the wear track, leading to a different tribology and corrosion response at anodic potential. The tribofilm will have accommodated most if not all shear in the contact and protects the surface from wear.

Chapter 7 – Conclusions

Understanding the tribocorrosion behaviour of Titanium alloys and other metallic materials in biological environments is complex because many physical, chemical and electrochemical processes occur. However, this project has identified important aspects such as:

Microstructure does have an effect on tribocorrosion behaviour of Titanium alloys since the presence of α phase is linked to lower material loss. However, the electrochemical condition plays the most important role since at anodic potential Titanium alloys show an improvement of wear properties and lower material loss due to the lubricating behaviour of oxide layer and tribofilm. It suggests that the development of new Titanium alloys must be concentrated on β phase alloys, since it has a lower elastic modulus and nontoxic elements; and on surface engineering properties of their oxide films which has been demonstrated that the lubricating effect of proteins reduce wear rate.

These Titanium alloys show that strain hardening is an important factor for developing new alloys since it reduces friction and material loss and promising characteristics. However, CoCr alloy are still a better choice to these Titanium alloys due to their higher wear resistance.

The most important findings are:

- The ion release at anodic potential enhances protein absorption.
- Proteins act as solid lubricant which reduces the contact stress and reduces friction.
- Titanium alloys have lowest material loss at anodic potential.
- The presence of a hard phase, such as α, results in a lower material loss.

Important findings are summarized below:

- The passive film is influenced by tribocorrosion.
- β alloy is the most active and the αβ alloy is the noblest alloy at sliding potentiodynamic test.
- When subjected to rubbing, all alloys experienced an increase in corrosion current and a drop of the potential (more active) due to the constant exposure of the bare metal during depassivation and repassivation.

- The COF is around 0.29 at anodic potential; 0.3 at OCP and 0.4 at cathodic potential 0.5N for all alloys, where the αβ alloy exhibited the lowest values.

- The Nβ alloy showed the most stable COF evolution.

- The COF and wear track volume increased with load, and it increased at cathodic potential and OCP. At anodic potential, the COF remained approximately constant. This is due to the formation of a thicker tribofilm at anodic potential. Also, it varies with alloy composition.

- The COF and wear track volume are lower at anodic potential and higher at cathodic potential and increases with normal load.

- At cathodic potential, all alloys show a current drop when rubbing starts at all normal loads and it remained negative during rubbing.

- At OCP, all alloys presented a potential drop, representing the removal of the passive layer. The Nβ alloy show the highest and β the lowest drop at all normal applied loads. The lowest values of OCP were obtained for the αβ alloy at 0.5N, Nβ alloy at 1N and αβ alloy at 2N, indicating these are the noblest alloys during sliding OCP test.

- At anodic potential, all alloys have the ability to repassivate during rubbing indicating they are resistant to wear accelerated corrosion.

- All alloys show a running in stage, except the Nβ alloy.

- The tribocorrosion behaviour is dependent of the microstructure, normal load and tribofilm formation. At OCP, all alloys show similar behaviour where a cathodic drop up to −1 V is seen after rubbing starts for all alloys on all normal loads.

- At 0.5N load, the αβ alloy showed the lowest and β the highest volume loss. However, with the increase of normal load to 1N and 2N, the αβ alloy still presented the lowest and Nβ alloy presented the highest volume loss. The Nβ alloy exhibited an increase of volume loss as the load was increased.

- The αβ alloy presented the lowest material loss at all normal loads in all electrochemical conditions, due to the α phase present in this alloy.

- The total material loss is higher at cathodic potential than OCP and anodic potential respectively. This indicates that the presence of oxides and tribofilm reduce friction due to the high corrosion resistance of these alloys. Also, the total material loss increases with normal load.

- The specific wear rate is high at cathodic potential and lower at anodic potential. This is another indication of the positive effect of the oxide on tribocorrosion behaviour of these alloys. However, it increases from 0.5N to 1N and slightly reduced at 2N.

- The αβ alloy exhibited the lowest specific wear rate at all normal loads in all electrochemical conditions.

- The mechanical wear is dominant by material removal. It increases with normal load and it is higher at cathodic potential. The material loss in titanium alloys is due to the poor wear resistance.

- The mechanistic approach identified that the material loss for all alloys at all normal loads at cathodic potential and OCP is due to pure wear.

- There is an increase of electrochemical contribution at anodic potential for all alloys at all loads. However, this contribution is still low in comparison to mechanical contribution where the αβ alloy at 0.5N at anodic potential show the highest electrochemical contribution (8%).

- The electrochemical contribution as well as the mechanical contribution increases with normal load.

- The percentage of electrochemical and mechanical contribution on material loss do not change with load.

- The synergistic approach identified that the material loss due to pure wear (Wo) is higher than the total material loss (T). The material loss due to pure corrosion is negligible since the alloys of this study are passive metals. However, it increases with wear (ΔCw). Finally, the effect of corrosion on wear (ΔWc) has a negative value which suggest that corrosion does not have effect of enhancing wear rate and it has a positive effect of reducing friction. That is why the material loss volume is lower at anodic potential.

- All components of synergistic approach increase with normal load.

- The percentage of total contribution of corrosion (Cw) on total material loss is zero. This confirms that mechanical wear (Wc) is main caused by material loss of these Titanium alloys on tribocorrosion. Wc increases with normal load.

- The αβ alloy has a higher effect of wear on corrosion, consequently a higher material loss due to corrosion enhanced by wear, than the β alloy and it may be linked to the galvanic coupling due to two different phases. However, the total material loss on all alloys are predominantly due to

197

mechanical wear, and the presence of α phase on the αβ alloy makes this alloy more resistant to mechanical wear. This is the reason for the αβ alloy presenting the lowest material loss.

- The backscattered and secondary electrons images of the worn surfaces show a less transient surface at anodic potential than at cathodic and OCP. The surfaces are characterized by the presence of grooves and scratches (ploughing surface). Areas with dark contrast are seen in all alloys, which indicates the formation of tribofilm. Isolated debris were identified. The roughness was high for all alloys and it increased with normal load, but it was not found relationship with potential applied.

- The surface roughness increased with normal load. It is higher at anodic potential and lower at cathodic potential. This is due the presence of oxides formed on the anodic tested surfaces, confirmed by SEM images.

- The tribofilm was formed on the worn surface of all alloys in all conditions but it is not homogeneously distributed. It had a greater intensity in the αβ alloy and is O and C rich. The tribofilm formation seems to be beneficial reducing friction and its formation is not related to the material composition, but with electrochemical and load conditions. This film has the ability to act as a lubricant and it has an important role preventing wear.

- The dominant wear mechanism was abrasive wear in all alloys and it does not change with normal load or composition.

- A slight increase of the mechanical proprieties is seen on the worn surfaces when compared to the unworn surface. However, it is not clear what the relationship is between material loss and these proprieties.

- The presence of refined grains area in all electrochemical conditions was observed on all alloys. The presence of α, α'', β and ω phase were also identified but no cracks or twinning was observed.

- The Nβ, β and βω alloys present the minor formation of α'' and in the β an amount of ω phases in the subsurface in the anodic condition. It suggests that tribocorrosion process induce α'' and ω transformation on these alloys and those transformation occur simultaneously.

Chapter 8 – Future work

It is suggested the following topics in order to obtain a clearer understanding of the tribocorrosion behaviour of the titanium alloys.

- Further investigation must be made by other electrochemical techniques such as EIS in order to fully understand the behaviour of the oxides formed on these alloys.
- The effect of heat treatment as well as the grain size on tribocorrosion behaviour.
- The effect of the sliding speed on the tribocorrosion behaviour.
- Build a wear map and Stribeck curve for a better understanding of the lubricating regime of these alloys.
- The effect of protein concentration and effect of biological species on wear, corrosion and tribocorrosion behaviour.
- Analysis of the used counterpart (alumina ball) to identify any material transfer.
- Analysis of the electrolyte (bovine serum) to identify the nature of the formed ions.
- Identify the nature of tribofilm and how it changes with normal load and potential applied.
- Influence of different cathodic and anodic potentials on tribofilm formation.
- Time dependence of corrosion and wear and transition point.
- The relationship between normal load and the extension of the refined grain area on the subsurface of the worn area.
- Effect of corrosion, tribology and tribocorrosion on material degradation.
- Perform a comparison study with CP Ti and Ti64 and dry test.
- Tests in a range up to 50°C.
- Tribocorrosion test in different potentials and for a longer period.
- Influence of pH
- Chemical composition analysis at worn surfaces.

References

1. Ma, L.*, et al.*, *The effect of lubrication on the friction and wear of Biolox(R)delta.* Acta Biomater, 2012. **8**(6): p. 2348-59.

2. Temenoff, J.S.*, et al.*, *Biomaterials: the intersection of biology and materials science.* Vol. 1. 2008: Pearson/Prentice Hall Upper Saddle River, NJ, USA:.

3. Rack, H.*, et al.*, *Titanium alloys for biomedical applications.* Materials Science and Engineering: C, 2006. **26**(8): p. 1269-1277.

4. Bronzino, J.D., *Biomedical engineering handbook.* Vol. 2. 1999: CRC press.

5. Niinomi, M., *Mechanical properties of biomedical titanium alloys.* Materials Science and Engineering: A, 1998. **243**(1): p. 231-236.

6. Kurtz, S.*, et al.*, *Projections of primary and revision hip and knee arthroplasty in the United States from 2005 to 2030.* J Bone Joint Surg Am, 2007. **89**(4): p. 780-5.

7. Zeng, P.*, et al.*, *Characterisation of the wear mechanisms in retrieved alumina-on-alumina total hip replacements.* Wear, 2017. **376**: p. 212-222.

8. Mathew, M.T.*, et al.*, *Significance of tribocorrosion in biomedical applications: overview and current status.* Advances in tribology, 2009. **2009**.

9. Niinomi, M., *Recent metallic materials for biomedical applications.* Metallurgical and materials transactions A, 2002. **33**(3): p. 477-486.

10. National Joint Registry for England, W.N.I.*, et al.*, *16th annual report 2019.* 2019. **16th**.

11. Zhou, Y.-L.*, et al.*, *Microstructures and mechanical properties of Ti–Mo alloys cold-rolled and heat treated.* Materials Characterization, 2011. **62**(10): p. 931-937.

12. Geetha, M.*, et al.*, *Ti based biomaterials, the ultimate choice for orthopaedic implants–a review.* Progress in materials science, 2009. **54**(3): p. 397-425.

13. Kobayashi, E.*, et al.*, *Mechanical properties and corrosion resistance of Ti-6Al-7Nb alloy dental castings.* J Mater Sci Mater Med, 1998. **9**(10): p. 567-74.

14. Long, M.*, et al.*, *Titanium alloys in total joint replacement--a materials science perspective.* Biomaterials, 1998. **19**(18): p. 1621-39.

15. Okazaki, Y.*, et al.*, *Corrosion resistance and corrosion fatigue strength of new titanium alloys for medical implants without V and Al.* Materials Science and Engineering: A, 1996. **213**(1-2): p. 138-147.

16. Okazaki, Y.*, et al.*, *Effect of alloying elements on anodic polarization properties of titanium alloys in acid solutions.* Materials Transactions, JIM, 1994. **35**(1): p. 58-66.

17. Mohammed, M.T.*, et al.*, *Beta Titanium Alloys: The Lowest Elastic Modulus for Biomedical Applications: A Review.* Int. J. Chem., Nucl., Metall. Mater. Eng, 2014. **8**: p. 1123-1127.

18. Li, Y.*, et al.*, *New Developments of Ti-Based Alloys for Biomedical Applications.* Materials (Basel), 2014. **7**(3): p. 1709-1800.

19. Hussein, M.A.*, et al.*, *Wear characteristics of metallic biomaterials: a review.* Materials, 2015. **8**(5): p. 2749-2768.

20. Kuroda, D.*, et al.*, *Design and mechanical properties of new β type titanium alloys for implant materials.* Materials Science and Engineering: A, 1998. **243**(1-2): p. 244-249.

21. Sahu, S.*, et al.*, *Potentiodynamic behaviour of Ti alloys in physiological solution containing lubricant.* Materials Letters, 2010. **64**(1): p. 12-14.

22. Mischler, S., *Triboelectrochemical techniques and interpretation methods in tribocorrosion: a comparative evaluation.* Tribology International, 2008. **41**(7): p. 573-583.

23. Runa, M.J.*, et al.*, *Tribocorrosion response of the Ti6Al4V alloys commonly used in femoral stems.* Tribology International, 2013. **68**: p. 85-93.

24. More, N.S.*, et al.*, *Tribocorrosion behavior of β titanium alloys in physiological solutions containing synovial components.* Materials Science and Engineering: C, 2011. **31**(2): p. 400-408.

25. National Joint Registry for England, W.N.I.*, et al.*, *12th annual report 2015.* 2015: National Joint Registry.

26. Garellick, G.*, et al.*, *Swedish Hip Arthroplasty Register: Annual Report, 2008.* Department of Orthopaedics, Sahlgrenska University Hospital, 2009.

27. Kiefer, H., *Differences and opportunities of THA in the USA, Asia and Europe*, in *Bioceramics and Alternative Bearings in Joint Arthroplasty*. 2007, Springer. p. 3-8.

28. Jacobs, M.A*., et al.*, *Comparison of wear rates for metal-on polyethylene and metal-on-metal hips.* The Journal of Arthroplasty, 1997. **12**(2): p. 225.

29. Yew, A*., et al.*, *Analysis of contact mechanics in McKee-Farrar metal-on-metal hip implants.* Proceedings of the institution of mechanical engineers, Part H: Journal of engineering in medicine, 2003. **217**(5): p. 333-340.

30. Tipper, J.L*., et al.*, *(iv) The science of metal-on-metal articulation.* Current Orthopaedics, 2005. **19**(4): p. 280-287.

31. Rieker, C.B*., et al.*, *Development and validation of a second-generation metal-on-metal bearing: laboratory studies and analysis of retrievals.* The Journal of arthroplasty, 2004. **19**(8): p. 5-11.

32. Howie, D.W*., et al.*, *Metal-on-metal resurfacing versus total hip replacement—the value of a randomized clinical trial.* Orthopedic Clinics, 2005. **36**(2): p. 195-201.

33. Rodrigues, N.R*., et al.*, *Preliminary investigation on the tribocorrosion behaviour of nanotubular structured Ti6Al4V surfaces.* Materials Letters, 2018. **213**: p. 214-217.

34. Yan, Y., *Corrosion and trib-corrosion behaviour of metallic orthopaedic implant materials.* 2006.

35. Mercer, R., *Anthology of orthopaedics.* Edinburgh, London: Livingstone LTD, 1966.

36. Dowson, D*., et al.*, *Metal-on-metal hip joint tribology.* Proceedings of the Institution of Mechanical Engineers, Part H: Journal of Engineering in Medicine, 2006. **220**(2): p. 107-118.

37. Gomez, P.F*., et al.*, *Early attempts at hip arthroplasty: 1700s to 1950s.* The Iowa orthopaedic journal, 2005. **25**: p. 25.

38. Chan, F.W*., et al.*, *Wear and lubrication of metal-on-metal hip implants.* Clinical Orthopaedics and Related Research®, 1999. **369**: p. 10-24.

39. McKee, G.K*., et al.*, *Replacement of arthritic hips by the McKee-Farrar prosthesis.* The Journal of bone and joint surgery. British volume, 1966. **48**(2): p. 245-259.

40. Charnley, J., *Arthroplasty of the hip. A new operation.* Lancet, 1961. **1**: p. 1129-1132.

41.   Boutin, P., *L'arthroplastie totale de la hanche par prothèse en alumine.* International Orthopaedics, 1977. **1**(2): p. 87-94.

42.   Catledge, S.A.*, et al.*, *Structural and mechanical properties of nanostructured metalloceramic coatings on cobalt chrome alloys.* Applied physics letters, 2003. **82**(10): p. 1625-1627.

43.   Ma, L., *Wear Behaviour of Biolox delta ceramic Composite for Joint Replacements.* 2010.

44.   Learmonth, I.D.*, et al.*, *Clinical experience with metal-on-metal total joint replacements: indications and results.* Proceedings of the Institution of Mechanical Engineers, Part H: Journal of Engineering in Medicine, 2006. **220**(2): p. 229-237.

45.   Niinomi, M., *Metallic biomaterials.* J Artif Organs, 2008. **11**(3): p. 105-10.

46.   Wang, K., *The use of titanium for medical applications in the USA.* Materials Science and Engineering: A, 1996. **213**(1-2): p. 134-137.

47.   Ikeda, T.*, et al.*, *Polyneuropathy caused by cobalt–chromium metallosis after total hip replacement.* Muscle & nerve, 2010. **42**(1): p. 140-143.

48.   Khan, W.S.*, et al.*, *Chromium, cobalt and titanium metallosis involving a Nottingham shoulder replacement.* The Journal of bone and joint surgery. British volume, 2008. **90**(4): p. 502-505.

49.   Oldenburg, M.*, et al.*, *Severe cobalt intoxication due to prosthesis wear in repeated total hip arthroplasty.* The Journal of arthroplasty, 2009. **24**(5): p. 825-e15.

50.   Czekaj, J.*, et al.*, *Metallosis and cobalt–chrome intoxication after hip resurfacing arthroplasty.* Journal of Orthopaedic Science, 2016. **21**(3): p. 389-394.

51.   Black, J.*, et al.*, *Metallosis associated with a stable titanium-alloy femoral component in total hip replacement. A case report.* JBJS, 1990. **72**(1): p. 126-130.

52.   Steens, W.*, et al.*, *Chronic cobalt poisoning in endoprosthetic replacement.* Der Orthopade, 2006. **35**(8): p. 860-864.

53.   Sumner, D.R.*, et al.*, *Functional adaptation and ingrowth of bone vary as a function of hip implant stiffness.* J Biomech, 1998. **31**(10): p. 909-17.

54.   Oh, I.-H.*, et al.*, *Mechanical properties of porous titanium compacts prepared by powder sintering.* Scripta Materialia, 2003. **49**(12): p. 1197-1202.

55. Semlitsch, M.F.*, et al.*, *Joint replacement components made of hot-forged and surface-treated Ti-6Al-7Nb alloy.* Biomaterials, 1992. **13**(11): p. 781-8.

56. Okazaki, Y.*, et al.*, *Comparison of metal release from various metallic biomaterials in vitro.* Biomaterials, 2005. **26**(1): p. 11-21.

57. McGregor, D.B.*, et al.*, *Evaluation of the carcinogenic risks to humans associated with surgical implants and other foreign bodies - a report of an IARC Monographs Programme Meeting. International Agency for Research on Cancer.* Eur J Cancer, 2000. **36**(3): p. 307-13.

58. Lan, C.*, et al.*, *Microstructure, texture evolution and mechanical properties of cold rolled Ti-32.5 Nb-6.8 Zr-2.7 Sn biomedical beta titanium alloy.* Journal of Materials Science & Technology, 2018. **34**(5): p. 788-792.

59. Thair, L.*, et al.*, *Nitrogen ion implantation and in vitro corrosion behavior of as-cast Ti–6Al–7Nb alloy.* Corrosion Science, 2002. **44**(11): p. 2439-2457.

60. Williams, D.F., *On the mechanisms of biocompatibility.* Biomaterials, 2008. **29**(20): p. 2941-53.

61. Calin, M.*, et al.*, *Designing biocompatible Ti-based metallic glasses for implant applications.* Mater Sci Eng C Mater Biol Appl, 2013. **33**(2): p. 875-83.

62. Hallab, N.J.*, et al.*, *Lymphocyte responses in patients with total hip arthroplasty.* Journal of Orthopaedic Research, 2005. **23**(2): p. 384-391.

63. Sargeant, A.*, et al.*, *Hip implants: paper V. Physiological effects.* Materials & design, 2006. **27**(4): p. 287-307.

64. Laing, P.G.*, et al.*, *Tissue reaction in rabbit muscle exposed to metallic implants.* J Biomed Mater Res, 1967. **1**(1): p. 135-49.

65. Germain, M.A.*, et al.*, *Comparison of the cytotoxicity of clinically relevant cobalt-chromium and alumina ceramic wear particles in vitro.* Biomaterials, 2003. **24**(3): p. 469-79.

66. Tipper, J.L.*, et al.*, *Wear and functional biological activity of wear debris generated from UHMWPE-on-zirconia ceramic, metal-on-metal and alumina ceramic-on-ceramic hip prostheses during hip simulator testing.* Friction, Lubrication, and Wear of Artificial Joints, Professional Engineering Publishing: Bury St Edmunds, 2003: p. 7-28.

67. Devine, T.M.*, et al.*, *Wrought cobalt-chromium surgical implant alloys.* Journal of Materials Science, 1972. **7**(1): p. 126-128.

68. Chen, Q.*, et al.*, *Metallic implant biomaterials.* Materials Science and Engineering: R: Reports, 2015. **87**: p. 1-57.

69. Goldberg, J.R.*, et al.*, *The electrochemical and mechanical behavior of passivated and TiN/AlN-coated CoCrMo and Ti6Al4V alloys.* Biomaterials, 2004. **25**(5): p. 851-864.

70. Barril, S.*, et al.*, *Influence of fretting regimes on the tribocorrosion behaviour of Ti6Al4V in 0.9 wt.% sodium chloride solution.* Wear, 2004. **256**(9-10): p. 963-972.

71. Hiromoto, S.*, et al.*, *Effect of Albumin on Fretting-Corrosion Mechanism of a T–Al–V Alloy.* European cells and materials, 2004. **7**(2): p. 40-41.

72. Hatem, A.*, et al.*, *Tribocorrosion behavior of DLC-coated Ti-6Al-4V alloy deposited by PIID and PEMS+ PIID techniques for biomedical applications.* Surface and Coatings Technology, 2017. **332**: p. 223-232.

73. Trino, L.D.*, et al.*, *Titanium surface bio-functionalization using osteogenic peptides: Surface chemistry, biocompatibility, corrosion and tribocorrosion aspects.* Journal of the mechanical behavior of biomedical materials, 2018. **81**: p. 26-38.

74. Lima, P.*, et al.*, *Tribocorrosion behavior of Ti–C–O–N nanostructured thin films (black) for decorative applications.* Tribology International, 2013. **68**: p. 1-10.

75. Bailey, R.*, et al.*, *Corrosion and Tribocorrosion Performance of Pack-Carburized Commercially Pure Titanium with Limited Oxygen Diffusion in a 0.9% NaCl Solution.* Journal of Bio-and Tribo-Corrosion, 2018. **4**(1): p. 6.

76. Manhabosco, T.M.*, et al.*, *Tribocorrosion of diamond-like carbon deposited on Ti6Al4V.* Tribology letters, 2009. **33**(3): p. 193-197.

77. Mallia, B.*, et al.*, *The corrosion–wear response of Cr–Ti coatings.* Wear, 2007. **263**(1-6): p. 679-690.

78. Hill, M.R.*, et al.*, *Preliminary tribological evaluation of nanostructured diamond coatings against ultra-high molecular weight polyethylene.* Journal of Biomedical Materials Research Part B: Applied Biomaterials: An Official Journal of The Society for Biomaterials, The Japanese Society for Biomaterials, and The Australian Society for Biomaterials and the Korean Society for Biomaterials, 2008. **85**(1): p. 140-148.

79. Basak, A.K.*, et al., Corrosion–wear behaviour of thermal sprayed nanostructured FeCu/WC–Co coatings.* Wear, 2006. **261**(9): p. 1042-1050.

80. Jacobs, J.J.*, et al., Can metal levels be used to monitor metal-on-metal hip arthroplasties?* The Journal of arthroplasty, 2004. **19**(8): p. 59-65.

81. Merola, M.*, et al., Materials for Hip Prostheses: A Review of Wear and Loading Considerations.* Materials, 2019. **12**(3): p. 495.

82. Licausi, M.P.*, et al., Tribocorrosion mechanisms of Ti6Al4V in artificial saliva by zero-resistance ammetry (ZRA) technique.* Journal of Bio-and Tribo-Corrosion, 2015. **1**(1): p. 8.

83. Choubey, A.*, et al., Tribological behaviour of Ti-based alloys in simulated body fluid solution at fretting contacts.* Materials Science and Engineering: A, 2004. **379**(1-2): p. 234-239.

84. Souza, S.A.*, et al., Effect of the addition of Ta on microstructure and properties of Ti–Nb alloys.* Journal of alloys and compounds, 2010. **504**(2): p. 330-340.

85. von Recum, A.F., *Handbook of biomaterials evaluation: scientific, technical and clinical testing of implant materials*. 1998: CRC Press.

86. Alam, M.O.*, et al., Response of Ti–6Al–4V and Ti–24Al–11Nb alloys to dry sliding wear against hardened steel.* Tribology International, 2002. **35**(6): p. 357-362.

87. Lee, T.*, et al., Tribological and corrosion behaviors of warm-and hot-rolled Ti-13Nb-13Zr alloys in simulated body fluid conditions.* International journal of nanomedicine, 2015. **10**(Suppl 1): p. 207.

88. Fellah, M.*, et al., Comparative Tribological study of biomaterials AISI 316L and Ti-6Al-7Nb.* TMS, 2014. **237**: p. 237-246.

89. Wang, S.*, et al., Tribological behaviour of titanium alloy modified by carbon–DLC composite film.* Surface Engineering, 2015. **31**(12): p. 934-941.

90. Majumdar, P.*, et al., Wear response of heat-treated Ti–13Zr–13Nb alloy in dry condition and simulated body fluid.* Wear, 2008. **264**(11-12): p. 1015-1025.

91. Wimmer, M.A.*, et al., Wear mechanisms in metal-on-metal bearings: The importance of tribochemical reaction layers.* Journal of Orthopaedic Research, 2010. **28**(4): p. 436-443.

92.   Chandramohan, P.*, et al.*, *Laser additive manufactured Ti–6Al–4V alloy: tribology and corrosion studies.* The International Journal of Advanced Manufacturing Technology, 2017. **92**(5-8): p. 3051-3061.

93.   Hutchings, I.*, et al.*, *Tribology: friction and wear of engineering materials*. 2017: Butterworth-Heinemann.

94.   Leyens, C.*, et al.*, *Titanium and titanium alloys: fundamentals and applications*. 2003: John Wiley & Sons.

95.   Runa, M.*, et al.*, *In vitro Evaluation of Tribocorrosion Induced Failure Mechanisms at the Cell-Metal Interface for the Hip Implant Application.* Advanced Engineering Materials, 2017. **19**(5): p. 1600797.

96.   Smith, L.S.*, et al.*, *Welding titanium: A designers and users handbook*. 1999: Titanium Information Group.

97.   Murray, N.G.D.*, et al.*, *Mechanical and physical properties of Titanium-12molybdenum-6zirconium-2iron beta titanium alloy*, in *Titanium, Niobium, Zirconium, and Tantalum for Medical and Surgical Applications*. 2006, ASTM International.

98.   Afonso, C.R.*, et al.*, *High resolution transmission electron microscopy study of the hardening mechanism through phase separation in a beta-Ti-35Nb-7Zr-5Ta alloy for implant applications.* Acta Biomater, 2010. **6**(4): p. 1625-9.

99.   Bertolini, R.*, et al.*, *Influence of the machining cooling strategies on the dental tribocorrosion behaviour of wrought and additive manufactured Ti6Al4V.* Biotribology, 2017(11): p. 60-68.

100.   Wang, Z.*, et al.*, *Tribocorrosion behaviour of a biomedical Ti-25Nb-3Mo-3Zr-2Sn alloy in Ringer's solution.* Mater Sci Eng C Mater Biol Appl, 2017. **76**: p. 1094-1102.

101.   Sadeghpour, S.*, et al.*, *A new multi-element beta titanium alloy with a high yield strength exhibiting transformation and twinning induced plasticity effects.* Scripta Materialia, 2018. **145**: p. 104-108.

102.   Silva, J.I.*, et al.*, *Corrosion and tribocorrosion behavior of Ti-TiB-TiNx in-situ hybrid composite synthesized by reactive hot pressing.* J Mech Behav Biomed Mater, 2017. **74**: p. 195-203.

103.   Davoren, B.*, et al.*, *Tribocorrosion of friction-stir-welded Ti6AL4V in 3.5% NaCl aqueous solution.* Wear, 2017. **390**: p. 246-252.

104. Yang, X.*, et al., Corrosion-wear of beta-Ti alloy TMZF (Ti-12Mo-6Zr-2Fe) in simulated body fluid.* Acta Biomater, 2016. **42**: p. 429-439.

105. Bao, M.*, et al., Tribocorrosion Behavior of Ti–Cu Alloy in Hank's Solution for Biomedical Application.* Journal of Bio-and Tribo-Corrosion, 2018. **4**(2): p. 29.

106. Akahori, T.*, et al., Fatigue, fretting fatigue and corrosion characteristics of biocompatible beta type titanium alloy conducted with various thermo-mechanical treatments.* Materials transactions, 2004. **45**(5): p. 1540-1548.

107. Lu, J.*, et al., Effect of microstructure characteristic on mechanical properties and corrosion behavior of new high strength Ti-1300 beta titanium alloy.* Journal of Alloys and Compounds, 2017. **727**: p. 1126-1135.

108. Dănăilă, E.*, et al. The Effect of Normal Force on Tribocorrosion Behaviour of Ti-10Zr Alloy and Porous TiO2-ZrO2 Thin Film Electrochemical Formed.* IOP Publishing.

109. Geetha, M.*, et al., Influence of microstructure and alloying elements on corrosion behavior of Ti–13Nb–13Zr alloy.* Corrosion Science, 2004. **46**(4): p. 877-892.

110. Zhou, Y.L.*, et al., Corrosion resistance and biocompatibility of Ti–Ta alloys for biomedical applications.* Materials Science and Engineering: A, 2005. **398**(1-2): p. 28-36.

111. Miller, P.D.*, et al., Friction and wear properties of titanium.* Wear, 1958. **2**(2): p. 133-140.

112. Ureña, J.*, et al., Strategies for improvement the wear and tribocorrosion behaviour of titanium alloys.*

113. Niinomi, M.*, et al., Corrosion wear fracture of new β type biomedical titanium alloys.* Materials Science and Engineering: A, 1999. **263**(2): p. 193-199.

114. Li, S.J.*, et al., Wear characteristics of Ti–Nb–Ta–Zr and Ti–6Al–4V alloys for biomedical applications.* Wear, 2004. **257**(9-10): p. 869-876.

115. Jaffee, R.I., *The physical metallurgy of titanium alloys.* Progress in metal physics, 1958. **7**: p. 65-163.

116. Wanhill, R.*, et al., Fatigue of beta processed and beta heat-treated titanium alloys.* 2011: Springer Science & Business Media.

117. Inoue, A., *Stabilization of metallic supercooled liquid and bulk amorphous alloys.* Acta materialia, 2000. **48**(1): p. 279-306.

118. Zhao, X*., et al., Effect of deformation-induced ω phase on the mechanical properties of metastable β-type Ti–V alloys.* Materials Transactions, 2012. **53**(8): p. 1379-1384.

119. Shao, G*., et al., On the ω phase formation in Cr–Al and Ti–Al–Cr alloys.* Acta materialia, 2000. **48**(14): p. 3671-3685.

120. Shao, G*., et al., Prediction of ω phase formation in Ti–Al–X alloys.* Materials Science and Engineering: A, 2002. **329**: p. 914-919.

121. Ping, D., *Review on ω phase in body-centered cubic metals and alloys.* Acta Metallurgica Sinica (English Letters), 2014. **27**(1): p. 1-11.

122. Zheng, Y*., et al. On the mechanism of nucleation and growth of omega phase in beta titanium alloys'.*

123. Lopes, E.S.N*., et al., Effects of double aging heat treatment on the microstructure, Vickers hardness and elastic modulus of Ti–Nb alloys.* Materials characterization, 2011. **62**(7): p. 673-680.

124. Gragg, J.E., *The omega phase in titanium-vanadium alloys.* 1964.

125. He, G*., et al., Ti alloy design strategy for biomedical applications.* Materials Science and Engineering: C, 2006. **26**(1): p. 14-19.

126. Weiss, I*., et al., Thermomechanical processing of beta titanium alloys—an overview.* Materials Science and Engineering: A, 1998. **243**(1-2): p. 46-65.

127. Abdel-Hady, M*., et al., General approach to phase stability and elastic properties of β-type Ti-alloys using electronic parameters.* Scripta Materialia, 2006. **55**(5): p. 477-480.

128. Mohammed, M.T., *Development of a new metastable beta titanium alloy for biomedical applications.* Karbala International Journal of Modern Science, 2017. **3**(4): p. 224-230.

129. Buciumeanu, M*., et al., Tribocorrosion behavior of additive manufactured Ti-6Al-4V biomedical alloy.* Tribology International, 2018. **119**: p. 381-388.

130. Semlitsch, M*., et al., Titanium-aluminium-niobium alloy, development for biocompatible, high strength surgical implants.* Biomed Tech (Berl), 1985. **30**(12): p. 334-9.

131. Donachie, M.J., *Titanium and Titanium alloys: source book: a collection of outstanding articles from the technical literature.* 1982: ASM international.

132. Cui, W.F*., et al., Microstructures and properties of biomedical TiNbZrFe β-titanium alloy under aging conditions.* Materials Science and Engineering: A, 2009. **527**(1-2): p. 258-262.

133. Zhou, Y.-L.*, et al.*, *Microstructures and mechanical properties of Ti–50 mass% Ta alloy for biomedical applications.* Journal of Alloys and Compounds, 2008. **466**(1-2): p. 535-542.

134. Cordeiro, J.M.*, et al.*, *Development of binary and ternary titanium alloys for dental implants.* Dental Materials, 2017. **33**(11): p. 1244-1257.

135. Banerjee, R.*, et al.*, *A novel combinatorial approach to the development of beta titanium alloys for orthopaedic implants.* Materials Science and Engineering: C, 2005. **25**(3): p. 282-289.

136. Wang, Z.*, et al.*, *Tribocorrosion behavior of Ti-30Zr alloy for dental implants.* Materials Letters, 2018. **218**: p. 190-192.

137. Yazdi, R.*, et al.*, *Bio-corrosion behaviour of oxygen diffusion layer on Ti-6Al-4V during tribocorrosion.* Corrosion Science, 2017. **128**: p. 23-32.

138. Landolt, D.*, et al.*, *Tribocorrosion of passive metals and coatings.* 2011: Elsevier.

139. Nakagawa, M.*, et al.*, *Corrosion behavior of pure titanium and titanium alloys in fluoride-containing solutions.* Dental materials journal, 2001. **20**(4): p. 305-314.

140. Ling, F.-W.*, et al.*, *Deformation behavior and texture development in beta Ti-V alloys.* Metallurgical Transactions, 1974. **5**(1): p. 179.

141. Moore, M.A.*, et al.*, *Plastic deformation below worn surfaces.* Metallurgical Transactions A, 1976. **7**(12): p. 1833-1839.

142. Uhlig, H.H., *Uhlig's corrosion handbook.* Vol. 51. 2011: John Wiley & Sons.

143. Saikko, V., *A multidirectional motion pin-on-disk wear test method for prosthetic joint materials.* Journal of Biomedical Materials Research: An Official Journal of The Society for Biomaterials, The Japanese Society for Biomaterials, and the Australian Society for Biomaterials, 1998. **41**(1): p. 58-64.

144. Roberge, P.R., *Handbook of corrosion engineering.* 2000: McGraw-Hill.

145. Davis, J.R., *Corrosion: Understanding the basics.* 2000: Asm International.

146. Stansbury, E.E.*, et al.*, *Fundamentals of electrochemical corrosion.* 2000: ASM international.

147. Marcus, P., *Corrosion mechanisms in theory and practice.* 2011: CRC press.

148. Kaesche, H., *Corrosion of metals: physicochemical principles and current problems.* 2012: Springer Science & Business Media.

149. Landolt, D., *Corrosion and surface chemistry of metals.* 2007: EPFL press.

150. Cao, L*., et al.*, *The Tribocorrosion and Corrosion Properties of Thermally Oxidized Ti6Al4V Alloy in 0.9 wt.% NaCl Physiological Saline.* Coatings, 2018. **8**(8): p. 285.

151. Jacobs, J.J*., et al.*, *Metal degradation products: a cause for concern in metal-metal bearings?* Clinical Orthopaedics and Related Research®, 2003. **417**: p. 139-147.

152. McCafferty, E., *Introduction to corrosion science. 2010.* Alexandria: Springer.

153. Contu, F*., et al.*, *Corrosion behaviour of CoCrMo implant alloy during fretting in bovine serum.* Corrosion science, 2005. **47**(8): p. 1863-1875.

154. Zhang, Y*., et al.*, *Influence of microstructure evolution on tribocorrosion of 304SS in artificial seawater.* Corrosion Science, 2014. **88**: p. 423-433.

155. Vieira, A.C*., et al.*, *Mechanical and electrochemical deterioration mechanisms in the tribocorrosion of Al alloys in NaCl and in NaNO3 solutions.* Corrosion Science, 2012. **54**: p. 26-35.

156. Atapour, M*., et al.*, *Corrosion behavior of β titanium alloys for biomedical applications.* Materials Science and Engineering: C, 2011. **31**(5): p. 885-891.

157. Lucas, L.C*., et al.*, *Susceptibility of surgical cobalt-base alloy to pitting corrosion.* Journal of biomedical materials research, 1982. **16**(6): p. 799-810.

158. Kuhn, A.T., *Corrosion of Co-Cr alloys in aqueous environments.* Biomaterials, 1981. **2**(2): p. 68-77.

159. Khan, M.A*., et al.*, *Conjoint corrosion and wear in titanium alloys.* Biomaterials, 1999. **20**(8): p. 765-772.

160. Rossi, S*., et al.*, *Wear-corrosion of nitrided steel: corrosion potential monitoring to evaluate the effect of test parameters.* Materials and Corrosion, 2000. **51**(8): p. 552-556.

161. Wang, Y*., et al.*, *Influence of bias voltage on structure and tribocorrosion properties of TiSiCN coating in artificial seawater.* Materials Characterization, 2017. **127**: p. 198-208.

162. Syrett, B.C*., et al.*, *Pitting resistance of new and conventional orthopedic implant materials—effect of metallurgical condition.* Corrosion, 1978. **34**(4): p. 138-148.

163. Williams, D.F., *Corrosion of implant materials.* Annual review of materials science, 1976. **6**(1): p. 237-266.

164. Huth, S., *Metallic materials for tribocorrosion systems*, in *Tribocorrosion of Passive Metals and Coatings*. 2011, Elsevier. p. 265-295.

165. Lin, H.Y*., et al., In vitro biocorrosion of Co☐ Cr☐ Mo implant alloy by macrophage cells.* Journal of Orthopaedic Research, 2004. **22**(6): p. 1231-1236.

166. Kamachimudali, U*., et al., Corrosion of bio implants.* Sadhana, 2003. **28**(3-4): p. 601-637.

167. Hanawa, T., *Corrosion measurements of biomedical metallic materials.* Zairyo-to-Kankyo, 2000. **49**(8): p. 463-468.

168. Hensten-Pettersen, A*., et al., Systemic toxicity and hypersensitivity.* Biomaterials Science, 2004.

169. Brodner, W*., et al., Elevated serum cobalt with metal-on-metal articulating surfaces.* The Journal of bone and joint surgery. British volume, 1997. **79**(2): p. 316-321.

170. Elfick, A*., et al., The influence of femoral head surface roughness on the wear of UHMWPE sockets in cementless total hip replacements.* J. Biomed. Mater. Res.: Appl. Biomechanics, 1999. **48**(5): p. 712-718.

171. Muñiz, C.S*., et al., Reference values for trace and ultratrace elements in human serum determined by double-focusing ICP-MS.* Biological trace element research, 2001. **82**(1-3): p. 259-272.

172. Black, J*., et al., Serum concentrations of chromium, cobalt and nickel after total hip replacement: a six month study.* Biomaterials, 1983. **4**(3): p. 160-164.

173. Visuri, T*., et al., Cancer risk after McKee-Farrar total hip replacement.* Orthopedics, 1991. **14**(2): p. 137-142.

174. Willert, H.G*., et al., Wear behavior and histopathology of classic cemented metal on metal hip endoprostheses.* Clinical Orthopaedics and Related Research (1976-2007), 1996. **329**: p. S160-S186.

175. Koegel, A*., et al., Release of corrosion products by F-75 cobalt base alloy in the rat. I: Acute serum elevations.* Journal of biomedical materials research, 1984. **18**(5): p. 513-522.

176. de De Micheli, S.M*., et al., Electrochemical study of corrosion in NiCr dental alloys.* Biomaterials, 1982. **3**(4): p. 209-212.

177. Stemp, M.*, et al.*, *The effect of mechanical and electrochemical parameters on the tribocorrosion rate of stainless steel in sulphuric acid.* Wear, 2003. **255**(1-6): p. 466-475.

178. Jacobs, J.J.*, et al.*, *Metal release in patients who have had a primary total hip arthroplasty. A prospective, controlled, longitudinal study.* JBJS, 1998. **80**(10): p. 1447-58.

179. Hallab, N.J.*, et al.*, *Orthopedic implant fretting corrosion.* 2003, De Gruyter.

180. Donachie, M.J., *Titanium: a technical guide.* 2000: ASM international.

181. Lütjering, G.*, et al.*, *Beta Alloys.* 2007: Springer.

182. Revathi, A.*, et al.*, *Degradation mechanisms and future challenges of titanium and its alloys for dental implant applications in oral environment.* Materials Science and Engineering: C, 2017. **76**: p. 1354-1368.

183. Kelly, R.G.*, et al.*, *Electrochemical techniques in corrosion science and engineering.* 2002: CRC Press.

184. Polmear, I., *Light alloys: from traditional alloys to nanocrystals.* 2005: Elsevier.

185. Ho, W.-F., *A comparison of tensile properties and corrosion behavior of cast Ti–7.5 Mo with cp Ti, Ti–15Mo and Ti–6Al–4V alloys.* Journal of Alloys and Compounds, 2008. **464**(1-2): p. 580-583.

186. Wang, Y.B.*, et al.*, *Corrosion behaviour and biocompatibility evaluation of low modulus Ti–16Nb shape memory alloy as potential biomaterial.* Materials Letters, 2009. **63**(15): p. 1293-1295.

187. Mareci, D.*, et al.*, *Electrochemical behaviour of Ti alloys containing Mo and Ta as β-stabilizer elements for dental application.* Transactions of Nonferrous Metals Society of China, 2013. **23**(12): p. 3829-3836.

188. Nnamchi, P.S.*, et al.*, *Mechanical and electrochemical characterisation of new Ti–Mo–Nb–Zr alloys for biomedical applications.* Journal of the mechanical behavior of biomedical materials, 2016. **60**: p. 68-77.

189. Thair, L.*, et al.*, *Influence of microstructural changes on corrosion behaviour of thermally aged Ti-6Al-7Nb alloy.* Materials and Corrosion, 2004. **55**(5): p. 358-366.

190. Geetha, M.*, et al.*, *Effect of thermomechanical processing on microstructure of a Ti–13Nb–13Zr alloy.* Journal of Alloys and Compounds, 2001. **329**(1-2): p. 264-271.

191. Mohammed, M.T.*, et al., Effect of thermo-mechanical processing on microstructure and electrochemical behavior of Ti–Nb–Zr–V new metastable β titanium biomedical alloy.* Transactions of Nonferrous Metals Society of China, 2015. **25**(3): p. 759-769.

192. Vasilescu, E.*, et al., In vitro biocompatibility and corrosion resistance of a new implant titanium base alloy.* Journal of Materials Science: Materials in Medicine, 2010. **21**(6): p. 1959-1968.

193. Cvijović-Alagić, I.*, et al., Wear and corrosion behaviour of Ti–13Nb–13Zr and Ti–6Al–4V alloys in simulated physiological solution.* Corrosion Science, 2011. **53**(2): p. 796-808.

194. Alves, A.P.R.*, et al., A study on corrosion resistance of the Ti–10Mo experimental alloy after different processing methods.* Materials Science and Engineering: C, 2004. **24**(5): p. 693-696.

195. Mohammed, M.T.*, et al., Influence of thermomechanical processing on biomechanical compatibility and electrochemical behavior of new near beta alloy, Ti-20.6 Nb-13.6 Zr-0.5 V.* International journal of nanomedicine, 2015. **10**(Suppl 1): p. 223.

196. Mohammed, M.T.*, et al., Microstructure, mechanical properties and electrochemical behavior of a novel biomedical titanium alloy subjected to thermo-mechanical processing including aging.* Journal of Alloys and Compounds, 2015. **634**: p. 272-280.

197. De Almeida, L.H.*, et al., Corrosion resistance of aged Ti–Mo–Nb alloys for biomedical applications.* Journal of Alloys and Compounds, 2014. **615**: p. S666-S669.

198. Chelariu, R.*, et al., Metastable beta Ti-Nb-Mo alloys with improved corrosion resistance in saline solution.* Electrochimica Acta, 2014. **137**: p. 280-289.

199. Ponthiaux, P.*, et al., Electrochemical techniques for studying tribocorrosion processes.* Wear, 2004. **256**(5): p. 459-468.

200. Stachowiak, G.W.*, et al., Adhesion and adhesive wear.* Engineering Tribology, Butterworth-Heinemann, ABD, 2001: p. 533-553.

201. Garcıa, I.*, et al., Corrosion-wear of passivating materials in sliding contacts based on a concept of active wear track area.* Wear, 2001. **249**(5-6): p. 452-460.

202. Lebeck, A.O., *Parallel sliding load support in the mixed friction regime. Part 1—The Experimental Data.* Journal of tribology, 1987. **109**(1): p. 189-195.

203. Wang, X.*, et al.*, *The effect of laser texturing of SiC surface on the critical load for the transition of water lubrication mode from hydrodynamic to mixed.* Tribology International, 2001. **34**(10): p. 703-711.

204. Williams, J., *Engineering tribology.* 2005: Cambridge University Press.

205. Dowson, D.*, et al.*, *A hip joint simulator study of the performance of metal-on-metal joints: Part II: design.* The Journal of arthroplasty, 2004. **19**(8): p. 124-130.

206. Szucs, M.*, et al.*, *The stribeck curve in cold flat rolling.* International Journal of Material Forming, 2017. **10**(1): p. 99-107.

207. Kayaba, T.*, et al.*, *Frictional properties of surface films in air and in high vacuum.* Wear, 1978. **47**(1): p. 93-105.

208. Souza, J.C.M.*, et al.*, *Wear and corrosion interactions on titanium in oral environment: literature review.* Journal of Bio-and Tribo-Corrosion, 2015. **1**(2): p. 13.

209. Yan, Y.*, et al.*, *Understanding the role of corrosion in the degradation of metal-on-metal implants.* Proc Inst Mech Eng H, 2006. **220**(2): p. 173-81.

210. Landolt, D.*, et al.*, *Electrochemical methods in tribocorrosion: a critical appraisal.* Electrochimica acta, 2001. **46**(24-25): p. 3913-3929.

211. Peterson, M.B., *Classification of wear processes.* Wear control handbook, 1980: p. 9-15.

212. Akagaki, T.*, et al.*, *Effects of additives on wear mode and morphology of wear debris generated in the lubricated sliding of steel.* Wear, 1991. **143**(1): p. 119-135.

213. Straffelini, G., *Friction and wear: methodologies for design and control.* 2015: Springer.

214. Katti, K.S., *Biomaterials in total joint replacement.* Colloids and surfaces B: Biointerfaces, 2004. **39**(3): p. 133-142.

215. Scholes, S.C.*, et al.*, *The wear of metal-on-metal total hip prostheses measured in a hip simulator.* Proceedings of the Institution of Mechanical Engineers, Part H: Journal of Engineering in Medicine, 2001. **215**(6): p. 523-530.

216. Oonishi, H.*, et al.*, *Alumina hip joints characterized by run-in wear and steady-state wear to 14 million cycles in hip-simulator model.* Journal of

Biomedical Materials Research Part A: An Official Journal of The Society for Biomaterials, The Japanese Society for Biomaterials, and The Australian Society for Biomaterials and the Korean Society for Biomaterials, 2004. **70**(4): p. 523-532.

217. Hanawa, T.*, et al.*, *Surface modification of metals and alloys in a human body environment.* Corrosion Engineering, 1998. **47**(12): p. 895-908.

218. Stachowiak, G.*, et al.*, *Engineering tribology.* 2013: Butterworth-Heinemann.

219. Czichos, H.*, et al.*, *Tribology Handbook Friction and Wear.* German: sn, 1992.

220. Zum Gahr, K.H., *Microstructure and wear of materials.* Vol. 10. 1987: Elsevier.

221. Totten, G.E.*, et al.*, *Mechanical tribology: materials, characterization, and applications.* 2004: CRC Press.

222. Dalmaz, G.*, et al.*, *Tribology Research: From Model Experiment to Industrial Problem: a Century of Efforts in Mechanics, Materials Science and Physico-chemistry.* 2001: Elsevier.

223. Khonsari, M.*, et al.*, *Applied Tribology 2e: Bearing design and lubrication, John Willy & Sons.* 2008, Ltd.

224. Neville, A.*, et al.*, *Compatibility between tribological surfaces and lubricant additives—how friction and wear reduction can be controlled by surface/lube synergies.* Tribology International, 2007. **40**(10-12): p. 1680-1695.

225. Flour, L., *Contact fatigue of automotive gears: evolution and effects of residual stresses introduced by surface treatments.* Fatigue & Fracture of Engineering Materials & Structures, 2000. **23**(3): p. 217-228.

226. Burwell Jr, J.T., *Survey of possible wear mechanisms.* Wear, 1957. **1**(2): p. 119-141.

227. Wood, R.J.K.*, et al.*, *A critical review of the tribocorrosion of cemented and thermal sprayed tungsten carbide.* Tribology International, 2018. **119**: p. 491-509.

228. Archard, J., *Contact and rubbing of flat surfaces.* Journal of applied physics, 1953. **24**(8): p. 981-988.

229. Liao, Y.*, et al.*, *CoCrMo metal-on-metal hip replacements.* Phys Chem Chem Phys, 2013. **15**(3): p. 746-56.

230. Wright, K.W.J.*, et al.*, *Wear studies on prosthetic materials using the pin-on-disc machine.* Biomaterials, 1982. **3**(1): p. 41-48.

231. Espallargas, N.*, et al.*, *A metal ion release study of CoCrMo exposed to corrosion and tribocorrosion conditions in simulated body fluids.* Wear, 2015. **332**: p. 669-678.

232. Mischler, S.*, et al.*, *Wear of CoCrMo alloys used in metal-on-metal hip joints: a tribocorrosion appraisal.* Wear, 2013. **297**(1-2): p. 1081-1094.

233. Mischler, S.*, et al.*, *The role of passive oxide films on the degradation of steel in tribocorrosion systems.* Wear, 1999. **225**: p. 1078-1087.

234. Villanueva, J.*, et al.*, *Corrosion, tribology, and tribocorrosion research in biomedical implants: progressive trend in the published literature.* Journal of Bio-and Tribo-Corrosion, 2017. **3**(1): p. 1.

235. Landolt, D.*, et al.*, *Third body effects and material fluxes in tribocorrosion systems involving a sliding contact.* Wear, 2004. **256**(5): p. 517-524.

236. Diomidis, N.*, et al.*, *Tribo-electrochemical characterization of metallic biomaterials for total joint replacement.* Acta Biomater, 2012. **8**(2): p. 852-9.

237. Okazaki, Y., *Effect of friction on anodic polarization properties of metallic biomaterials.* Biomaterials, 2002. **23**(9): p. 2071-2077.

238. Cao, S.*, et al.*, *Tribocorrosion of passive metals in the mixed lubrication regime: theoretical model and application to metal-on-metal artificial hip joints.* Wear, 2015. **324**: p. 55-63.

239. Yan, Y.*, et al.*, *Real-time corrosion measurements to assess biotribocorrosion mechanisms with a hip simulator.* Tribology International, 2013. **63**: p. 115-122.

240. ASTM, *G119 - 09(2016): Standard Guide for Determining Synergism Between Wear and Corrosion.* 2016: West Conshohocken, PA, USA: ASTM International.

241. Yan, Y.*, et al.*, *Tribocorrosion in implants—assessing high carbon and low carbon Co–Cr–Mo alloys by in situ electrochemical measurements.* Tribology International, 2006. **39**(12): p. 1509-1517.

242. Martin, É.*, et al.*, *Influence of microstructure and texture on the corrosion and tribocorrosion behavior of Ti–6Al–4V.* Tribology International, 2010. **43**(5-6): p. 918-924.

243. Celis, J.P.*, et al.*, *Tribo-corrosion of materials: interplay between chemical, electrochemical, and mechanical reactivity of surfaces.* Wear, 2006. **261**(9): p. 939-946.

244. Mathew, M.T.*, et al.*, *Wear-corrosion synergism in a CoCrMo hip bearing alloy is influenced by proteins.* Clin Orthop Relat Res, 2012. **470**(11): p. 3109-17.

245. Akonko, S.*, et al.*, *Effects of cathodic protection on corrosive wear of 304 stainless steel.* Tribology Letters, 2005. **18**(3): p. 405-410.

246. Espallargas, N.*, et al.*, *Tribocorrosion behaviour of overlay welded Ni–Cr 625 alloy in sulphuric and nitric acids: Electrochemical and chemical effects.* Tribology International, 2010. **43**(7): p. 1209-1217.

247. Mischler, S.*, et al.*, *Effect of Corrosion on the Wear Behavior of Passivating Metals in Aqueous.* Thin Films in Tribology, 1993. **25**: p. 245.

248. Jemmely, P.*, et al.*, *Tribocorrosion behaviour of Fe–17Cr stainless steel in acid and alkaline solutions.* Tribology International, 1999. **32**(6): p. 295-303.

249. Barril, S.*, et al.*, *Triboelectrochemical investigation of the friction and wear behaviour of TiN coatings in a neutral solution.* Tribology International, 2001. **34**(9): p. 599-608.

250. Mischler, S.*, et al.*, *Influence of passivity on the tribocorrosion of carbon steel in aqueous solutions.* Wear, 2001. **251**(1-12): p. 1295-1307.

251. Revie, R.W., *Corrosion and corrosion control: an introduction to corrosion science and engineering.* 2008: John Wiley & Sons.

252. Neville, A.*, et al.*, *Characterisation of high-grade alloy behaviour in severe erosion–corrosion conditions.* Wear, 1999. **233**: p. 596-607.

253. Marques, I.d.S.V.*, et al.*, *Tribocorrosion behavior of biofunctional titanium oxide films produced by micro-arc oxidation: synergism and mechanisms.* journal of the mechanical behavior of biomedical materials, 2016. **60**: p. 8-21.

254. Mathew, M.T.*, et al.*, *TiCxOy thin films for decorative applications: tribocorrosion mechanisms and synergism.* Tribology International, 2008. **41**(7): p. 603-615.

255. Khan, M.A.*, et al.*, *The corrosion behaviour of Ti–6Al–4V, Ti–6Al–7Nb and Ti–13Nb–13Zr in protein solutions.* Biomaterials, 1999. **20**(7): p. 631-637.

256. Benea, L. *Bio and nanomaterials in tribocorrosion systems*. IOP Publishing.

257. Yan, Y*., et al.*, *In-situ electrochemical study of interaction of tribology and corrosion in artificial hip prosthesis simulators.* J Mech Behav Biomed Mater, 2013. **18**: p. 191-9.

258. Slonaker, M*., et al.*, *Review of wear mechanisms in hip implants: paper II–ceramics IG004712.* Materials & design, 2004. **25**(5): p. 395-405.

259. Savarino, L*., et al.*, *Ion release in patients with metal-on-metal hip bearings in total joint replacement: A comparison with metal-on-polyethylene bearings.* Journal of Biomedical Materials Research: An Official Journal of The Society for Biomaterials, The Japanese Society for Biomaterials, and The Australian Society for Biomaterials and the Korean Society for Biomaterials, 2002. **63**(5): p. 467-474.

260. Lindquist, M*., et al.*, *Tribofilm formation and tribological properties of TiC and nanocomposite TiAlC coatings.* Wear, 2009. **266**(3-4): p. 379-387.

261. Namus, R*., et al.*, *Correlation of the wear transition in CoCrMo alloys with the formation of a nanocrystalline surface layer and a proteinaceous surface film.* Wear, 2017. **376**: p. 223-231.

262. Sun, Y., *Sliding wear behaviour of surface mechanical attrition treated AISI 304 stainless steel.* Tribology International, 2013. **57**: p. 67-75.

263. Vieira, A.C*., et al.*, *Influence of pH and corrosion inhibitors on the tribocorrosion of titanium in artificial saliva.* Wear, 2006. **261**(9): p. 994-1001.

264. Albayrak, Ç*., et al.*, *Tribocorrosion behavior of duplex treated pure titanium in simulated body fluid.* Wear, 2013. **302**(1-2): p. 1642-1648.

265. Niinomi, M*., et al.*, *Development of new metallic alloys for biomedical applications.* Acta biomaterialia, 2012. **8**(11): p. 3888-3903.

266. Kumar, S*., et al.*, *Corrosion behaviour of Ti–15Mo alloy for dental implant applications.* Journal of Dentistry, 2008. **36**(7): p. 500-507.

267. Obadele, B.A*., et al.*, *Tribocorrosion behaviour of laser cladded biomedical grade titanium alloy.* Materials and Corrosion, 2015. **66**(10): p. 1133-1139.

268. Bartolomeu, F*., et al.*, *Multi-material Ti6Al4V & PEEK cellular structures produced by Selective Laser Melting and Hot Pressing: A tribocorrosion study targeting orthopedic applications.* Journal of the mechanical behavior of biomedical materials, 2019. **89**: p. 54-64.

269. Yan, Y*., et al., (iv) Tribofilm on hip implants.* Orthopaedics and Trauma, 2013. **27**(2): p. 93-100.

270. Hallab, N.J*., et al., Interfacial kinetics of titanium-and cobalt-based implant alloys in human serum: Metal release and biofilm formation.* Journal of Biomedical Materials Research Part A: An Official Journal of The Society for Biomaterials, The Japanese Society for Biomaterials, and The Australian Society for Biomaterials and the Korean Society for Biomaterials, 2003. **65**(3): p. 311-318.

271. Wimmer, M.A*., et al., The acting wear mechanisms on metal-on-metal hip joint bearings: in vitro results.* Wear, 2001. **250**(1-12): p. 129-139.

272. Liao, Y*., et al., Graphitic tribological layers in metal-on-metal hip replacements.* Science, 2011. **334**(6063): p. 1687-1690.

273. Yan, Y*., et al., Electrochemical instrumentation of a hip simulator: a new tool for assessing the role of corrosion in metal-on-metal hip joints.* Proceedings of the Institution of Mechanical Engineers, Part H: Journal of Engineering in Medicine, 2010. **224**(11): p. 1267-1273.

274. Yan, Y*., et al., Tribofilm formation in biotribocorrosion–does it regulate ion release in metal-on-metal artificial hip joints?* Proceedings of the Institution of Mechanical Engineers, Part J: Journal of Engineering Tribology, 2010. **224**(9): p. 997-1006.

275. Sumita, M*., et al., Failure Processes in biometallic materials.* 2003.

276. Nnamchi, P.S.U., *A novel approach to Property driven design of Titanium alloys for Biomedical applications.* 2014.

277. Dimah, M.K*., et al., Study of the biotribocorrosion behaviour of titanium biomedical alloys in simulated body fluids by electrochemical techniques.* Wear, 2012. **294**: p. 409-418.

278. Licausi, M.-P*., et al., Influence of the fabrication process and fluoride content on the tribocorrosion behaviour of Ti6Al4V biomedical alloy in artificial saliva.* Journal of the mechanical behavior of biomedical materials, 2013. **20**: p. 137-148.

279. Lee, Y.-S*., et al., Differences in Wear Behaviors at Sliding Contacts for β-Type and (α+ β)-Type Titanium Alloys in Ringer's Solution and Air.* Materials Transactions, 2015. **56**(3): p. 317-326.

280. Niinomi, M.*, et al.*, *Frictional wear characteristics of biomedical Ti–29Nb–13Ta–4.6 Zr alloy with various microstructures in air and simulated body fluid.* Biomedical Materials, 2007. **2**(3): p. S167.

281. Hacisalihoglu, I.*, et al.*, *Tribocorrosion properties of different type titanium alloys in simulated body fluid.* Wear, 2015. **332**: p. 679-686.

282. Niinomi, M., *Mechanical biocompatibilities of titanium alloys for biomedical applications.* Journal of the mechanical behavior of biomedical materials, 2008. **1**(1): p. 30-42.

283. Wang, L.*, et al.*, *Contact mechanics studies of an ellipsoidal contact bearing surface of metal-on-metal hip prostheses under micro-lateralization.* Medical engineering & physics, 2014. **36**(4): p. 419-424.

284. Palacios-Carvajal, J.*, et al.*, *The reason for failures of hip prostheses.* Orthopaedics International Edition, 1996. **4**: p. 11-16.

285. Dao, M.*, et al.*, *Computational modeling of the forward and reverse problems in instrumented sharp indentation.* Acta materialia, 2001. **49**(19): p. 3899-3918.

286. Li, X.*, et al.*, *A review of nanoindentation continuous stiffness measurement technique and its applications.* Materials characterization, 2002. **48**(1): p. 11-36.

287. Oliver, W.C.*, et al.*, *An improved technique for determining hardness and elastic modulus using load and displacement sensing indentation experiments.* Journal of materials research, 1992. **7**(6): p. 1564-1583.

288. Ramamurty, U.*, et al.*, *Nanoindentation for probing the mechanical behavior of molecular crystals–a review of the technique and how to use it.* CrystEngComm, 2014. **16**(1): p. 12-23.

289. Giannakopoulos, A.E.*, et al.*, *Determination of elastoplastic properties by instrumented sharp indentation.* Scripta materialia, 1999. **40**(10): p. 1191-1198.

290. Pignatelli, I.*, et al.*, *Vertical scanning interferometry: a new method to quantify re-/de-mineralization dynamics of dental enamel.* Dental Materials, 2016. **32**(10): p. e251-e261.

291. Dillon, R.O.*, et al.*, *Use of Raman scattering to investigate disorder and crystallite formation in as-deposited and annealed carbon films.* Physical Review B, 1984. **29**(6): p. 3482.

292. Gnanavel, S., *et al.*, *Electrochemical Behavior of Biomedical Titanium Alloys Coated with Diamond Carbon in Hanks' Solution.* Journal of Materials Engineering and Performance, 2018. **27**(4): p. 1635-1641.

293. Wang, S., *et al.*, *The improvement of wettability, biotribological behavior and corrosion resistance of titanium alloy pretreated by thermal oxidation.* Tribology International, 2014. **79**: p. 174-182.

294. Contu, F., *et al.*, *Serum effect on the electrochemical behaviour of titanium, Ti6Al4V and Ti6Al7Nb alloys in sulphuric acid and sodium hydroxide.* Corrosion science, 2004. **46**(9): p. 2241-2254.

295. Huang, W., *et al.*, *Wear and Electrochemical Corrosion Behavior of Biomedical Ti–25Nb–3Mo–3Zr–2Sn Alloy in Simulated Physiological Solutions.* Journal of Bio-and Tribo-Corrosion, 2015. **1**(1): p. 1.

296. Wimmer, M.A., *et al.*, *The effect of contact load on CoCrMo wear and the formation and retention of tribofilms.* Wear, 2015. **332**: p. 643-649.

297. Espallargas, N., *et al.*, *A new experimental technique for quantifying the galvanic coupling effects on stainless steel during tribocorrosion under equilibrium conditions.* Wear, 2013. **307**(1-2): p. 190-197.

298. Zavieh, A.H., *et al.*, *The effect of friction modifiers on tribocorrosion and tribocorrosion-fatigue of austenitic stainless steel.* Tribology International, 2017. **111**: p. 138-147.

299. Guadalupe, S., *et al.*, *Applicability of a recently proposed tribocorrosion model to CoCr alloys with different carbides content.* Wear, 2017. **376**: p. 203-211.

300. Diomidis, N., *et al.*, *Assessment of the surface state behaviour of Al71Cu10Fe9Cr10 and Al3Mg2 complex metallic alloys in sliding contacts.* Intermetallics, 2009. **17**(11): p. 930-937.

301. Favero, M., *et al.*, *Effect of the applied potential of the near surface microstructure of a 316L steel submitted to tribocorrosion in sulfuric acid.* Journal of Physics D: Applied Physics, 2006. **39**(15): p. 3175.

302. Yan, Y., *et al.*, *Biotribocorrosion of CoCrMo orthopaedic implant materials—assessing the formation and effect of the biofilm.* Tribology international, 2007. **40**(10-12): p. 1492-1499.

303. Hlady, V., *et al.*, *Protein adsorption on solid surfaces.* Current Opinion in Biotechnology, 1996. **7**(1): p. 72-77.

304. Dalbert, V.*, et al.*, *The effects of microstructures and repassivation kinetics on the tribocorrosion resistance of ferrite and ferrite-martensite stainless steels.* Wear, 2019. **420**: p. 245-256.

305. Pejaković, V.*, et al.*, *Tribocorrosion behaviour of Ti6Al4V in artificial seawater at low contact pressures.* Tribology International, 2018. **119**: p. 55-65.

306. Sun, Y.*, et al.*, *Effect of electrochemical potential on tribocorrosion behavior of low temperature plasma carburized 316L stainless steel in 1 M H2SO4 solution.* Surface and Coatings Technology, 2011. **205**(17-18): p. 4280-4290.

307. Mathew, M.T.*, et al.*, *Tribolayer formation in a metal-on-metal (MoM) hip joint: an electrochemical investigation.* J Mech Behav Biomed Mater, 2014. **29**: p. 199-212.

308. Chu, P.K.*, et al.*, *Characterization of amorphous and nanocrystalline carbon films.* Materials Chemistry and Physics, 2006. **96**(2-3): p. 253-277.

309. Fischer, A., *Subsurface microstructural alterations during sliding wear of biomedical metals. Modelling and experimental results.* Computational Materials Science, 2009. **46**(3): p. 586-590.

310. Purcek, G.*, et al.*, *Mechanical and wear properties of ultrafine-grained pure Ti produced by multi-pass equal-channel angular extrusion.* Materials Science and Engineering: A, 2009. **517**(1-2): p. 97-104.

311. Kucukomeroglu, T., *Effect of equal-channel angular extrusion on mechanical and wear properties of eutectic Al–12Si alloy.* Materials & Design, 2010. **31**(2): p. 782-789.

312. Humphreys, F.J.*, et al.*, *Recrystallization and related annealing phenomena.* 2012: Elsevier.

313. Zavieh, A.H.*, et al.*, *The role of surface chemistry and fatigue on tribocorrosion of austenitic stainless steel.* Tribology International, 2016. **103**: p. 368-378.

314. Perret, J.*, et al.*, *EBSD, SEM and FIB characterisation of subsurface deformation during tribocorrosion of stainless steel in sulphuric acid.* Wear, 2010. **269**(5-6): p. 383-393.

315. Munoz, A.I.*, et al.*, *Tribocorrosion mechanisms in sliding contacts*, in *Tribocorrosion of Passive Metals and Coatings.* 2011, Elsevier. p. 118-152.

316. Correa, D.R.N.*, et al.*, *Tribocorrosion behavior of β-type Ti-15Zr-based alloys.* Materials Letters, 2016. **179**: p. 118-121.

317. Mathew, M.T.*, et al.*, *What is the role of lipopolysaccharide on the tribocorrosive behavior of titanium?* Journal of the mechanical behavior of biomedical materials, 2012. **8**: p. 71-85.

318. Sadiq, K.*, et al.*, *Wear mapping of CoCrMo alloy in simulated bio-tribocorrosion conditions of a hip prosthesis bearing in calf serum solution.* Materials Science and Engineering: C, 2015. **49**: p. 452-462.

319. Hodge, C.*, et al.*, *Tribo-corrosion mechanisms of stainless steel in soft drinks.* Wear, 2010. **270**(1-2): p. 104-114.

320. Purandare, Y.P.*, et al.*, *Velocity effects on erosion–corrosion of CrN/NbN "superlattice" PVD coatings.* Surface and Coatings Technology, 2006. **201**(1-2): p. 361-370.

321. Bozzini, B.*, et al.*, *Evaluation of erosion–corrosion in multiphase flow via CFD and experimental analysis.* Wear, 2003. **255**(1-6): p. 237-245.

322. Bello, J.O.*, et al.*, *Synergistic effects of micro-abrasion–corrosion of UNS S30403, S31603 and S32760 stainless steels.* Wear, 2007. **263**(1-6): p. 149-159.

323. Sinnett-Jones, P.E.*, et al.*, *Micro-abrasion–corrosion of a CoCrMo alloy in simulated artificial hip joint environments.* Wear, 2005. **259**(7-12): p. 898-909.